# A model study on the influence of the 11-year solar cycle on the atmosphere

Dissertation
zur Erlangung des akademischen Grades
"Doktor der Naturwissenschaften"
am Fachbereich Geowissenschaften der
Freien Universität Berlin

vorgelegt von

Anne Kubin

Februar 2011

Gutachter: Prof. Dr. Ulrike Langematz, Freie Universität Berlin
Prof. Dr. Joanna D. Haigh, Imperial College London

Tag der Disputation: 21. Juni 2011

**Kurzzusammenfassung**

Die 11-jährige Variabilität der totalen und spektralen Sonneneinstrahlung ist ein wichtiger Antrieb für natürliche Klimaschwankungen. In der vorliegenden Arbeit ist der Einfluss des 11-jährigen Sonnenzykluses auf die Atmosphäre mit dem Klima-Chemie-Modell EMAC-FUB untersucht worden. Der Schwerpunkt der Analysen lag auf dem Sonnensignal in der Troposphäre, das in erster Linie mit Hilfe eines multiplen linearen Regressionsansatzes untersucht wurde. Es konnte gezeigt werden, dass der Sonnenzyklus die troposphärische Zirkulation auf der hemisphärischen und regionalen räumlichen Skala und auf einer saisonalen Zeitskala beeinflusst. Dabei koppelt das Sonnensignal in natürliche Variabilitätsmoden der Atmosphäre ein und verstärkt diese. In den im Rahmen dieser Arbeit durchgeführten Modellsimulationen konnte die Variation der spektralen Sonneneinstrahlung hauptsächlich indirekt über Änderungen der chemischen Zusammensetzung in der Stratosphäre, über geänderte meridionale stratosphärische Temperaturgradienten und über die modifizierte vertikale Ausbreitung von planetarischen Wellen auf die Troposphäre wirken. Es konnte weiterhin gezeigt werden, dass die Art der als Randbedingung verwendeten Meeresoberflächentemperaturen (beobachtet oder modelliert) das Auftreten des solaren Signals in der Troposphäre, speziell in der Sommermonsunzirkulation, entscheidend beeinflussen. Der mögliche Einfluss der solaren Variabilität auf die Meeresoberflächentemperaturen und die stratosphärische quasi-zweijährige Schwingung des Windes in den Tropen und die daraus resultierenden Wechselwirkungen sind Unsicherheitsquellen für die Interpretation der Modellresultate. Dies konnte insbesondere im Zusammenhang mit einer multiplen linearen Regressionsanalyse gezeigt werden.

**Abstract**

The 11-year variability of total and spectral solar irradiance is an important forcing of natural climate variability. In the present study the state-of-the-art chemistry climate model EMAC-FUB has been used to investigate the influence of the 11-year solar cycle on the atmosphere. The analyses focussed on the solar signal in the troposphere which has been examined by means of a multiple linear regression approach. It could be shown that the 11-year solar cycle influences the tropospheric circulation on a hemispheric and regional spatial scale and on a seasonal time scale. The solar signal, though, couples into natural modes of atmospheric variability and amplifies them. In the model simulations performed in the context of this study the spectral solar irradiance variation could primarily affect the troposphere indirectly via composition changes in the stratosphere, altered stratospheric meridional temperature gradients and modified vertical propagation of planetary waves. Moreover, it could be shown that the use of observed or modelled sea surface temperatures as lower boundary condition decisively influences the appearance of the solar signal in the troposphere, in particular, in the summer monsoon circulation. The possible solar influence on the sea surface temperatures as well as on the quasi-biennial oscillation of tropical stratospheric winds and the resulting interactions between the forcings are sources of uncertainty for the interpretation of model results. This could be shown, in particular, in connection with a multiple linear regression analysis.

# Contents

# Chapter 1

# Introduction

Virtually all the energy that is present in the Earth's atmosphere, as kinetic energy of the wind or thermal energy of an airmass, originates from the Sun. Solar irradiance in interaction with the Earth's orbital parameters provides the basis for a huge number of meteorological and climatological processes on our planet.

The solar output is, however, not constant in time. It varies on different time scales ranging from days to decades, centuries and millions of years. Besides variations in total solar irradiance also the spectral composition of the solar radiation changes in time.

The focus of this study is on the decadal timescale, i.e., the 11-year sunspot cycle. The questions to be pursued are the following: How does the 11-year solar cycle affect the Earth's atmosphere, its composition and the circulation? How does the solar signal in the troposphere look like? How is the 11-year solar signal in the stratosphere transferred downward to the troposhere? And finally: What is the contribution of the 11-year solar signal to climate variability?

Finding an answer to the latter question is important in view of climate change studies. The Intergovernmental Panel on Climate Change (IPCC) states in its last report (IPCC, 2007) a still low level of scientific understanding of the effect of natural climate change forcings such as solar irradiance variations. With the general circulation models used for the IPCC simulations it is, however, difficult to study exactly this aspect. Most of these models do not represent the stratosphere in its complete vertical extension, a region of the atmosphere that is directly affected by changes in spectral solar irradiance. The spectral solar irradiance changes themselves are not represented in the coarse radiation parameterisations implemented in most of the general circulation models. This forms another major obstacle for studies of the solar influence on climate.

One can think of solar irradiance changes as a necessary boundary condition for the Earth' climate system, as a source of variability that is always present in the background and that humankind can not influence. On the other hand, there is the ongoing

anthropogenic climate change due to the emission of greenhouse gases such as carbon dioxide, methane, nitrous oxide or chlorofluorocarbons. It is, therefore, crucial to increase the level of scientific understanding of the solar influence, also in order to separate the anthropogenic from the natural effects on climate. It is important to note that the currently ongoing climate change is very likely caused by human activities associated with the emission of greenhouse gases (IPCC, 2007). Solar variability was a major contributor to climate variability in the past, e.g., in the first half of the twentieth century (e.g., Solanki and Krivova, 2003). However, the temperature increase observed over the last 150 years, in particular in the second half of the twentieth century can not be reproduced by model simulations when only natural forcings are allowed to act (e.g., Hegerl et al., 2007).

The aim of the present study is to investigate the influence of the 11-year solar cycle on the ozone abundance, the radiative heating, the temperature and the circulation of the stratosphere and on the circulation of the troposphere including temperature and precipitation changes. The methods chosen to achieve this goal range from mechanistic sensitivity studies with a general circulation model to transient coupled chemistry-climate model simulations.

These studies are carried out in the context of the "Project on Solar Effects on Chemistry and Climate including Ocean interactions (ProSECCO)" which is funded as part of the German Research Foundation's priority program "Climate And Weather of the Sun-Earth System (CAWSES)". The project is aimed at the investigation of solar influence on the Earth's atmosphere, its composition and the circulation at time scales ranging from decades to centuries. Scientists at the Institut für Meteorologie at Freie Universität Berlin co-operate with researchers at the Max-Planck-Institut für Chemie in Mainz in driving the research.

This report is structured as follows: Different aspects of solar variability are described in chapter 2. In chapter 3 the fundamentals of the atmospheric climatology and its variability are recalled. Chapter 4 deals with the atmospheric response to the variable solar irradiance, including an overview on the status of research from observational and modelling studies. Moreover, proposed mechanisms for the downward transfer of the solar signal from the stratosphere to the troposphere are presented. Chapter 5 introduces the general circulation and chemistry-climate model used for this study, respectively. The design of the experiments conducted to investigate the 11-year solar influence is described in the second part of this chapter along with analysis methods. In chapter 6 the set-up and the results of a mechanistic momentum forcing study in analogy of the 11-year solar cycle are presented. The effect of the 27-day solar rotational cycle on ozone and temperature which is pronounced during the maximum phases of the 11-year cycle is investigated in chapter 7. The focus of chapter 8 is on the 11-year solar signal in the stratosphere and troposphere in a series of transient or equilibrium simulations with different experimental designs and boundary conditions. The model results are compared with observational

data. Aspects of interactions between important forcings and the possibility of a misattribution of modelled variability to one of the forcings are studied in chapter 9. The report is summarised in chapter 10.

# Chapter 2

# The Variable Sun

This chapter provides an introduction of the Sun's structure, its energy source and the emitted radiation. Furthermore, it covers the origin of solar variability and gives a phenomenological survey of its different aspects.

## 2.1 The structure of the Sun

The Sun is the central celestial body of our planetary system and the only star that is close enough to observe details on its surface from the Earth. It is a star of intermediate size and luminosity. In the Hertzsprung-Russel diagram which shows a star's brightness against its temperature the Sun is located in the main sequence with the spectral class G2. The analysis of the emitted solar radiation and the observation of surface features give an insight into the chemical composition and the physical processes inside the Sun.

The Sun is a gaseous sphere with no discernable deviation from the spherical shape. It consists of 92.1% hydrogen, 7.8 % helium, 0.061 % oxygen, 0.030 % carbon, 0.0084 % nitrogen, 0.0076 % neon, 0.0037 % iron, 0.0031 % silicon, 0.0024 % magnesium and 0.0015 % sulfur (Hoyt and Schatten, 1997). Within the Sun the gas pressure decreases from the centre to the surface. The gas pressure is balanced by the hydrostatic pressure caused by the gases' own weight. Some of the Sun's fundamental properties are summarised in table 2.1 (from Gondolatsch et al. (1990), Hoyt and Schatten (1997) and Raith (2002)).

**Table 2.1:** Fundamental properties of the Sun

| | |
|---|---|
| Radius | $6.960 \cdot 10^5$ km |
| Mass | $1.989 \cdot 10^{30}$ kg |
| Average density | $1.41\,\mathrm{g/cm^3}$ |
| Effective surface temperature | 5780 K |
| Luminosity | $3.85 \cdot 10^{26}$ W |
| Average distance from Earth | $149.6 \cdot 10^6$ km |

Based on the knowledge of the Sun's radius, mass, luminosity, surface temperature and the chemical composition of the outer layers it is possible to deduce a model for the Sun's interior, particularly, for the distribution of pressure and temperature and for the transport of energy. It is assumed that the Sun consists of a core, surrounded by a radiative zone and a convective zone. The Sun's surface as it is visible from the Earth, called the photosphere, is a very thin layer, which is only a few hundreds of kilometers thick (cf. Fig. 2.1). The adjacent layer above is named the chromosphere, bordering to the corona. The latter two are only visible during total solar eclipses or with the aid of a coronograph which blocks the direct sunlight and thus simulates a total eclipse.

Within the core the solar energy is generated by fusion reactions, forming helium from hydrogen atoms. From model calculations it is assumed that the temperature in the core region ranges from $13.0 \cdot 10^6$ to $15.5 \cdot 10^6$ K and the pressure from $2 \cdot 10^{16}$ to $3 \cdot 10^{16}$ Pa. Under these circumstances the gases are highly ionised, i.e., the electrons are removed from the atoms, forming a so called plasma of nuclei, protons (hydrogen nuclei) and electrons. There are two essential pathways for the fusion processes. The first is the proton-proton-chain (pp-chain) which forms helium from four protons and takes place at temperatures above $5 \cdot 10^6$ K. On the left hand side Figure 2.2 lists the involved reactions and depicts them schematically on the right hand side.

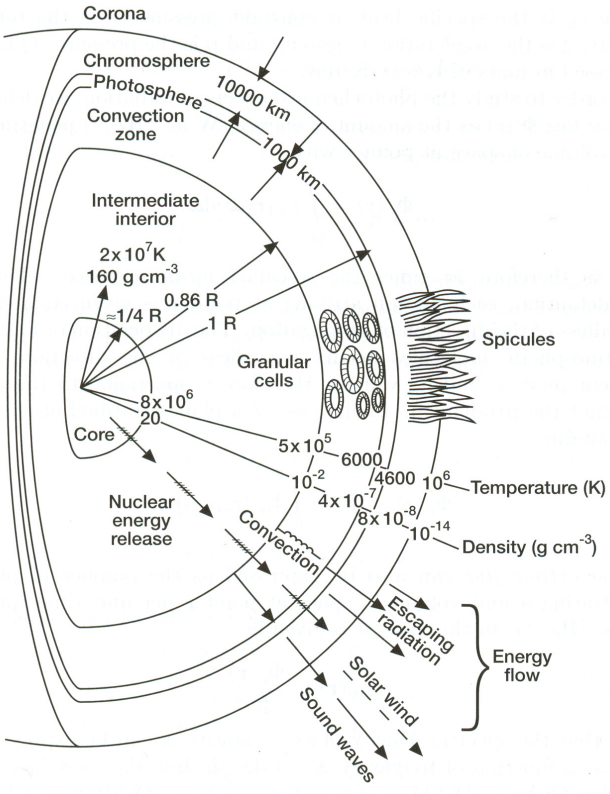


**Figure 2.1:** Schematical illustration of the Sun's interior and atmosphere with specifications of temperature, density and the thickness of the individual layers. From Brasseur and Solomon (2005)

$$^{1}_{1}\mathrm{H} + {}^{1}_{1}\mathrm{H} \longrightarrow {}^{2}_{1}\mathrm{D} + \mathrm{e}^{+} + \nu_e$$

$$^{2}_{1}\mathrm{D} + {}^{1}_{1}\mathrm{H} \longrightarrow {}^{3}_{2}\mathrm{He} + \gamma$$

$$^{3}_{2}\mathrm{He} + {}^{3}_{2}\mathrm{He} \longrightarrow {}^{4}_{2}\mathrm{He} + {}^{1}_{1}\mathrm{H} + {}^{1}_{1}\mathrm{H}$$

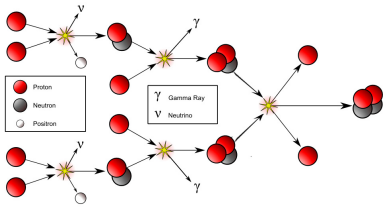


**Figure 2.2:** Proton-proton-chain nuclear fusion processes in the core of the Sun.

In the reaction equations of Figure 2.2, $\mathrm{e}^{+}$ denotes a positron, i.e., an elementary particle with the mass of an electron but positively charged, $\nu_e$ is an electron neutrino, a particle that escapes from the Sun immediately due to the very weak interaction with other matter and $\gamma$ stands for a Gamma radiation quantum. $^{2}_{1}\mathrm{D}$ denotes deuterium, an isotope of hydrogen, the nucleus of which contains one neutron in contrast to $^{1}_{1}\mathrm{H}$. The first reaction of the pp-chain rarely happens, due to the high kinetic energy that is required to overcome the Coulomb repulsion of the two positively charged protons. The low rate of this first reaction determines the time scale for the entire chain which is about $10^{10}$ a (Raith, 2002).

The other fusion process involves heavier elements, in particular, carbon, nitrogen and oxygen, in which the carbon acts as a catalyser, and is, therefore, called the CNO cycle (also known as the Bethe-Weizsäcker-cycle after Hans A. Bethe and Carl Friedrich von Weizsäcker, who were the first to describe this mechanism). It is listed, on the left hand side, and depicted, on the right hand side, of Figure 2.3. The CNO cycle proceeds faster than the pp-chain on a time scale of about $10^{8}$ a (Raith, 2002) but it requires higher temperatures to operate than the pp-chain. It becomes the dominant source of energy at temperatures of above $20{\cdot}10^{6}$ K. As the core temperature of the Sun is about $15.5{\cdot}10^{6}$ K the CNO cycle only contributes a minor part to the solar energy production. The released energy for both types of fusion processes averagely amounts to 25.6 MeV (Gondolatsch et al., 1990). With the Sun's given luminosity of $3.85{\cdot}10^{26}$ W (cf. Table 2.1) it is estimated that about $9.4{\cdot}10^{37}$ fusion processes happen every second.

$$^{1}_{1}\mathrm{H} + {}^{12}_{6}\mathrm{C} \longrightarrow {}^{13}_{7}\mathrm{N} + \gamma$$

$$^{13}_{7}\mathrm{N} \longrightarrow {}^{13}_{6}\mathrm{C} + \mathrm{e}^{+} + \nu_e$$

$$^{13}_{6}\mathrm{C} + {}^{1}_{1}\mathrm{H} \longrightarrow {}^{14}_{7}\mathrm{N} + \gamma$$

$$^{14}_{7}\mathrm{N} + {}^{1}_{1}\mathrm{H} \longrightarrow {}^{15}_{8}\mathrm{O} + \gamma$$

$$^{15}_{8}\mathrm{O} \longrightarrow {}^{15}_{7}\mathrm{N} + \mathrm{e}^{+} + \nu_e$$

$$^{15}_{7}\mathrm{N} + {}^{1}_{1}\mathrm{H} \longrightarrow {}^{12}_{6}\mathrm{C} + {}^{4}_{2}\mathrm{He}$$

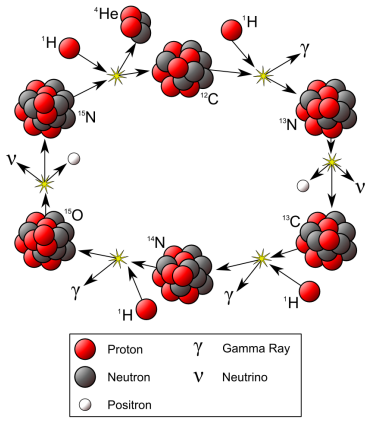


**Figure 2.3:** Nuclear fusion processes in the core of the Sun. CNO or Bethe-Weizsäcker cycle.

The energy produced in the core region is transported by radiation through the radiative zone and, subsequently, by convection through the convective zone. Due to interactions of photons with matter the radiative energy transport proceeds relatively slowly, on a timescale of the order of 10 million years. At a depth of about 150 000 km below the surface a steep temperature gradient develops as a result of a lower ionization rate. A dynamic equilibrium is established where ions capture electrons and electrons are again removed from atoms at the same rate. In particular, the removal of electrons happens by photoionisation, i.e., the photons ascending from the radiative zone are strongly absorbed in this layer. Radiative processes are no longer sufficient to maintain a thermal equilibrium. Hence, convection replaces radiation as the primary energy transport process.

The convection zone borders on the photosphere, which constitutes the Sun's surface as we see it from Earth (Figure 2.4). The name 'photosphere' literally means 'light sphere' and it denotes the region of the Sun where photons can finally escape into space and possibly reach the Earth and its atmosphere. The photosphere is only about 200 km to 400 km thick, which is very thin compared to the Sun's radius of about 700 000 km. Photons reaching the Earth originate from different depths inside the photosphere. This is due to the limited free path length in the layer. Photons from the bottom of the photosphere near the limb of the solar disc cannot escape towards the Earth. They are absorbed within the photosphere. Hence, the light from the limb is emitted in outer, cooler regions of the photosphere which is the reason for the limb darkening of the Sun. At the centre of the solar disc the free path length is sufficient to allow photons from deeper and hotter regions of the photosphere to escape into space towards the Earth which makes the Sun appear brighter at the centre. From that the temperature in the photosphere was estimated to 7000 K at the bottom and 4600 K at the top (Gondolatsch et al., 1990). The Sun's surface does appear not even but granulated. These granules are formed by the ascending and descending motion in the convection cells of the subjacent convective zone. They have a life time of the order of 10 minutes and a horizontal extent of about 1000 km. The so called supergranules are much larger, with diameters of about 35 000 km. They are observed by the Doppler shift where higher frequencies, i.e., a blue shift, indicate upwelling and lower frequencies, i.e., a red shift, show downwelling. Their lifetime is of the order of a day. The edges of supergranules form the so called network.

A close inspection of the continuous solar spectrum by William Hyde Wollaston and Joseph von Fraunhofer in the early 19th century revealed a number of dark lines that are now named Fraunhofer lines. These are absorption lines which emerge when light is transmitted through a gas. At certain wavelengths that correspond to the difference of two energy levels of an arbitrary element the photon is absorbed. At a radiative equilibrium the absorbed radiation has to be reemitted. However, the reemission happens isotropic, i.e., with no preferential direction. That means the incident radiation directed towards the Earth is attenuated but not completely extinguished. There is a rest intensity in each absorption line. Fraunhofer absorbtion lines provide information about the composition

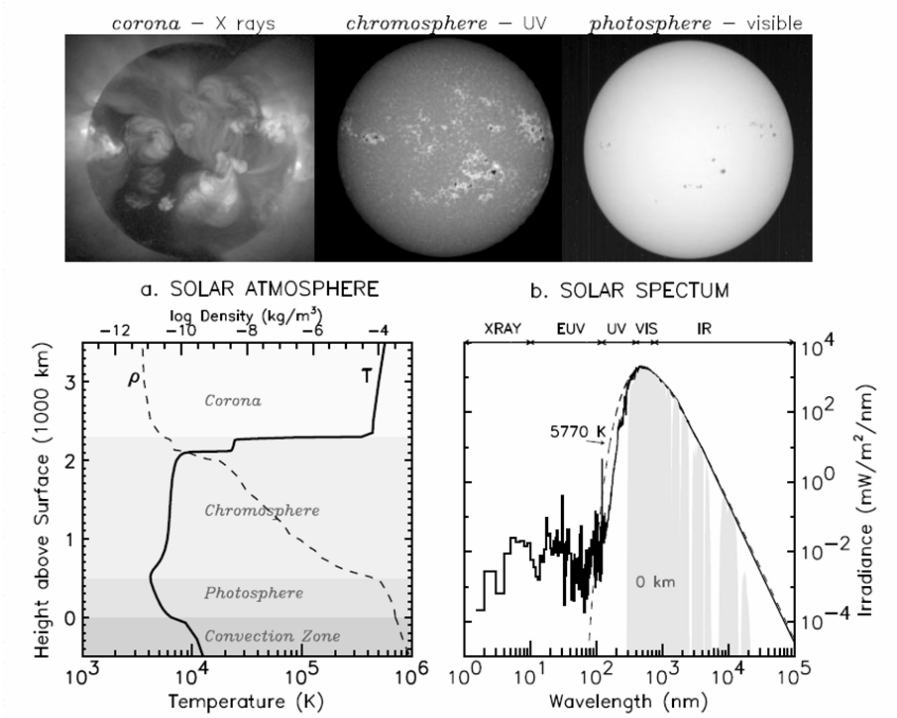


**Figure 2.4:** a) Characteristics of temperature and density at the Sun's surface and in its atmosphere. b) Solar irradiance spectrum. Above from left to right: Photos of the corona (X-ray emission), the chromosphere (Ca II K emission) and the photosphere taken on 10 January 1992. From Lean (1997).

of the solar atmosphere but not about the abundance of individual species. Moreover, they contain moreover information about the physical conditions, such as, pressure and temperature in different layers of the photosphere. Some Fraunhofer lines emerge in the Earth's atmosphere. They can be distinguished from solar lines as they change strength with the solar zenith angle. So far, 63 elements have been definitely detected on the Sun. Missing elements are either extremely rare as measured on Earth or on meteorites (e.g., bismuth, thallium, uranium) or the excitation energy is too high for absorbtion lines to be generated at the prevailing temperature in the Sun's atmosphere (e.g., argon, mercury, neon).

Above the photosphere the so called chromosphere extends (Figure 2.4). In the literature different figures for the thickness of the chromosphere can be found ranging from 1800 km (Lean, 1997) to 3000 km (Scheffler and Elsässer, 1990). The light intensity is $10^5$ times lower than that of the photosphere near the limb. Thus, the chromosphere is outshined by the photosphere. The name 'chromosphere', literally 'color sphere', derives from the rose-coloured margin as which this region only during eclipses appears. It is characterised by an emission line spectrum, dominated by the $H_\alpha$ line (656.3 nm) of hydrogen. The spectral lines of helium were first discovered in a chromospheric spectrum in 1868 (Gondolatsch et al., 1990). They are not present in the photospheric light due to the temperature, and, hence, energy not being sufficiently high for an excitation. The

element was unknown on Earth and, thus named helium deriving from the Greek word helios, meaning Sun. It was not before 1895 that helium was isolated on Earth (Gondolatsch et al., 1990). The temperature in the chromosphere slowly rises with altitude and, then, increases rapidly in a thin region which forms the transition to the corona. Simultaneously, the density decreases with altitude over several orders of magnitude (see lower left panel of Figure 2.4). It is assumed that sound waves generated in the convection zone are responsible for the steep temperature gradient in the uppermost layers of the chromosphere. These waves propagate upwards and deposit their energy as their amplitudes increase with decreasing density, thus, heating the surrounding area. At a height of about 1500 km above the photosphere luminous gas languets seem to grow like blades of grass. They are called spiculae and are part of the chromospheric network. Spiculae are clustered in regions that can be identified by the edges of photospheric supergranules, thus, forming the mesh of the network.

The corona, literally 'crown', constitutes the outer atmosphere of the Sun (Figure 2.4). From terrestrial observations during total solar eclipses or with coronographs it can be traced to five solar radii above the Sun's surface. Spaceborne measurements reveal an extent up to 50 solar radii. The temperature within the corona reaches values of the order of magnitude of 1 to $2{\cdot}10^6$ K. The coronal light can be divided into three fractions, the K-, E-, and F-corona (kontinuierlich (German for continuously), emission line, Fraunhofer corona). The K-corona dominates up to 0.3 solar radii with a sharply decreasing intensitiy above. It is generated by scattering of photospheric light at free electrons. The absence of Fraunhofer lines in the K-corona can be explained by Doppler broadening due to the high kinetic energies of the free electrons owing to the high temperature. The E-corona is superposed to the continuous spectrum of the K-corona at altitudes up to 0.5 solar radii. It contains about 30 emission lines in the visible part of the spectrum. The strongest optical emission line is found at 530.3 nm. For a long time it has not been possible to relate it to any known element. It was not before 1940 that it was identified as an emission line from $Fe^{13+}$. Highly ionised metal or noble gas atoms yield further emission lines. Beyond the visible the E-corona spectrum extends to the extreme ultra violet and even to X-ray wavelenghts. The F-corona in the original sense has nothing to do with the Sun but arises from scattering of photospheric light at interplanetary dust. It is observed at heights exceeding 1.5 solar radii above the photosphere. Moreover, the corona is the source of radio waves which are generated as bremsstrahlung when free electrons change direction or speed in the electrostatic field of ions. The shape of the corona varies with solar activity. In quiet periods long rays of light near the equator and shorter rays near the poles are seen whereas the rays point radially outward and are more evenly distributed at periods of high solar activity.

The lower right panel in Figure 2.4 shows the solar irradiance as a function of wavelength. It is seen that the Sun radiates a large part of its energy in the visible and infrared domain of the spectrum with the maximum located at about 500 nm. Above approximately 300 nm the Sun's radiation emission resembles that of a black body at a

temperature of about 5770 K (Lean, 1997), indicated by a dashed line in Figure 2.4b. Other authors specify higher temperatures for the equivalent blackbody radiation, e.g., 5780 K (Gondolatsch et al., 1990) or 5900 K (Brasseur and Solomon, 2005). Total solar irradiance (TSI) is defined as the integral of solar irradiance over all wavelengths. Earlier it was denoted the "solar constant", which is misleading as the TSI is variable in time, indeed. The average value of TSI is approximately 1365 $W/m^2$ (Fröhlich and Lean, 2004). This is the radiation incident on an imaginary plane perpendicular to the rays at the distance of 1 AU, i.e., the average Sun-Earth distance. It is, however, the radiation incident at the top of the atmosphere and not on the Earth's surface. Absorption, scattering and reflection attenuate the incident radiation in the Earth's atmosphere so that only a fractional amount reaches the surface (for a more detailed survey, see chapter 3).

## 2.2 Solar variability

The Sun is variable on a broad range of temporal and spatial scales. On the temporal scale variations are observed with periodicities of, e.g., about 27 days, which is the average period for the Sun's rotation around its axis, or 11 years, which is the period in which the number of sunspots waxes and wanes, or 80 years, which modulates the 11-year cycle and is called the Gleissberg cycle. The manifestation of the former two in the Earth's atmosphere are subjects of this study. A large fraction of the solar variability is driven by the magnetic field. It is therefore appropriate to discuss the main features of the solar magnetic field in the beginning of this section. This discussion follows Scheffler and Elsässer (1990). In the following subsections the focus will be on the dominant phenomena of the decadal timescale.

The Sun's magnetic field is assumed to work according to the dynamo principle. Consider an accidentally existing very weak initial magnetic field. The convective circulation inside the Sun transports highly conductive matter, in other words charge carrier, relative to this weak initial field. The induced electrical currents generate their own magnetic field which may in turn reinforce the initial field considerably. The solar dynamo is thus located at the base of the convection zone. The magnetic field has a life time of the order of $10^3$ years. It is said to be 'frozen' in the matter.

The starting point for a consideration of the magnetic field-driven variability is a poloidal magnetic field. These field lines reach from pole to pole (cf. Figure 2.5a). The 'frozen' field lines have to be located on surfaces of equal angular velocity. The differential rotation of the Sun, with an average period of 27-days but with polewards decreasing angular velocity, now leads to a gradual deformation of the field lines parallel to the equator (Figure 2.5b). The field lines are virtually wound up. The field line density increases, i.e., the magnetic field is intensified. The initially poloidal field is thus converted into a toroidal field (Figure 2.5c). The decay of the toroidal field is then governed by the horizontal diffusion in the supergranules. The polarity just opposite to the polarity of

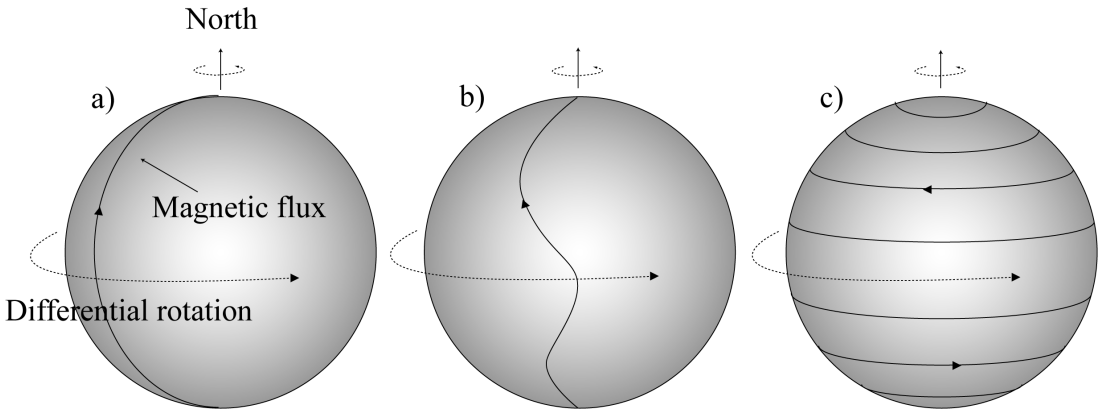


**Figure 2.5:** Conversion of an initially poloidal magnetic field (a) into a toroidal field (c) by means of differential rotation.

the corresponding pole is transported polewards by and by neutralising the poles field and ultimately reversing it. The poloidal field is dominant during solar activity minima whereas the toroidal field dominates during the activity maxima (Solanki, 2002). In fact magnetic flux tubes form beneath the Sun's surface, become distorted in the direction parallel to the equator during activity maxima and foraminate the surface.

The solar magnetic field in general and the magnetic field of sunspots in particular can be measured using the Zeeman effect, i.e., the splitting of spectral lines in the presence of a magnetic field (Gondolatsch et al., 1990) where the amount of splitting is directly proportional to the field strength. In addition, the light from each part of the splitted spectral line is uniquely circular polarised depending on the polarity of the magnetic field.

### 2.2.1 Sunspots

During periods of high solar activity solar magnetic field anomalies manifest themselves most visibly in the dark sunspots that emerge at the solar surface, i.e., in the photosphere. Larger sunspots may be seen by naked eye when the sun is low above the horizon or when an appropriate filter is applied. The following description is based on Solanki (2002, 2003) and Gondolatsch et al. (1990).

Sunspots are characterised by a dark core, the so called umbra, and a less dark surrounding area, called the penumbra, which are clearly visible on the image in Figure 2.6. It is the existence of the penumbra which distinguishes a sunspot from a pore on the Sun's surface. Sunspots exhibit diameters from $3.5{\cdot}10^6$ to $60{\cdot}10^6$ m. Once the diameter of a growing pore exceeds the lower limit for spots the penumbra develops abruptly, sector by sector.

The brightness within the umbra and penumbra is significantly reduced, by up to 80% and 25%, respectively, compared to the normal photosphere, i.e., the quiet sun. According to the Planck function, brightness is closely associated with temperature. Hence,

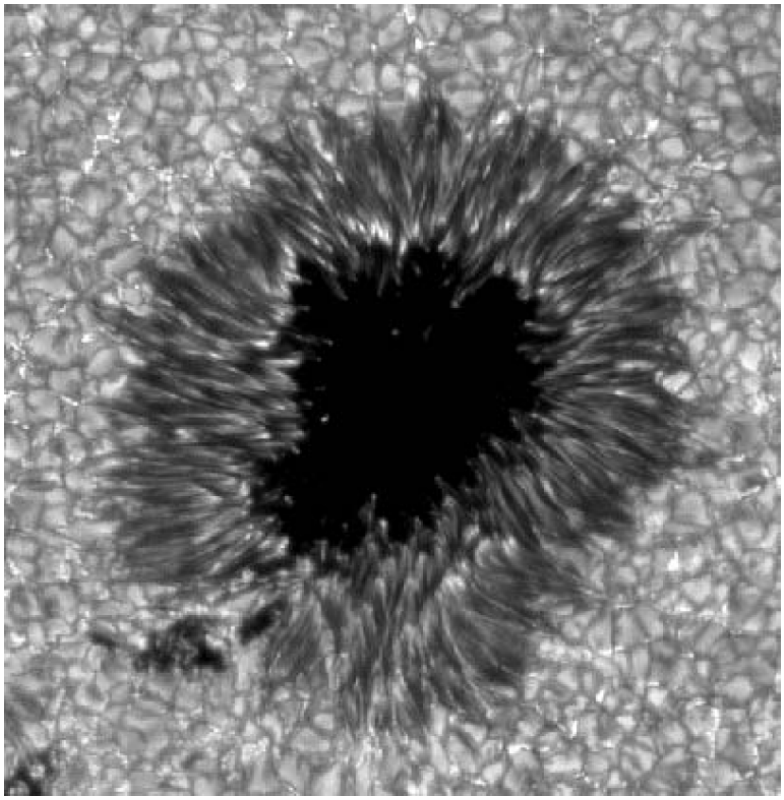

**Figure 2.6:** Image of a sunspot taken at 430.6 nm with a bandwidth of 1 nm. The maximum diameter is estimated to $3{\cdot}10^4$ km. The surrounding bright cells with dark boundaries are granular convection cells. Adapted from Solanki (2003).

the temperature within a sunspot is considerably lower than that of the quiet sun. The umbra is cooler by 1000 to 1900 K, the penumbra is 250 to 400 K cooler. At these temperatures molecules may also exist and their absorption lines are found in the spectra of spots. It is assumed that the strong magnetic field inside a sunspot inhibits the convection of energy and, thus, causes the cooling.

Sunspots start to decay as soon as they are formed, in some cases even before they are fully formed. The life time of sunspots may vary from hours to months. The larger the spot the longer its life time.

There are records about the observation of sunspots from ancient China dating back 2000 years before present. Around the year 1611 Galileo Galilei and Christoph Scheiner rediscovered the dark spots on the Sun with the help of the newly invented telescope. The cyclical appearance of the spots with a period of about 11 years was discovered by Heinrich Schwabe in 1843. George Ellery Hale identified the magnetic field as the origin of the sunspots in 1908. It was also Hale who, together with Seth Barnes Nicholson, found the underlying 22-year period of the polarity changes of the solar magnetic field (Hale and Nicholson, 1925).

Around minimum solar activity there are times without a single spot on the solar disc, while at periods of maximum activity several spots may be present simultaneously.

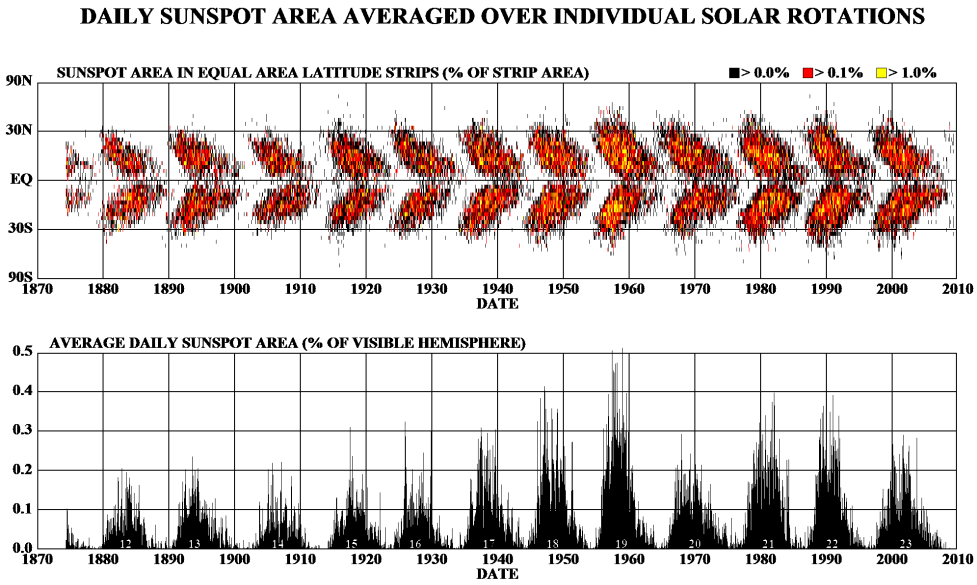


**Figure 2.7:** Butterfly diagram. The sunspot area is depicted as a function of heliographic latitude and time (upper panel) and as a histogram giving the fractional area. The Schwabe cycles are numbered (lower panel).

At the beginning of a new solar cycle the first sunspots appear at approximately $\pm 30\,^\circ$ heliographic latitude. This is due to the fact that sunpots are always located inside active regions and these are restricted to an activity belt between $\pm 35\,^\circ$ heliographic latitude. During the course of the cycle the spots appear closer and closer to the Sun's equator. Richard Christopher Carrington was the first to notice this behaviour in the 1850s. Displaying the sunspot area as a function of heliographic latitude and time results in a butterfly-like shape, see Figure 2.7. It may happen that spots appear at higher latitudes, marking the beginnig of a new cycle, even before the last spots belonging to the last cycle have vanished close to the equator. (See for example the onset of cycle 21 in the late 1970s in Figure 2.7.) Currently, solar activity is increasing. After an unusually long and deep minimum the solar cycle 24 has begun.

Sunspots tend to occur in bi-polar groups of preceding (p) and following (f) spots. The p-spots on the northern and southern hemisphere have opposite polarity, i.e., a p-spot with northern polarity in the northern hemisphere is followed by an f-spot with southern polarity and vice versa in the southern hemisphere. This polarity is constant during an 11-year cycle. It changes for the next cycle, thus, repeating with a period of 22 years (Hale and Nicholson, 1925). The bi-ploar groups basically run parallel to the solar equator but p-spots are often observed at slightly lower latitudes than the f-spots.

From the properties of sunspots alone it can be concluded that the irradiance decreases in periods of high solar activity. However, measurements show that the opposite is true, i.e., the solar irradiance is enhanced during activity maxima. This is due to the brightening effect of faculae which is described in more detail in the following subsection.

### 2.2.2 Faculae

In contrast to dark sunspots the bright faculae are less visible, in white light only near the limb. From this and the fact that they seem to disappear in white light near the centre of the disk one can infer that their emissions originate in upper layers. The faculae occur in the vicinity of spots as can be seen in the photospheric and chromospheric exposures of Figure 2.4. They appear earlier and live longer than the associated spots. Due to their longer lifetime faculae appearing at the limb are evidence for sunspots that formed and decayed on the hemisphere turned away from Earth. The name faculae is reserved for bright phenomena in the photosphere. Corresponding regions in the chromosphere above are called plages (Lean, 1997). They are detectable at certain wavelenghts, e.g., at the calcium K Fraunhofer line (393.4 nm) or the $H_\alpha$ line (656.3 nm). Kiepenheuer (1954) cites the Greenwich observers (1923): "Faculae may occur at higher heliographic latitudes than the spots but they show the same latitudinal progression over the course of a solar cycle. Even at polar latitudes short-lived faculae may be observed. In general, faculae change their form rapidly. It is hardly possible to recognise an individual feature at successive rotations."

Inside faculae the temperature at the photospheric base is higher than in the surrounding areas. The difference is estimated to be 100K (Kiepenheuer, 1954). Moreover, the temperature of faculae increases with height.

## 2.3 Solar irradiance variations

Since the early years of the 20th century it has been assumed that facular brightening dominates over sunspot darkening (C.G. Abbot, see Hoyt and Schatten (1997)) and it was ultimately proven by satellite measurements in 1980 (Willson et al., 1980). This implies a weak overall increase of TSI of about 0.1% during maximum solar activity.

*Total solar irradiance changes*

The TSI is monitored from satellites outside the Earth's atmosphere. The most common spaceborne instrument used for TSI measurements is called active cavity radiometer. In general, it consists of a blackened cavity which is alternately exposed to or shaded from sunlight. Furthermore, the cavity is electrically heated to maintain a heat flow at a preset value. When exposed to the Sun the absorption of the solar radiation generates a heat flow, thus, less electrical energy is needed to heat the cavity. The difference between the electrical power during the closed and open phases equals the radiative power (Fröhlich, 2004). This type of cavity radiometer is self-calibrating.

However, the accuracy of TSI measurements by individual radiometers is of the order of 0.1-0.2 %, which is insufficient to measure 11-year changes of about 0.1 %. Since 1978 different radiometers on different satellites have measured TSI (The Hickey-Frieden (HF)

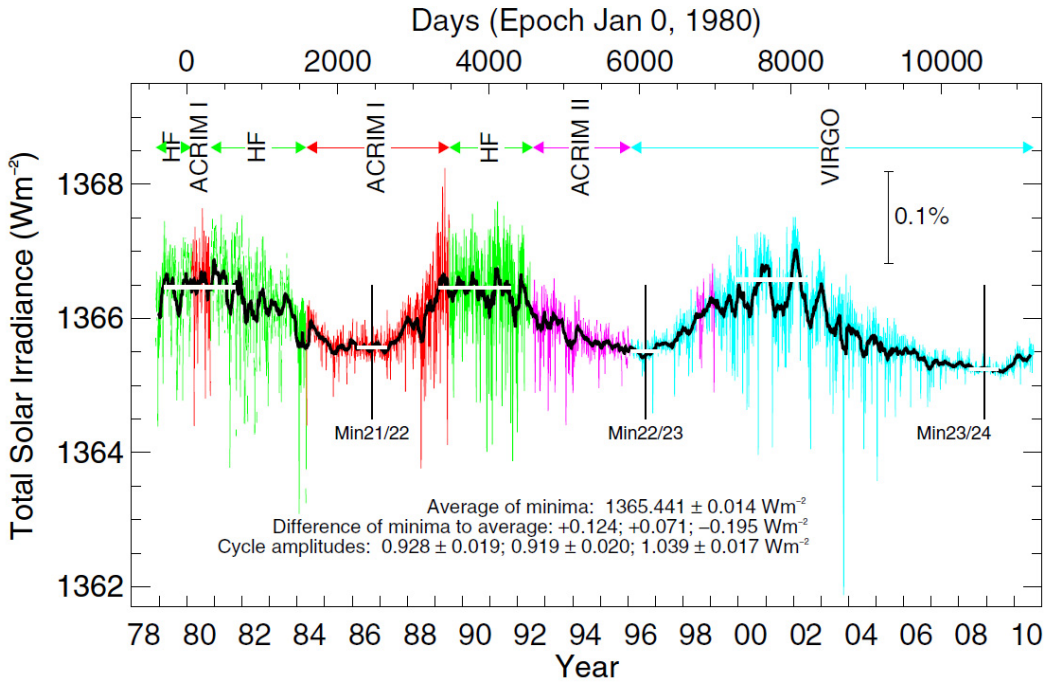


**Figure 2.8:** Total solar irradiance (TSI) in $W/m^2$ as measured by several spaceborne instruments. Update available at the website of Physikalisch-Meteorologisches Observatorium Davos - World Radiation Center (http://www.pmodwrc.ch/pmod.php?topic=tsi/composite/SolarConstant)

radiometer on NIMBUS 7, the active cavity radiometer irradiance monitor (ACRIM I) on the Solar Maximum Mission (SMM), the Earth's radiation budget experiment (ERBE) on the Earth radiation Budget Satellite (ERBS), ACRIM II on the Upper Atmosphere Research Satellite (UARS), the Variability of solar IRradiance and Gravity Oscillations (VIRGO) instrument on the Solar and Heliospheric Observatory (SOHO) and ACRIM III on ACRIMSat). This allows to construct a composite time series, incorporating information about the degradation of individual instruments while operating in space. In particular, there have always been two or more measurement platforms operating simultaneously, hence permitting cross-calibration between two instruments. It was thus possible to obtain the as yet 32 years long composite TSI series shown in Figure 2.8 with an overall accuracy that is sufficient to estimate the 11-year solar cycle changes. (Fröhlich and Lean, 2004; Lean et al., 2005).

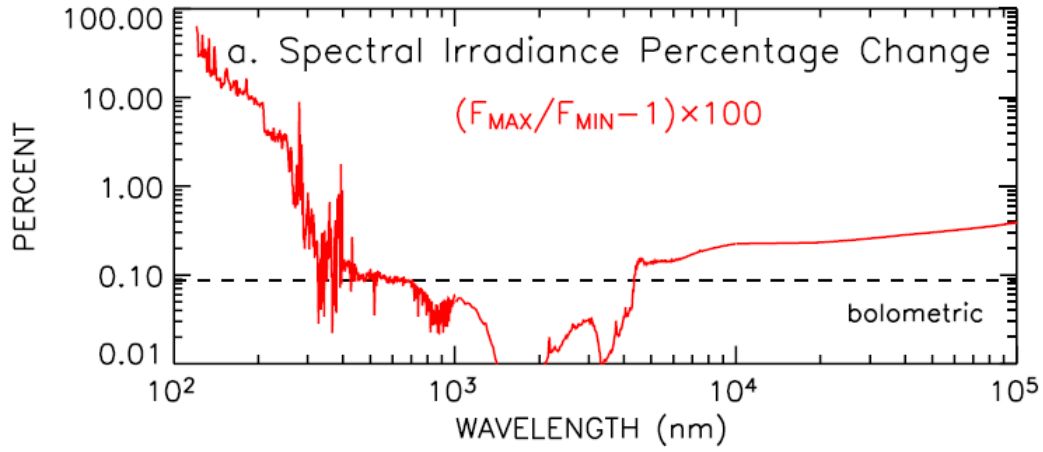


**Figure 2.9:** Relative changes in spectral solar irradiance between 11-year solar maximum and solar minimum. Amplitudes of UV changes are based on UARS measurements, longwards of 400 nm theoretical estimates are used. Adapted from Fröhlich and Lean (2004)

*Spectral solar irradiance changes*

The Sun's spectrum is not uniformly affected by solar activity, as is seen from Figure 2.9. When spectrally resolved the solar output is most variable at wavelengths that are much shorter or considerably longer than the peak of the irradiance in the visible at about 500 nm - in the ultraviolet (UV) to X-ray range and, respectively, at radio frequencies. The amplitude of irradiance change between solar maximum and minimum at 250 nm is 3%, at 200 nm it is 8% and at the Lyman-$\alpha$ line (121.5 nm) it is 50 to 100% (Figure 2.9).

In the near UV, the visible and the infrared (IR) part of the spectrum sunspot darkening and facular brigthening modulate the solar irradiance. At wavelengths shorter than 300 nm, i.e., in the UV, the enhanced emission from faculae and plages dominates solar variability. The influence of the dark sunspots rises with increasing wavelength. Unfortunately, the observational database for the spectral irradiance changes is not very good. Only intermittent measurements at wavelength below 400 nm exist, e.g., from the Solar Mesosphere Explorer (SME) or the SOLar STellar Irradiance Comparison Experiment (SOLSTICE) and the Solar Ultraviolet Spectral Irradiance Monitor (SUSIM), both onboard UARS. Therefore, empirical variability models have to be employed to fill the gaps. These are parameterisations of different solar activity proxies. For example, Lean et al. (1997) use a multiple linear regression approach of the form

$$F(\lambda, t) = a(\lambda) + b(\lambda) \cdot P_F^{PROX}(t) + c(\lambda) \cdot P_S^{320}(t).$$

In the above equation $P_S^{320}(t)$ stands for the time-dependent darkening by sunspots as measured at 320 nm. $P_F^{PROX}(t)$ represents the time series of a proxy for facular brightening, in this case the magnesium MgII index (core-to-wing ratio of the doublet at 280 nm) is used as it is closely related to faculae and chromospheric plages. The regression model

is fitted to track the TSI variations as close as possible. However, the results are imperfect, underestimating both the influence of spots and faculae on the rotational time scale. This yields a modelled TSI that is slightly lower than the observed value during facular increases and slightly higher than the observations during periods with numerous sunspots (see Figure 5 of Lean et al., 2005). Other approaches obtain the sunspot darkening regressor by extracting the size and location of spots from visible images (Lean et al., 1998) or magnetograms (Krivova et al., 2003). Besides the MgII index the chromospheric calcium CaII index is used (Lean, 2000) or the size and location of plages are derived from images taken at the Ca K Fraunhofer line at 393.4 nm (Lean et al., 1998).

# Chapter 3

# Fundamentals of the Atmospheric Climatology and Variability

Before discussing the changes in the Earth's atmosphere induced by the 11-year solar cycle it is necessary to recall the fundamental characteristics of the individual layers of the atmosphere and the absorption of solar irradiance. Subsequently, the basic circulation features of each layer are introduced along with aspects of coupling between the layers.

## 3.1 The structure of the atmosphere

The Earth's atmosphere ranges from the surface to about 1000 km. It is composed of 78.09 % nitrogen, 20.95 % oxygen, 0.93 % argon, and a number of trace gases (e.g., carbon dioxide, methane, nitrous oxide), see Table 3.1 (Hupfer and Kuttler, 1998; Brasseur and Solomon, 2005).

The layer directly above the surface is called the troposphere, see Figure 3.1. It reaches from the surface to altitudes between 8 and 18 km, being higher in the tropics and lower near the poles. In the troposphere the temperature decreases with height, on average with a lapse rate of 0.65 K/100m. About 50 % of the atmosphere's mass are situated below 500 hPa ($\approx 5$ km). In the lowermost 1500 m, named the planetary boundary layer, bottom friction is important. In the free troposphere above frictional processes may be neglected. The troposphere is the region of the atmosphere where all the processes that we commonly denote as "weather" take place, i.e., in particular processes that involve phase changes of water like cloud formation, rain, hail, fog, etc.

At 8 to 18 km, depending on latitude, temperature reaches a minimum and starts after an isothermal region of variable height to increase with altitude above, cf. Figure 3.1. This marks the tropopause, i.e., the interface between the troposphere and the stratosphere. The reason for the temperature increase in the stratosphere is the absorption of ultraviolet solar radiation and the associated heating in the ozone layer at about 25 km

**Table 3.1:** Mean composition of the atmosphere. After Hupfer and Kuttler (1998) and Brasseur and Solomon (2005).

| Compound | Volume fraction | Mass fraction |
|---|---|---|
| Nitrogen ($N_2$) | 78.09 % | 76.47 % |
| Oxygen ($O_2$) | 20.95 % | 23.53 % |
| Argon (Ar) | 0.93 % | 1.29 % |
| Carbon dioxide ($CO_2$) | 0.038 % | 0.015 % |
| Neon (Ne) | 18.180 ppmv | 12.75 ppm |
| Helium (He) | 5.240 ppmv | 0.73 ppm |
| Methan ($CH_4$) | 1.760 ppmv | 0.97 ppm |
| Krypton (Kr) | 1.140 ppmv | 3.30 ppm |

($\approx$ 25 hPa) (for details see section 3.2). The temperature increase with height forms a very effective barrier for vertical mixing from the layer below. For instance, stratospheric water vapour concentrations are an order of magnitude lower than in the troposphere because of the lack of an in-situ source and the freeze-drying that occurs at the tropopause. The temperature maximum is found at 50 km ($\approx$ 1 hPa) with a value of about 0 °C. This

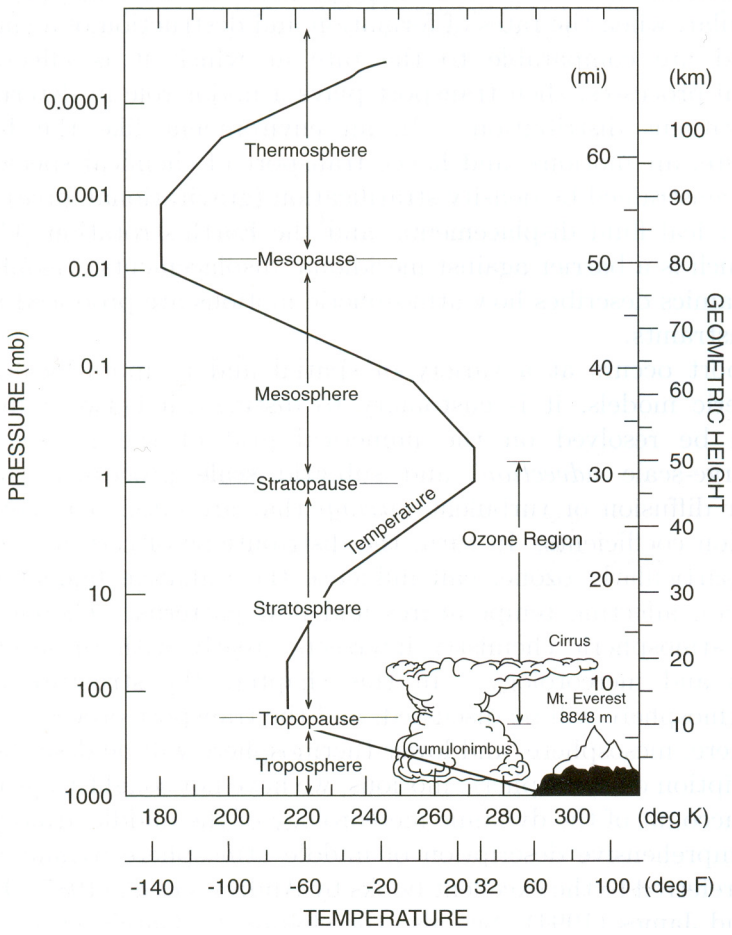


**Figure 3.1:** Structure of the atmosphere as defined by the temperature change with height. From Brasseur and Solomon (2005).

forms the top of the stratosphere and the interface to the next higher layer and is called the stratopause.

The mesosphere between 50 and 85 km is characterised by a decrease in temperature with height. In this regard it resembles the troposphere but with a much lower air density. The temperature lapse rate amounts to $\approx 0.3\,\mathrm{K}/100\mathrm{m}$. The mesopause, i.e., the upper boundary of the mesosphere is the coldest region in the atmosphere with temperature values as low as -90 °C, see Figure 3.1. Noctilucent clouds occur in the mesosphere at polar and subpolar latitudes and may be observed from the surface.

The adjacent layer above is called the thermosphere. Between the surface and about 100 km the composition of air is roughly constant. Above that height diffusive processes become important leading to a segregation of air into its constituents. The exosphere above 500 km forms the transition region from the atmosphere to space where molecules and atoms can escape from the Earth's gravitational field. The temperature increases with height throughout the thermosphere and exosphere, reaching values up to 2000 °C. Besides the classification according to the temperature change with height one can devide the atmosphere into neutral and ionised layers. The absorption of EUV radiation with wavelengths shorter than 100 nm leads to ionisation of the absorber, producing ions and free electrons. This takes place above 70 km and forms the so called ionosphere. The maximum electron density is found at 250 to 300 km.

It becomes clear from the above section that the structure of the atmosphere is inseparably connected with the absorption of solar radiation which is discussed in the next section.

## 3.2 Absorption of solar radiation in the atmosphere

At the end of section 2.1 it was mentioned that $1365\,\mathrm{W/m^2}$ (Fröhlich and Lean, 2004) of total solar irradiance (TSI) arrive at the top of the atmosphere. The Earth reflects a fraction of the solar energy back to space and absorbs the remainder at a rate of

$$(1 - A)\mathrm{TSI}/4,$$

where A is the Earth's albedo. The division by 4 is done to account for the Earth's sphericity, i.e., the Earth intercepts $\pi \mathrm{R}_E^2 \mathrm{TSI}$ solar energy per unit time (where $\mathrm{R}_E$ is the mean radius of the Earth), but this has to be averaged over the surface area of the Earth sphere, $4\pi \mathrm{R}_E^2$.

The penetration depth of the solar radiation depends on wavelength; the shorter the wavelength the higher in the atmosphere the radiation is absorbed. Absorption of radiation may have several consequences: On the one hand, a molecule may be excited, on the other hand, it may be photolysed, i.e. it is split up. An excited molecule may release its excess energy at a collision with other molecules or atoms. The photolysis products may

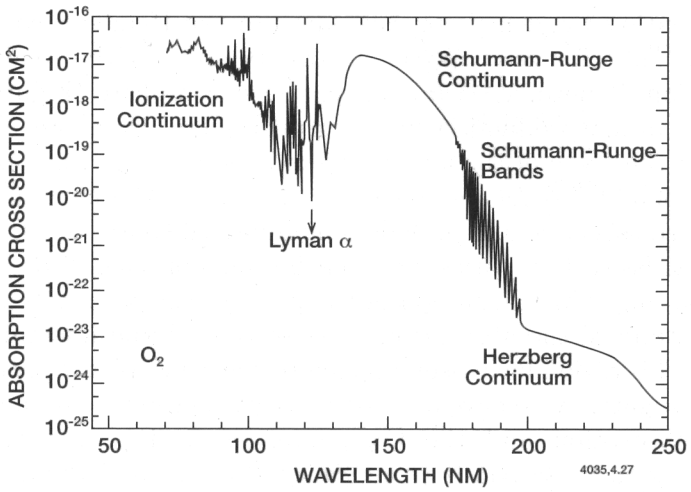


**Figure 3.2:** Spectral distribution of molecular oxygen absorption cross section. From Brasseur and Solomon (2005).

recombine likewise releasing energy which ultimately ends up as heat. Hence, the chemical (photodissociation) and thermal (heating) effect of radiation absorption are closely connected. However, the assumption that absorbed solar energy is entirely converted into heat at the location of absorption is only correct in the lower atmosphere where collisions are frequent and recombinations fast. It is not valid at higher altitudes where recombinations may take place several thousands of kilometers away from the absorption location (Brasseur and Solomon, 2005). The two main absorbers are molecular oxygen, $O_2$, and especially in the stratosphere ozone, $O_3$.

Molecular oxygen absorbs radiation in the Schumann-Runge continuum (137-175 nm) and the adjacent Schumann-Runge bands (175-200 nm), see Figure 3.2. Furthermore, $O_2$ absorbs in the Herzberg continuum (195-242 nm) which gives a slight contribution to heating in the stratosphere. In the middle and upper mesosphere the absorption of radiation at the Lyman-$\alpha$ wavelength by $O_2$ contributes to the heating.

The absorption of short-wave radiation by $O_3$ takes place in the Hartley band (200-300 nm) as well as in the temperature dependent Huggins bands (310-350 nm), see Figure 3.3. Absorption in the Chappuis bands (410-750 nm) is much weaker but occurs near the peak of the solar spectrum and is, therefore, important in particular in the lower stratosphere and even in the troposphere.

Figure 3.4 shows on the right hand side the contributions of different absorbers to heating of the atmosphere from the surface to 100 km. UV-absorption in the Hartley and Huggins bands of $O_3$ is the most important source of heat in the stratosphere and mesosphere. It amounts to about 10 K/day near the stratopause on average, and up to 15 K/day near the summer pole, provided the present ozone distribution. $O_2$ absorption becomes important above 75 to 80 km and takes over as the dominant heating process in the lower thermosphere (Brasseur and Solomon, 2005). Moreover, carbon dioxide and

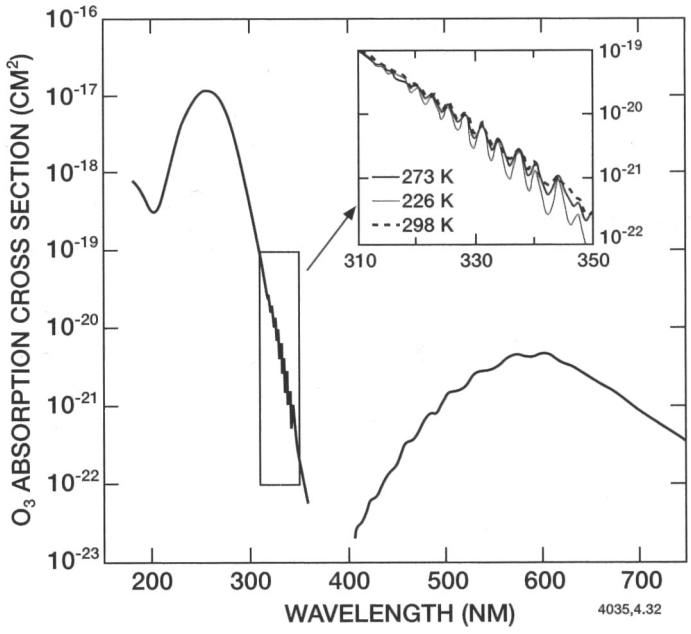


**Figure 3.3:** Spectral distribution of ozone absorption cross section in the Hartley band (200-300 nm), Huggins bands (310-350 nm) and Chappuis bands (410-750 nm). From Brasseur and Solomon (2005).

water vapour absorb solar near-infrared radiation which is important for the heat budget of the lower atmosphere. For completeness also the left hand side of Figure 3.4 shall be briefly described here: Thermal emission, mainly by carbon dioxide, antagonises the short-wave heating in the stratosphere. Minor contributions to cooling come from the infrared bands of ozone and water vapour. In the troposphere infrared emission by water vapour is

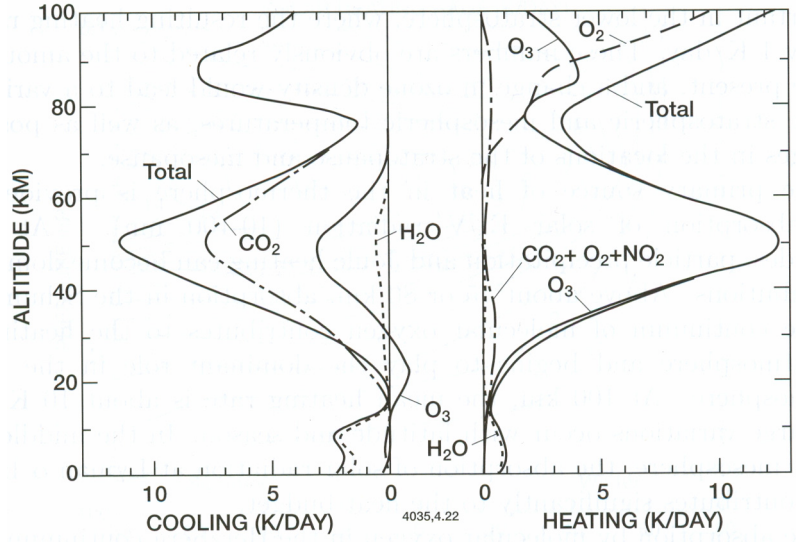


**Figure 3.4:** Vertical profiles of solar short-wave heating (right) and terrestrial long-wave cooling (left). From Brasseur and Solomon (2005), originally from London (1980).

the most important cooling process. For a comprehensive description of radiative transfer in the Earth's atmosphere see Liou (2002) or Brasseur and Solomon (2005).

## 3.3 The climatology of the troposphere and the middle atmosphere

In this section a brief survey on the basic atmospheric circulation and some of its features will be given. Their reaction on the 11-year solar variability are investigated in the remaining chapters of this work. For a more comprehensive description it is referred to the work of Holton (1992) concerning the troposphere and Andrews et al. (1987) concerning the middle atmosphere.

### Troposphere

The basis for the tropospheric circulation is the differential insolation in different latitudes. The resulting temperature gradient between the region of strongest insolation and consequently strongest heating, i.e., the tropics and the regions with an energy deficit, i.e., the poles is the driving force behind the circulation. Near the equator, air is forced to ascend. At the top of the troposphere it moves polewards and descends at about 30 ° northern and southern latitude, respectively, flowing back to the equator near the surface. This direct circulation is named the Hadley cell. In principle, such a direct cell could operate to reduce the temperature gradient between the tropics and the poles provided the Earth would not rotate. Due to the rotation the poleward flowing air is deflected towards the east and the equatorward flowing air near the surface towards the west. This

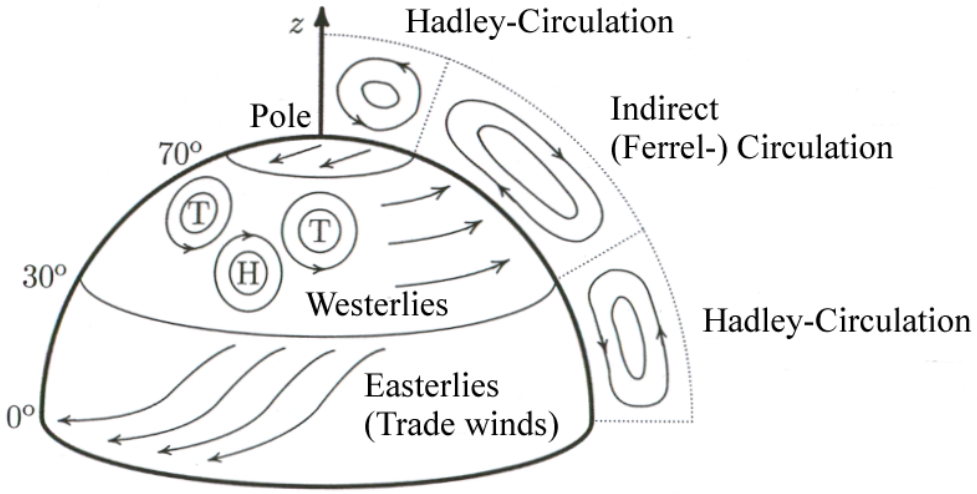


**Figure 3.5:** General circulation in the troposphere, near the surface and in the latitude-height-plane, adapted from Etling (2002).

introduces a zonal component into the flow, renders the poleward heat transport ineffective and generates a zone of baroclinic instability in the mid latitudes (Etling, 2002). The emerging baroclinic eddies, i.e., cyclones and anticyclones take over the meridional heat transport. In the zonal mean a weak indirect so called Ferrel cell develops with ascending motion poleward of 45 ° and descending motion equatorward of 45 °. Near the poles there are minor direct Hadley cells. Figure 3.5 illustrates the zonal mean flow in the latitude-height-plane as well as the surface flow associated with the direct and indirect circulation cells.

A leading mode of variability in the northern hemispheric troposphere is the North Atlantic Oscillation (NAO) which sometimes is considered together with the Pacific-North American Oscillation (PNA) as part of a more general circulation pattern, the Arctic Oscillation (AO), sometimes also denoted as Northern Annular Mode (NAM). The NAO is defined by the surface pressure difference between a station on the Azores and a station on Iceland. A high NAO index represents a stronger than average pressure gradient and, hence, stronger zonal winds over the European Atlantic coast, western and central Europe. This is accompanied by relatively warm air masses from the Atlantic, leading to a mild winter in western and central Europe and to wetter conditions in northern Europe. In contrast, a low NAO index stands for a weaker pressure gradient. The cyclone tracks over the Atlantic Ocean are displaced towards the Mediterranean, leading to wetter conditions there. Winters in central Europe tend to be colder than the average (Haigh, 2004). An analogue mode of variability, the Southern Annular Mode (SAM), is found on the southern hemisphere.

### Stratosphere

The circulation in the stratosphere is largely determined by the temperature distribution due to radiative heating and cooling and shows a strong seasonal dependence. Additionally, dynamic influences appear that cause significant departures from radiative equilibrium in particular in the winter stratosphere. During solstice seasons maximum heating occurs at the summer pole and maximum cooling at the winter pole, see Figure 3.6a and 3.6c, respectively. At the equinoxes the heating is strongest at the equator and cooling occurs at both poles. The zonal mean wind is in approximate thermal wind balance with the temperature field, as can be seen from Figures 3.6b and 3.6d, which means that the vertical shear of the zonal wind is proportional to the horizontal temperature gradient (Andrews et al., 1987).

The winter circulation in particular on the northern hemisphere deserves some extra attention. Beginning at autumnal equinox the northern polar cap cools radiatively due to the proceeding absence of short-wave solar radiation. As a consequence of the low temperature the air column shrinks, forming a strong low pressure system which is called the polar vortex. The flow around this vortex is characterised by intense westerly winds as

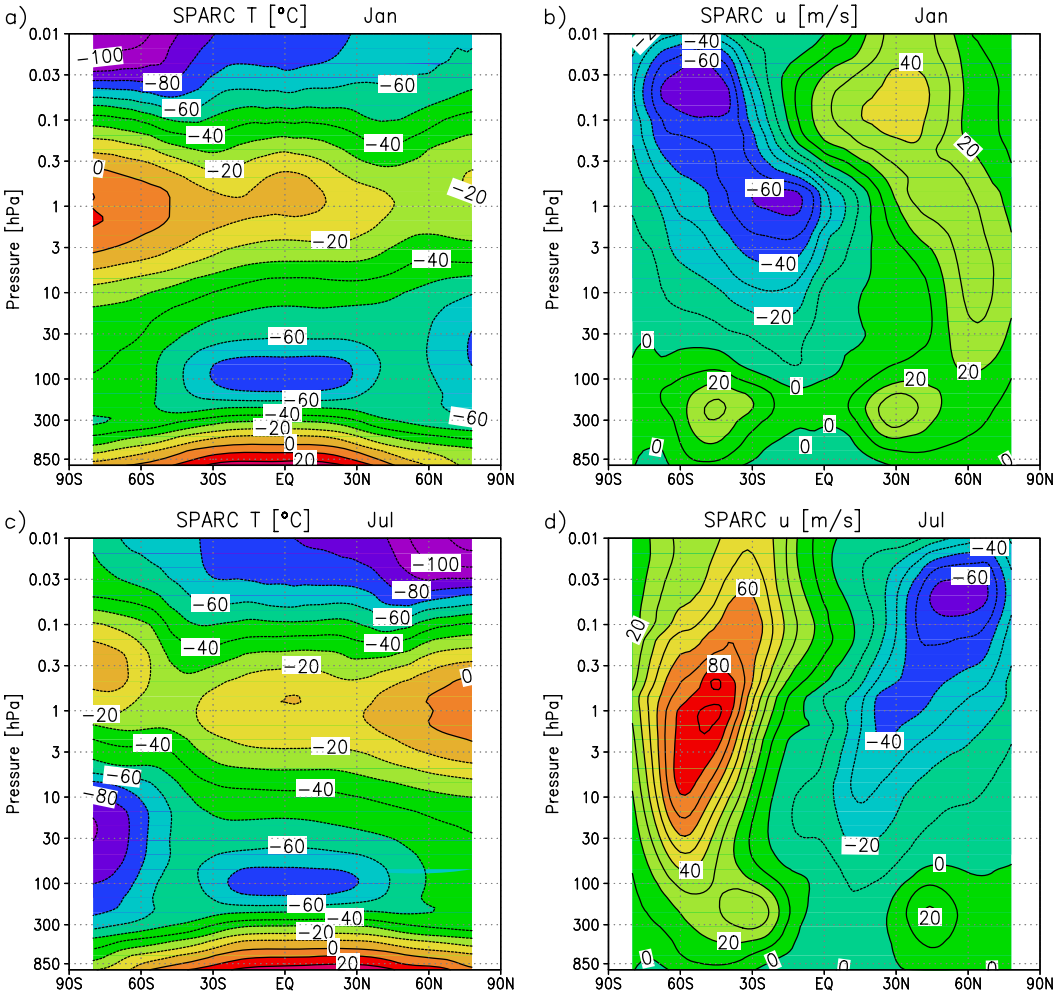


**Figure 3.6:** SPARC climatology of zonal mean temperature in °C and zonal mean zonal wind in m/s for January (a and b) and July (c and d) as a function of latitude and pressure. Negative wind velocities denote easterly winds. Based on Randel et al. (2002) and Randel et al. (2004).

can be seen in the zonal mean as depicted in Figure 3.6b. So far the development is radiatively determined. However, the westerly wind in the stratosphere allows planetary waves with wavenumbers 1 to 3 from the troposphere to propagate upwards, thus coupling both layers. With decreasing air density the wave amplitudes grow and finally the waves break, transferring their momentum and energy to the mean flow. By that the westerly mean flow is decelerated and eventually reversed to easterlies. Simultaneously, the temperature in the polar cap increases due to the dynamical heating by the waves. Consequently, the polar vortex breaks down. It is either displaced away from the pole or it is split into two parts, when the causing wave was a wavenumber 2 disturbance. Such events are called sudden stratospheric warmings. They are classified as major stratospheric warmings when at 10 hPa the north pole temperature exceeds the zonal mean temperature at 60 °N and simultaneously the zonal wind at the 10 hPa-level at 60 °N is reversed to easterlies. A stratospheric warming is said to be a minor event if only the temperature criterion is

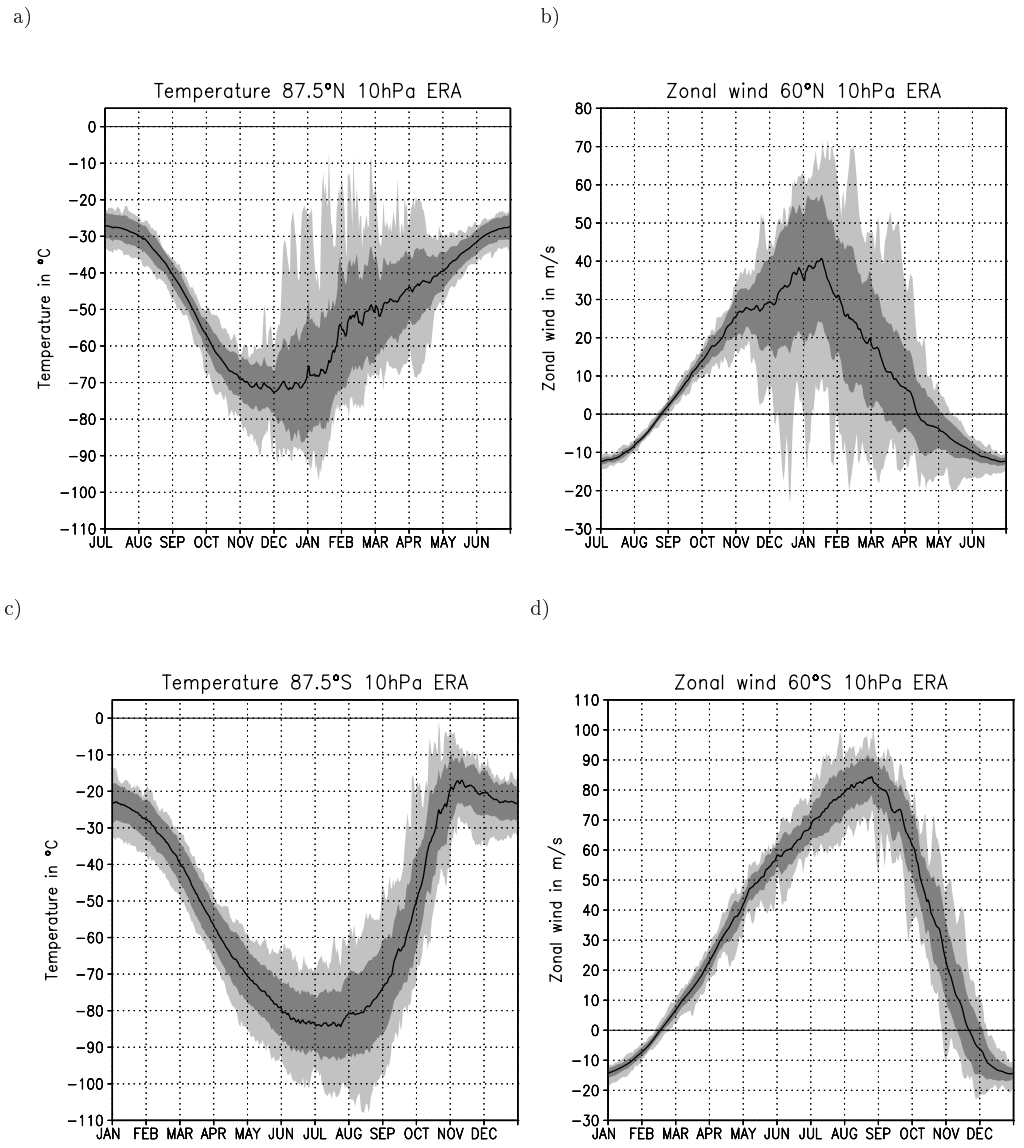


**Figure 3.7:** Long term zonal mean daily means of a) Temperature at 87.5 °N, b) Zonal wind at 60 °N, c) Temperature at 87.5 °S and d) Zonal wind at 60 °S at 10 hPa derived from ERA-40 data over the time period 1979 to 2001 (thick black curves). The standard deviation is given by the dark shaded range and the extrema by the light shaded region. Note the different value ranges for the zonal wind in the northern and southern hemisphere.

fulfilled but no wind reversal is observed. A detailed description on the phenomenology of sudden stratospheric warmings can be found in Labitzke (1999). Due to the occurence of sudden stratospheric warmings the northern hemispheric winter circulation exhibits a pronounced interannual variability which may mask any other influence such as solar variability.

Figure 3.7a and 3.7c show daily mean values of the zonal mean temperature at the respective pole at 10 hPa in the northern and southern hemisphere computed from ERA-40 reanalysis data over the period from 1979 to 2001. For this period satellite data

were assimilated into the reanalysis model system. The end date of 2001 was chosen to exclude the exceptional major stratospheric warming that occurred in the southern hemisphere winter in 2002 and led to a vortex split. Along with the mean values the standard deviation and the extreme values are displayed. The quiet northern summer season with very low variability can be easily distinguished from the very variable winter season. On the southern hemisphere the variability is comparable to that of the northern hemisphere in summer, it is somewhat higher in autumn and lower in mid-winter and spring. In particular there are no such strong warm extrema as in the northern hemisphere winter. In Figure 3.7b and 3.7d the corresponding zonal mean zonal winds for 60 °N and 60 °S are depicted. It is seen that the circulation in the southern hemisphere winter is much less variable than the northern hemispheric winter circulation. The long term mean zonal wind velocity is considerably higher in southern winter than in northern winter. This is a consequence of the rare occurrence of minor or even major sudden stratospheric warmings in the south. That in turn is due to the lower planetary wave activity in the southern mid-latitudes which can be attributed to the zonally symmetric form of the Antarctic continent and the absence of sharp land-sea contrasts as they are found on the northern hemisphere.

*The Quasi-Biennial Oscillation*

In the tropical lower stratosphere another important phenomenon, the Quasi-Biennial Oscillation (QBO) is observed, which shall be briefly described here. Between 20 °S and 20 °N and pressure levels of 10 and 100 hPa westerly and easterly wind regimes alternate with a variable period ranging from 22 to 34 months, on average 27 months. The regimes propagate downward at an average rate of about 1 km/month, whereas westerly shear zones descend more rapidly and uniformly than easterly shear zones. The phase shift from the westerly to the easterly regime is often delayed between 30 and 50 hPa. Usually, the amplitude of the easterlies (30 to 35 m/s) is larger than that of the westerlies (15 to 20 m/s) (Naujokat, 1986; Labitzke et al., 1996; Marquardt, 1997). Figure 3.8 depicts these characteristics from observational data obtained at three different tropical stations.

The QBO arises from the interaction of vertically propagating equatorial waves (Kelvin and Rossby-gravity waves) with the mean flow. For instance, in a westerly mean flow westward travelling waves can propagate vertically but eastward travelling waves are absorbed thereby amplifying the westerlies by the transfer of their momentum to the background flow. In this way the peak westerlies descend to lower altitudes. Above, the westward moving waves dissipate, weaken the westerly wind and, finally, reverse it to an easterly wind. Due to the absorption of westward travelling waves in an easterly background wind the peak easterlies propagate downward replacing the west phase of the QBO (Andrews et al., 1987).

The phase of the QBO can influence the stability of the northern polar vortex. The so called Holton-Tan-relationship states that in winters with QBO west phase the polar vortex tends to be stable and undisturbed while it is frequently weakened by the

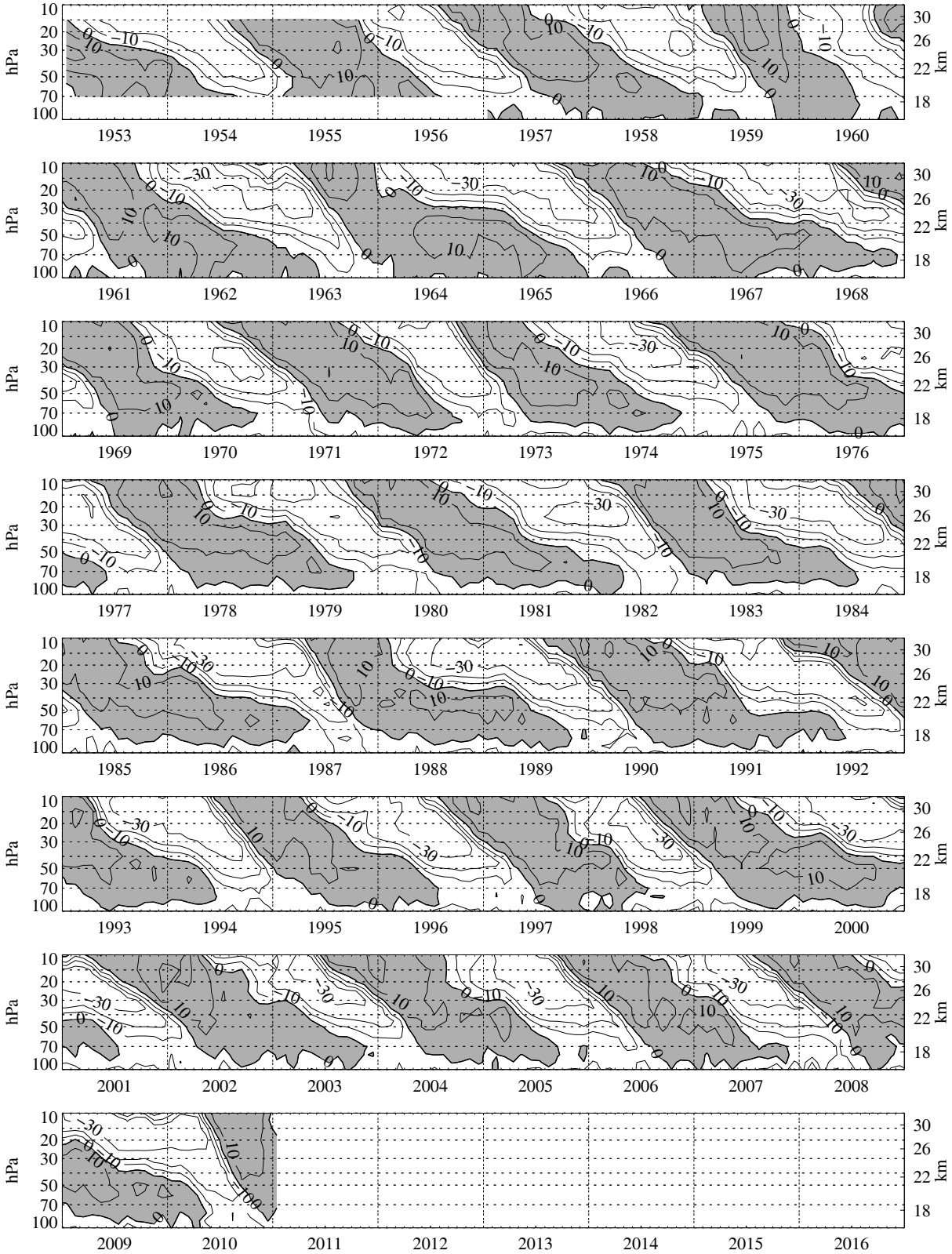


**Figure 3.8:** Time-height section of monthly mean zonal winds (m/s) at equatorial stations: Canton Island, 3 °S/172 °W (Jan 1953 - Aug 1967), Gan/Maledive Islands, 1 °S/73 °E (Sep 1967 - Dec 1975) and Singapore, 1 °N/104 °E (since Jan 1976). Contour interval is 10 m/s. Westerlies are shaded (updated from Naujokat, 1986).

occurence of sudden stratospheric warmings in the QBO east phase (Holton and Tan, 1980). The reason for this relationship is the different latitudinal extent of the region in which planetary waves can propagate under QBO east or west conditions. The position of the zero wind line which is situated south of the equator during the QBO west phase and north of the equator in the east phase is a good indicator for planetary wave propagation. As these waves can only propagate in westerly background winds they are confined to the northern hemisphere outside the lowest latitudes in the QBO east phase which raises the probability for a poleward propagation and an associated weakening of the polar vortex. The opposite is true for the QBO west phase, planetary waves can propagate equatorward and may even cross the equator, rendering it unlikely to cause a sudden stratospheric warming. However, the Holton-Tan-relationship does only hold for solar minimum conditions as was described by Labitzke and van Loon (1988) who calculated the correlation between the February 30 hPa geopotential height and the 10.7 cm solar radio flux separately for QBO east and west conditions. In doing so they investigated the QBO influence on the solar-polar vortex relationship. The result was an anti-correlation during QBO east phase and a positive correlation in the west phase, i.e. a warmer polar vortex at solar min/QBO east and solar max/QBO west and a colder vortex in the other cases (solar max/QBO east and solar min/QBO west). A slightly different approach was chosen by Gray et al. (2001) who analysed the solar influence on the QBO-polar vortex relation. Their results clearly confirmed the Holton-Tan-relationship for solar minimum conditions but the reversal of this relationship under solar maximum conditions was not very pronounced. A reason may have been the lower number of solar maximum compared to solar minimum years in the analysed time series.

Above the height region in which the QBO is active another zonal wind oscillation is observed. It is strongest at the stratopause level ($\approx$1 hPa) and has a period of roughly six months, which gave it the name semiannual oscillation (SAO). The easterly phases of the SAO are found in the solstice seasons with the January easterlies being stronger than those in July. The west phases appear in April/May and in October, i.e. some time after vernal and autumnal equinox, respectively, with the former frequently being stronger than the latter. The observed wind speed ranges from -35 to -60 m/s during the January easterlies and from 10 to 25 m/s during the vernal westerlies (Gray et al., 2001). The SAO westerly phase is generated by high-speed Kelvin waves that can unaffected by the QBO propagate into the mesosphere. The easterly phase arises from a combination of easterly momentum advection by the residual mean meridional circulation (see next subsection) directed towards the winter pole and a planetary-wave forcing from the winter hemisphere (Andrews et al., 1987).

*Wave-mean flow interaction*

The atmospheric circulation is frequently regarded as a mean flow with superposed deviations from the mean denoted as waves or "eddies". Especially in the stratosphere this approximation is justified. Mean flow and waves can interact in a two-way process, i.e.

the mean flow determines the propagation conditions for waves and the waves can significantly influence the mean flow (and thereby their own propagation conditions). The following examination relies on Andrews et al. (1987).

Considering a zonal mean flow $\overline{u}$ and deviations from the zonal mean $u'$, the actual zonal wind velocity can be written as

$$u = \overline{u} + u'. \tag{3.1}$$

$\overline{u}$ is a Eulerian mean as it is taken over longitude $\lambda$ at a fixed latitude $\varphi$, altitude $z$ and time $t$:

$$\overline{u}(\varphi, z, t) = (2\pi)^{-1} \int_0^{2\pi} u(\lambda, \varphi, z, t) \quad d\lambda. \tag{3.2}$$

Applying the separation (3.1) to all the variables in the primitive equations in spherical coordinates and taking the zonal average yields the Eulerian mean equations:

$$\frac{\partial \overline{u}}{\partial t} + \frac{\overline{v}}{a\cos\varphi}\frac{\partial(\overline{u}\cos\varphi)}{\partial\varphi} - f\overline{v} + \overline{w}\frac{\partial \overline{u}}{\partial z} - \overline{X} = -\frac{1}{a\cos^2\varphi}\frac{\partial(\overline{v'u'}\cos^2\varphi)}{\partial\varphi} - \frac{1}{\rho_0}\frac{\partial(\rho_0\overline{w'u'})}{\partial z} \tag{3.3}$$

$$\frac{\partial \overline{v}}{\partial t} + \frac{\overline{v}}{a}\frac{\partial \overline{v}}{\partial\varphi} + \overline{w}\frac{\partial \overline{v}}{\partial z} + \overline{u}(f + \frac{\overline{u}}{a}\tan\varphi) + \frac{1}{a}\frac{\partial\overline{\Phi}}{\partial\varphi} - \overline{Y} = -\frac{1}{a\cos\varphi}\frac{\partial(\overline{v'^2}\cos\varphi)}{\partial\varphi} - \frac{1}{\rho_0}\frac{\partial(\rho_0\overline{w'v'})}{\partial z} - \frac{\overline{u'^2}}{a}\tan\varphi \tag{3.4}$$

$$\frac{\partial\overline{\Phi}}{\partial z} - \frac{R\overline{\theta}}{H}e^{-\kappa z/H} = 0 \tag{3.5}$$

$$\frac{1}{a\cos\varphi}\frac{\partial(\overline{v}\cos\varphi)}{\partial\varphi} + \frac{1}{\rho_0}\frac{\partial(\rho_0\overline{w})}{\partial z} = 0 \tag{3.6}$$

$$\frac{\partial\overline{\theta}}{\partial t} + \frac{\overline{v}}{a}\frac{\partial\overline{\theta}}{\partial\varphi} + \overline{w}\frac{\partial\overline{\theta}}{\partial z} - \overline{Q} = -\frac{1}{a\cos\varphi}\frac{\partial(\overline{v'\theta'}\cos\varphi)}{\partial\varphi} - \frac{1}{\rho_0}\frac{\partial(\rho_0\overline{w'\theta'})}{\partial z} \tag{3.7}$$

In the above equations $a$ denotes the Earth's radius, $\rho_0 = \rho_0(z)$ the basic density, $f$ the Coriolis parameter ($f = 2\Omega\sin\varphi$), $\overline{X}$ and $\overline{Y}$ the horizontal components of friction and $\overline{Q}$ the diabatic heating. $R$ represents the gas constant for dry air and H is a mean scale height, typically about 7 km for middle atmosphere studies. All the terms involving mean quantities are written on the left hand side of the equations whereas all the variables associated with the wave disturbances are written on the right hand side. Hence, the wave induced deviations from the zonal mean and the corresponding momentum fluxes ($\overline{v'u'}$, $\overline{w'u'}$) and heat fluxes ($\overline{v'\theta'}$, $\overline{w'\theta'}$) act to change the mean circulation. With given adequate initial and boundary conditions the above system of partial differential equations can be solved numerically to predict the temporal evolution of the zonal mean circulation.

However, since there tends to be a strong cancellation between the eddy flux terms and the mean flow in the Eulerian mean equations with the diabatic heating as a small residual this formulation is rather inefficient when it comes to a diagnosis of the eddy

forcing of the mean flow. On the other hand, an air parcel will only rise to a higher equilibrium altitude if it is diabatically heated, i.e., the parcels potential temperature is adjusted to the potential temperature of the ambient air. Thus, it is the residual mean meridional circulation associated with diabatic processes that determines the vertical displacement of air parcels and, consequently, the mean meridional mass flow and ultimately the transport of trace species in the latitude-height-plane. Andrews and McIntyre (1976) defined the so called transformed Eulerian mean equations (TEM).

Formally, a residual mean meridional circulation in the latitude-height-plane is introduced:

$$\begin{aligned} \overline{v}^* &\equiv \overline{v} - \frac{1}{\rho_0}\frac{\partial}{\partial z}\left(\frac{\rho_0 \overline{v'\theta'}}{\partial\overline{\theta}/\partial z}\right), \\ \overline{w}^* &\equiv \overline{w} + \frac{1}{a\cos\varphi}\frac{\partial}{\partial\varphi}\left(\frac{\cos\varphi\,\overline{v'\theta'}}{\partial\varphi}\right), \end{aligned} \tag{3.8}$$

with the residual meridional velocity $\overline{v}^*$ and the residual vertical velocity $\overline{w}^*$. From this definition it is seen that the residual vertical velocity $\overline{w}^*$ represents the portion of the mean vertical velocity $\overline{w}$ whose contribution to the adiabatic temperature change is not canceled by the eddy heat flux divergence.

Substitution of $\overline{v}^*$ and $\overline{w}^*$ into the Eulerian mean equations yields the transformed Eulerian mean equations:

$$\frac{\partial\overline{u}}{\partial t} + \frac{\overline{v}^*}{a\cos\varphi}\frac{\partial(\overline{u}\cos\varphi)}{\partial\varphi} - f\overline{v}^* + \overline{w}^*\frac{\partial\overline{u}}{\partial z} - \overline{X} = \frac{1}{\rho_0 a\cos^2\varphi}\nabla\cdot F, \tag{3.9}$$

$$\overline{u}\left(f + \frac{\overline{u}\tan\varphi}{a}\right) + \frac{1}{a}\frac{\partial\overline{\Phi}}{\partial\varphi} = G, \tag{3.10}$$

$$\frac{\partial\overline{\Phi}}{\partial z} - \frac{R\overline{\theta}}{H}e^{-\kappa z/H} = 0, \tag{3.11}$$

$$\frac{1}{a\cos\varphi}\frac{\partial(\overline{v}^*\cos\varphi)}{\partial\varphi} + \frac{1}{\rho_0}\frac{\partial(\rho_0\overline{w}^*)}{\partial z} = 0, \tag{3.12}$$

$$\frac{\partial\overline{\theta}}{\partial t} + \frac{\overline{v}^*}{a}\frac{\partial\overline{\theta}}{\partial\varphi} + \overline{w}^*\frac{\partial\overline{\theta}}{\partial z} - \overline{Q} = -\frac{1}{\rho_0}\frac{\partial}{\partial z}\left(\frac{\rho_0}{a}\frac{\partial\overline{\theta}/\partial\varphi}{\partial\overline{\theta}/\partial z}\overline{v'\theta'} + \rho_0\overline{w'\theta'}\right). \tag{3.13}$$

The vector $F$ is the so called Eliassen-Palm flux (EP-flux). It is given by

$$F^{(\varphi)} \equiv \rho_0 a\cos\varphi\left(\frac{\partial\overline{u}}{\partial z}\frac{\overline{v'\theta'}}{\partial\overline{\theta}/\partial z} - \overline{v'u'}\right), \tag{3.14}$$

$$F^{(z)} \equiv \rho_0 a\cos\varphi\left[\left(f - \frac{1}{a\cos\varphi}\frac{\partial(\overline{u}\cos\varphi)}{\partial\varphi}\right)\frac{\overline{v'\theta'}}{\partial\overline{\theta}/\partial z} - \overline{w'u'}\right], \tag{3.15}$$

and its divergence reads as

$$\nabla \cdot F \equiv \frac{1}{a\cos\varphi}\frac{\partial}{\partial\varphi}\left(F^{(\varphi)}\cos\varphi\right) + \frac{\partial F^{(z)}}{\partial z}. \tag{3.16}$$

The quantity $G$ in equation (3.10) represents all terms that lead to deviations from the gradient-wind balance between $\overline{u}$ and $\overline{\Phi}$ and is in most cases of secondary importance. If the components of the EP-flux were written in the quasi-geostrophic approximation it would become clear that $F^{(\varphi)}$ is primarily a measure for the eddy momentum flux whereas $F^{(z)}$ is a measure for the eddy heat flux. A closer examination of the EP-flux components reveals that it is the combined effect of momentum and heat fluxes that, by way of the EP-flux divergence, alters the mean flow. From equation (3.9) it becomes clear that a divergence of the EP-flux ($\nabla \cdot F > 0$) generates an eastward directed acceleration whereas a convergence ($\nabla \cdot F < 0$) leads to a westward directed acceleration of the zonal mean flow. For the polar night jet, i.e. an intense westerly mean flow, this implies a strengthening in case of EP-flux divergence and a weakening in case of EP-flux convergence. However, it was shown by Charney and Drazin (1961) that for linear, steady, adiabatic and frictionless wave disturbances the divergence of the EP-flux vanishes exactly, hence, these waves do not exert a force on the zonal mean flow and are unable to accelerate it.

A generalisation of the Eliassen-Palm flux for three-dimensional quasi-geostrophic stationary waves was derived by Plumb (1985). The three-dimensional flux is parallel to the group velocity of the stationary large-scale Rossby-waves. It is thus possible to identify regions of wave forcing and propagation (McDaniel and Black, 2005).

$$F_s = p\,\cos\varphi\,\times\begin{pmatrix} v'^2 - \dfrac{1}{2\Omega a\sin 2\varphi}\dfrac{\partial(v'\Phi')}{\partial\lambda} \\ -u'v' + \dfrac{1}{2\Omega a\sin 2\varphi}\dfrac{\partial(u'\Phi')}{\partial\lambda} \\ \dfrac{2\Omega\sin\varphi}{S}\left[v'T' - \dfrac{1}{2\Omega a\sin 2\varphi}\dfrac{\partial}{\partial\lambda}(T'\Phi')\right] \end{pmatrix} \tag{3.17}$$

In the above formulation the geostrophic and thermal wind relations have been used in order to include only first derivatives of observed quantities instead of second derivatives of the streamfunction. This helps to prevent the amplification of noise due to successive differentiations. The quantity $S$ in the vertical component of the Plumb-flux is the static stability given by

$$S = \frac{\partial\hat{T}}{\partial z} + \frac{\kappa\hat{T}}{H} \tag{3.18}$$

where $\hat{\mathrm{T}}$ denotes the areal average of temperature north of 20 °N, $\kappa = R/c_p$ is the adiabatic exponent and $H$ the scale height.

The Plumb-flux in the middle and upper troposphere is generally directed upwards, eastward and equatorward during northern winter at mid-latitudes. As it represents sta-

tionary waves the maximum wave activity is found downstream of the strongest orographic forcing and in regions with pronounced gradients in the diabatic heating rate, i.e. the west coast of the North Atlantic Ocean (Plumb, 1985). When zonally averaged the meridional and vertical component of the Plumb-flux reduce to the EP-flux associated with these waves.

# Chapter 4

# The Influence of the 11-year Solar Cycle on the Atmosphere

Keeping the basic information about the middle atmospheric and tropospheric climatology in mind this chapter provides a survey on the status of research concerning the influence of the 11-year solar irradiance variation on the atmosphere as it is known from observations and from model studies. Furthermore, possible mechanisms for the solar influence are introduced.

Since the discovery of the stratosphere by Léon-Philippe Teisserenc de Bort and Richard Aßmann in 1902 atmospheric scientists were dependent on ground based observations to obtain information from the middle and upper atmosphere. Ascends of radiosondes and ozone sondes yielded invaluable data but those observations were made at single points in space. Comprehensive observations of the upper and lower atmosphere for all latitudes and longitudes were first available with the advent of operational satellites in 1979. The 30 years that have passed since then may appear a long time but in terms of solar cycles they cover less than three complete cycles. This is an insufficient basis for a statistical analysis of the solar influence on the atmosphere.

During the average lifetime a human experiences between six to eight solar cycles. Thus, in order to quantify the solar influence on the atmosphere continuous measurements of meteorological and chemical fields such as wind, temperature and ozone, in particular in the middle atmosphere, are tasks for several generations. This statement is similarly valid for the measurement of solar irradiance.

From the observations of total solar irradiance changes (Section 2.3) of the order of $1\,\mathrm{Wm}^{-2}$ or $0.1\,\%$ over the course of the 11-year solar cycle a global mean surface temperature response of the order of $0.07\,\mathrm{K}$ can be estimated when a climate sensitivity parameter of $0.5\,\mathrm{K}(\mathrm{Wm}^{-2})^{-1}$ is assumed for the solar cycle radiative forcing (Gray et al., 2010 and references therein). This is a very low value and from observations it is known that regionally the 11-year solar cycle irradiance changes can cause a larger climate

variation. Thus, the very simple translation of the radiative forcing into a global scale surface temperature change can only be the first guess. More complicated mechanisms are required to explain the observed changes.

This section is dedicated to a survey of the relevant literature based on the review by Gray et al. (2010). It is the aim to provide an up-to-date overview of the status of research in the field of solar influence on the stratosphere and troposphere divided into observational and modelling results as well as proposed mechanisms to explain the observed changes. It is, however, restricted to the influence of solar irradiance changes. Effects due to precipitating particles and cosmic rays are beyond the scope of this report and are, therefore, not discussed.

Reanalysis data sets are in this section treated as 'observations'. This is justified in so far only data from 1978 onwards are considered as from that time satellite observations have been available for assimilation into the reanalysis models. The quality of the middle atmospheric data was thereby substantially improved.

## 4.1 Evidence from observations

In section 2.3 it was noted that 11-year solar irradiance changes are strongly dependent on wavelength with the highest variability in the UV part of the spectrum. Short-wave radiation and in particular UV radiation is absorbed in the upper atmosphere by molecular oxygen and in the stratosphere by ozone (cf. section 3.2). Simultaneously, UV radiation at wavelengths below 242 nm photodissociates molecular oxygen and provides atomic oxygen to form ozone (ibid.). Hence, 11-year solar cycle changes in UV solar irradiance should become manifest in the stratospheric ozone abundance and the associated radiative heating and temperature.

### 4.1.1 The solar signal in the stratosphere

#### Ozone

Randel and Wu (2007) estimate the annual mean ozone response to 11-year solar variability by applying a multiple linear regression technique to ozone data observed by the Stratospheric Aerosol and Gas Experiment (SAGE) I and II from 1979 to 1981 and from 1984 to 2005. Ozone responds to the solar irradiance change with two statistically significant maxima of about 2 % per 100 units of the 10.7 cm solar radio flux (multiply by 1.3 to obtain an average minimum to maximum change) at mid-latitudes in the upper stratosphere at 3 hPa (40 km), see Figure 4.1. In the tropical middle stratosphere the solar signal in ozone shows a local minimum and takes even insignificant negative values. Towards lower altitudes the ozone solar response increases again. These results confirm the findings of Soukharev and Hood (2006) who performed a multiple linear regression

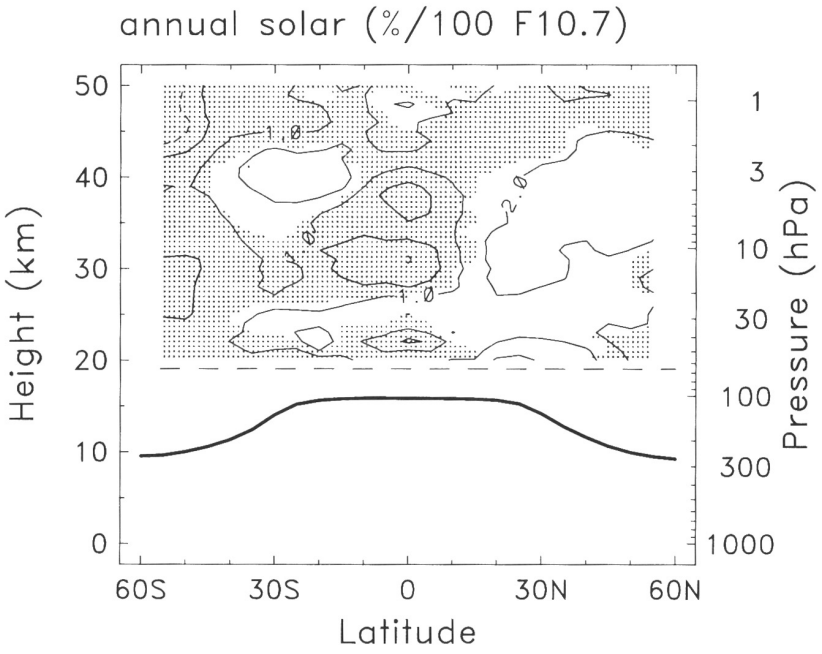


**Figure 4.1:** Annual mean zonal mean solar regression coefficient of ozone in % per 100 units F10.7 cm solar radio flux. Unshaded changes are statistically significant. Adapted from Randel and Wu (2007).

analysis on several satellite data sets including SAGE, the Solar Backscattered Ultraviolet instrument (SBUV) and the Halogene Occultation Experiment (HALOE). The common feature of all three data sets is the tropical response which is significantly positive in the upper and lower stratosphere, and near zero or even negative in the middle stratosphere.

Chandra (1991) as well as Hood (1997) and Labitzke and van Loon (1997a) found higher values of total ozone at higher solar activity. With the help of a multiple linear regression analysis Soukharev and Hood (2006) could confirm this result using satellite and ground based measurements. It is assumed that ozone in the lower stratosphere is mainly responsible for the observed total column changes because of the high number density in this region.

### Temperature

A multiple linear regression analysis of observed temperatures (combined data measured by the Stratospheric Sounding Unit (SSU) and the Microwave Sounding Unit, channel 4 (MSU4) from 1979 to 2005) by Randel et al. (2009) shows a solar cycle induced change of the order of 1 K which peaks in the tropical upper stratosphere and at the stratopause (Figure 4.2). This signal is statistically significant. Significantly higher temperatures are found at the stratopause level at high latitudes, too. At mid-latitudes, in particular in the middle and lower stratosphere the temperature response is weak and insignificant. Similar

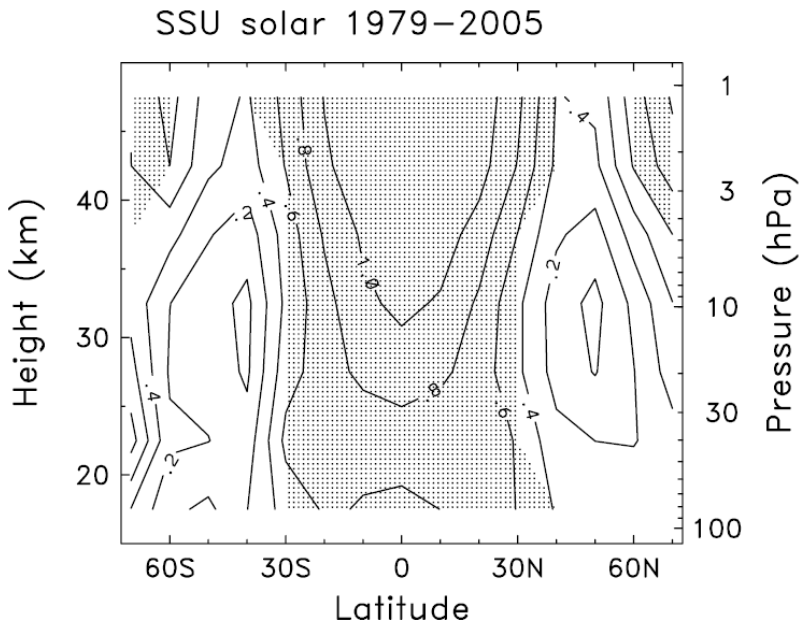


**Figure 4.2:** Annual mean solar regression coefficient of temperature in K per 125 units F10.7 cm solar radio flux. Shaded regions highlight statistical significance. From Randel et al. (2009).

to the solar signal in ozone the temperature response increases again in the tropical lower stratosphere, reaching a value of about 0.8 K per 125 units F10.7 cm solar radio flux.

Frame and Gray (2010), providing an update of an earlier publication by Crooks and Gray (2005), analyse the ERA-40 data set (Uppala et al., 2005) extended by ECMWF operational analyses from 1978 to 2008 by means of a multiple linear regression model. They find a statistically significant annual mean temperature response in the equatorial stratopause region of about +1.5 K. Moreover, there are significant positive reactions to the increased solar irradiance in the low-latitude lower stratosphere between 20 and 30 km as well as in the lowermost stratosphere at the equator of the order of 0.75 K. An examination of the annual cycle of the temperature response shows that the upper stratospheric temperature signal is present throughout most of the year and it is strongest in March. Though, the authors express a caveat concerning the lower stratospheric temperature signal: its magnitude is sensitive to the presence of (linear) trends in the data set. Frame and Gray (2010) were, however, able to demonstrate that the lower stratospheric temperature signal is unlikely to be strongly influenced by the major volcanic eruptions in 1982 and 1991, respectively, which occurred at the end of 11-year solar cycle maxima.

Correlation analyses performed by Karin Labitzke and her co-authors revealed a positive correlation between 30 hPa-temperatures in the subtropics and the F10.7 cm solar radio flux, i.e., higher temperatures during periods of higher solar activity (Labitzke, 2004a and references therein). The signal is particularly pronounced under QBO east conditions. It is present throughout the year. Under QBO west conditions the signal is

weaker and disappears for some months.

### Zonal wind

The zonal mean zonal wind responds to increased solar irradiance with two westerly anomalies at 30°S and 35°N with the southern hemispheric signal being stronger than that in the northern hemisphere (Frame and Gray, 2010). The zonal wind response is dominated by a poleward and downward movement of westerly anomalies in the respective winter hemisphere. In the southern hemisphere this is confined to a region north of 45°S, in the northern hemisphere the anomalies propagate further polewards. However, the month of February marks an exception in that it shows a strong and statistically significant easterly zonal wind anomaly associated with a likewise statistically significant positive temperature anomaly. This is likely linked to the occurrence of sudden stratospheric warmings.

The poleward and downward movement of stratospheric solar induced zonal wind anomalies in the respective winter season was noted earlier in a composite analysis of NCEP-CPC data (a precursor data set to the NCEP-NCAR reanalyses (Kalnay et al., 1996)) by Kodera and Kuroda (2002).

### Geopotential height

The pioneering work of Labitzke (1987) and Labitzke and van Loon (1988) revealed the association between the 11-year solar cycle and the winter north polar geopotential height at 30 hPa in the lower stratosphere which is mainly determined by the temperature in the layers below. However, they discovered the important role the QBO plays as additional condition. The correlation between, e.g., the sunspot number and the 30 hPa height at the north pole is only clearly visible when the winters are stratified according to the phase of the QBO. The subtropical geopotential height of the 30 hPa-level in July is higher during periods of solar maximum. This signal is particularly pronounced under QBO east conditions (Labitzke, 2003). However, the solar signal is present throughout the year (Labitzke, 2004b). When the QBO is westerly the solar influence on the geopotential height is less clear and not as persistent as in the QBO east phase.

Haigh and Roscoe (2009), using a combined solar/QBO index, found an influence on the breakup date of the Antarctic polar vortex which is delayed at solar maximum/QBO west or at solar minimum/QBO east. This effect has the second largest influence on the vortex breakup date after ozone depletion.

### 4.1.2 The solar signal in the troposphere

It is difficult to detect an 11-year solar signal in the troposphere due to the small amplitude of the signal. The presence of other forcings as increasing greenhouse gases, volcanic eruptions and aerosol changes, some of which may cause climate changes with the same sign as the solar influence further complicate the investigation. Relatively short data records, short in terms of 11-year solar cycles, high internal variability of the troposphere and large errors associated with, e.g., estimates of vertical velocities make it additionally challenging to find solar induced changes in the tropospheric circulation.

*Temperature*

Frame and Gray (2010) in their analysis of ERA-40 data and Haigh (2003) using NCEP-NCAR reanalyses showed that the annual mean temperature at mid-latitudes is significantly higher at high levels of solar activity. The bands of anomalous warming emerge from a positive temperature anomaly in the tropical lower stratosphere and reach through the depth of the troposphere down to the surface (Haigh, 2003). The seasonal march of the signal as described by Frame and Gray (2010) shows the strongest near-surface positive temperature anomalies in northern mid- and late winter as well as in southern mid-winter. In the equinox seasons the signal is present in both hemispheres, but not necessarily symmetric to the equator. Gleisner and Thejll (2003) obtained a qualitatively similar result with a slightly different approach applied to NCEP-NCAR reanalyses. They report increased layer thicknesses which primarily reflect higher temperatures within the layer in the upper (500 hPa to 200 hPa) and lower (1000 hPa to 500 hPa) troposphere at higher solar activity. The changes exhibit a three-banded structure with maxima at mid-latitudes in both hemispheres and in the tropics.

*Zonal Wind*

Haigh et al. (2005) using NCEP-NCAR reanalyses found an annual mean zonal wind response which implies weaker and poleward displaced mid-latitude jets during periods of higher solar activity. Frame and Gray (2010) confirm this result, showing that the tropospheric signal becomes significant in northern late winter and spring (February and March) as well as in southern late winter (September). The mechanism by which this tropospheric zonal wind response develops was studied by Haigh et al. (2005) and Simpson et al. (2009) and is discussed in section 4.2.

*Precipitation and circulation*

The 11-year solar cycle influence on the meridional circulation in the tropics, i.e., the Hadley cell, is not yet clearly identified. On the one hand, some authors report indications for a strengthened upwelling in the tropics (Labitzke and van Loon, 1995; van Loon et al., 2004; van Loon et al., 2007). On the other hand, Kodera (2004) and Kodera and Shibata (2006) using the same NCEP-NCAR reanalysis data set as van Loon et al. (2007)

found an enhanced convection off the equator in the Indian monsoon and a suppressed upwelling near the equator. Simultaneously, the northward directed meridional wind over the western Indian Ocean and the eastern African continent and the southern Arabian peninsula is reported to correlate positively with the F10.7 cm solar radio flux, i.e., it is stronger during periods of high solar activity. Further support for a stronger Indian monsoon at high solar activity was found by Bhattacharyya and Narasimha (2005). The results of Haigh et al. (2005) point towards a weaker and broader Hadley cell under solar maximum conditions. The above-mentioned poleward shift of the tropospheric mid-latitude jets is accompanied by a poleward shift of the indirect Ferrel cell (Haigh et al., 2005). Gleisner and Thejll (2003) report a similarly poleward extended Hadley cell and a modulation of the mid-latitude Ferrel cell.

Kodera (2005) detects a link between solar induced stratospheric changes and convective activity in the Indian and eastern Pacific Ocean which yields a response that resembles the ENSO pattern. Meehl et al. (2009) show a solar signal in observed precipitation that is in agreement with the shift away from the equator of the ITCZ and the South Pacific convergence zone (SPCZ). Precipitation is enhanced to the north and to the southwest of the climatological maxima. This pattern is a consequence of a "cold tongue" of anomalously low SSTs in the Pacific. Indications for a solar cycle influence on (large scale) precipitation can also be inferred, e.g., from records of lake sediments (Berggren et al., 2010) which show lower deposition rates of matter containing $^{10}$Be at higher solar activity.

*Modes of variability*

For a long time the discussion about solar influence on the atmosphere has focused on the mean climate. Within the last decade a number of studies were performed which consider the impact of 11-year solar irradiance changes on the leading modes of atmospheric variability.

Kodera (2002) and Kodera (2003) report a solar cycle modulation of the North Atlantic Oscillation which implies changes in the spatial structure. Ogi et al. (2003b) found in NCEP-NCAR reanalysis data that under solar maximum conditions the wintertime NAO influences the atmospheric circulation in the following summer in the sense that near-surface air temperatures over northern Eurasia and subarctic North America are higher when the NAO index in the preceding winter was positive. The seasonal link was proposed to involve snow cover over the northern land masses as well as sea ice and SSTs to memorize the wintertime anomalies (Ogi et al., 2003a).

From a study by Kuroda (2007) it is known that the solar cycle modulation of the winter NAO and its possible reappearance in summer in the ERA-40 data is particularly pronounced under QBO west conditions. It is, furthermore, found that besides the surface conditions (i.e., snow cover, sea ice, sea surface temperature as assumed by Ogi et al. (2003a)) ozone plays a role in communicating the winter anomaly to the summer. This

is further investigated by Kuroda et al. (2008) who conclude that at positive values of the NAO index a negative ozone anomaly in the lower stratosphere is created in the winter of solar maximum years by a weaker meridional circulation which in turn arises from weaker wave-mean flow interaction. The ozone anomaly persists until the following autumn and may, thus, lead to anomalous lower temperatures in summer. A vertical dipole temperature signal develops in June with a positive temperature anomaly below the negative one in the lower stratosphere and persists until August. A corresponding zonal wind anomaly emerges in the upper troposphere through the thermal wind relationship. This summer signal is located poleward of the winter NAO signal as was noted by Ogi et al. (2003b) and Kuroda (2007). The key results of Kuroda et al. (2008) did not change when an other independent ozone data set was used.

Similar results are reported for the Southern Annular Mode in late winter and its persistence until the following autumn by Kuroda and Kodera (2005). The authors suggest a negative ozone anomaly in the lower stratosphere to be the agent that conveys the late winter signal to the summer. Snow and ice cover as proposed by Ogi et al. (2003b) are considered to play a minor role in the southern hemisphere due to the few continents. Kuroda and Yamazaki (2010) report a significantly stronger correlation between the SAM and the zonal mean zonal wind in years with high solar activity than in low solar activity phases. The correlation reaches from the surface to the upper stratosphere and persists until summer during solar maxima whereas it is confined to the troposphere and vanishes quickly during solar minima. The QBO is found to play a minor role in the modulation of the SAM (Kuroda and Yamazaki, 2010).

*Blocking*

Barriopedro et al. (2008) examined the dependence of blocking frequency in northern winter on the phase of the solar cycle. They found that the overall blocking frequency in the northern hemisphere is not influenced by the 11-year solar cycle. However, solar activity was found to modulate the preferred locations for blockings over the Atlantic and the Pacific Ocean. A significant shift of blocking activity in the Atlantic sector towards the west and an eastward shift in the Pacific sector were detected under solar maximum conditions. Stratification according to the QBO phase yielded a more evident solar signal when the winds in the equatorial lower stratosphere are westerly.

Huth et al. (2008) analysed the occurrence frequency of certain synoptic types over Europe and found a tendency towards less westerly dominated circulation types during solar minima. Easterly and northerly types were found to prevail when solar activity is low instead. Vice versa does this imply an enhanced zonal flow under solar maximum conditions. Barriopedro et al. (2010) made an attempt to correlate the occurrence of autumn high-storm-surge events in Venice with solar activity and report a significant increase of such events when solar activity is high. They identify the solar modulation of large scale geopotential height anomaly patterns in the sense of Huth et al. (2008) as a reason for this.

*Surface temperature*

An examination of basin average sea surface temperatures by White et al. (1997) using two independent SST data sets yielded variations in phase with the 11-year solar cycle in the Atlantic, Indian and Pacific Oceans. The global average maximum change was reported to be $0.08 \pm 0.02\,\mathrm{K}$ on decadal (11-year period) scales and $0.14 \pm 0.02\,\mathrm{K}$ on interdecadal (22 year period) scales. The value of $0.08 \pm 0.02\,\mathrm{K}$ is of the same order of magnitude as the $0.07\,\mathrm{K}$ that is obtained from a simple energetic consideration which translates the TSI variation of $1\,\mathrm{W/m^2}$ into a global mean temperature change at the surface. When a lag of 1 to 2 years was introduced the highest correlations between SSTs and solar activity could be reached. This is the time scale within which the upper layers of the ocean ($<$100 m) are expected to reach equilibrium. Roy and Haigh (2010) report higher SSTs in the equatorial Pacific at solar maxima and point out the importance of the analysis method and the length of the analysed data record.

The temperatures over land are also influenced by the 11-year solar cycle as is shown in analyses by Camp and Tung (2007a) and Tung and Camp (2008). Higher temperatures are found during periods of higher solar activity. The signal is robust to changes of the data set and the analysis method.

## 4.2 Possible mechanisms

Most of the observed evidence for an 11-year solar signal in meteorological parameters collected above was obtained by statistical methods such as multiple linear regression or simple correlation analyses. This is sufficient to identify a signal but does not provide any information whether there is a physical mechanism behind the statistical relationship and if there is how it works. Hence, in order to understand the numerous indications for an 11-year solar cycle influence on the stratosphere and the troposphere, attempts have been made to develop possible mechanisms that explain the observations. The earliest effort dates back to Hines (1974). In what follows two possible mechanisms are presented that are currently subject of intensive research and discussion. Subsequently, a possible mechanism especially for the development of the extratropical tropospheric solar signal as outlined by Haigh et al. (2005) is given.

Based on the work of Hines (1974), Kodera and Kuroda (2002) proposed a mechanism for solar influence which acts via stratospheric pathways and influences the lower stratosphere and the troposphere indirectly. Therefore, it is called the "**top-down mechanism**". It is schematically illustrated in Figure 4.3. Spectral solar irradiance changes affect the production rate of stratospheric ozone via the photolysis of molecular oxygen. Because of the prominent role ozone plays in the radiative heating of the stratosphere an altered ozone abundance influences the radiative balance. Indirectly, e.g., via the thermal wind relationship, this has an effect also on the circulation which may itself feed back on the ozone distribution through altered transport. During periods of high solar activity

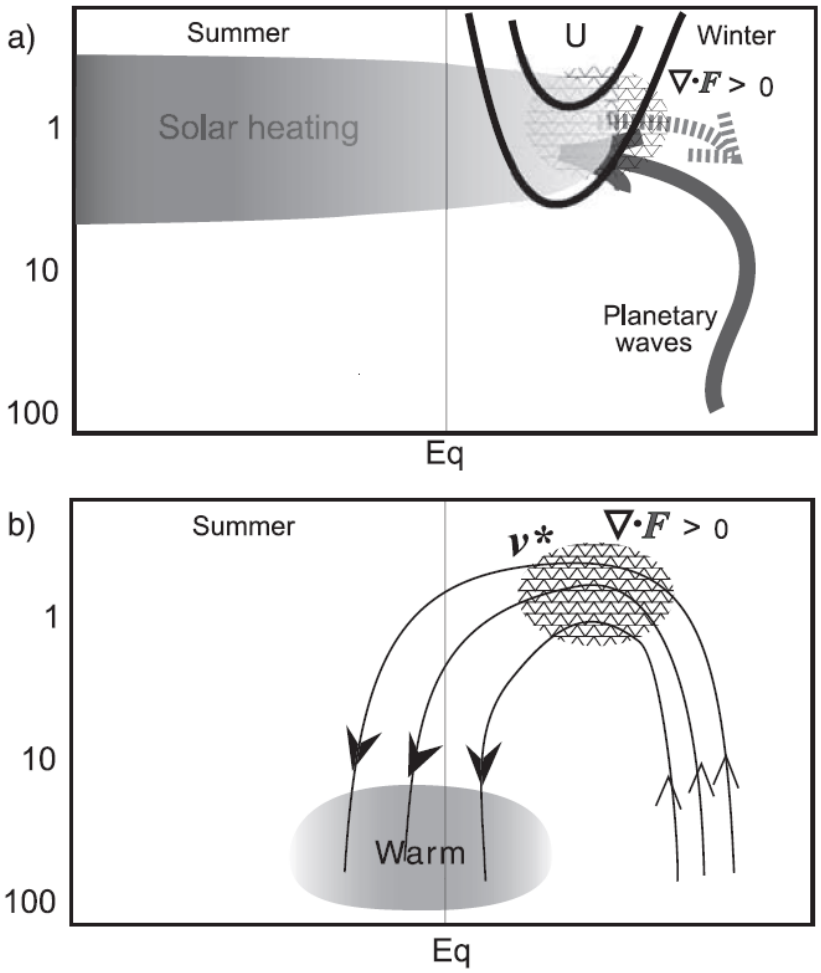


**Figure 4.3:** Schematic illustration of the solar influence on the circulation in the (lower) stratosphere. Anomalies from the long term mean during solstice season are shown. a) Differential heating (shaded) strengthens the polar night jet (bold contours) which deflects planetary waves from the subtropics (dashed arrow) creating anomalous EP-Flux divergence (stippled). b) Reduced wave forcing weakens the Brewer-Dobson circulation (arrows) which leads to an adiabatic warming in the tropical lower stratosphere (shaded). From Kodera and Kuroda (2002).

the solar UV output is enhanced which causes anomalous heating in the upper stratosphere and increases the meridional temperature gradient (shaded region in Figure 4.3a). In response to the higher latitudinal temperature gradient the zonal wind increases with height to maintain thermal wind balance. This effect is supposed to be particularly strong during solstice seasons. A higher zonal wind velocity implies a change of propagation conditions for planetary waves. These waves can propagate in a westerly mean flow with a velocity below a wavenumber-dependent threshold. Thus, a stronger mean flow causes planetary waves to break (dashed arrow in Figure 4.3a) and dissipate at lower altitudes, thereby, depositing their momentum and temperature anomalies on the background mean flow (stippled area in Figure 4.3a). This leads to a poleward and downward displacement of zonal wind anomalies in the winter hemisphere as time progresses. Towards late win-

ter these zonal wind anomalies can reach into the troposphere and down to the surface. The altered wave-mean flow interaction in the stratosphere, moreover, affects the residual mean meridional circulation (MMC) or Brewer-Dobson circulation in the latitude-height plane which is driven by the dissipation of planetary waves. In consequence, the MMC which is directed upwards in the tropics and the summer hemisphere and downward at high latitudes in the winter hemisphere is weakened, i.e., less upwelling occurs in the tropics and less downwelling near the winter pole during solar maxima (arrows in Figure 4.3b). The associated adiabatic temperature changes lead to a relative warming in the tropical lower stratosphere (shaded region in Figure 4.3b) due to the weaker upwelling, on the one hand, and to a relative cooling at high latitudes on the winter hemisphere due to the decreased downwelling, on the other hand. The relative warming in the lowermost tropical stratosphere is supposed to affect the tropopause height and temperature and, thereby, the tropospheric Hadley cell which is postulated to be weaker than average during periods of high solar activity.

The direct mechanism, the so called **bottom-up mechanism**, was brought into discussion by Meehl et al. (2003). It involves stronger heating at the surface in the cloud-free subtropic areas due to slightly higher TSI levels at solar maximum. This results in enhanced sea surface temperatures, increased evaporation from the sea surface and a humidity convergence in the intertropical convergence zone (ITCZ), thereby, reinforcing the upward branch of the Hadley circulation. As a consequence the trade winds are strengthened as is the downwelling in the subtropics. This provides a positive feedback as subsiding air masses warm adiabatically, reduce clouds and, thus, support the stronger heating in cloud free areas. Furthermore, the enhanced Hadley cell affects the sea surface temperatures at the equator which are lower than average during periods of high solar activity due to the forced upwelling of cold deep water (Meehl et al., 2008) which is also found during cold phases of the El Niño-Southern Oscillation, so called La Niña events. The Walker circulation in the equatorial Pacific is stronger during solar maxima consistent with the La-Niña like response in SSTs.

A version of the bottom-up mechanism that may help to overcome the apparent discrepancy between the postulated strengthening of the Hadley circulation in the bottom-up framework and the expected weakening of tropical upwelling in the top-down mechnanism is proposed by van Loon et al. (2007). They suggest that an initially stronger Hadley circulation causes stronger trade winds which in turn imply enhanced upwelling of cold water to the Pacific Ocean surface, hence extending the tongue of cold water westward. The cooler than average ocean surface, however, reduces precipitation over the western Pacific and, thus, weakens the Hadley circulation. The east-west Walker circulation is reinforced and extended farther west than on average.

### Mechanism for extratropical tropospheric changes

Haigh et al. (2005) examine the tropospheric response to different heating anomalies in the lower stratosphere with the aid of a simplified General Circulation Model (GCM). In particular they consider a case which resembles the 11-year solar signal in the equatorial lower stratosphere, i.e., a heating with a limited latitudinal extent. In response to this perturbation they find a slight weakening on the equatorward flank of the tropospheric subtropical jet and a strengthening on the poleward side. This implies a poleward shift of the jet. In addition, the Hadley cells are found to be weakened and expanded polewards. The initial heating perturbation was highly exaggerated (5 K compared to the ≈1 K found in observations). However, the qualitative response was invariant with respect to changes in the magnitude of the applied heating. The proposed mechanism originates in an increase in static stability caused by the lower stratospheric heating. In response to that the tropopause is lowered and the wave fluxes are reduced in this region. In particular, the poleward eddy momentum flux ($\overline{u'v'}$) is affected by the changes. The eddy forcing disturbs the thermal wind balance in the upper troposphere which is restored by an anomalous mean meridional circulation the ascending and descending branches of which coincide with the temperature anomalies. The horizontal branches, however, are affected by Coriolis acceleration and coincide with the zonal wind anomalies. An analysis of the vertically integrated momentum budget revealed the crucial role that poleward eddy momentum flux changes play in maintaining the zonal wind anomalies. The ability of the simplified GCM to reproduce observed tropospheric changes despite the absence of moist processes suggests that these processes are not an important part of the mechanism. The authors concluded that the tropospheric response depends on the sign and the meridional distribution of the lower stratospheric temperature anomaly.

Simpson et al. (2009) confirmed the results of Haigh et al. (2005) and added an investigation of the temporal evolution of the tropospheric response to a heating perturbation in the equatorial lower stratosphere. As a consequence of altered meridional and vertical temperature gradients in the lower stratosphere the horizontal eddy momentum flux in the upper troposphere changes. This drives then an anomalous meridional circulation and leads to zonal wind acceleration throughout the troposphere. Consistent changes in temperature, zonal wind and mean meridional circulation develop until a three-cell anomaly pattern is established and an equilibrated state is reached. A close inspection of the contributing terms in the momentum balance confirmed the importance of changes in horizontal eddy momentum flux.

## 4.3 The 11-year solar signal in model studies

In this chapter's introduction it was mentioned that observations of the solar influence on the atmosphere are long-term tasks. In the meantime, in order to learn more about the

impact of solar variability on the atmosphere one has to make use of a computer model of the atmosphere, a so called General Circulation Model (GCM).

But a General Circulation Model alone, which simulates the absorption of short-wave solar radiation and the emission of terrestrial long wave radiation, the heating and motion in the atmosphere, to name the key processes, is not sufficient for a simulation of the solar impact as solar irradiance variations affect the chemical composition of the atmosphere. Hence, a so called Chemistry Climate Model (CCM) which accounts for the interaction between the abundance of chemical species and the model dynamics is better adapted for that purpose. Chemistry, radiation and dynamics interact in such a model in different ways. The incident solar radiation may alter the chemical composition of the atmosphere by photolysis. On the one hand, the abundance of absorbing gases affects the radiative heating rates which in turn determine the temperature. On the other hand, the altered temperature field influences the rate constants of chemical reactions. Besides the chemical-radiative feedback trace species may also be transported by the atmospheric circulation.

Depending on the mechanism one intends to investigate, e.g., an Atmosphere-Ocean GCM (AO-GCM) with prescibed TSI or spectral irradiance variations may be employed or a CCM simulation with varying spectral solar irradiances but with fixed SSTs is the preferred method. Currently, endeavours are made to couple stratosphere-resolving chemistry climate models with interactive deep ocean models to enable the study of both the top-down and the bottom-up mechanism in one model. First results from such AO-CCM simulations are reported by Shindell et al. (2006), Meehl et al. (2009) and Lee et al. (2009).

Due to limited computer time so called equilibrium simulations with prescribed perpetual solar maximum and minimum irradiance conditions, respectively, are a widely used method to gain insight into processes that are relevant for the appearance of the solar signal. Only recently, so called transient CCM simulations with time varying forcings have become affordable in terms of computing resources, e.g., in the framework of the SPARC CCMVal initiative (Eyring et al., 2005; Austin et al., 2008; Eyring et al., 2008; SPARC CCMVal, 2010).

In the first model studies only (total) irradiance variations were included until Haigh (1994) noted the importance of the associated ozone changes which have a positive feedback on radiative heating in the stratosphere. In early GCM studies including solar induced ozone changes Haigh (1996, 1999) was able to show the solar influence on the lower atmosphere. A coordinated GCM intercomparison study was performed with the focus exclusively on the solar influence on the atmosphere (Matthes et al., 2003). However, the simulations that accounted for total and spectral irradiance changes in combination with associated ozone changes prescribed to the GCMs could by definition not obtain the observed secondary maximum in ozone increase as this is assumed to be related to changes in ozone transport. During the last decade CCMs have been developed and applied to

study the solar cycle effect on the middle and lower atmosphere (e.g., Tourpali et al., 2003; Egorova et al., 2004; Rozanov et al., 2004, Langematz et al., 2005; Shindell et al., 2006; Schmidt and Brasseur, 2006; Marsh et al., 2007; Austin et al., 2007; 2008). For a comprehensive review of the development in the field of modelling of solar influence during the last three decades see Gray et al. (2010).

### 4.3.1 Evidence for the suggested mechanisms

In GCM simulations with prescribed solar irradiance and associated ozone changes but with fixed climatological SSTs Matthes et al. (2004, 2006) were able to confirm the **top-down mechanism** suggested by Kodera and Kuroda (2002). They found a poleward and downward movement of solar induced polar night jet anomalies, a weaker planetary wave activity and in consequence a decelerated MMC and a warming in the equatorial lower stratosphere under solar maximum conditions. Matthes et al. (2010) performed perpetual solar maximum and minimum simulations with a CCM, again with fixed climatological SSTs, and fixed prescribed QBO phases. They point out the importance of the QBO for the appearance of the secondary maximum in ozone and temperature change in the tropical lower stratosphere which is found to be particularly pronounced during QBO east phases. Furthermore, they identify a combination of ozone production and vertical advection to be responsible for the lower stratospheric signal in the tropics at QBO east. The annual mean solar signal in ozone and temperature near the stratopause is unaffected by the QBO phase.

Schmidt and Brasseur (2006) analysed the response to 11-year solar forcing by means of solar maximum and minimum equilibrium simulations with a CCM. In addition to an annual mean ozone and temperature response in the upper stratosphere that compares well with observations they could reproduce the realistic shape of the tropical ozone and temperature change. In a follow-up study, Schmidt et al. (2010) found the ozone and temperature response in the lower tropical stratosphere, hence their results contradict the assumption of Austin et al. (2008) that time varying forcings are necessary to obtain a realistic vertical structure in the tropical ozone and temperature signal. The tropical lower stratospheric ozone and temperature maxima are in these equilibrium simulations a result of solar forcing alone, regardless of the QBO phase, which is a discrepance to the results of Matthes et al. (2010). Other forcings were not included in the simulations in order to facilitate the attribution of the response.

Yamashita et al. (2010) obtained from a transient CCM simulation with varying observed SSTs a dynamical response in line with Kodera and Kuroda (2002) and also a warming and enhanced ozone in the tropical lower stratosphere. In an additional experiment with fixed SSTs a similar response on the same order of magnitude was found, which indicates the solar variation to be the main cause for the lower stratospheric response. Interestingly, the low-latitude lower stratospheric response also appears in a third experiment with fixed solar irradiance but varying observed SSTs, but there at a slightly lower

altitude. This supports the analysis of White et al. (2003) who found an 11-year period in the observed SSTs. However, these experiments span a period of 21 years from 1980 to 2000. Furthermore, the authors evaluate a simulation of a longer period (1960-2006) and cannot retrieve a similar signal in ozone. They, therefore, discuss the possibility of the response being an artefact of interference due to the short analysis period. The role of ENSO variability and solar irradiance variability for the appearance of the tropical lower stratospheric response is also discussed by Marsh and Garcia (2007) who attribute a significant fraction of the solar signal instead to SST changes.

Meehl et al. (2003, 2008) performed AO-GCM studies with a coupled ocean-atmosphere model that does not resolve the full stratosphere. Solar forcing was included by varying TSI values, thus, precluding the indirect mechanism which acts via increased UV absorbtion but favouring the **bottom-up mechanism**. The results support an enhancing effect of higher total solar irradiance on the climatological precipitation maxima in the tropical Pacific during northern winter. The ITCZ as well as the South Pacific convergence zone (SPCZ) are found to be shifted off the equator due to a westward extended cold SST anomaly in response to stronger oceanic upwelling due to stronger trade winds, i.e., a La Niña type response. Precipitation in the ITCZ and SPCZ is further amplified by this feedback. The Hadley and the Walker cell circulation is accelerated.

However, White et al. (2003) and White (2006) studied the thermal budget of the ocean heat storage and found that the observed solar signal is too strong to be explained by the direct TSI variations, only. In particular, air temperature anomalies in the lower troposphere were found to be higher than temperature anomalies in the tropical upper ocean. Moreover, an upward increase of temperature anomalies towards the upper troposphere and lower stratosphere was found. This makes it unlikely that the bottom-up mechanism is the only actor but suggests a combination of top-down influences involving UV irradiance changes and TSI changes at the surface being operative.

Model studies by Rind et al. (2008) and Meehl et al. (2009) support the conclusion that both mechanisms are active and that they both act in the same sense, hence, reinforce each other and produce a larger solar signal especially in the troposphere than one of them alone.

Rind et al. (2008) present results from a comprehensive series of model simulations using different resolutions, different SST data sets (observed, modelled, climatological) and with online calculated ozone chemistry or prescribed observed ozone changes. The authors found the stratospheric response to be highly repeatable and due to the higher UV absorption at solar maximum. The tropospheric response varied with the SST data set used, being weaker but still present when climatological SSTs were prescribed at the lower boundary. The use of interactive and climatological SSTs influenced the extent of the tropospheric poleward jet shift and Hadley cell deceleration whereas with observed SSTs the signal was not that clear. The resolution of the model was found to have no systematic influence on the results.

In a study by Meehl et al. (2009) results from a coupled atmosphere-ocean-chemistry-climate model (AO-CCM) are shown and compared to simulations with a GCM (no fully resolved stratosphere, no interactive chemistry) and a CCM (fully resolved stratosphere, interactive chemistry, fixed climatological SSTs). It appears that the coupled AO-CCM is able to simulate observed changes in surface temperature and precipitation best. The GCM and the CCM can, limited by their design, simulate part of the total response with regard to the qualitative appearance (region and sign) and magnitude of the solar signal. For example, the CCM shows an increase in precipitation over the Indian Ocean during solar maximum winters which is retrieved with a higher magnitude in the AO-CCM results. The GCM, however, captures the precipitation decrease over the equatorial Pacific and the increase of rainfall off the equator which is also seen in the AO-CCM. Thus, the results of Meehl et al. (2009) present further evidence for the assumption made by, e.g., Rind et al. (2008) that both the top-down and the bottom-up mechanism are active in producing an atmospheric response to 11-year solar irradiance variations.

### 4.3.2 The tropospheric solar signal

The AO and NAO modes of variability were found to be eastward extended into Europe in solar max years in a CCM study by Tourpali et al. (2005). Simultaneously, the vertical extension into the stratosphere is higher during solar maximum than during solar mininmum. The steepest pressure gradient is displaced from the classical NAO index (Iceland-Portugal) to a Greenland-Mediterranean axis which may imply lower values for the classical NAO index in solar max years. The Pacific centre of action was found to be absent.

Lee and Hameed (2007) simulated an effect of the 11-year solar cycle on the Northern Annular Mode (NAM) in summer with stronger easterlies and higher temperatures (negative NAM phase) during solar maximum. Lee et al. (2008) further found a reduced variability of stratospheric temperatures in summer.

Kuroda and Shibata (2006) were able to confirm the observational study by Kuroda and Kodera (2005) with a CCM simulation. In particular, they obtained a SAM signal with large vertical extent from the troposphere to the upper stratosphere in late winter which persisted until the following autumn under solar maximum conditions. At solar minimum the signal was confined to the troposphere and not persistent. A significant tendency towards stronger stratosphere-troposphere coupling in southern winter is reported by Kuroda et al. (2007) who also identify it as the reason behind the observed SAM modulation by the solar cycle in late winter and spring. A stronger SAM at solar maximum was also found by Rind et al. (2008). However, Matthes et al. (2010) found the stronger SAM only during the QBO east phase.

Matthes et al. (2006) could simulate the downward transfer of the solar signal from the stratosphere to the troposphere during northern winter in a GCM with prescribed

ozone changes. Following a period of anomalously weak planetary wave activity in late autumn and early winter statistically significant zonal mean zonal wind changes reach down to the surface. This is connected with NAM-like geopotential height anomalies with lower than average heights over the pole and positive anomalies at mid-latitudes which appear consistently from the middle stratosphere to the surface. In consequence, the surface temperature over central and eastern Europe is enhanced under solar maximum conditions, as is expected during a positive NAO/NAM phase. The near surface signal in temperature confirms an earlier result from a CCM simulation by Rozanov et al. (2004). At low latitudes the solar signal manifests in a reduction in zonal mean upwelling associated with reduced zonal mean precipitation. The regions contributing the most to this signal are the Indian Ocean, the maritime continent and the western Pacific.

Shindell et al. (2006) using a fully coupled AO-CCM could confirm the observed tropospheric jet shift. Lee et al. (2009), however, report increases in specific humidity and an accelerated Hadley circulation under solar maximum conditions. Simultaneously, the ITCZ is shifted northward in their equilibrium AO-CCM simulations during northern winter. The response in northern summer implies a southward shift of the ITCZ and a broadening of the Hadley cell. Moreover, they found a strengthened Walker circulation in both solstice seasons.

### 4.3.3 Open questions

From previous model studies some important prerequisites for the successful simulation of the 11-year solar signal could be identified by several authors: a high resolution short wave radiation scheme to capture the strong wavelength dependence of the solar irradiance changes (Chapter 3 of SPARC CCMVal, 2010), a realistic background climatology (Matthes et al., 2004) and an assimilated or self-consistenly modelled QBO. The role that the QBO plays for the appearance of the solar signal is not yet fully understood (Matthes et al., 2010; Schmidt et al., 2010).

CCM model simulations still have deficiencies in reproducing the 11-year solar signal from observations as is discussed by, e.g., Austin et al. (2008) or in SPARC CCMVal (2010). However, improvements have been achieved in the recent past concerning the vertical structure of the solar signal in ozone. The CCMs that include solar irradiance variability in both the radiative heating code and in the ozone photochemistry could simulate a more realistic vertical ozone change profile with an upper stratospheric response close to observations and, in particular, with the secondary maximum in the lower tropical stratosphere (Figure 4.4c). Analogue improvements are seen in the associated temperature signal in the upper and lower stratosphere (Figure 4.4a). However, the uncertainties associated with the lower stratospheric secondary maxima are high as is seen in Figures 4.4b and 4.4d. According to the top-down mechanism it is assumed that solar induced dynamical changes lead to the secondary maxima in ozone and temperature change. It

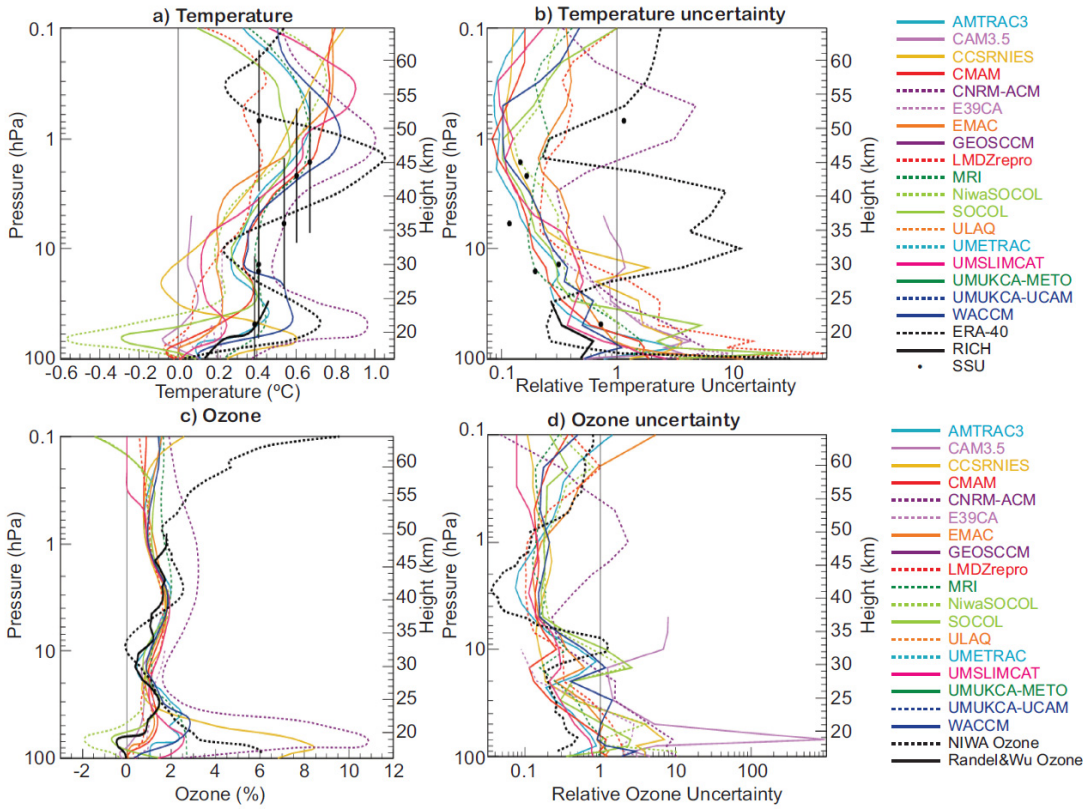


**Figure 4.4:** Annual mean solar regression coefficient in the tropics (averaged over 25°S-25°N) of a) temperature in K per 100 units F10.7 radio flux along with b) the relative uncertainty of the temperature fit, and of c) ozone in % per 100 units F10.7 radio flux along with d) the relative uncertainty of the ozone fit. Displayed are the results from 18 CCMs (coloured profiles) and from five observational data sets (solid, dashed and dotted black profiles), NIWA-3D ozone, 1979-2004, Randel&Wu ozone (1979-2005), RICH radiosonde data (1960-2004), ERA-40 (1979-2001), and SSU data (1979-2005). Note that the Randel&Wu ozone data are displayed in DU/km, whereas the CCMs and the NIWA-3D ozone data are on pressure levels. From SPARC CCMVal (2010), Chapter 8.

was speculated which factors might be responsible for the improvement. Possible candidates are (non-linear) interactions between the 11-year solar cycle, the QBO and El-Niño - Southern Oscillation (ENSO), or an aliasing effect between ENSO and the 11-year solar variability (Marsh and Garcia, 2007). Lee and Smith (2003) and Smith and Matthes (2008) point out the possibility of an incorrect attribution of QBO and volcanic signals.

The QBO may itself be influenced by the 11-year solar cycle as discussed by, e.g., Salby and Callaghan (2000) or Pascoe et al. (2005) who found longer lasting west phases during periods of high solar activity. Salby and Callaghan (2006) report an 11-year period in the power spectrum of the QBO. However, there is an ongoing debate whether these findings might be an artefact of a too short observational time series (Fischer and Tung, 2008; Kuai et al., 2009).

From the above literature survey it emerges that the reaction of the upper stratosphere to a changing solar irradiance has become relatively well established during the

last decade, although, it is not completely understood. The solar signal in ozone and temperature in the lower stratosphere is less well understood. In this context the following questions arise:

- Which forcings are necessary to let the secondary maximum of ozone and temperature in the tropical lower stratosphere emerge?
- How do these forcings interact to produce the observed response?
- How important is the presence of the tropical lower stratospheric signals, in particular, of the temperature signal, for the solar signal in the troposphere?

In the troposphere, however, a possible solar signal is often masked by high internal variability and, also by the effects of other forcings such as increasing greenhouse gas concentrations and, therefore, difficult to detect. Open questions in connection with the solar signal in the troposphere are:

- How does the solar signal in the troposphere look like?
- How much of the stratospheric solar signal is transferred downward to the troposphere and by which mechanism?
- In which way are natural modes of climate variability affected by the solar influence?
- Which factors such as lower boundary conditions or temporal evolution of the forcings influence the tropospheric solar signal?

In the following chapters an attempt is made to find answers for the above questions and to, thereby, contribute to the ongoing debate about the influence of the 11-year solar irradiance variability on the atmosphere. This is done by means of simulations with a numerical model which can be used as GCM or as CCM. A description of the model and its climatology is given in the next chapter.

# Chapter 5

# Model Description and Design of Experiments

In the previous chapter it was explained that a Chemistry Climate Model (CCM) which accounts for the interaction between the abundance of chemical species and the model dynamics is well adapted for the simulation of solar influence on the atmosphere. Chemistry, radiation and dynamics interact in such a model in different ways. The incident solar radiation may alter the chemical composition of the atmosphere by photolysis. On the one hand, the abundance of absorbing gases affects the radiative heating rates which in turn determine the temperature. On the other hand, the altered temperature field influences the rate constants of chemical reactions. Apart from the chemical-radiative feedback trace species may also be transported by the atmospheric circulation.

The model used for this study is introduced in the first section of this chapter. In the second section the model climatology is described and compared to observations. The third section (5.3) contains descriptions of the respective experiments, a series of transient and equilibrium simulations that are aimed at the investigation of the 11-year solar signal in the middle and lower atmosphere. The multiple linear regression model that was used for the analysis of the transient experiments is described in section 5.4.

## 5.1 The MA-ECHAM5/MESSy model system

The MA-ECHAM5/MESSy chemistry climate model system (hereafter denoted as EMAC-FUB[1]) is based on the 5th generation European Centre Hamburg general circulation model ECHAM5 (Roeckner et al., 2003; Roeckner et al., 2004; Roeckner et al., 2006) which is ultimately based on the ECMWF forecast model (Simmons et al., 1989). The

[1]The name EMAC-FUB is in accordance with the literature (Austin et al., 2010) used for the L39 version of the model system as employed at the Institute for Meteorology of Freie Universität Berlin (FUB). EMAC denotes the L90 version developed and run at the Max-Planck-Institute for Chemistry in Mainz.

model was extended from the original low-top version (upper lid at 10 hPa) to a middle atmosphere version reaching from the surface to 0.01 hPa, which corresponds to an approximate altitude of 80 km (Manzini et al., 2006; Giorgetta et al., 2006). ECHAM5 is a spectral model, i.e., the governing equations for the temporal evolution of vorticity, divergence, temperature, log-pressure and surface geopotential are solved in spectral space. The above prognostic variables are represented as truncated series of spherical harmonics. The truncation of T42 implies that waves up to zonal wavenumber 42 are explicitly resolved. To each spectral horizontal discretisation there is a corresponding Gaussian grid with almost regularly distributed grid points (approximately $2.8° \times 2.8°$). At these points all quantities that are not treated in spectral representation are evaluated, e.g., non-linear terms and parameterisations of sub-grid scale processes or abundances and tendencies of trace species.

The vertical discretisation divides the atmosphere into layers. It is based on a hybrid coordinate which follows the terrain near the surface and becomes more and more equal to levels of constant pressure in the stratosphere. There are two resolutions for the vertical discretisation, one with 39 layers (L39) and one with 90 layers (L90) between the surface and 80 km. Figure 5.1a gives an impression of the vertical discretisation with both the low and the high resolution. It is seen from Figure 5.1b that the layer thickness in the L90 version is about 700 m throughout the upper troposphere, the lower and the middle stratosphere. The thickness increases towards the stratopause at about 50 km but is still

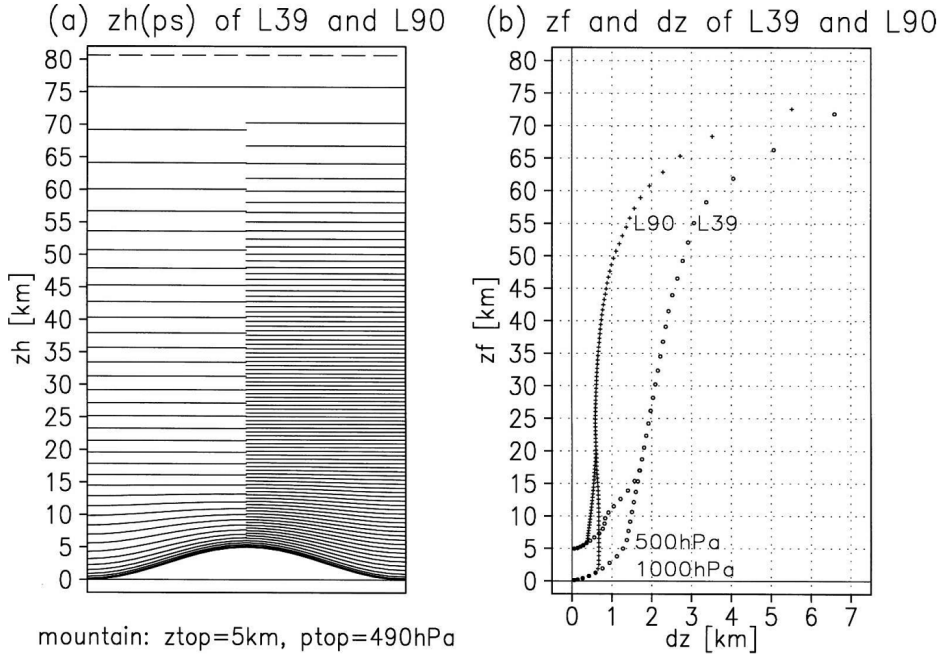


**Figure 5.1:** Vertical coordinate in the 39- and 90-level version of EMAC. a) Height of the hybrid half levels (solid lines) and of the uppermost full level (dashed line) in km. The sinusoidal mountain is 5 km high. b) Height of the hybrid full levels (zf) and layer thickness (dz) in km, open circles for L39, crosses for L90. From Giorgetta et al. (2006).

below 1 km. In the lower mesosphere the layer thickness increases rapidly to up to several kilometers. The distance between the levels in the lower and middle stratosphere is sufficiently small to model the vertically propagating equatorial waves and their interaction with the mean flow and, thus, to generate an internal QBO. In contrast, the layer thickness in the L39 version increases linearly from about 1.4 km in the upper troposphere to approximately 3 km at the stratopause. Higher up the increase takes place more rapidly. Due to the coarse resolution in the lower and middle stratosphere this model version is not able to generate an internal QBO. For details on nudging of the QBO in the L39 configuration see section 5.1.4.

EMAC-FUB uses the Modular Earth Submodel System (MESSy) (Jöckel et al., 2005; Jöckel et al., 2006) interface to couple a number of submodels representing lower and middle atmospheric processes such as chemistry, photolysis, land and ocean surface emissions, dry and wet deposition of trace species, etc. All submodels follow the MESSy philosophy. The most important aspect of this philosophy is that a module must not interfere with any other part of the code when switched off. This structure allows to readily replace single modules. The interactive chemistry scheme MECCA1 (Sander et al., 2005) allows to configure, e.g., stratospheric and/or tropospheric chemistry, rate constants of specific reactions and the numerical solver. In general, the modular structure opens the possibility for tailor-made configurations depending on the purpose and the focus of the simulation to be performed.

The ability of the model to consistently simulate the evolution of key trace species such as ozone, water vapour or $NO_y$ has been demonstrated in several studies (Jöckel et al., 2006; Lelieveld et al., 2007; Brühl et al., 2007).

It was mentioned above that sub-grid scale processes are included in the model as parameterisations. In the following subsections some parameterisations which are important for the simulation of solar influence on the middle atmosphere and troposphere are introduced.

### 5.1.1 The high resolution short-wave radiation scheme FUBRad

As mentioned in chapter 2 the variation of the total solar irradiance over one 11-year solar cycle is of the order of 0.1%. Significantly higher variability is observed at short wavelenghts in the ultraviolet (UV) region ranging from about 5% between 220 and 260 nm to 8% at 200 to 210 nm up to more than 50% at the Lyman-$\alpha$ wavelength (121.6 nm). Nissen et al. (2007) showed that the conventional radiation scheme of the underlying MA-ECHAM5 model that uses one band from the UV to the near-infrared region is not capable to account for these detailed changes. It is impossible to model the solar cycle effect on the atmosphere with such a coarse radiation scheme. A high resolution short-wave radiation scheme is needed and is available with the FUBRad scheme that was developed at Freie Universität Berlin. A detailed description of the scheme can be found in Nissen et al. (2007) and references therein.

The FUBRad scheme operates from the top of the model atmosphere to 70 hPa. This is due to the fact that below that level clouds may occur and the scheme does not include any routines to deal with backscattering processes on cloud droplets. It uses 49 spectral intervals from the Lyman-$\alpha$ wavelength (121.6 nm) to the visible spectral range (682.5 nm). Compared with other SW radiation schemes comprising two to four intervals this is a high resolution, but in comparison to line-by-line schemes which have 1 nm-intervals the resolution of FUBRad is rather coarse. Absorption by ozone in the Hartley (10 intervals from 243.5 nm to 277.5 nm), Huggins (18 intervals from 277.5 nm to 362.5 nm) and Chappuis (407.5 nm to 682.5 nm) bands and by molecular oxygen at the Lyman-$\alpha$ wavelength (121.6 nm), in the Schumann-Runge continuum (3 intervals from 125 nm to 175 nm) and bands (175 nm to 205 nm) as well as in the Herzberg continuum (15 intervals from 206 nm to 243 nm) is taken into account. Furthermore, it accounts for an incomplete conversion of radiative energy into heat involving airglow in the Hartley bands, the Schumann-Runge continuum and the Lyman-$\alpha$ line. FUBRad calculates the absorption in the downward beam and connects to the standard SW radiation scheme (Fouquart and Bonnel, 1980) which operates below 70 hPa. The upward calculation is done reversely, the Fouquart and Bonnel scheme hands the tropospheric albedo over to FUBRad which calculates the backscattered path.

### 5.1.2 The photolysis scheme

In order to model the influence of solar variability on atmospheric composition it has to be accounted for changing photolysis rates. This is done in EMAC-FUB by the submodel JVAL which calculates the photolysis rate coefficients $J(\lambda)$

$$J(\lambda) = \int_{\lambda_1}^{\lambda_2} \epsilon(\lambda)\, \sigma(\lambda)\, q_\lambda(\lambda)\, d\lambda, \tag{5.1}$$

where $\lambda$ denotes the wavelength, $q_\lambda$ the actinic flux, i.e., the number of photons per unit area (typically $cm^2$) and unit time (s) in the wavelength interval $\lambda$ to $\lambda + d\lambda$, $\sigma$ the absorption cross section which may depend on temperature and pressure and $\epsilon$ the quantum yield, i.e., how much of the incident radiation actually leads to photodissociation of the molecule (Brasseur and Solomon, 2005). Since the photolysis rate is expressed in $s^{-1}$ sometimes the name photolysis frequency is used.

The actinic fluxes are incorporated for eight spectral intervals from the UV to the visible region of the spectrum as well as for the Lyman-$\alpha$ wavelength which is relevant in the mesosphere. Together with pre-calculated effective absorption cross-sections for more than 50 tropospheric and stratospheric species and the knowledge of cloud cover, cloud water content and climatological aerosol from the base model it is then possible to compute the photolysis rates using a delta-twostream-method (Landgraf and Crutzen, 1998).

### 5.1.3 Gravity-wave parameterisations

In the previous chapter the importance of a realistic background climatology for the simulation of the 11-year solar signal was emphasised (Matthes et al., 2003, 2004). A major aspect is the correct simulation of the polar night jet in terms of peak wind velocities and spatial structure. In reality gravity waves (GW) play an outstanding role for the strength and the shape of the polar night jet as they propagate from the troposphere upwards into the stratosphere and mesosphere where they dissipate and deposit their momentum onto the mean flow, thereby decelerating the jet. There are two types of gravity waves. Transient GW are generated in connection with deep convection or fronts within synoptic systems. Orographic GW emerge when air is forced to flow over mountains.

As gravity waves are a sub-grid scale phenomenon in a CCM with the above-mentioned horizontal and vertical discretisation, their effect has to be parameterised in order to be taken into account. The parameterisation simulates the vertical propagation and, ultimately, the dissipation of a continuous GW spectrum which has its origin in the troposphere. EMAC-FUB uses the transient gravity wave parameterisation based on the work of Hines (1997a, 1997b) the concrete implementation of which is described by Manzini et al. (2006). The transient GW source spectrum is basically controlled by a latitude- and time-independent value for the GW wind velocity variance at the launch level of the waves, by default 1 m/s. With the default value the climatological polar night jet was too weak, in particular, in the middle stratosphere. For this reason, a series of test simulations was performed and evaluated to determine the optimal value for the control parameter of 0.92 m/s within the context of this study. The effects of orographic gravity waves are parameterised using the methods described by Lott and Miller (1997) and Lott (1999).

### 5.1.4 Nudging of equatorial stratospheric winds towards observations

The EMAC-FUB model is primarily used in the horizontal resolution of $2.8^\circ \times 2.8^\circ$ (T42) and with 39 levels from the surface to 0.01 hPa ($\approx$ 80 km). Limitations of available computing and data storage resources are the main reasons for this. With this vertical resolution the model does not generate a self-consistent QBO, but simulates permanent easterlies in the QBO domain (Giorgetta et al., 2006). Therefore, if a QBO shall be accounted for in a simulation, observed equatorial winds have to be assimilated. An extended data set based on Naujokat (1986) is used for this purpose. A series of test simulations was performed to find a suitable nudging time constant. The requirements were that the observed amplitude of the equatorial wind oscillation should be reproduced as accurately as possible and that the overlying semi-annual oscillation is simulated correctly and not affected by the nudging in the levels below. It was recommended to limit the nudging to the lower and middle stratosphere and to a narrow region north and south of the equator (Thomas et al., 2009; Marco Giorgetta, 2008, personal communication). The applied

**Table 5.1:** Nudging weights and half widths for the assimilation of observed equatorial winds

| Pressure (hPa) | 6 | 8 | 10 | 12 | 15 | 20 | 25 | 30 | 35 |
|---|---|---|---|---|---|---|---|---|---|
| Weight | 0 | 0.2 | 0.5 | 1.0 | 1.0 | 1.0 | 1.0 | 1.0 | 1.0 |
| Half width | 0 | 8.5 | 8.5 | 8.375 | 8.25 | 8.125 | 8.0 | 7.875 | 7.75 |
| Pressure (hPa) | 40 | 45 | 50 | 60 | 70 | 80 | 90 | 100 | |
| Weight | 1.0 | 1.0 | 1.0 | 1.0 | 1.0 | 0.5 | 0.2 | 0 | |
| Half width | 7.625 | 7.5 | 7.375 | 7.25 | 7.125 | 7.0 | 7.0 | 0 | |

weighting factors and the half widths that were used in the three test simulations are given in table 5.1. The core domain for the nudging extends from 70 to 12 hPa in the vertical and from 7 °S to 7 °N. No nudging is applied outside the domain 10 °S to 10 °N. The relaxation time constants of 10, 15 and 20 days were tested.

Figure 5.2a shows the zonal mean zonal wind amplitude at 50 hPa obtained with the three different nudging time constants along with the observed values from Singapore. It is seen that the westerlies are simulated best with a time constant of 10 days. On the other hand, the easterlies are understimated with all tested time constants. Figure 5.2b shows profiles of the equatorial wind at a certain time step (15 May 2002) along with the observed values at Singapore as they were used in the model. It is clearly seen that the nudging is applied only in a limited height domain. It is, furthermore, seen that the relaxation towards observed winds in the lower stratosphere is sufficient to obtain a realistic zonal mean equatorial wind at the levels above, i.e., the overlying easterly phase is simulated correctly. This is due to the filtering effect that the lower stratospheric equatorial winds have on the upward propagation of Kelvin- and Rossby-gravity waves

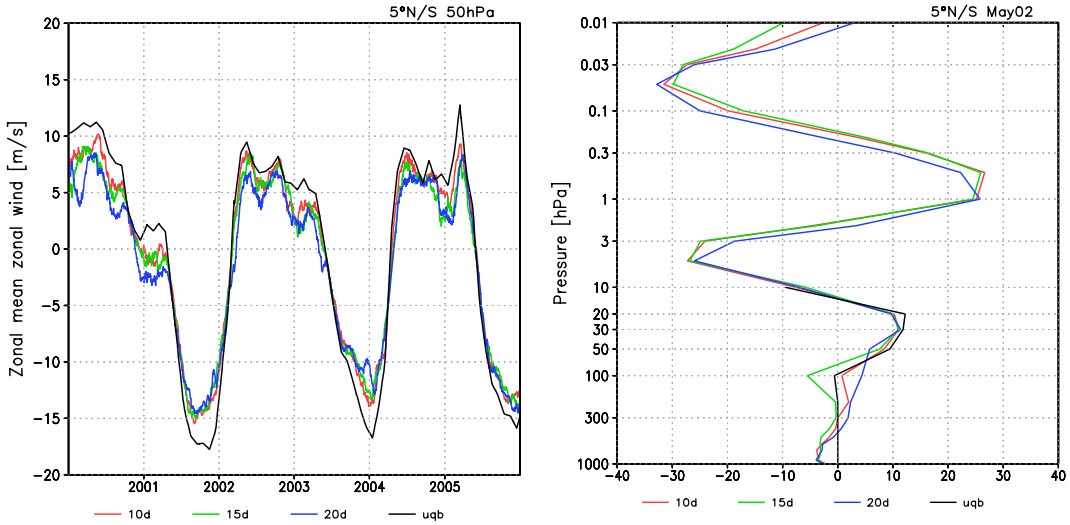


**Figure 5.2:** a) Time series of zonal mean equatorial wind at 50 hPa averaged from 5°S to 5°N. Red curve: 10 d nudging time constant, green curve: 15 d, and blue curve: 20 d. Black curve: observed wind at Singapore as used in the model. b) Profiles of zonal mean equatorial wind averaged from 5°S to 5°N.

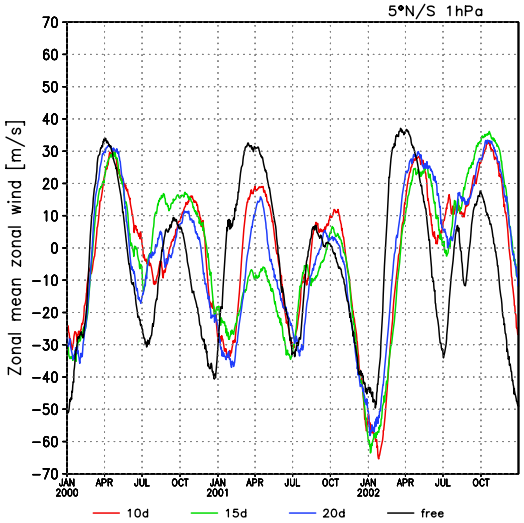


**Figure 5.3:** Time series of zonal mean equatorial wind at 1 hPa averaged from 5°S to 5°N. Red curve: 10 d nudging time constant, green curve: 15 d, and blue curve: 20 d. The black curve depicts the zonal mean zonal wind as it is obtained in a simulation without nudging of the QBO.

(not shown) which cause the opposite QBO phase on top of a given phase below.

At higher levels, typically 1 hPa, the semi-annual oscillation is observed. The nudging towards observed winds in the equatorial lower stratosphere may influence this oscillation. Figure 5.3 depicts the zonal mean zonal wind amplitude at 1 hPa for the three tested time constants and for a simulation without QBO nudging. In the absence of a nudged QBO the main characteristics of the SAO are well captured in the model as is shown by the black curve in Figure 5.3. The easterly phases are found in January and July with the January easterlies being stronger than those in July. The west phases appear in April/May and in October with the former frequently being stronger than the latter (cf. section 3.3 for a comparison with observations). The curves from the QBO-nudging experiments follow the black curve in its seasonality but do sometimes over- or underestimate the amplitude found in the unnudged simulation. However, the amplitudes of all, the nudged and unnudged simulations, are within the range of observed values (Garcia et al., 1997): Maximum easterlies between -35 and -60 m/s are typically found at 1 hPa in January. The observed maximum westerlies in April or May attain values between 10 and 25 m/s at 1 hPa. Hence, it can be stated that the assimilation of observed zonal mean zonal winds in the layers below does not affect the SAO adversely.

In the light of the above results the relaxation time constant of 10 days was chosen to be applied where appropriate in the following experiments with L39 vertical resolution.

## 5.2 The model climatology

The climatology of the zonal mean temperature and the zonal mean zonal wind for the months of January and July is given in Figure 5.4. This climatology was obtained by averaging over two simulations with interactive chemistry under present day (year 2000) conditions in T42L39 resolution. In total the average was taken over 60 years. The details for the experimental set-up are given in subsection 5.3.3.

Compared to the SPARC-climatology (Randel et al., 2002) derived from observations (Figure 3.6) the model simulates a generally consistent climate. However, a closer inspection reveals some discrepancies, e.g., the modelled temperature in the tropical tropopause region is lower than the observed one (Figure 5.4a and c). An additional comparison with ERA-40 zonal mean temperatures (not shown), though, supports the EMAC-FUB results. The modelled stratospheric temperatures generally agree with the observed ones with the

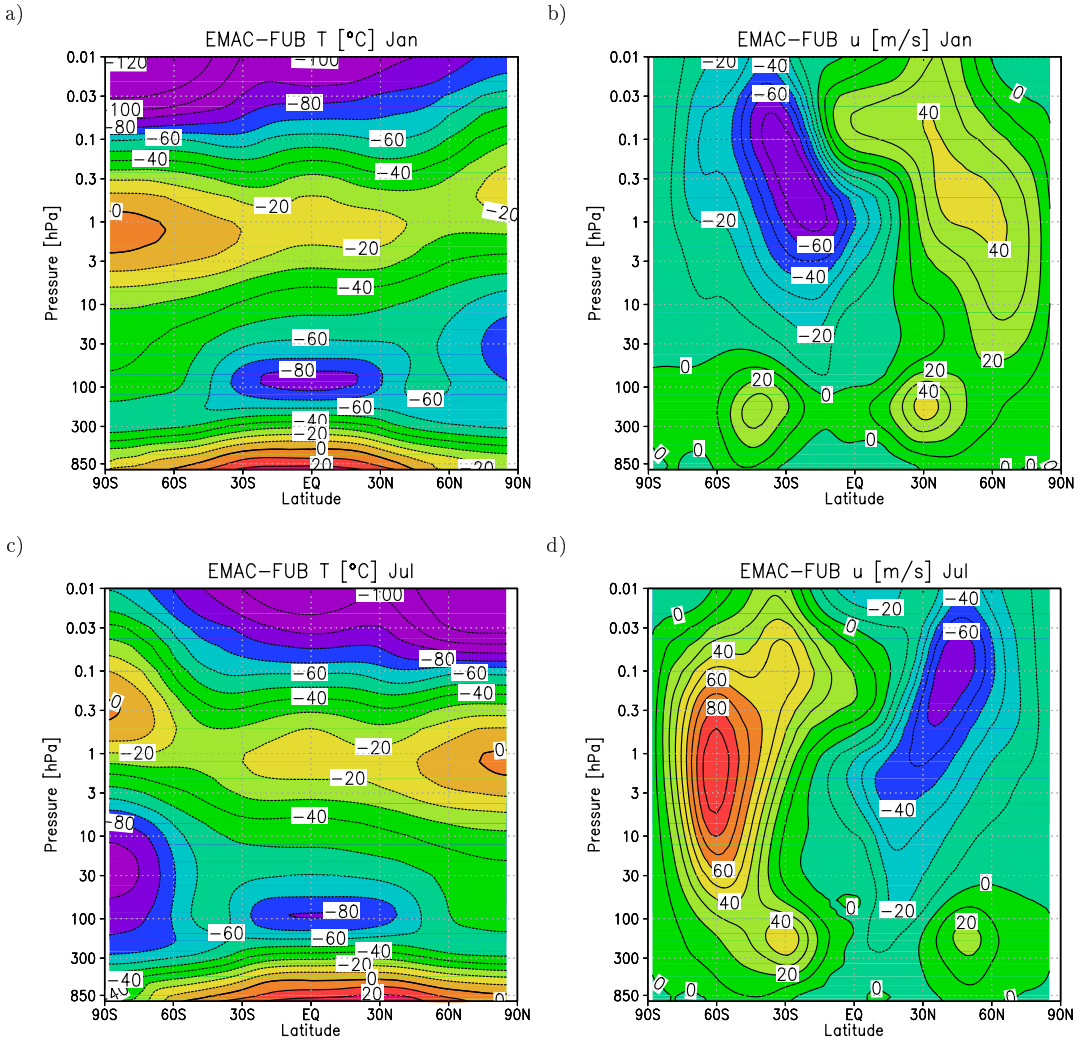


**Figure 5.4:** Climatology of zonal mean temperature in °C (a and c) and zonal mean zonal wind in m/s (b and d) for January and July as simulated by EMAC-FUB.

exception of a somewhat lower maximum at the summer pole stratopause (at about 1 hPa or 50 km) where the observations show values slightly above 10 °C in January whereas in EMAC-FUB they do not exceed 10 °C. EMAC-FUB also underestimates the observed temperature by some degrees in the tropical stratopause region. The model results in the winter hemisphere lower stratosphere are in good agreement with the observations. In the mesosphere the model is biased towards lower than observed temperatures in January as well as in July. This is particularly true in the respective summer mesosphere where the lowest temperatures occur in the atmosphere and at equatorial latitudes.

Considering the zonal mean zonal wind climatology of EMAC-FUB it can be stated that the polar night jet in the northern hemisphere in January (Figure 5.4b) shows a realistic tilt towards lower latitudes with increasing height. The maximum value of about 45 m/s in the model is located somewhat below the observed maximum of the same magnitude. A difference can be noted in the northern high-latitude lower stratosphere in January (Figure 5.4b) where the modelled wind velocities are weaker than the observed ones. In contrast, the tropospheric subtropical jets in January and July are stronger in the model than in the observations. The southern hemispheric polar night jet in July (Figure 5.4d) is considerably stronger than its northern hemispheric counterpart (90 m/s compared to 45 m/s) which is consistent with the observations. In EMAC-FUB it is in a very upright position which is not the case in the observations where at higher altitudes (above 0.5 hPa) the maximum is situated at lower latitudes. The summer hemisphere easterlies are quantitatively in good agreement with the observed winds. However, the observed tilt of the jet axis from high latitudes near the upper boundary of the domain towards subtropical latitudes at the stratopause level is not as strong in the model. The axis of the easterlies is too steep in the latitude-height-plane.

The underestimation of the zonal mean zonal wind in the northern winter lower stratosphere is an indication for a higher interannual variability in the model than in reality. Figure 5.5 shows the long term daily means of zonal mean temperature and zonal mean zonal wind at 10 hPa, i.e., in the middle stratosphere, along with its standard deviation and the extrema. By comparison with the analogue figures obtained from ERA-40 data from 1979 to 2001 (cf. Figure 3.7) it becomes apparent that EMAC-FUB indeed exhibits too much interannual variability in the northern hemisphere, in particular, too early in autumn and winter. The north-polar temperature in ERA-40 shows a sudden increase in variability in the last ten days of November whereas no such abrupt increase can be found in the EMAC-FUB results. They are more variable already in early November. This is reflected in the extrema of the zonal mean zonal wind at 60 °N which show negative values, i.e., easterly winds and, thus, by definition major stratospheric warmings beginning in the second half of November. As a consequence the zonal mean zonal wind in the model does not reach the observed values in mid- and late winter. This is a known problem of the MA-ECHAM5 base model as discussed by Charlton et al. (2007). In the southern hemisphere the model captures the maxima and minima of zonal mean zonal wind at 60 °S well (see Figure 5.5d). In addition the timing of seasonal transitions is rea-

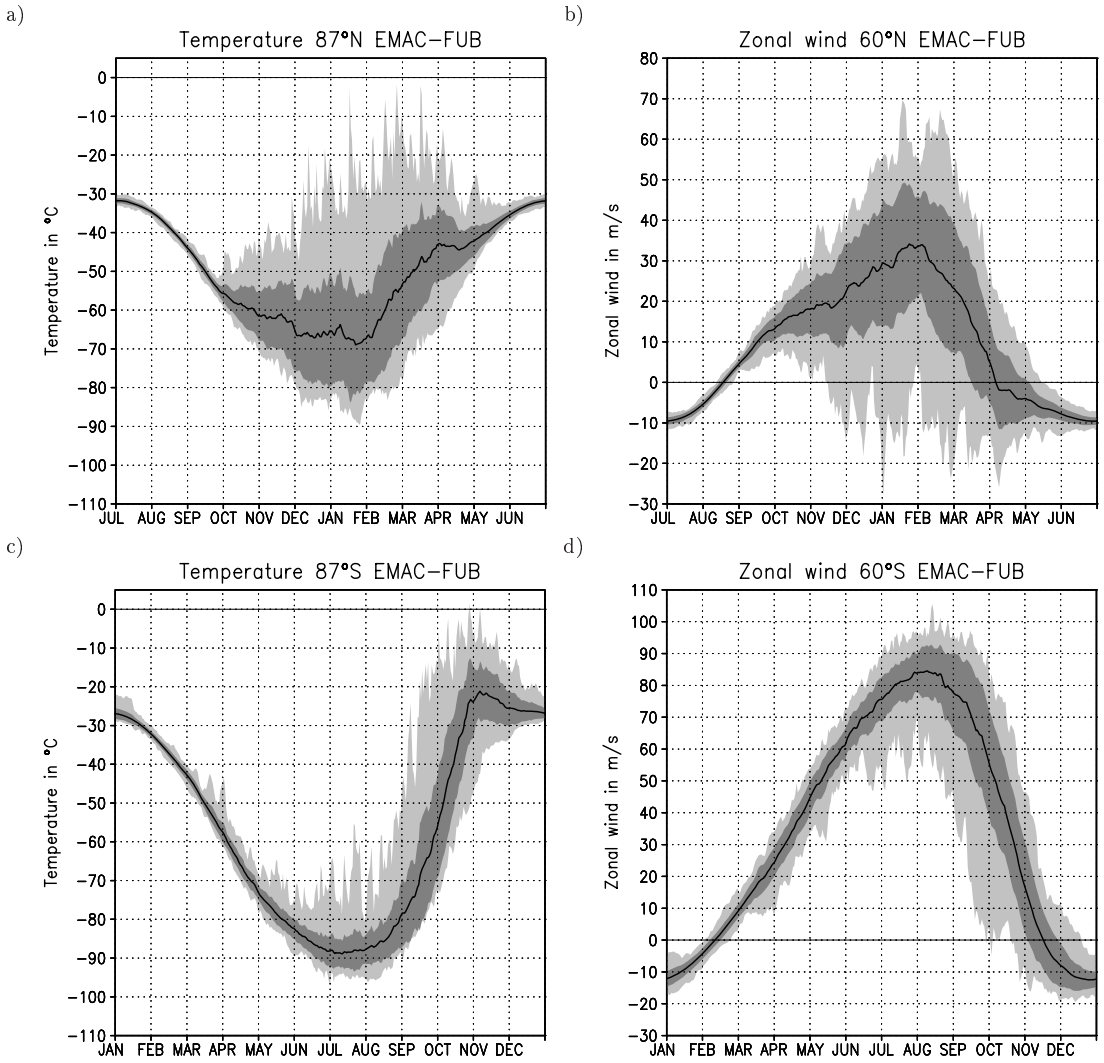


**Figure 5.5:** Long term daily mean zonal mean temperature at 87.5 ° and 10 hPa and of zonal mean zonal wind at 60 ° and 10 hPa on the respective hemisphere as simulated by EMAC-FUB (thick black curves) along with the standard deviation (dark shaded range) and the extrema (light shaded region).

sonable. The EMAC-FUB results show a standard deviation which is comparable to the observed. However, in terms of the extrema the model exhibits more variability than the ERA-40 data. Temperature during southern winter is by about 5 K lower in EMAC-FUB than in the observations. At the same time the modelled temperature's standard deviation is considerably reduced compared to the observed one. The observed low extrema below -100 °C are not found in the model.

The observed variability of total ozone in the northern and southern polar caps in the period 1990 to 2000 is shown in Figure 5.6a and 5.6b on a monthly basis. By comparison with the interactively modelled total ozone from a transient simulation with observed SSTs as lower boundary condition (see section 5.3.1 for details) spanning the same period of time (Figure 5.6c and 5.6d) it is seen that the variability over most parts of the year is comparable in the observations and in the model.

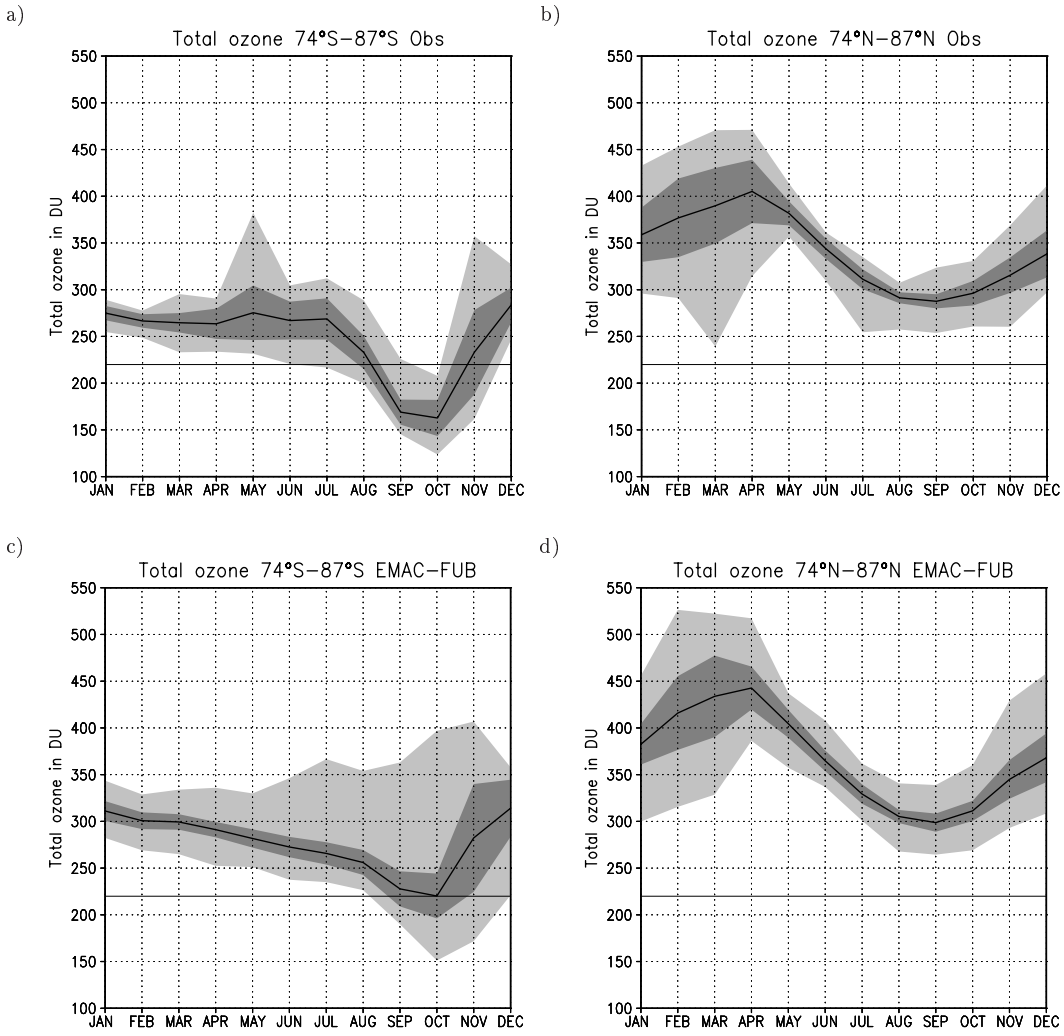


**Figure 5.6:** Long term monthly mean zonal mean total ozone from the period 1990 to 2000 averaged over the polar caps from 74° to 87° a) and b) observed by TOMS, SBUV and ground based measurements and c) and d) simulated by EMAC-FUB (thick black curves) along with the standard deviation (dark shaded range) and the extrema (light shaded region). The horizontal line marks the 220 DU-level as threshold for the ozone hole definition. (The data sets are the TOMS/SBUV Version 8 Merged Ozone Data Sets, Total Ozone Revision 05, obtained from http://acdb-ext.gsfc.nasa.gov/Data_services/merged/, data gaps were filled with ground based measurements (Fioletov et al., 2002)).

However, the observed minima in southern spring (September and October) at about 170 DU are deeper than the simulated ones at about 220 DU. This is due to a meanwhile known bug in the parameterisation of polar stratospheric clouds (Christoph Brühl, 2010, personal communication) which inhibits a realistic occurrence of these clouds and, thus, leads to an underestimation of heterogeneous ozone depletion. In the northern hemisphere spring (March and April) total ozone peaks at about 405 DU in the observations. The model produces a too high maximum up to 445 DU with a large spread of possible extreme values, especially, in March. On the other hand, the model does well in August and September when total ozone in the northern polar cap reaches its minimum.

## 5.3 Design of the experiments

In this section the CCM experiments that were set up to investigate different aspects of the 11-year solar variability are described in detail. A series of CCM simulations was conducted in order to qualitatively and quantitatively investigate the 11-year solar signal in the middle and lower atmosphere. A transient simulation intended to simulate the recent past as accurately as possible is chosen as a reference experiment. Starting from this basis different aspects of the experimental set-up have been changed to examine their influence on the 11-year solar signal in the atmosphere. In detail

- the vertical resolution has been increased,
- the transient set-up has been replaced by two equilibrium perpetual solar maximum and minimum experiments,
- in lieu of interactive chemistry ozone climatologies representative for solar maximum and minimum have been prescribed to the (GCM-)model,
- a different sea surface temperature (SST) and sea ice data set has been applied as lower boundary condition, and finally,
- the two important forcing time series of QBO and SSTs have been band pass filtered in order to exclude any solar influence on these forcings.

In the following the experiments performed to investigate the 11-year solar signal in the atmosphere are described. This description starts with the reference transient simulation. In this context a detailed list of the employed MESSy submodels for the CCM configuration of EMAC-FUB is given. Afterwards, only deviations from this list are mentioned. The description of the other experiments refers closely to the basic set-up by specifying the differences between the actual simulation and the reference experiment.

Apart from this series of 11-year solar cycle simulations two sensitivity studies were performed, one with EMAC-FUB in GCM mode and an artificially enhanced westerly wind in the winter hemisphere and one with the EMAC-FUB CCM about the response of ozone to variability associated with the 27-day solar rotational cycle. Two separate chapters are dedicated to the experimental set-up and the results of these experiments, see chapter 6 and 7, respectively.

### 5.3.1 Transient simulation of the past

The key issue of this study is to investigate the influence of the 11-year solar cycle on the atmosphere, more precisely on ozone, temperature, winds, wave propagation, upwelling and precipitation in the troposphere and stratosphere. The most realistic approach to model the solar influence is a transient simulation which is aimed at reproducing the past as accurately as possible. Such an experiment was set up in the framework of CCMVal including daily spectrally resolved solar irradiances (Lean et al., 2005), i.e., the 11-year solar cycle explicitly included with realistic increases and decreases of solar activity. The

boundary conditions were specified according to the REF-B1 scenario (Eyring et al., 2008). Observed SSTs and sea ice data from the HadISST1 data set (Rayner et al., 2003) were prescribed at the surface. The abundances of greenhouse gases (GHGs) and ozone depleting substances (ODSs) were likewise taken from observations. Surface emissions of ozone and aerosol precursor substances (CO, VOCs, $NO_x$, $SO_2$) were taken from the RETRO dataset (Schultz et al., 2008). The effects of three major volcanic eruptions, Mt. Agung in 1963, El Chichon in 1982 and Mt. Pinatubo in 1991, were included.

The EMAC-FUB model system was used in the spatial resolution of $2.8° \times 2.8°$ (T42) and with 39 levels from the surface to 0.01 hPa ($\approx$ 80 km). With this resolution in the vertical direction the model is unable to generate an internal QBO, therefore the nudging towards observed winds as described in section 5.1.4 was applied. The following submodels were coupled to the base model:

| | |
|---|---|
| CLOUD | Cloud cover and precipitation |
| CONVECT | Convection |
| CVTRANS | Convective tracer transport |
| DRYDEP | Dry deposition of gas phase tracers and aerosols (Kerkweg et al., 2006a) |
| H2O | Water vapour sources and transport in the middle atmosphere |
| HETCHEM | Heterogeneous reaction rates |
| JVAL | Photolysis (Landgraf and Crutzen, 1998) |
| LNOX | $NO_x$ production by lightning |
| MECCA1 | Interactive chemistry (Sander et al., 2005) |
| OFFLEM | Offline emissions of trace species (Kerkweg et al., 2006b) |
| ONLEM | Online emissions of trace species (Kerkweg et al., 2006b) |
| PSC | Formation of polar stratospheric clouds and associated denitrification and dehydration (Buchholz, 2005) |
| QBO | QBO nudging |
| RAD4ALL | Radiation parameterisation including the high resolution short-wave radiation scheme FUBRad (Nissen et al., 2007) |
| SCAV | Scavenging and wet deposition of species (Tost et al., 2006) |
| SEDI | Sedimentation of aerosol particles (Kerkweg et al., 2006a) |
| TNUDGE | Tracer nudging (Kerkweg et al., 2006b) |
| TROPOP | Tropopause diagnostics |
| VAHR | Additional heating rates due to volcanic eruptions |

Prior to the evaluated period from 1960 to 2005 two years spin-up were computed to allow the model to adjust to the new boundary conditions and to avoid trends in the evaluated period. This experiment is regarded as reference. Detailed results are shown and discussed in section 8.1.

From the experimental design and the model configuration without an interactive ocean model it becomes obvious that this simulation (and all the other simulations to be

described in the following subsections) is well suited to study the indirect solar influence which is supposed to act via stratospheric pathways (top-down mechanism). Changes in ozone and radiative heating in the stratosphere alter the zonal wind and the propagation conditions for planetary waves, thereby, communicating the solar signal to lower levels (Kodera and Kuroda, 2002). However, it is possible that a direct solar influence which is effective at the surface (bottom-up mechanism, Meehl et al., 2008) is included in the prescribed observed SSTs.

This simulation was performed at an SGI Altix parallel computer of HLRN, Konrad-Zuse-Zentrum in Berlin. The solar signal in this simulation is shown, compared with observations and discussed in section 8.1.

### 5.3.2 Transient simulation of the past with enhanced vertical resolution

A very similar simulation spanning the time period 1960 to 2000 was performed using EMAC in the higher vertical resolution with 90 layers between the surface and the upper mesosphere (80 km). In this configuration the QBO develops spontaneously. However, in order to be consistent with the prescribed observed SSTs and to ensure the correct phase the equatorial winds were weakly nudged using a time constant of 70 days.

In addition to the submodels mentioned in the preceding subsection, two newly developed submodels were used:

| | |
|---|---|
| SPACENOX | Ionising effects of galactic cosmic rays and subsequent downward transport of NO into the polar winter mesosphere (Baumgaertner et al., 2009) |
| SPE | Solar proton events and associated precipitating particles causing production of $NO_x$ and $HO_x$ and destruction of stratospheric ozone (Baumgaertner et al., 2010) |

This simulation was performed by CAWSES-ProSECCO project partners at the Max-Planck-Institute for Chemistry, Mainz on an IBMp690 Power4 parallel computer at the Max-Planck-Society computing centre (RZG) in Garching. Results and a comparison to the results of the reference simulation are given in section 8.2.

### 5.3.3 Solar max and min equilibrium simulations with interactive chemistry

Another way to investigate the 11-year solar cycle influence on the middle and lower atmosphere are so called equilibrium experiments. The model simulates a certain number of years under perpetual solar maximum and minimum conditions, respectively. This set-up is not realistic in the sense that the atmosphere is forced into a permanent solar maximum or minimum circulation state as opposed to the real increase and decay of solar activity with the 11-year cycle. However, it is a convenient way to study the solar

influence on the atmosphere, in particular, with regard to limited computing resources. To obtain 30 years of solar maximum and minimum a simulation of 10 solar cyles, i.e., 110 years, would be neccessary, which is very computer time intensive.

Two equilibrium simulations with EMAC-FUB (T42L39) were set up to simulate 30 years under perpetual solar maximum and minimum conditions, respectively. To both simulations the same boundary conditions were prescribed except for the solar irradiance. The boundary conditions were chosen according to the recommendations for a CCMVal REF-B0 scenario (Eyring et al., 2008). In particular, the SSTs and sea ice data were taken from the observational HadISST1 data set (Rayner et al., 2003) and averaged over the period from 1995 to 2004. Abundances of GHGs, ODSs and aerosols were prescribed to be representative for the year 2000 conditions. Surface emissions of ozone and aerosol precursor substances (CO, VOCs, $NO_x$, $SO_2$) were taken from the RETRO data set, averaged over the years 1998 to 2000 and repeated each year. No volcanic eruptions were included. The prescribed solar irradiances were taken from the data set by Judith Lean (Lean et al., 2005). The monthly mean irradiances from November 1989 were used for solar maximum and from September 1986 for solar minimum. The list of employed submodels is the same as for the transient simulation in section 5.3.1 except for the additional heating rates due to volcanic eruptions (VAHR).

The observed equatorial zonal mean zonal wind time series that was actually assimilated into the model simulation covers the time period 1957 to 1989. It was prescribed to both the perpetual solar maximum and solar minimum simulation, to ensure that the QBO in both simulations is running in parallel. From that and the above description it becomes obvious that apart from the solar irradiance all other boundary conditions were identical. Thus, the resulting differences in any simulated quantity can be attributed to the solar irradiance changes.

Again, there were two years of spin-up computed for both the solar maximum and solar minimum simulation prior to the evaluated period to allow the model to adjust to the new boundary conditions and to avoid trends in the evaluated period. The actual production runs cover 30 years of simulation each. They were executed on an IBMp690 Power4 supercomputer of HLRN, Konrad-Zuse-Zentrum in Berlin. The results are shown and compared with the results of the transient reference simulation in section 8.3.

### 5.3.4 Solar maximum and minimum equilibrium simulations without interactive chemistry

The equilibrium experiments from the above section were repeated with EMAC-FUB in GCM mode, i.e., without interactive chemistry and related processes. It is, thus, possible to asses the influence of interactive chemistry on the solar signal. Only the following submodels were used: CLOUD, CONVECT, H2O, RAD4ALL, TROPOP. The model was run in T42L39 resolution. No QBO nudging was applied. Consequently, the model

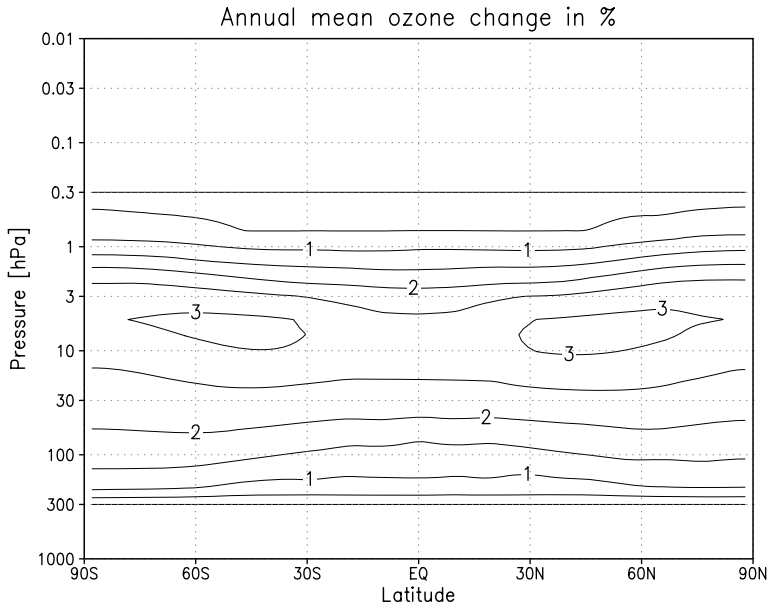


**Figure 5.7:** Annual mean relative ozone change between solar maximum and minimum (max-min/min) as prescribed to EMAC-FUB in GCM mode.

simulates permanent weak easterlies in the latitude and height region of the QBO. With the interactive chemistry modules disabled ozone can not react to the imposed solar irradiance changes. Therefore, it is necessary to prescribe an ozone climatology which has to be adjusted to the solar maximum and minimum conditions, respectively. As basic ozone climatology an updated version of Fortuin and Langematz (1995) is used and relative (percentaged) changes are added or subtracted to obtain fields for solar maximum and minimum. The solar induced ozon changes were calculated with a fully interactive two-dimensional radiation-chemistry-transport model to which the solar irradiances from September 1986 (min) and November 1989 (max) (Lean, 1997) were prescribed (Haigh, 1994). The maximum ozone change is found between 5 and 10 hPa at mid-latitudes where it amounts to 3%, see Figure 5.7. The limited vertical extent of the ozone changes in Figure 5.7 is due to the radiation-chemistry-transport model domain. It does not mean that ozone outside this region is insensitive to solar irradiance changes.

Like with the other simulations there were two years of spin-up computed for both the solar maximum and solar minimum simulation prior to the evaluated period. The production runs span 25 years of simulation each. They were executed on an IBMp690 Power4 supercomputer of HLRN, Konrad-Zuse-Zentrum in Berlin. The results are shown in section 8.4 and compared with the results of the equilibrium simulation including interactive chemistry, on the one hand, and with the reference simulation, on the other hand.

### 5.3.5 Transient simulation with modelled SSTs and sea ice

Most CCMs have not been coupled to an interactive ocean model, yet. Therefore, SSTs and sea ice coverage have to be prescribed to the model as lower boundary condition. Depending on the focus of the respective study it might be appropriate or even neccessary to use SSTs and sea ice data that were pre-calculated by an Atmosphere-Ocean-GCM. In a comparative study Garny et al. (2009) found significant differences in the climatologies of ozone and temperature in simulations with prescribed either observed or modelled SSTs and sea ice data. Furthermore, tropical upwelling and the Brewer-Dobson-Circulation and the trends in these quantities were affected by the choice of the SSTs and sea ice.

To investigate the possible influence that the usage of a modelled instead of an observed SST and sea ice data set may have on the 11-year solar signal a 140 year long CCM simulation covering the period 1960 to 2100 is performed and analysed. The goal of this simulation is to project the future development of atmospheric dynamics and chemistry, in particular, of stratospheric ozone. Boundary conditions were specified according to the recommendations for a SPARC CCMVal scenario SCN2d simulation (Eyring et al., 2008), i.e., for a consistent simulation from the past to the end of the 21st century including natural variability as the 11-year solar cycle, the QBO, and, at least in the past, volcanic eruptions. Anthropogenic forcings by emission of GHGs and ODSs follow the widely used Special Report on Emission Scenarios (SRES) A1B scenario. Emissions of other species such as $SO_2$, $NO_x$, CO or VOCs were taken from the RETRO dataset for the past and were prescribed according to the adjusted B2 baseline scenario of IIASA (International Institute for Applied Systems Analysis) for the future. The submodels coupled to EMAC-FUB for this simulation are the same as for the transient reference simulation (see section 5.3.1). The horizontal and vertical resolution are also unchanged compared to the reference run (T42L39).

The SST and sea ice data come from a coupled atmosphere-ocean GCM simulation with ECHAM5-MPIOM performed at the Max-Planck-Institute for Meteorology in Hamburg. The GCM simulation followed the SRES A1B scenario and covered the 20th and the 21st century (Heinz-Jürgen Punge, 2008, personal communication).

Even if the focus of this simulation is on the future development of stratospheric ozone, the set-up is well suited to study the 11-year solar signal in the past with the different lower boundary conditions. Another interesting aspect in this context is the analysis of the 11-year solar signal in a future climate, in particular, in the second half of the 21st century.

This simulation was executed on an IBM Power6 parallel computer at the European Centre for Medium Range Weather Forecast (ECMWF) in Reading, United Kingdom. Results of the comparison with the reference transient simulation as well as the 11-year solar signal in a future climate are presented in section 8.5.

### 5.3.6 Transient simulation with fixed SSTs and GHGs

To investigate the 11-year solar signal in the absence of GHG-induced climate change a transient simulation with fixed SSTs, sea ice and GHGs is analysed. However, the prescribed observed and projected development of the ODS abundances nonetheless induces an anthropogenic climate change since some of the ODSs simultaneously act as greenhouse gases (e.g., CFC-11, CFC-12). The fixed SSTs represent the conditions at the year 1960. An average over the period 1955 to 1964 was computed with the aim to even possible extrema associated with the El Niño-Southern Oscillation phenomenon. Other boundary conditions for this simulation follow the recommendations given by Eyring et al. (2008) for an SCN2c experiment and are similar to the previously described SCN2d simulation. The period covered with this experiment is 140 years long, beginning in 1960 and ending 2100.

The original goal with this simulation is to study the development of stratospheric ozone if no man-made climate change was going on. This helps to understand the influence that a GHG-induced cooling of the stratosphere has on the recovery of the ozone layer. However, in connection with the above described reference simulation (section 5.3.1) that uses observed SSTs and the simulation with modelded SSTs (previous section) this set-up allows further investigations on the role of the SSTs for the appearance of the 11-year solar signal.

This simulation was performed at an SGI Altix parallel computer of HLRN, Konrad-Zuse-Zentrum in Berlin. Results of the comparison with the reference transient simulation as well as with the simulation with modelled SSTs are shown and discussed in section 8.5.

### 5.3.7 Transient simulation with filtered forcings

While modeling the influence of the 11-year solar cycle on the atmosphere one should be aware that the SSTs and the QBO might themselves be influenced by the solar variability. This is true for experimental set-ups with prescribed observed SSTs and equatorial winds as well as for simulations with an interactive ocean and a self-consistently modelled QBO. Marsh and Garcia (2007) and Austin et al. (2008) discuss the possibility of aliasing between the 11-year solar influence and ENSO effects, depending on the considered time period. Lee and Smith (2003) and Smith and Matthes (2008) deal with the difficulties in separating the QBO and the solar signal in the middle atmosphere especially in the context of multiple linear regression analysis.

In view of this issue coordinated CCM simulations were proposed by the SPARC SOLARIS (SOLAR Influence for SPARC) initiative (Matthes and Kodera, 2011). The intention was to use linearly independent forcing time series. To that end the observed QBO time series was band pass filtered in order to exclude periods of about 11 years that

may be due to a solar influence on the QBO. In return only periods between 0.75 and 4 years were retained. Likewise the observed SSTs and the sea ice coverage (HadISST) were band pass filtered to remove possible 11-year solar induced variability, on the one hand, and a possible QBO influence on the SSTs, on the other hand. Ultimately, periods below two years (i.e., the annual cycle) and from 3 to 7 years were retained.

From the simulation forced with the filtered time series it might be expected to see the "pure" solar signal. However, non-linear interaction between the forcings cannot be excluded. Apart from the filtered QBO, SST and sea ice data this simulation uses the same submodels and boundary conditions as the reference run described in section 5.3.1. The same horizontal and vertical resolution as for the reference run was specified.

This simulation was executed on an IBM Power6 parallel computer at ECMWF in Reading, United Kingdom. Results from the comparison of the filtered EMAC-FUB simulation with the reference run are shown in chapter 9. Moreover, the output of the Japanese MRI-CCM and WACCM of the National Center for Atmospheric Research (NCAR) that used a similar experimental set-up is displayed and discussed in yonder chapter.

Table 5.2 summarises the GCM and CCM simulations that were set up and performed to investigate the 11-year solar signal in the atmosphere. The transient simulations

**Table 5.2:** Summary of the performed simulations. For details see the text.

| Transient simulations | | | | | | | |
|---|---|---|---|---|---|---|---|
| Simulation | Period | Solar Variability | GHGs | ODSs | SSTs/ Sea ice | Volcanic eruptions | QBO |
| REF-B1 L39 Sec. 5.3.1 | 1960-2005 | Obs | Obs | Obs | Obs | Yes | Obs |
| REF-B1 L90 Sec. 5.3.2 | 1960-2000 | Obs | Obs | Obs | Obs | Yes | intern |
| SCN2d Sec. 5.3.5 | 1960-2100 | Obs repeating in future | SRES A1B | Obs A1 | MPI-OM | Yes in the past | Obs repeating in future |
| SCN2c Sec. 5.3.6 | 1960-2100 | Obs repeating in future | fixed at 1960 level | Obs A1 | fixed averaged 1955-1964 | Yes in the past | Obs repeating in future |
| REF-B1 filtered Sec. 5.3.7 | 1960-2005 | Obs | Obs | Obs | MPI-OM filtered | Yes | Obs filtered |
| Equilibrium simulations | | | | | | | |
| CCM max/min Sec. 5.3.3 | 30 yrs | fixed max Nov 1989 min Sep 1986 | fixed 2000 | fixed 2000 | fixed average 1995-2004 | No | Obs |
| GCM max/min Sec. 5.3.4 | 25 yrs | fixed max Nov 1989 min Sep 1986 | fixed at 2000 level | fixed at 2000 level | fixed AMIP averaged 1950-2006 | No | No |

are named following the CCMVal recommendations (Eyring et al., 2008).

## 5.4 Methods of analysis - The multiple linear regression model

Results from the equilibrium experiments described in sections 5.3.3 and 5.3.4 are analysed by computing the long term mean differences between a solar maximum and a solar minimum experiment.

The analysis by computation of long term mean differences is no longer sufficient for the transient experiments described in sections 5.3.1, 5.3.2, 5.3.5, 5.3.6 and 5.3.7. It is in principle possible to define threshold values for a certain influencing quantity and then form composits. Subsequently, composit mean values are computed and their difference is analysed. The disadvantage of this approach is the impossibility to clearly attribute an effect to a causing "mechanism". For example, one might use the solar F10.7 radioflux to define periods of high and low solar activity and form the associated composits. There will certainly be an overlap between the composits according to solar influence and those according to, e.g., the QBO, ENSO or another influencing quantity. Hence, it is not possible to separate the effects that are due to the respective influences.

A commonly used method to analyse time series such as the results of a transient model simulation is to apply a multiple linear regression model. This approach establishes a linear relationship between a dependent quantity and a number of influencing quantities, also denoted as regressors, by calculating a least squares fit. It is, thus, a generalisation of the conventional linear regression method with one dependent and one independent variable. However, there are certain requirements for the regressors to fulfil. Above all, the regressor time series should be linearly independent. There might appear conflicts in such a way that the 11-year solar cycle may influence the QBO and the SSTs as outlined in section 5.3.7 (e.g., Smith and Matthes, 2008; Marsh and Garcia, 2007). Apart from that the solar cycle, the QBO and ENSO may influence the stratosphere at high northern latitudes in winter in an interdependent way (Labitzke and van Loon, 1988) which renders a linear regression approach insufficient.

In this study a multiple linear regression tool based on the work of Gregory Bodeker (Bodeker et al., 1998) is used. It was implemented at FUB by Markus Kunze and it was used for the analyses presented in Chapter 8 of SPARC CCMVal (2010).

A time dependent quantity $X(t)$ may be expressed as follows

$$\begin{aligned} X(t) \;=\; & A_{(N_A=4)} + \\ & B_{(N_B=2)} \times t + \\ & C_{(N_C=2)} \times \mathrm{QBO}(t+\Delta t) + \\ & D_{(N_D=2)} \times \mathrm{Solar}(t) + \\ & E_{(N_E=2)} \times \mathrm{Agung}(t) + \\ & F_{(N_F=2)} \times \mathrm{ElChichon}(t) + \\ & G_{(N_G=2)} \times \mathrm{Pinatubo}(t) + \\ & H_{(N_H=2)} \times \mathrm{ENSO}(t) + \\ & R(t). \end{aligned} \tag{5.2}$$

with the offset $A$, the linear trend $B \times t$, the QBO term, the Solar term, three terms representing the major volanic eruptions of Mt. Agung in 1963, El Chichon in 1982 and Mt. Pinatubo in 1991, the ENSO term and the residuals $R(t)$. The QBO term deserves closer attention. In the notation $\mathrm{QBO}(t+\Delta t)$ it is accounted for the equatorial zonal wind at a certain level, say 50 hPa, and an orthogonal zonal wind time series which is representative for the overlying opposite QBO phase, say at 30 hPa. The modelled zonal mean zonal wind from the respective simulation serves as QBO regressor. The F10.7 cm solar radio flux timeseries is used as regressor for solar influence. ENSO is represented by the Niño3.4 index, i.e., the average SST anomaly in the region bounded by 5 °N, 5 °S, 170 °W and 120 °W (e.g., Trenberth, 1997; Marsh and Garcia, 2007). The coefficients in equation 5.2 are expanded into Fourier series of the order $N_i$. This allows to take the annual, semi-annual and shorter periodicity into account. The coefficients $A$ to $H$ are then determined to fulfil the least squares condition.

Deviant from equation 5.2 effective stratospheric chlorine (ESC) is used as regressor instead of a linear trend when performing the fit for ozone. ESC is defined as the stratospheric abundance (in this case at 30 hPa) of total inorganic chlorine $\mathrm{Cl}_y$ plus 60 times the abundance of total inorganic bromine $\mathrm{Br}_y$ to account for the higher ozone depleting potential of $\mathrm{Br}_y$ (Newman et al., 2007).

# Chapter 6

# A Mechanistic Forcing Study

Before analysing the 11-year solar signal in transient and equilibrium CCM simulations a mechanistic momentum forcing study in analogy to the 11-year solar cycle effect was performed. To examine the dynamical fraction of the solar influence on the stratosphere and its effect on the troposphere the stratospheric zonal wind is artificially enhanced. By including an additional momentum source in the stratosphere it is assumed that the enhanced differential heating under solar maximum conditions has, via the thermal wind relationship, already led to a stronger polar night jet. Hence, the first step in the chain of cause and effect is skipped. For the model simulation this implies that the chemical-radiative feedback can be neglected, i.e., the chemistry module of the model system is not used - the model is run as a GCM. The solar irradiance is prescribed at an intermediate level. This experimental set-up is particularly well-suited to study the dynamical part of the solar signal, since by definition no radiative changes were applied.

This study is inspired by the work of Thuburn and Craig (2000) who included a mechanistic momentum force in the stratosphere of a GCM and found in response changes in tropopause height. Simultaneously, the tropospheric circulation was influenced by the stratospheric changes down to at least 5 km below the tropopause.

## 6.1 Experimental set-up

A height- and latitude-dependent momentum force was defined according to Thuburn and Craig (2000) and in the context of this study included in the stratosphere of EMAC-FUB:

$$F_m = f(p) \cdot sin(2\varphi)^2 \cdot 2\,\mathrm{m/s/day} \tag{6.1}$$

with

$$f(p) = \begin{cases} 1 \text{ for } p < 10\,\mathrm{hPa} \\ (100\,\mathrm{hPa} - p)/90\,\mathrm{hPa} \text{ for } 10\,\mathrm{hPa} < p < 100\,\mathrm{hPa} \\ 0 \text{ for } 100\,\mathrm{hPa} < p. \end{cases}$$

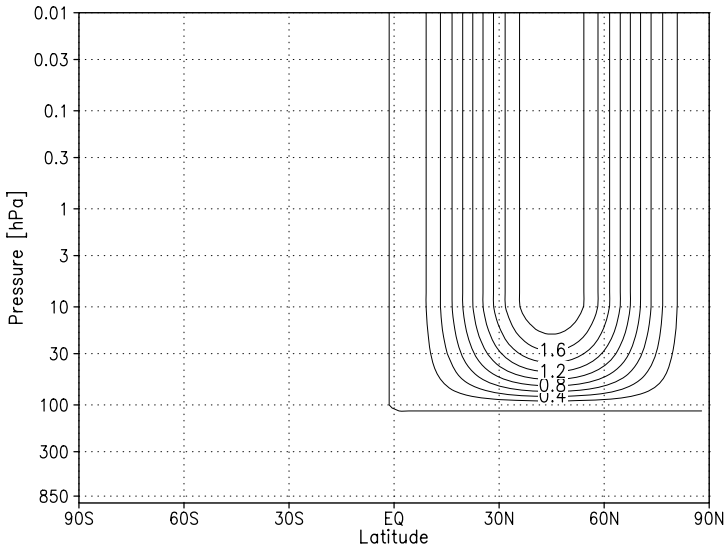


**Figure 6.1:** Momentum force as defined in equation 6.1 in m/s/day applied in January in the winter hemisphere stratosphere. Contour interval is 0.2 m/s/day.

The force was applied in the respective winter hemisphere, only. See Figure 6.1 for the January configuration. The complete code is printed in the Appendix. Furthermore, climatological SSTs (AMIP II 1956-2000) were used as lower boundary conditions.

A series of simulations in perpetual January or July mode with T42 horizontal and different vertical resolution (39 and 90 levels, respectively) was then carried out. A pair of simulations consisting of a control experiment and an experiment with applied momentum forcing was performed for each configuration. Thus, eight simulations were conducted in total for 30 months each. Only the last 27 month were analysed. The different vertical resolutions were chosen to assess the influence of the QBO on the results. As mentioned in the previous chapter, the L90 version of EMAC-FUB does internally generate a QBO, while the L39 version is not capable of simulating a QBO (cf. Section 5.1).

The perpetual season mode allows to perform a 'multi-year' simulation of a peculiar period with an affordable amount of computer time and was considered to be sufficient for this type of sensitivity study. The simulations were performed on the IBMp4 parallel computer of the HLRN, Konrad-Zuse-Zentrum Berlin. Results of the various GCM simulations are shown and discussed in the following sections.

## 6.2 Perpetual January experiments

As described in section 6.1 the applied momentum forcing acts to accelerate the zonal wind in the winter hemisphere stratosphere. The long-term mean differences in zonal mean zonal wind between the forced and the control experiment are depicted in Figure 6.2a. It is seen that the effect of the forcing is indirect, i.e., the maximum positive difference of about 18 m/s is shifted poleward and downward compared to the region of maximum

forcing. This implies an intensification of the strong westerly wind in the polar night jet. In the subtropical lower mesosphere a response of opposite sign is seen.

The zonal mean temperature adjusts to the zonal mean zonal wind changes in order to maintain thermal wind balance (cf. Section 3.3). The temperature response is shown in Figure 6.2b. A quadrupole pattern of temperature anomalies is found with a cooling of about -11 K in the polar lower stratosphere, a warming of about 9 K above, a cooling in the low-latitude upper stratosphere and a warming of about 4 K below in the tropical lower stratosphere. This tropical lower stratospheric warming deserves some extra attention. The existence of such a positive temperature anomaly in response to the 11-year solar cycle was reported from the analysis of several observational datasets (e.g., Labitzke et al., 2002; Frame and Gray, 2010).

It was argued by, e.g., Haigh et al. (2005) and Simpson et al. (2009) that the direct radiative effect of irradiance changes over the solar cycle is larger in the upper stratosphere but that a dynamical response may cause the observed secondary maximum in the temperature signal in the tropical lower stratosphere. As mentioned before, the current simulations are intended as analogies to the 11-year solar influence on the atmosphere at which it was assumed that the stronger differential radiative heating has already led to a stronger polar night jet. It has to be emphasised that no changes were applied to the radiative code of the model for these experiments. Thus, the response is in its entirety dynamically induced.

Figure 6.3a shows the long term mean difference of the Eliassen-Palm-Flux (EP-flux) vector (cf. equations 3.14 and 3.15) along with the difference in EP-flux divergence and the strongest positive zonal mean zonal wind anomaly in the northern hemisphere. The components of the EP-flux are scaled by the inverse of pressure to highlight changes in the

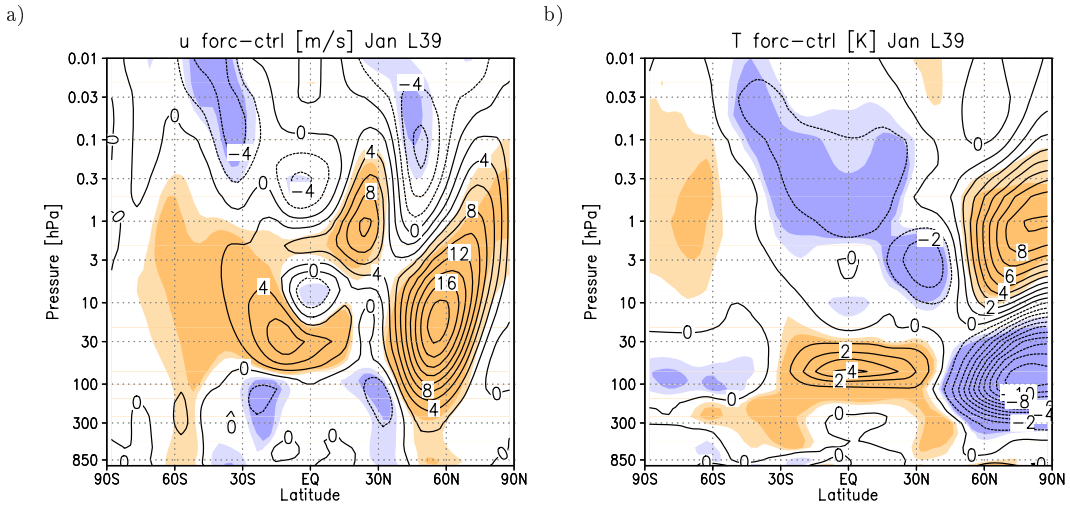


**Figure 6.2:** Long term mean differences between the forced and the control experiment. a) Zonal mean zonal wind in m/s, contour interval is 2 m/s; b) Zonal mean temperature in K, contour interval is 1 K. Light and dark shading indicates statistical significance at the 95% and 99% level.

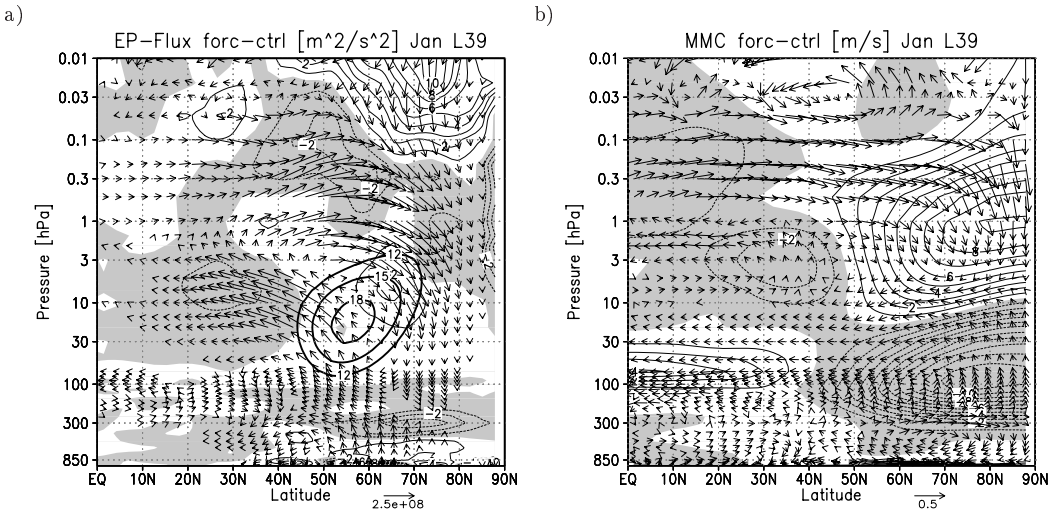


**Figure 6.3:** Long term mean differences between the forced and the control experiment. a) Eliassen-Palm-Flux vector (arrows) and its divergence (thin contours) in m/s/day, contour interval is 1 m/s/day, zonal wind difference (thick solid contours), contour interval 3 m/s; b) Residual mean meridional circulation (arrows) and zonal mean temperature (contours) in K, contour interval is 1 K. Shading indicates negative anomalies.

middle atmosphere. It is seen that wave activity is directed upwards and equatorwards in the mid- and low-latitude middle and upper stratosphere. Refraction (i.e., a change of the propagation direction) and even relative reflection (i.e., an inverion of the propagation direction) of waves occurs in the the mid- to high-latitude middle stratosphere, i.e., in the vicinity of the westerly wind anomaly. On the southern flank of the westerly anomaly the waves are refracted towards the equator while on its northern flank there are less waves propagating upwards in the forced experiment compared to the control simulation. The negative difference in EP-flux divergence is a relative convergence which acts to decelerate the westerly mean flow, i.e., the polar night jet. This is consistent with the easterly anomaly in the subtropical and mid-latitude lower mesosphere in Figure 6.2a.

Planetary wave activity drives the residual mean meridional circulation (MMC, cf. equations 3.8). Altered wave propagation and wave-mean flow interaction is, therefore, expected to influence the residual circulation. Figure 6.3b shows the difference in $\overline{v}^*, \overline{w}^*$, likewise scaled by the inverse of pressure, along with the zonal mean temperature difference. The undisturbed meridional circulation has its ascending branch in the tropics. In the stratosphere and mesosphere the residual flow is directed towards the winter pole where a descending motion is observed. The difference between the forced and the control experiment shows an upward anomaly in the polar lower stratosphere which turns equatorward further south and descends in the tropical lower stratosphere. This implies a weakening of the absolute circulation and is in agreement with the temperature anomalies. Less adiabatic cooling (i.e., relative warming) coincides with the region of decreased upwelling (i.e., relative downwelling) in the tropical lower stratosphere. Vice versa does less adiabatic warming (i.e., relative cooling) occur in the region of decreased downwelling

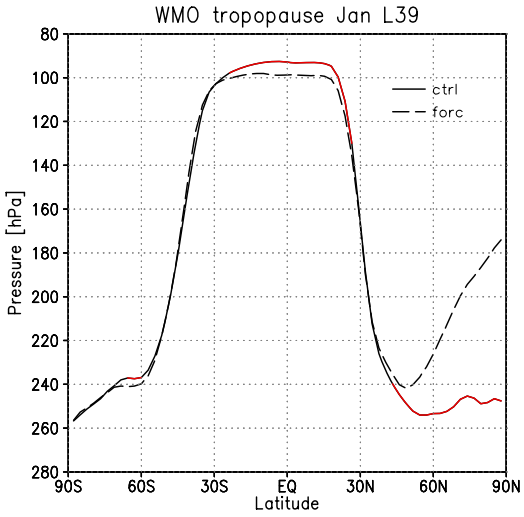


**Figure 6.4:** Long term mean tropoause pressure for the forced and the control experiment. The control curve is marked in red where the difference between forced and control experiment is statistically significant at the 95% level.

(i.e., relative upwelling) in the polar lower stratosphere. In the subtropical upper stratosphere where enhanced wave-mean flow interaction was noted there is an acceleration of the residual circulation. Again this is consistent with the temperature changes. The residual circulation is decelerated at the uppermost levels, coincident with a cooling of the polar and mid-latitude mesosphere.

The warming in the tropical lower stratosphere alters the vertical temperature gradient in the tropopause region and, thus, lowers the tropopause. Here, the tropopause is diagnosed according to the WMO lapse rate tropopause definition: The first tropopause is defined as the lowest level at which the lapse rate decreases to 2 K/km or less, provided also the average lapse rate between this level and all higher levels within 2 kilometers does not exceed 2 K/km (WMO, 1992). Figure 6.4 displays the pressure at which the tropopause was detected. In the tropics the tropopause is significantly (at the 95 %-level) lower in the forced experiment compared to the control run. The higher tropopause at high northern latitudes in the forced experiment has to be considered with caution since the existence of a tropopause according to the definition is questionable in this region as was noted by Thuburn and Craig (2000).

The tropopause separates the stratosphere from the troposphere. Whether it restricts the influence of the applied forcing to the middle atmosphere is investigated in the next subsection.

### The tropospheric signal

Figure 6.5 shows the tropospheric details from the surface to 100 hPa of Figure 6.2. Statistically highly significant changes in the zonal mean zonal wind and temperature throughout the mid-latitude troposphere are apparent. The tropospheric jet in the northern

hemisphere is weakened and displaced polewards as the zero change contour is located to the north of the jet core which is situated at 30 °N in the control simulation. The southern hemisphere jet is displaced polewards without a substantial weakening, since the zero change contour runs directly through the core of the jet at ≈ 45 °S. The temperature shows a banded structure with positive anomalies originating from the tropical lower stratospheric warming and reaching down to the surface equatorwards of ≈ 50 °N and negative anomalies poleward of 50 °N. To understand the temperature response an analysis of the residual mean meridional circulation ($\overline{v}^*$,$\overline{w}^*$) is useful. It reveals anomalous downward motion coinciding with the regions of the strongest warming in the northern and southern hemisphere. This is an indication for an anomalous counterclockwise circulation cell near the equator, an anomalous clockwise cell in the subtropics and another counterclockwise cell at mid-latitudes which is confirmed by an analysis of the stream function (not shown). Similar circulation changes were described by Haigh et al. (2005) and Simpson et al. (2009).

The Hadley circulation is influenced by the stratospheric changes as is seen in Figure

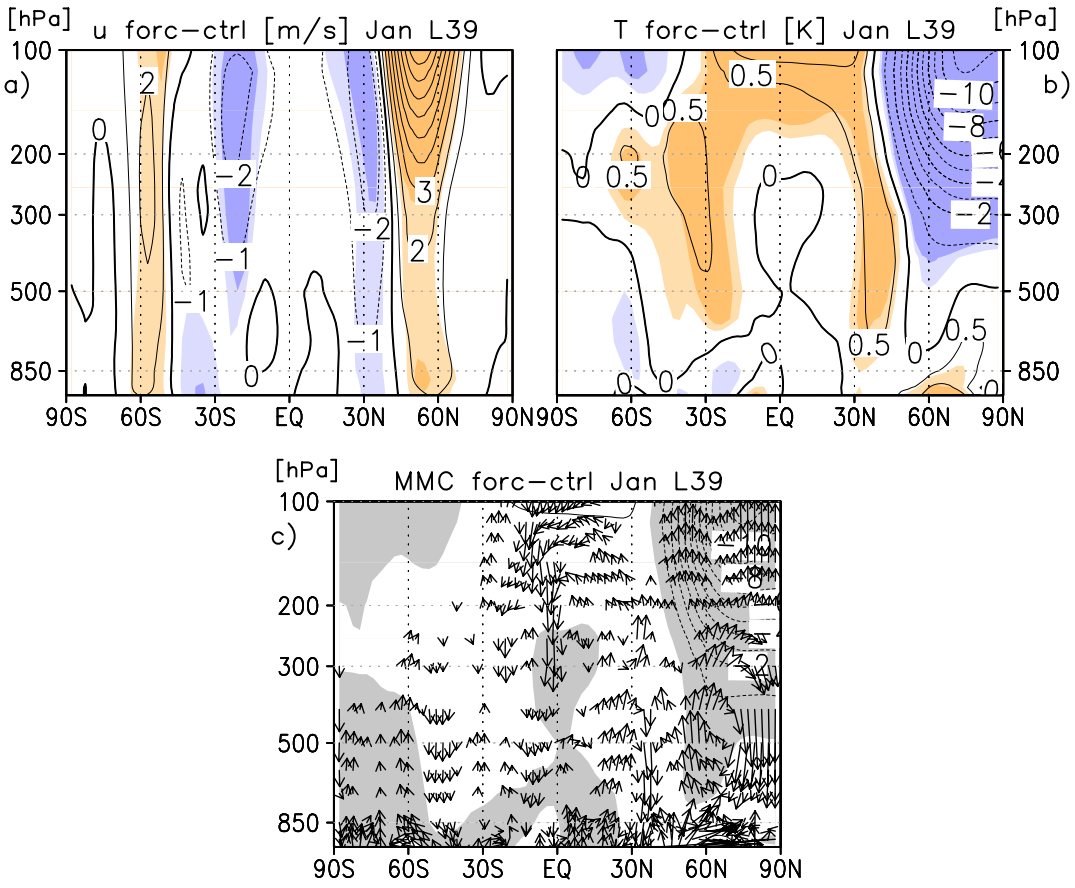


**Figure 6.5:** Long term mean differences between the forced and the control experiment. a) Zonal mean zonal wind in m/s, contour interval is 1 m/s; b) Zonal mean temperature in K, contour interval is 1 K. Light and dark shading indicates statistical significance at the 95% and 99% level, respectively. c) Arrows: Residual mean meridional circulation $\overline{v}^*$,$\overline{w}^*$, contours: Temperature differences, grey shading denotes negative temperature anomalies.

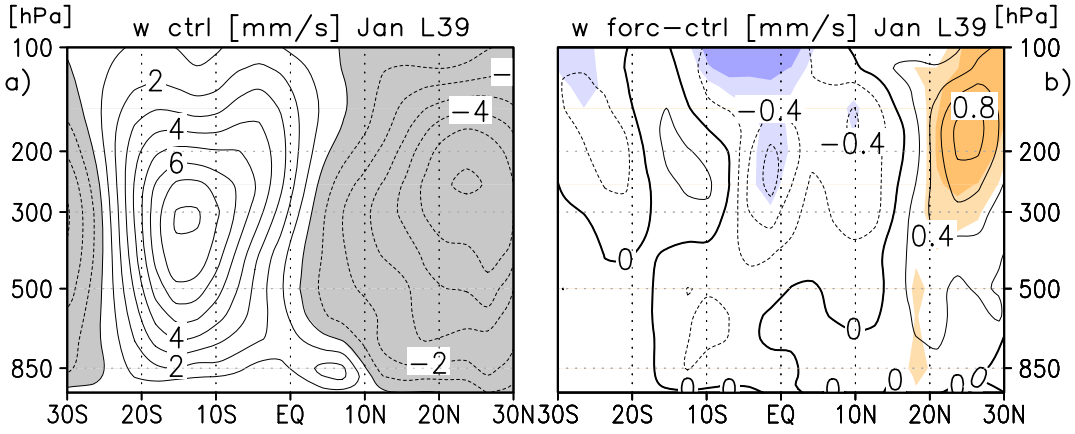


**Figure 6.6:** Long term mean vertical velocity $w$ in the tropical troposphere in mm/s. a) Absolute values from the control experiment, contour interval is 1 mm/s, negative values are shaded. b) Difference between the forced and the control experiment, contour interval is 0.2 mm/s, light and dark shading indicates statistical significance at the 95% and 99% level.

6.5c. There is a statistically highly significant upward anomaly in the descending branch on the winter hemisphere. Overall this implies a weakening of the Hadley circulation. These findings are confirmed by an analysis of the changes in tropical zonal mean convective precipitation (not shown) which is closely related to the upwelling of air in the intertropical convergence zone (ITCZ).

In order to see which regions contribute to the zonal mean precipitation signal latitude-longitude plots for the convective precipitation of the control experiment and the

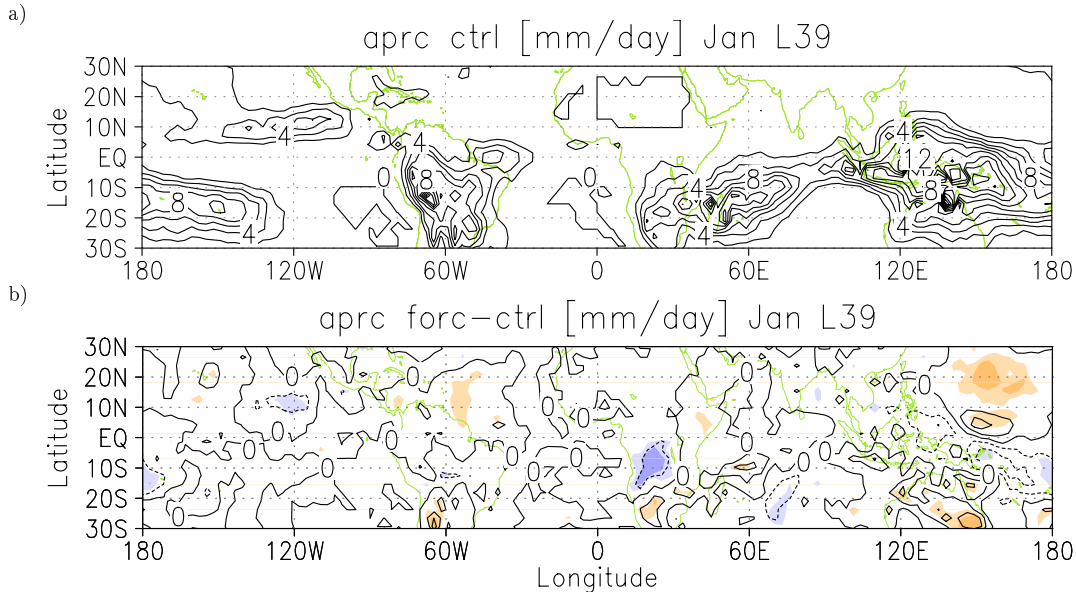


**Figure 6.7:** Long term mean convective precipitation in the tropical troposphere in mm/day; a) Absolute values of the control experiment, contour interval is 2 mm/day. b) Difference between the forced and the control experiment, contour interval is 1 mm/day, light and dark shading indicates statistical significance at the 95% and 99% level.

difference forced-control are given in Figure 6.7a and 6.7b. The changes affect the region of strongest convective precipitation in the western Pacific and over the maritime continent but also in the Indian Ocean and over central and southern Africa. The precipitation maximum over the western Pacific is significantly reduced. A further significant negative anomaly is seen over the African continent at about 10 °S.

The poleward displaced tropospheric jet in the northern hemisphere affects the North Atlantic and European cyclone tracks. This is supported by the difference in geopotential height and the temperature at the 1000 hPa-level which are displayed in Figure 6.8. A statistically highly significant negative geopotential height anomaly in the North American and Eurasian polar region is surrounded by positive anomalies which are strongest in the Pacific near the Alëutian Islands and in the Atlantic as well as over the Mediterranean and southern Europe. This anomaly pattern resembles the one of the Arctic Oscillation in its positive phase. It implies an enhanced transport of relatively warm and humid maritime air masses towards central and northern Europe. This is indeed seen in the significantly positive temperature anomaly over central, northern and eastern Europe in Figure 6.8b. The same holds for the United States, i.e., the region downstream of the positive anomaly over the Pacific. In contrast, there is a significant cooling over north-eastern Canada. These results should be primarily interpreted in a qualitative rather than in a quantitative sense.

Further confirmation for the influence on North Atlantic and European cyclone tracks is provided by the difference in large scale precipitation which is depicted in Figure 6.9b. The large scale rainfall is significantly reduced over the Mediterranean and significantly enhanced over the North Atlantic, north eastern Europe and farther east over Siberia. This is consistent with the above-mentioned enhanced transport of rela-

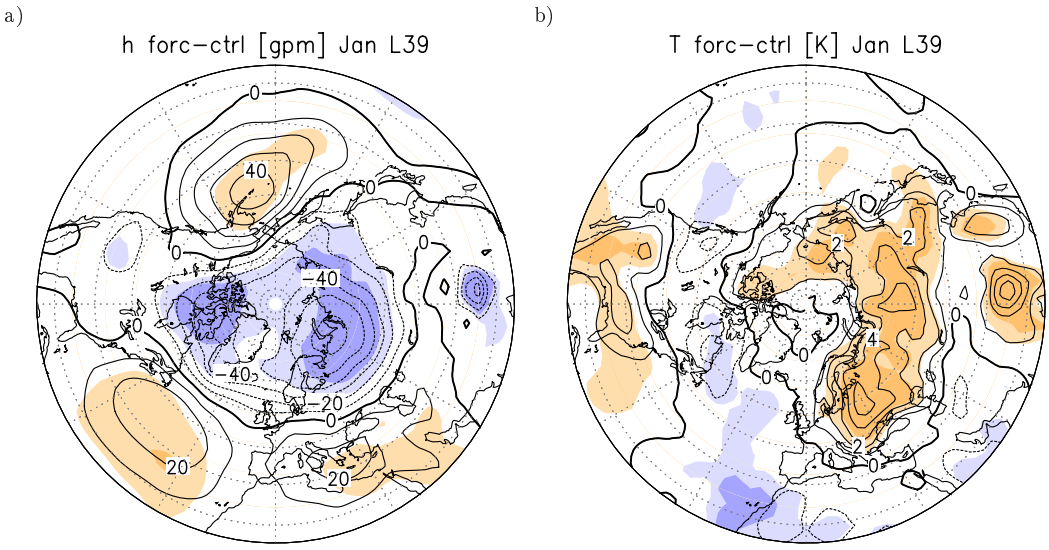


**Figure 6.8:** a) Long term mean geopotential height difference of the 1000 hPa-level in gpm, contour interval is 10 gpm. b) Long term mean temperature difference in K, contour interval is 1 K, light and dark shading indicates statistical significance at the 95% and 99% level.

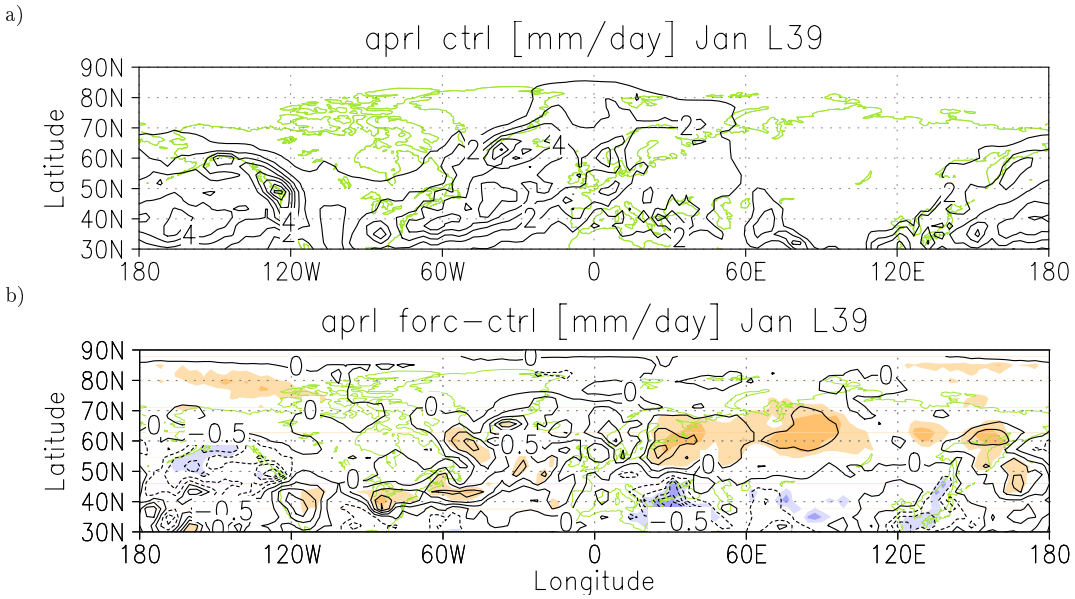


**Figure 6.9:** Long term mean large scale precipitation in the northern hemisphere troposphere in mm/day; a) Absolute values of the control experiment, contour interval is 1 mm/day. b) Difference between the forced and the control experiment, contour interval is 0.25 mm/day, light and dark shading indicates statistical significance at the 95% and 99% level.

tively warm and humid maritime air masses towards the Eurasian continent. Another significant negative anomaly is apparent over north western Canada, coincident with the negative temperature anomaly.

## 6.3 Perpetual July experiments

Compared to the changes in the northern hemisphere mid winter season described in the previous section the atmospheric response to the momentum forcing is much more intense in the southern hemisphere mid winter. From Figure 6.10a it is seen that the stratospheric polar night jet in the southern hemisphere is highly intensified by the momentum forcing and shifted towards the equator in the middle stratosphere. Zonal mean zonal wind absolute values reach about 120 m/s in the forced experiment. The reason for this strong reaction is the low interannual variability of the southern hemisphere winter circulation. The associated temperature response (Figure 6.10b) is a similar quadrupole pattern as was noted in the January experiment: The polar stratosphere is significantly cooled, a warming is seen above, the tropical mesosphere experiences cooling and the tropical lower stratosphere is warmer by up to 6 K.

The propagation of planetary waves is affected in a similar manner as in the northern hemisphere (not shown). On the poleward flank of the westerly zonal wind anomaly the upward propagation of waves is inhibited in the forced experiment while waves are refracted towards low latitudes on the equatorward flank of the westerly anomaly. The

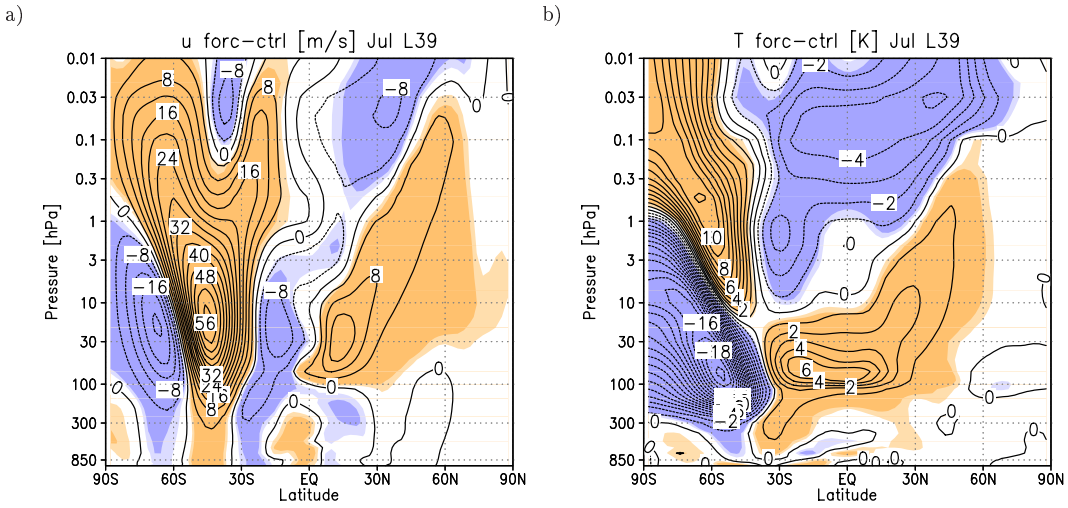


**Figure 6.10:** Long term mean differences between the forced and the control experiment. a) Zonal mean zonal wind in m/s, contour interval is 4 m/s; b) Zonal mean temperature in K, contour interval is 1 K. Light and dark shading indicates statistical significance at the 95% and 99% level.

associated effect on the residual mean meridional circulation is qualitatively comparable to that noted in the January experiment (not shown). Anomalous upwelling in the polar lower and middle stratosphere together with a northward directed flow in the equatorial lower stratosphere imply an absolutely weaker mean meridional circulation which is consistent with the negative and positive temperature differences, respectively. In the upper stratosphere and mesosphere the changes act to intensify the mean meridional circulation.

As might be expected from the higher temperatures in the tropical lower stratosphere the tropical tropopause is located at lower altitudes in the forced than in the control simulation also in the July experiments (not shown).

### The tropospheric signal

Figure 6.11 shows the tropospheric details from Figure 6.10 along with the tropospheric mean meridional circulation. The core of the tropospheric subtropical jet in the southern hemisphere is located at $\approx 35\,^{\circ}$S in the control experiment. From Figure 6.11a it becomes obvious that the jet is shifted poleward as the zero change contour passes through the core of the jet in the upper troposphere. This shift does not involve a weakening as was noted in the January experiment. The changes are statistically highly significant all the way down to the surface. In the northern hemisphere there is a weak and insignificant signal of the order of $\pm$ 0.5 m/s. The tropospheric temperature difference is characterised by a strong and significant cooling at southern hemisphere high and mid-latitudes and a significant warming in the subtropics (cf. Fig. 6.11b). There is a rudimentary comparable structure in the northern hemisphere as was the case in the January experiment.

Figure 6.11c demonstrates a strong influence of the applied stratospheric forcing on the meridional circulation in the troposphere. A region of anomalous downwelling is seen in the northern hemisphere between the equator and about 20 °N which comprises the region of strongest ascending motion in the Hadley circulation. The anomalous upwelling between the equator and 20 °S provides further evidence for a weaker meridional circulation in the tropics. At southern mid-latitudes anomalous upwelling is apparent, coincident with the negative temperature anomaly, and accompanied by anomalous downwelling south of 60 °S. The combination of both results in a slight shift towards lower latitudes as well as an equatorward extension of the Ferrel cell's ascending branch.

As with the January experiment the anomalies seen in the zonal mean tropical meridional circulation shall be analysed with respect to their regional structure in the latitude-longitude plane. This is done by means of convective precipitation which is depicted in Figure 6.12. Part a) of this Figure gives the basic state of the control simulation. Following the solar zenith the ITCZ is shifted to the northern hemisphere. The West African and Indian monsoon regions are clearly visible. The anomaly pattern in part b)

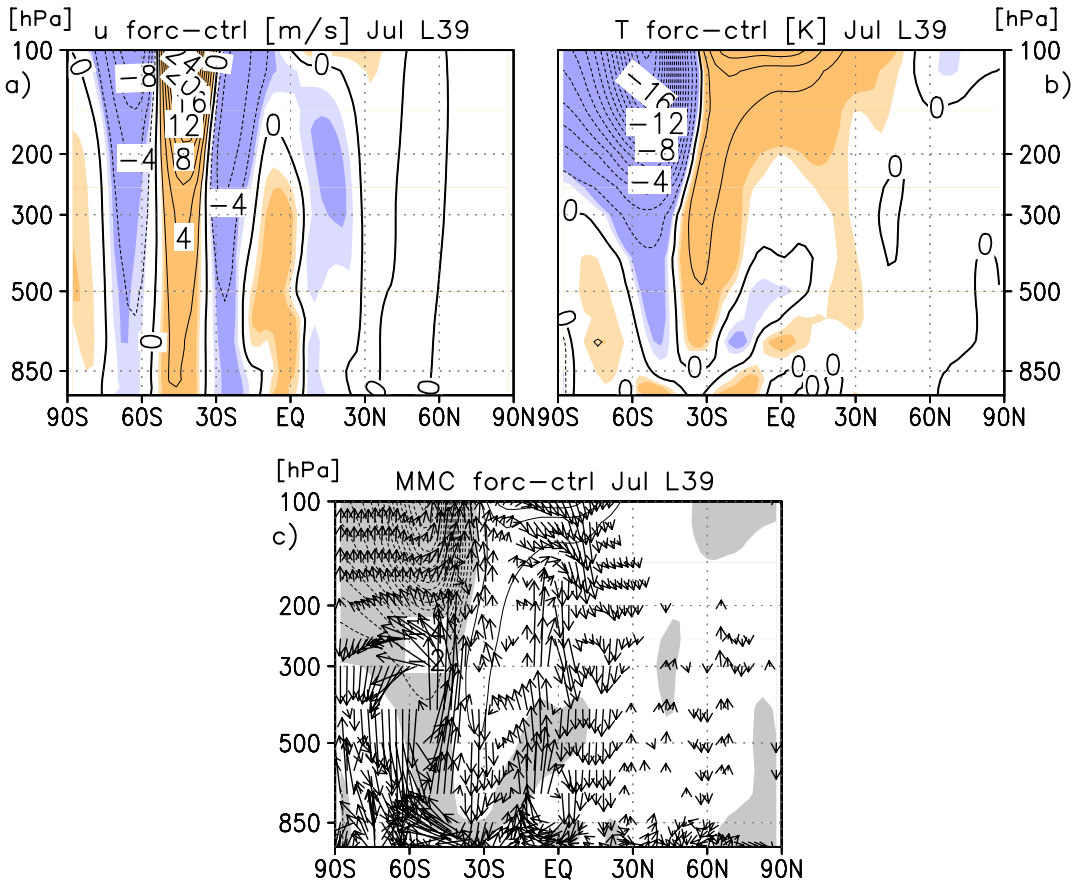


**Figure 6.11:** Long term mean differences between the forced and the control experiment. a) Zonal mean zonal wind in m/s, contour interval is 2 m/s; b) Zonal mean temperature in K, contour interval is 1 K. Light and dark shading indicates statistical significance at the 95% and 99% level, respectively. c) Arrows: Residual mean meridional circulation $\overline{v}^*, \overline{w}^*$, contours: Temperature differences, grey shading denotes neagtive temperature anomalies.

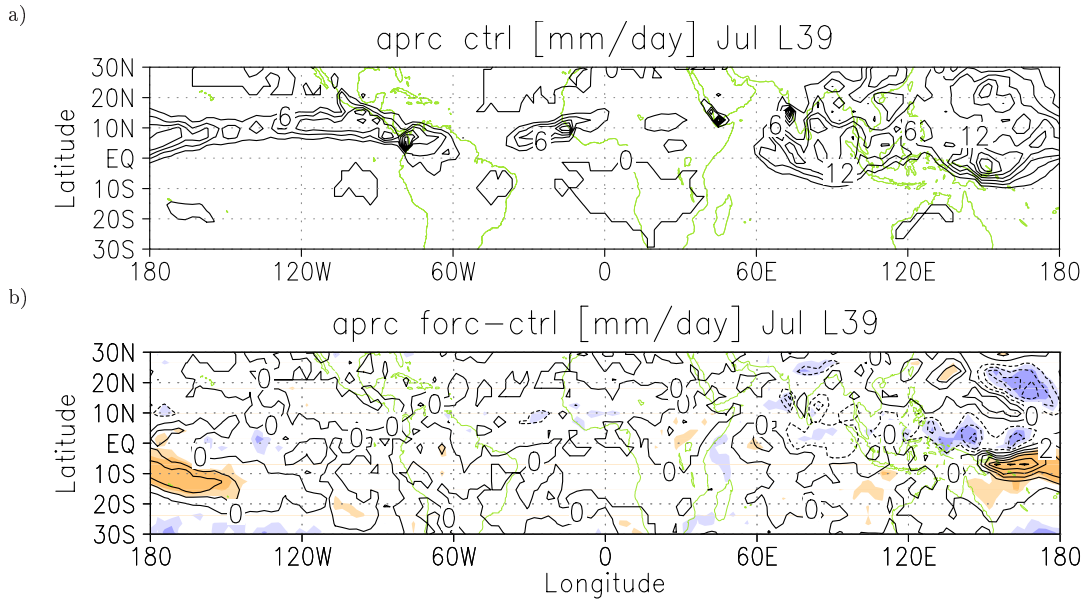


**Figure 6.12:** Long term mean convective precipitation in the tropical troposphere in mm/-day; a) Absolute values from the control experiment, contour interval is 3 mm/day. b) Difference between the forced and the control experiment, contour interval is 1 mm/day, light and dark shading indicates statistical significance at the 95% and 99% level.

shows a significant reduction of convective precipitation in the north western tropical and equatorial Pacific. The most prominent positive difference is seen over the maritime continent directly south of the equator stretching out to the south east. It is this positive anomaly which together with the negative anomalies around India and in the Pacific at $\approx 20\,^{\circ}$N dominates the zonal mean signal (not shown).

Going back to the strong zonal mean zonal wind changes it might be expected that

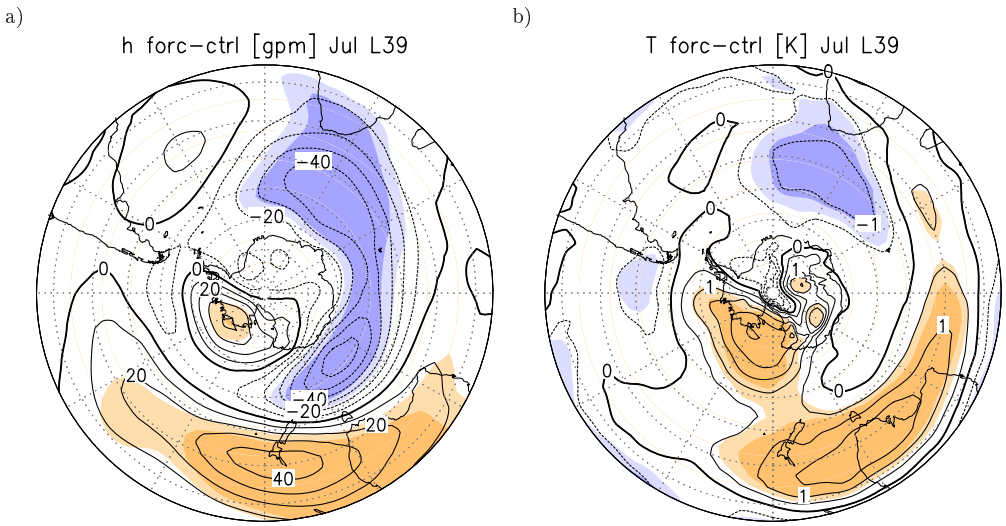


**Figure 6.13:** a) Long term mean geopotential height difference of the 700 hPa-level in gpm, contour interval is 10 gpm. b) Long term mean temperature difference in K, contour interval is 0.5 K, light and dark shading indicates statistical significance at the 95% and 99% level.

the geopotential height and temperature fields show similar anomalies as they did in the January experiments in the northern hemisphere. This is indeed the case as Figure 6.13 shows. The 700 hPa-level which is chosen instead of the 1000 hPa-level to account for the high topography of the Antarctic continent, is situated significantly lower over the Southern Ocean in the African, Indian and Australian sector in the forced run compared to the control simulation. This relative depression is surrounded by a positive anomaly which is strongest and statistically significant over New Zealand. The signal over Antarctica itself is split into two parts. A significantly positive anomaly appears along the coasts of the Amundsen and the Ross sea whereas a weak and insignificant negative anomaly covers the rest of the continent. The temperature difference shows higher temperatures over the Australian and Indian sector of the Southern Ocean which are statistically significant. A significant negative anomaly is seen south of Africa. Over the Antarctic continent predominatly positive anomalies are found.

The significant warming over parts of the Southern Ocean is likely due to enhanced cyclonic activity. This can be inferred from the difference in large scale precipitation in the same region ranging from 0 °E to 120 °W (cf. Figure 6.14). At the latter longitude, west of the Antarctic Peninsula the positive temperature anomaly and the enhanced large scale precipitation touch the coast. Concerning the precipitation changes, in particular, over the oceans it has to be stressed that the same climatological sea surface temperatures were emloyed for all these experiments. The described changes can, therefore, be clearly attributed to the stratospheric momentum forcing.

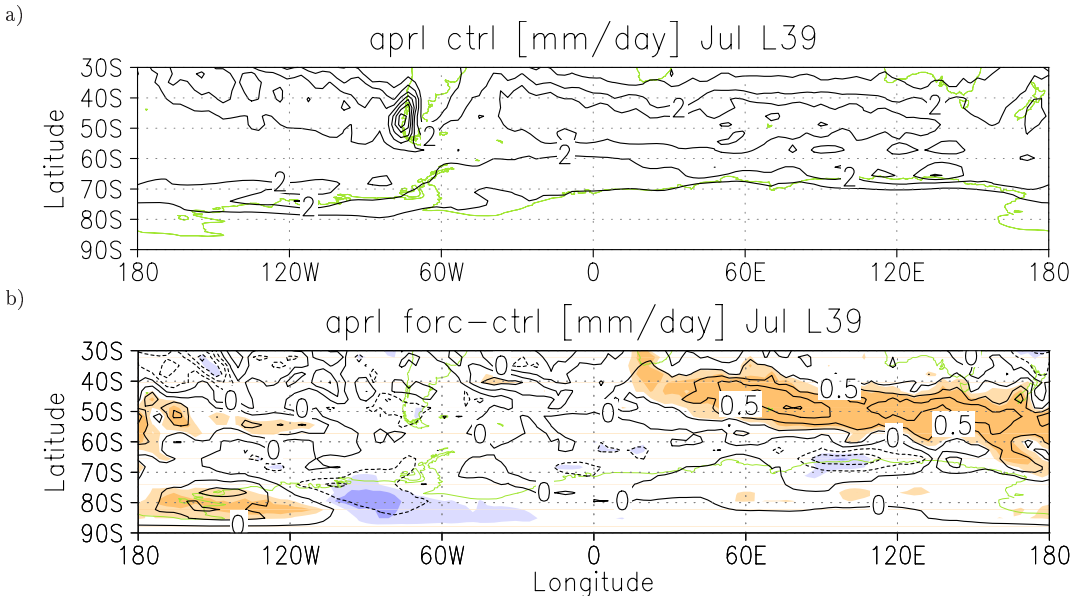


**Figure 6.14:** Long term mean large scale precipitation in the southern hemisphere troposphere in mm/day; a) Absolute values from the control experiment, contour interval is 1 mm/day. b) Difference between the forced and the control experiment, contour interval is 0.25 mm/day, light and dark shading indicates statistical significance at the 95% and 99% level.

## 6.4 The effect of a higher vertical resolution

A repetition of the perpetual season simulations employing a model version with a higher vertical resolution (90 instead of 39 layers between the surface and 80 km) yielded qualitatively the same results. The zonal wind signal in the northern hemisphere in January is even quantitatively comparable to the L39 results (cf. Figure 6.15a and Figure 6.2a). The strong zonal wind differences in the equatorial stratosphere, reaching from above the tropopause to the stratopause in Figure 6.15a, are associated with the QBO which is supposed to develop spontaneously in the model version with the high vertical resolution. However, in the control run there are permanent easterlies throughout the simulated 27-month period. In the forced run the equatorial zonal mean zonal wind changes sign which leads to the large differences in the long term mean. Against this backround it is clear that the differences in the equatorial stratosphere are statistically highly significant. On the other hand, a simulation over 27 months only covers one QBO cycle which is insufficient do establish any statistically well-grounded conclusion about the role of the QBO in these experiments. In the July simulation the zonal wind differences are enhanced in magnitude in the southern hemisphere using the L90 version (cf. Figure 6.15b).

Bsically, the temperature signal shows the same quadrupole pattern as with the lower vertical resolution (Figure 6.15c and d). In the January experiments a strong negative temperature anomaly in the equatorial upper stratosphere appears which is associated with the QBO-induced secondary circulation. The lower stratospheric response has even lost intensity with a warming of about 3 K at low latitudes and a cooling of -11 K at high latitudes. In the July experiments in consequence of the enhanced zonal wind signal the temperature anomalies are stronger as well, retaining the overall spatial pattern.

The tropospheric zonal wind differences are enhanced in the L90 experiments, both in January and in July (Figure 6.15a and 6.15b). In particular, the influence on the tropospheric jet in the respective summer hemisphere has increased. The tropospheric temperature signal in January (Figure 6.15c) still shows the two tails of positive anomalies that orignate in the lower stratospheric positive anomaly but the magnitude of the difference has increased. In July there is no major change on the winter hemisphere compared to the L39 results. On the summer hemisphere, however, the marginally significant weak positive temperature anomaly that reached down into the middle troposphere in the L39 experiments has disappeared (cf. Figure 6.15d). The tropopause height changes in the L90 January experiments are very similar to the results obtained with the L39 model version (not shown).

A comparison of the absolute tropical vertical velocity reveals a slightly slower Hadley circulation in the January experiment with the lower vertical resolution (Figure 6.6a) than in the high resolution one (Figure 6.16a). The same is true for the July experiments (not shown). The difference between the forced and the control January experiment (Figure 6.16c) shows two significant features: a weaker upwelling directly south

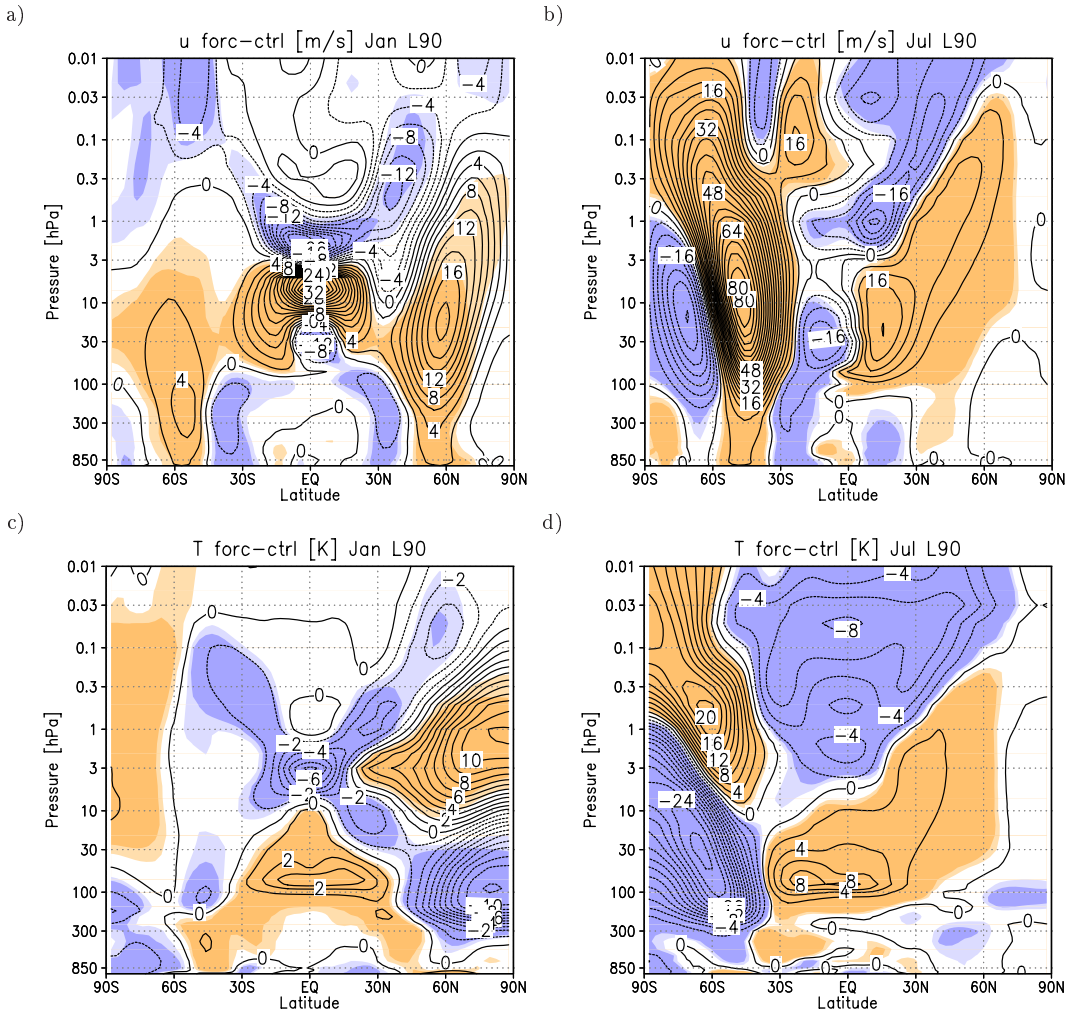


**Figure 6.15:** Long term mean differences between the forced and the control experiment with higher vertical resolution. Left: January; Right: July; a) and b) Zonal mean zonal wind in m/s; c) and d) Zonal mean temperature in K. Note the different contour intervals for January and July. Light and dark shading indicates statistical significance at the 95% and 99% level.

of the equator and a decrease in downwelling close to the core of the Hadley cell's descending branch. The respective July difference (Figure 6.16d) is dominated by a statistically highly significant positive anomaly in the descending region, i.e., the downward branch of the Hadley cell is weakened. The upward branch has become weaker and narrower as is evident from the negative anomaly on the northern flank of the upwelling region.

## 6.5 Summary and Discussion

With this idealized sensitivity study it has been shown that a positive temperature anomaly in the tropical lower stratosphere can be obtained via dynamical pathways exlusively. Furthermore, it has been shown that the tropospheric reaction to the low latitude lower stratospheric heating predicted from simulations with a simplified GCM (Haigh

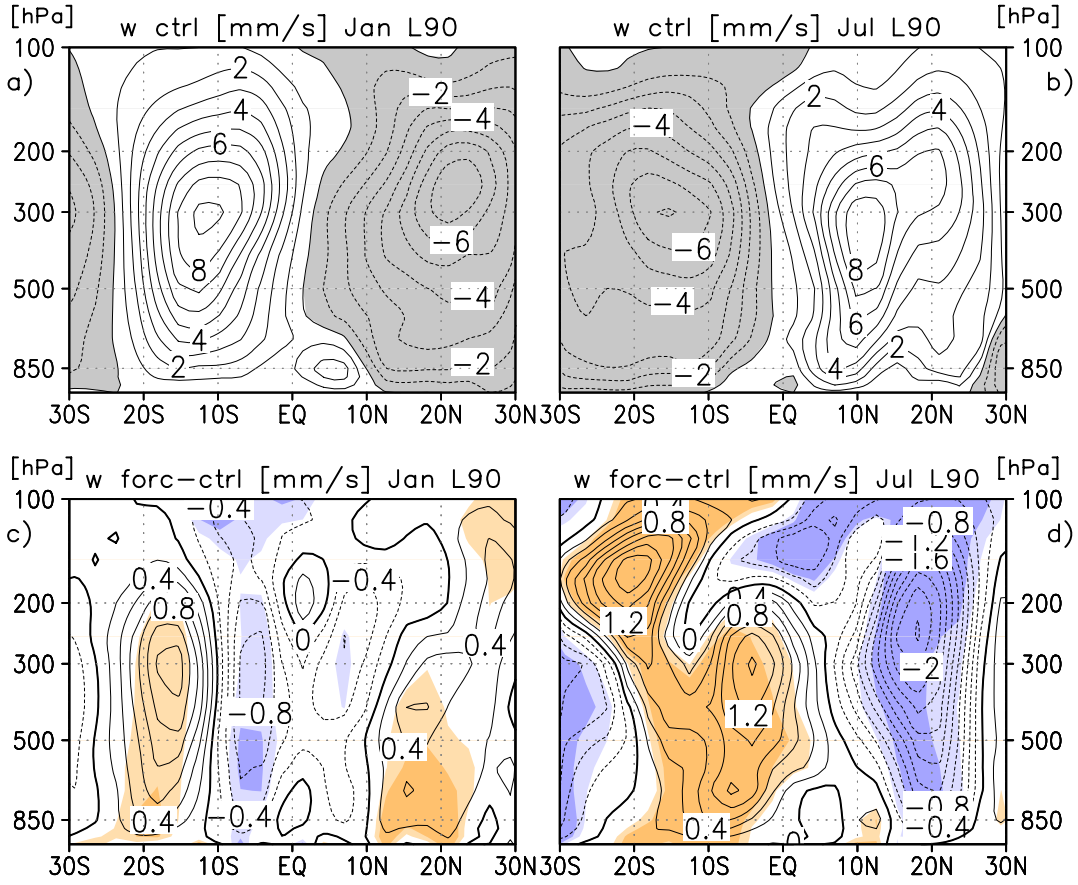


**Figure 6.16:** Vertical velocity $w$, Left: January, right: July; a) and b) Long term mean absolute values from the control experiment in mm/s, contour interval is 1 mm/s, negative values are shaded. c) and d) Long term mean difference between the forced and the control experiment, contour interval is 0.2 mm/s, light and dark shading indicates statistical significance at the 95% and 99% level.

et al., 2005) could be reproduced in a full GCM. The results are, moreover, qualitatively comparable to results obtained with a coupled ocean-atmosphere GCM (Yukimoto and Kodera, 2007). Beyond the response of zonal wind, temperature and geopotential height which was discussed by Haigh et al. (2005) and Yukimoto and Kodera (2007) an effect on the convective rainfall in the tropics as well as on the extratropical large-scale rainfall could be demonstrated for the first time. The precipitation changes are consistent with a weaker Hadley circulation and with poleward shifted cyclone tracks at mid-latitudes.

There was qualitative agreement between the temperature and zonal wind results obtained with the lower and the higher vertical resolution. Therefore, it can be concluded that the signal is robust in general and not significantly influenced by the vertical resolution. Quantitatively, the model version with higher vertical resolution yielded larger differences between the forced and the control simulation, in particular, in southern hemisphere winter.

In order to assess the influence of the QBO it would be useful to conduct experiments

with prescribed QBO phases. It might be expected that the warming of the tropical lower stratosphere is particularly pronounced during east phases of the QBO. This assumption is based on the observed positive correlation between the tropical and subtropical lower stratospheric temperature and the solar activity in QBO east phases, in particular, in July (Labitzke, 2004a) and on model results pointing in the same direction (Matthes et al., 2010).

With regard to the 11-year solar influence on the atmosphere, the mechanistic momentum forcing is thought as an analogy for, this implies a clear tropospheric reaction to a well-defined purely stratospheric forcing. The temperature disturbance in the lower stratosphere, even if it is possibly overestimated, gives an indication for the tropospheric response to be expected in a state-of-the-art CCM simulation with imposed spectral solar irradiance changes.

# Chapter 7

# The 27-day Solar Rotational Signal in the Middle Atmosphere

Besides the 11-year solar cycle there is a 27-day cycle of solar activity which is associated with the Sun's rotation about its axis (see section 2.2 for details). The 27-day periodicity becomes especially important during maxima of the 11-year cycle when several sunspots and faculae are present on the Sun's surface. The transit of spots and faculae over the solar disk modulates the short-wave solar irradiance that reaches the top of the Earth's atmosphere.

In connection with the Stratospheric Processes And their Role in Climate (SPARC) Chemistry Climate Model VALidation initiative (CCMVal) reference simulations (Eyring et al., 2008) a daily spectrally resolved irradiance time series spanning the time period 1950-2006 became available (Lean et al., 2005). Thereby, the following questions arose: How relevant is the variability at the rotational time scale for the 11-year solar signal? How does the mean ozone response averaged over one rotational cycle look like? Is it possible to quantify the influence of strong and weak 27-day variability on ozone in the middle atmosphere?

To address these questions two sensitivity simulations were set up. The details of the set-up are given below.

## 7.1 Experimental set-up

Two sensitivity simulations were run for four years each with a) prescribed daily spectral irradiances, i.e., the 27-day cycle explicitly included in this simulation (hereafter named CY for cycle) and b) mean irradiance values (hereafter named CO for constant). The EMAC-FUB CCM was used in T42 horizontal resolution and with 39 levels from the surface to 0.01 hPa ($\approx$ 80 km). The employed submodels are the same as for the transient

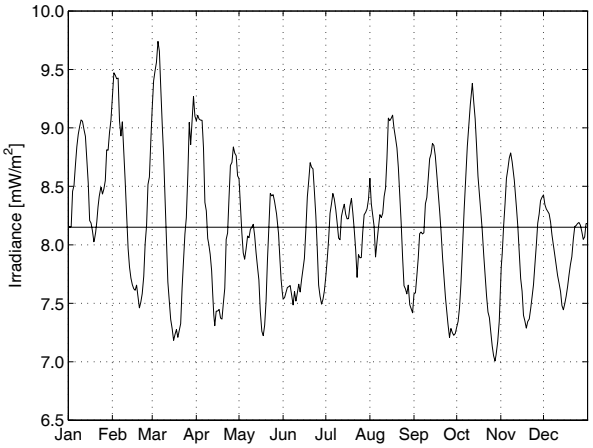


**Figure 7.1:** Irradiance at the Lyman-$\alpha$ wavelength. Time series used as input for the short-wave radiation scheme FUBRad in the CYclic simulation. The horizontal line indicates the mean value over the complete period which was prescribed for the COnstant simulation.

reference simulation (see the list in section 5.3.1) except for the QBO nudging and the additional heating due to major volcanic eruptions (VAHR).

As input for the short-wave radiation scheme FUBRad the period 9 October 1979 to 8 October 1980 was chosen, i.e., a period during solar maximum, when 27-day solar irradiance variations generally have larger amplitudes compared to solar minimum. The period has a minimum difference in irradiance between end and start to allow for cyclical repetitions for four years. Since the solar output is independent from the terrestrial annual cycle in simulation CY the selected irradiance period was applied to the model year (i.e., data of 9 October 1979 correspond to 1 January).

As an example the time series for the Lyman-$\alpha$ wavelength (121.6 nm) is shown in Figure 7.1. It is seen that the amplitude and frequency of the solar variability vary during the course of the year, with stronger and weaker 27-day cycles and sometimes a distinct 13.5-day variability (i.e., the first harmonic of the 27-day period caused by the tendency of sun spots to group on opposite sides of the Sun) which is typical for solar maximum conditions. In order to obtain the mean irradiances average values over the above-mentioned period were computed for each wavelength interval and prescribed to the four years of the CO simulation. The horizontal line in Figure 7.1 indicates the mean value for the Lyman-$\alpha$ wavelength (121.6 nm). The solar flux at 205 nm which is used for the correlation and sensitivity analyses in sections 7.2 and 7.3 is very similar in appearance (not shown). The actinic fluxes, as input for the photolysis scheme, were treated consistently.

Except for the radiation and photolysis schemes the same boundary conditions according to the recommendations of the SPARC CCMVal initiative (Eyring et al., 2008) for the reference experiment REF-B0 were imposed on both simulations. Climatological sea

surface temperatures and sea ice conditions were prescribed using 1995-2004 averaged HadlSST1 data. The concentrations of greenhouse gases (GHGs) and ozone depleting substances (ODSs) as well as background aerosol surface area densities were fixed at year 2000 conditions. Surface emissions of ozone and aerosol precursor substances (such as CO, volatile organic compounds (VOCs), $NO_x$, $SO_2$) were taken from the RETRO data set averaged over the period 1998-2000.

With this set-up four years involving 13.5 solar rotational cycles each, i.e., a total number of 54 solar cycles are obtained for analysis. The integration time of four years is chosen to represent atmospheric variability, however, it is too short to study a possible dynamical response. It has to be emphasised that the intention is to perform a sensitivity study by using a "reference" irradiance time series which contains a range of strong and weak solar irradiance variability and to produce a kind of an ensemble of 27-day solar cycles for the analysis.

The model was allowed to adjust to the imposed boundary conditions during a spin up period of about 15 months. This should prevent any drift or trend to be present in the 4-year evaluation period.

These simulations were performed on an IBMp5 parallel computer at ZeDat of Freie Universität Berlin. Results are shown and discussed in the following sections.

## 7.2 Response to daily irradiance variations

As was explained above two simulations representative for solar maximum conditions were performed running over four years each. One used spectrally resolved daily varying solar irradiances, thus, including the variability on the solar rotational time scale of about 27 days (denoted as CY). The other one (denoted as CO) used constant values for each spectral band obtained by averaging over the solar irradiance time series as exemplified in Figure 7.1.

In a first step daily mean data are averaged together to daily four-year mean data and are analysed at different latitude belts. To this end the difference cyclic minus constant (CY-CO) was computed, thus, removing the annual cycle from the data and extracting any signal forced by the 27-day variability in spectral solar irradiance. In this way no filter had to be applied to the anomaly data.

Figure 7.2 shows the four-year mean daily tropical ozone response to the imposed changes in solar irradiance (CY-CO anomalies) at different altitudes. While ozone in the middle stratosphere at 10 hPa is only weakly and temporarily influenced by the solar 27-day oscillation, it varies closely in phase with the solar irradiance for several months in the upper stratosphere at 3 hPa. In the mesosphere (0.03 hPa) there is an anti-correlation between ozone and solar irradiance, i.e., there is less ozone at higher solar irradiance. Simultaneously, mesospheric ozone is anti-correlated with OH. It is, furthermore, seen

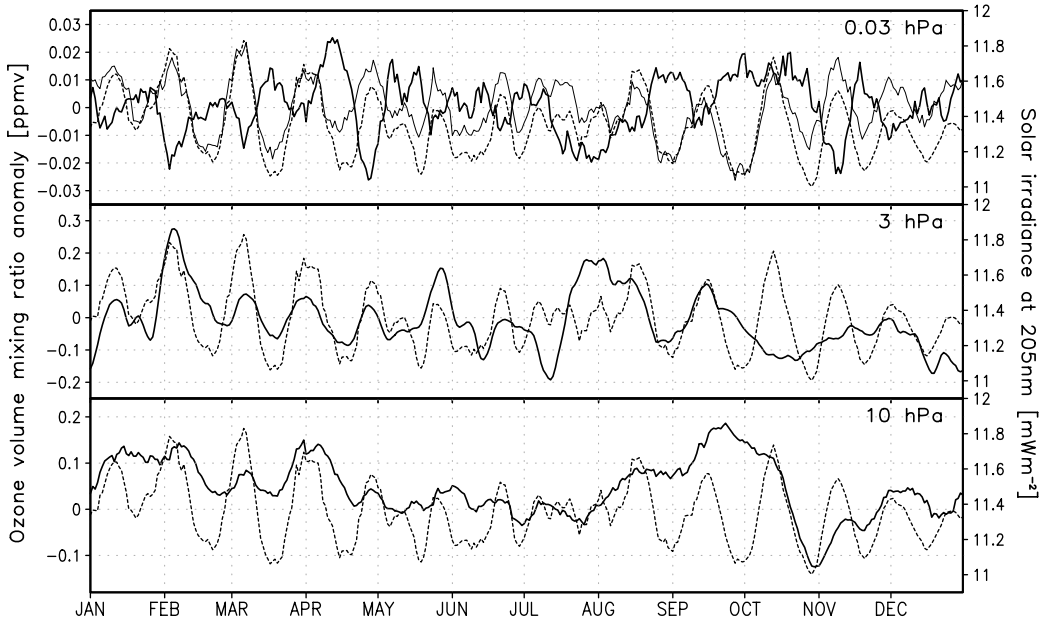


**Figure 7.2:** Time series of tropical daily four-year mean ozone anomalies (CY-CO, solid lines) averaged from 20°S to 20°N at 0.03 hPa (top), 3 hPa (middle), 10 hPa (bottom). The solar irradiance at 205 nm is depicted as dashed lines. The upper panel contains also OH anomalies responsible for ozone loss (thin solid line, left scale in $10^{-2}$ ppmv).

that the correlation between the two parameters is time dependent and may vanish, e.g., at 3 hPa in July, August and October. It should be noted that in the simulations mesospheric odd hydrogen and its response to UV variations were underestimated due to an inadvertent use of outdated product pathways for $H+HO_2$ (Hack et al., 1978) which lead to unrealistically high $H_2$ and too low $H_2O$.

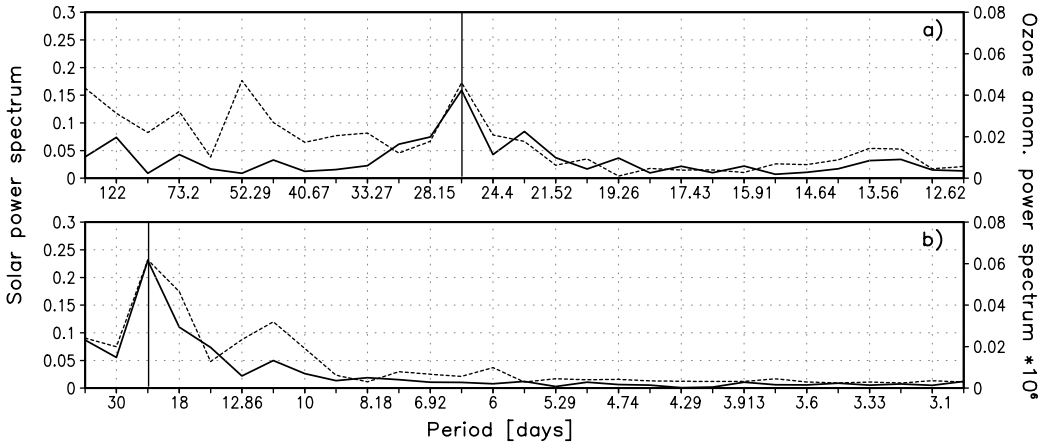


**Figure 7.3:** Power spectra of the daily solar irradiance at 205 nm (solid lines) and tropical daily four-year mean ozone anomalies (CY-CO, dashed lines) averaged from 20 °S to 20 °N at 3 hPa. a) Spectra of the entire 365-days time series, b) Spectra of the first 90 days with strong 27-day solar variability. The period of approximately 27 days is highlighted by a vertical line.

A Fourier analysis of the solar flux at 205 nm and of tropical ozone at 3 hPa was carried out. Figure 7.3a shows the spectra for the entire 365-day time series with clear maxima for both quantities at periods of about 27 and 13.5 days. The period of 13.5 days originates from the tendency of Sunspots to group on opposite sides of the Sun. Hence, they modulate the short-wave irradiance twice per rotation. The spectra over the first 90 days of the time series are shown in Figure 7.3b and exhibit a stronger amplitude at the 27-day period in solar irradiance as well as in ozone than is the case for the entire time series. The presence of the same periods in the time series of both quantities suggests a close relation between the solar irradiance variation and the ozone anomalies.

### Validation of the 27-day ozone and temperature response

Having identified a clear 27-day period in ozone consistent with the solar variability, the response of ozone and temperature is now analysed in more detail. A cross-correlation analysis of ozone volume mixing ratio and temperature anomalies with the solar flux at 205 nm was performed in order to validate the model response with observational results.

The cross-correlation of tropical (20 °S to 20 °N) and subtropical (20 ° to 40 °S and N) four-year mean ozone anomalies (CY-CO) with the solar flux at 205 nm is depicted in Figure 7.4a and 7.4b. The strongest positive correlations of about 0.4 to 0.6 are found in the upper stratosphere between 5 and 3 hPa in the tropics and subtropics, respectively. In the tropical lower mesosphere there is a second maximum of correlation between ozone and solar irradiance. Above about 0.1 hPa an anti-correlation appears in the tropics as well as in the subtropics which is a consequence of enhanced ozone loss due to increased photolytic production of OH, as explained in section 7.2. The abundance of OH increases by destruction of water vapour at the Lyman-$\alpha$ wavelength and is closely correlated with the solar flux at 205 nm (r=0.8 in the tropical mesosphere, Figure 7.2). A comparison of the modelled ozone response with the observational results of Hood and Zhou (1998) and Hood et al. (1991) shows consistency in the stratosphere and lower mesosphere up to about 0.05 hPa (approx. 69 km). Above that level the observed negative correlation decreases with altitude whereas the simulated negative correlation peaks at 0.03 hPa. Other model studies show the same negative ozone response above $\approx$ 70 km (Rozanov et al., 2006; Gruzdev et al., 2009; Grenfell et al., 2010). While for models which have their top at 80 km (Rozanov et al., 2006; Grenfell et al., 2010) the negative ozone response in the mesosphere might be due to an upper boundary effect, the fact that it also shows up in a model with the top in the thermosphere (Gruzdev et al., 2009) indicates that it is probably not a boundary effect in the 80 km-models. Differences might be also due to uncertainties related to the strong non-linear diurnal effects in the analysis of the simulations and observations.

The phase lags of the maximum ozone response are negative in the lower mesosphere and upper stratosphere and increase with decreasing altitude to become positive in the middle and lower stratosphere. This inclined position is in agreement with the

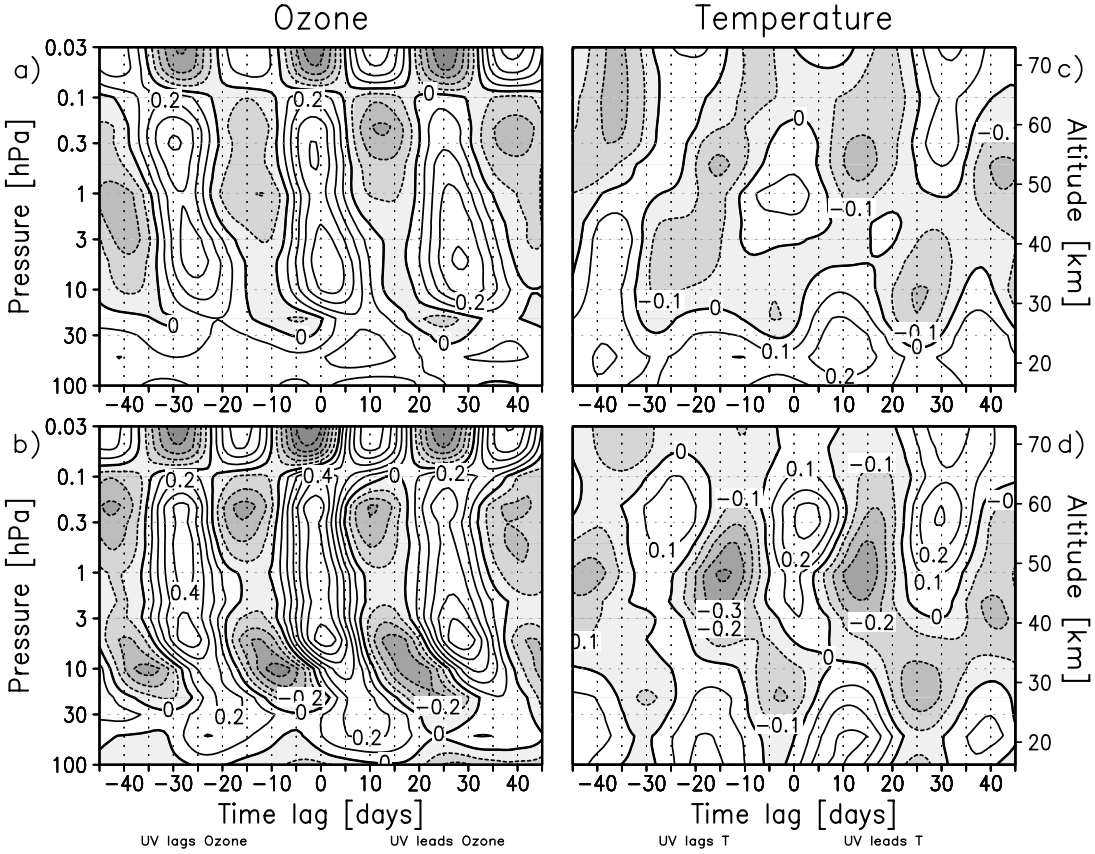


**Figure 7.4:** Cross-correlations of ozone [a)-b)] and temperature [c)-d)] anomalies with solar flux at 205 nm for the entire 365-days time series. a) and c) Tropics (20 °S to 20 °N), b) and d) subtropics (20 °S to 40 °S) and (20 °N to 40 °N). Contour interval is 0.1. Anti-correlations are shaded.

observational results of Keating et al. (1987) and Hood and Zhou (1998). It is caused by temperature feedbacks on the ozone response as discussed by Keating et al. (1987) and Brasseur et al. (1987). However, the observational results of Dikty et al. (2010) obtained in the years 2003 to 2008 neither show a negative phase lag of the maximum ozone response in the upper stratosphere nor an increase of the phase lag with decreasing altitude. Austin et al. (2007) found in a model study a non-uniform 27-day cycle ozone response at different maxima of the 11-year solar cycle. This may explain the difference in the phase lags between the studies of Hood and Zhou (1998) and Dikty et al. (2010). In comparison to other modelling studies (e.g., Grenfell et al., 2010; Gruzdev et al., 2009; Austin et al., 2007; Rozanov et al., 2006; Williams et al., 2001), the magnitude and phase lag of the ozone signal in EMAC-FUB are in good agreement.

Temperature feeds back on the ozone response by an acceleration of a number of ozone depleting reactions with increasing temperature, e.g., $O + O_3 \longrightarrow 2\ O_2$, $NO + O_3 \longrightarrow NO_2 + O_2$ or $Cl + O_3 \longrightarrow ClO + O_2$. Thus, a temperature disturbance in phase with the solar variations tends to reduce the ozone response whereas an out-of-phase temperature disturbance has the tendency to amplify the ozone signal. An intermediate

temperature phase produces a phase lag in the ozone response.

To investigate these possible feedback effects the temperature response is displayed in Figures 7.4c and 7.4d. The cross-correlations are generally weaker than those for ozone and the solar flux which is in agreement with observations (Hood and Zhou, 1998; Dikty et al., 2010). The strongest cross-correlations are found between 1 hPa and 0.2 hPa in the tropics and in the subtropics where the magnitude between 0.1 and 0.3 is in good agreement with the observations. However, the general cross-correlation pattern is different from that shown by Hood and Zhou (1998) (see their Figure 4). The positive correlation coefficients in the uppermost layers at low time lags are due to radiative heating at the Lyman-$\alpha$ and Schumann-Runge wavelengths. In the tropics and subtropics the strongest temperature response in the lower mesosphere lags the ultraviolet (UV) forcing by several days which is consistent with the negative ozone phase lags in this region according to Keating et al. (1987). In the middle and lower stratosphere the temperature phase lag increases to up to 10 days near 50 hPa in the tropics and up to 12 days near 50 hPa in the subtropics. Other models simulate comparable phase lags but there is a considerable spread among different model results.

The ozone and temperature sensitivities to changes in the UV were obtained from a linear regression at the time lag with the maximum absolute correlation coefficient.

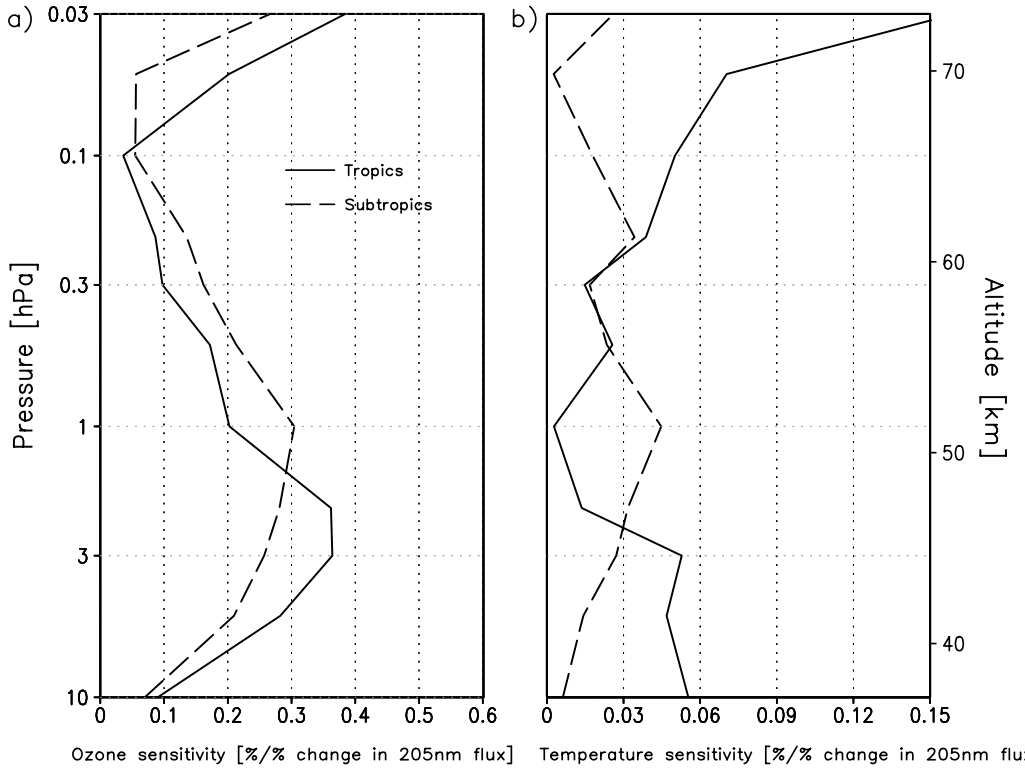


**Figure 7.5:** Ozone sensitivity (a) and temperature sensitivity (b) at the lag of maximum absolute correlation to changes in the solar flux at 205 nm in the tropics and subtropics in % per 1% change in 205 nm flux. The absolute values of the sensitivities are given.

They are displayed in Figure 7.5 from 10 to 0.03 hPa as this is the region where the correlation coefficients are large enough for a linear regression to be meaningful. The relative sensitivity is expressed in % ozone (temperature) change per 1% change in solar flux at 205 nm, respectively. Tropical stratospheric ozone is most sensitive to changes in the 205 nm solar flux at 3 hPa (Figure 7.5a). The relative sensitivity amounts to 0.37% per 1% change in the 205 nm flux. The subtropical ozone sensitivity peaks higher up at 1 hPa and a value of 0.31% per 1% change in the 205 nm flux. In the mesosphere the response increases again. The relative sensitivity (here negative) reaches about 0.38% per 1% increase in the 205 nm flux at 0.03 hPa in the tropics and about 0.26% at 0.03 hPa in the subtropics.

The temperature sensitivity in the tropics (Figure 7.5b) shows a peak at 3 hPa with a value of 0.054% per 1% change in the 205 nm flux. Approximately, equally strong sensitivities are found at 5 hPa and 10 hPa. These values are considerably lower than the 0.077% per 1% change in the 205 nm flux reported by Hood and Zhou (1998). The sensitivity in the subtropics is highest at 1 hPa with 0.045% per 1% change in the 205 nm flux. In the lower mesosphere the temperature sensitivity is of intermediate magnitude, with a maximum value of 0.034% per 1% change in the 205 nm flux at 0.2 hPa. However, it should be borne in mind that the correlations between temperature and the solar flux at 205 nm were relatively low, hence, the sensitivity results should not be overemphasised.

## 7.3 Results from the summer hemisphere - Strong versus weak 27-day variability

The goal of the analysis in this section is to quantify the impact of 27-day solar variability of different intensity. As can be seen from Figure 7.1, stronger 27-day cycles occurred in the daily irradiance time series from 11 January to 10 April while the variability was weaker and more irregular between 20 May and 18 August of the model year. In order to assess the purely radiative and photochemical signal the following analysis focuses on the respective summer hemisphere. This approach minimizes the influence of interannual dynamical effects in the winter stratosphere which, though, may themselves be influenced by the 27-day solar variability as discussed in subsection 7.5. As example results for strong 27-day variability during southern summer and for weak 27-day variability during northern summer are shown. Daily four-year means for 90 days of strong and weak 27-day variability, respectively, are considered. The analysis is performed for three latitude bands: the tropics (20 °S to 20 °N), the subtropics (20 ° to 40 °), and the mid-latitudes (40 ° to 60 °) of the respective summer hemisphere.

Figure 7.6 shows the cross-correlation of four-year mean ozone anomalies (CY-CO) with the solar flux at 205 nm. During the period of strong 27-day variability (Figure 7.6a-7.6c) there are strong positive correlations of the order of 0.6 to 0.8 in the stratosphere and lower mesosphere in all latitude bands. These values are higher than in the case of the

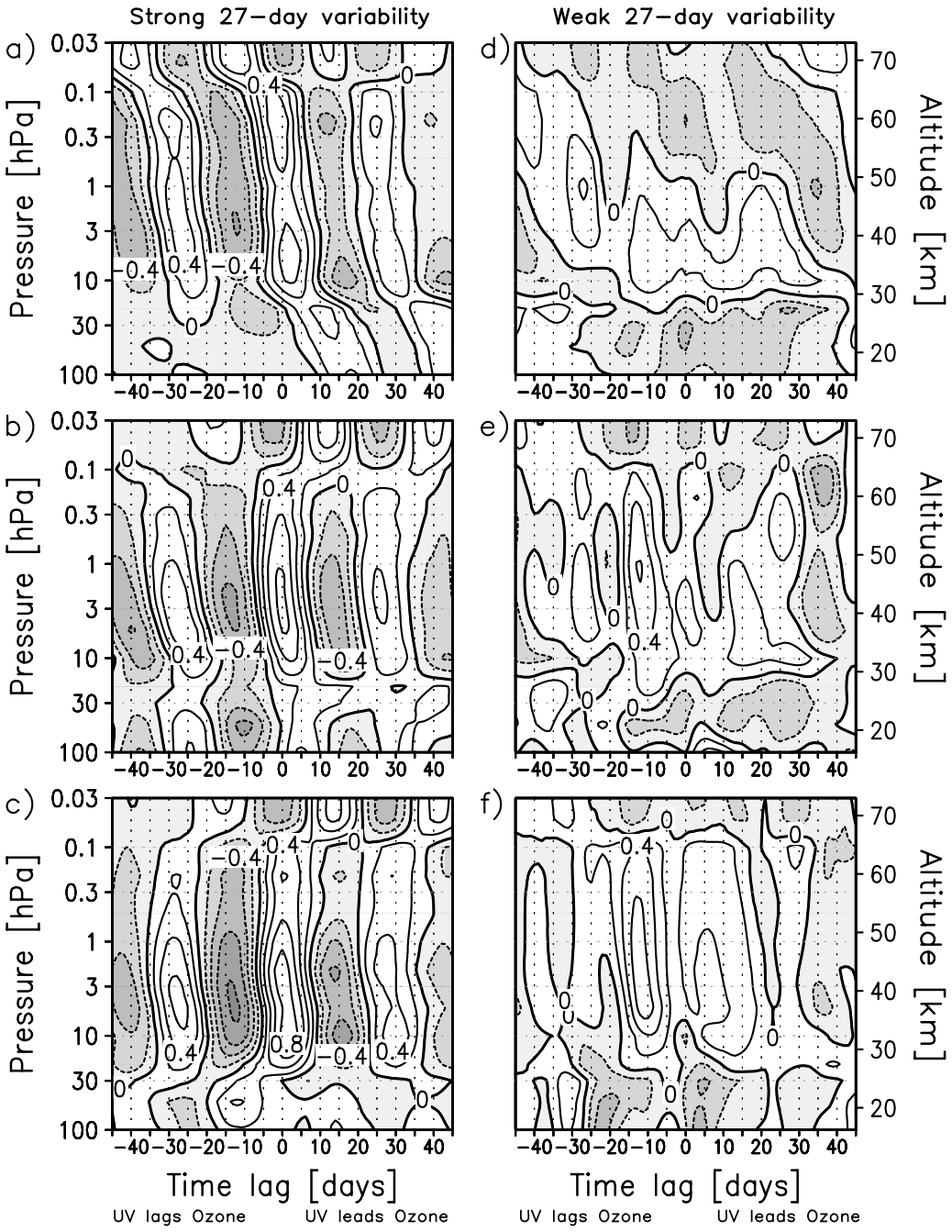


**Figure 7.6:** Cross-correlations of ozone anomalies (CY-CO) with the solar flux at 205 nm during (a-c) a period of strong 27-day variability in southern summer (11 January to 10 April) and (d-f) a period of weak 27-day variability in northern summer (20 May to 18 August). a and d) Tropics (20 °S to 20 °N), b and e) subtropics (20 ° to 40 °), c and f) mid-latitudes (40 ° to 60 °). Contour interval is 0.2. Anti-correlations are shaded.

whole period (Figure 7.4a and 7.4b). Moreover, the strongest positive correlations in the subtropics and at mid-latitudes do exceed the maximum in the tropics, as in the results for the whole year (Figure 7.4a and 7.4b). The time difference between two subsequent maxima of correlation ranges from 26 to 28 days, a result that reflects the clear period

in the solar irradiance variation during the 90 days from 11 January to 10 April. The maximum correlations are found at very small phase lags in the upper stratosphere, again similar to the 365-day period. At higher altitudes the phase lags become negative while they increase towards lower altitudes. In the tropics the phase lag reaches 2 days at 10 hPa and 5 days at 20 hPa. The denotation "UV lags ozone" for negative time lags in Figure 7.6 indicates the correlation of ozone with the preceding 27-day solar cycle.

In the simulation during northern summer a period exists with smaller amplitudes of the 27-day solar rotation cycle (cf. Figure 7.1), running from 20 May to 18 August. The amplitude of the 13.5-day period becomes as large as 80% of the one associated with the 27-day fundamental mode which can happen due to a special distribution of sunspots peaking on opposite sides of the sun. In comparison to the whole 365-day period, very different cross-correlation patterns appear during northern summer (Figure 7.6d-7.6f). There are clear 13-day fractions visible at extratropical latitudes and at negative time lags. The highest positive correlation coefficient in the tropics is only 0.35 while it ranges from 0.6 in the subtropics to 0.7 at mid-latitudes. These are lower values than in the period of strong 27-day variability but comparable to the whole 365-day period (Figure 7.4a and 7.4b).

Figure 7.7 shows ozone sensitivity profiles from 10 to 0.03 hPa. Relative sensitivities are given for the tropical and subtropical latitude belts. Additionally, the sensitivity obtained from the whole 365-day period is displayed. The sensitivity of ozone associated with the first harmonic of the 27-day cycle in the upper stratosphere is not necessarily the same as for a predominant 27-day period. Fioletov (2009) estimates that the tropical ozone sensitivity to a 1% change in the 205 nm flux at the 13.5-day period is somewhat lower than at the 27-day period below 40 km and vice versa above that level.

The highest relative sensitivity in the tropical stratosphere is found at 3 hPa. The values range from 0.35% per 1% change in the solar flux at 205 nm in the period of strong 27-day variability to 0.41% per 1% change in the solar flux at 205 nm in the period of weak 27-day variability. Hence, the ozone sensitivity seems to be enhanced during periods of weak 27-day cycles, however, with the low correlation coefficient of about 0.35 in the weak variability case this result should not be overinterpreted. The profiles for the period of strong variability and for the whole year are rather similar. The ozone sensitivity decreases towards higher altitudes, reaches a minimum at 0.1 hPa ($\approx$ 65 km) and increases again towards the middle and upper mesosphere. This indicates that periods of strong 27-day variability dominate during the 365-day period which is reasonable in view of the input time series (Figure 7.1). In the period of weak 27-day variability there is a second peak of ozone sensitivity in the lower mesosphere. Due to the low correlation coefficient the significance of this result is limited.

In the subtropics there is a notable difference between the stratospheric ozone sensitivities of the weak and the strong variability case. The profile of the former peaks at a value of 0.15% per 1% change in the 205 nm flux at 2 hPa, the latter attains its maximum

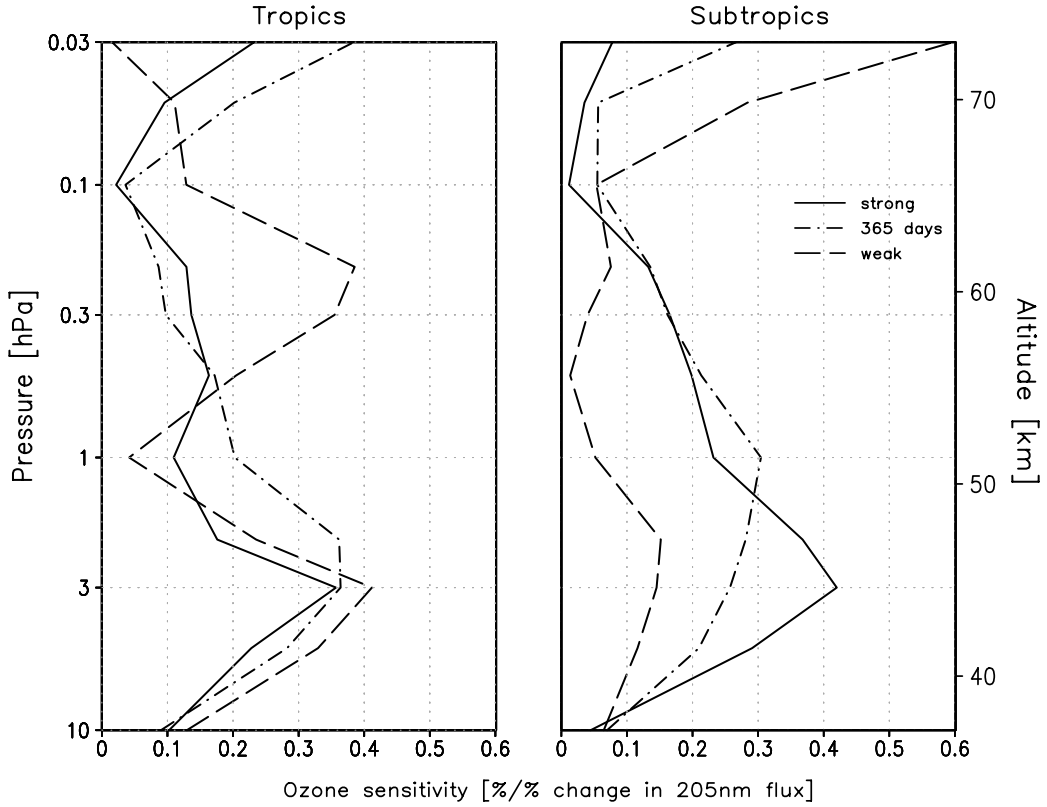


**Figure 7.7:** Ozone sensitivity at the lag of maximum absolute correlation to changes in the solar flux at 205 nm in different latitude bands during periods of strong (solid line) and weak (dashed line) 27-day variability in % per 1% change in 205 nm flux. The dash-dotted line represents the ozone sensitivity over the 356-day period. The absolute values of the sensitivities are given.

value of 0.42% per 1% change in the 205 nm flux at 3 hPa. The profile obtained from the entire 365-day period shows intermediate values at 3 hPa and 2 hPa. It peaks at a value of about 0.3% per 1% change in the 205 nm flux at 1 hPa. Towards higher altitudes the curves representing the strong variability period and the whole period become very similar as in the case of the tropics. In the tropical as well as in the subtropical mesosphere the ozone sensitivity computed over the 365-day period is higher than during the 90-day period of strong variability. The sensitivity obtained from the weak variability period during northern summer is lower than in the other two cases up to about 65 km. However, in the middle and upper mesosphere it is about twice as high as the sensitivity calculated from the 365-day period.

While in these simulations the signal in the tropics is too weak to confirm the result of Fioletov (2009); for the extratropics a similar result as Fioletov (2009) cannot be found. The relative ozone sensitivity at a pronounced 13.5-day period in the altitude region 40 to 50 km ($\approx$ 5 to 1 hPa) is about 0.15% per 1% change in the 205 nm flux which is lower than the 0.42% per 1% change in the 205 nm flux at the strong 27-day period (cf. Figure 7.7).

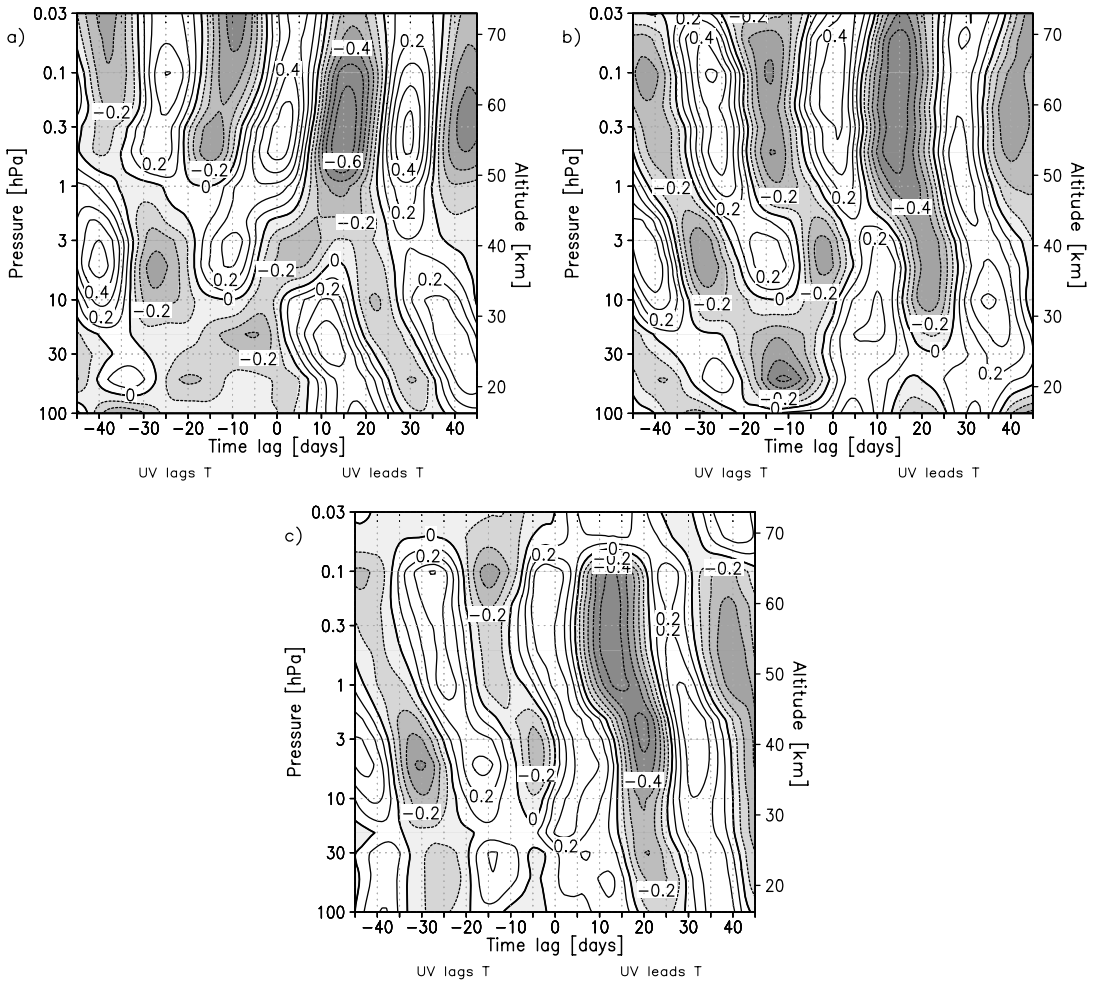


**Figure 7.8:** Cross-correlations of temperature anomalies (CY-CO) with solar flux at 205 nm during a period of strong 27-day variability, southern summer. a) Tropics (20 °S to 20 °N), b) subtropics (20 ° to 40 °), c) mid-latitudes (40 ° to 60 °). Contour interval is 0.1. Anti-correlations are shaded.

There is a dip in correlation as well as in ozone sensitivity in the tropics at about 1 hPa which is not found in other model simulations (e.g., Williams et al., 2001; Rozanov et al., 2006; Austin et al., 2007; Gruzdev et al., 2009; Grenfell et al., 2010) but which is also seen in observed correlation patterns (Hood and Zhou, 1998; Dikty et al., 2010). It appears most likely due to the diurnal cycle of ozone which is strongly damped by the calculation of daily mean values from the model output and by the day- and nighttime measurements of, e.g., the MLS instrument. This does not mean that ozone in this altitude region is insensitive to 27-day solar irradiance variability.

Another explanation for the local minimum in correlation as well as in ozone sensitivity at about 1 hPa may be found in the corresponding cross-correlations of temperature and UV irradiance. For both the entire 365-day time series (Figure 7.4c) and the 90-day period during southern summer (Figure 7.8a) the temperature is positively correlated with the UV irradiance at 1 hPa at zero phase lag, i.e., the temperatures are higher when

the UV irradiance is high. This tends to reduce the ozone response as the reaction rates of ozone depleting reactions increase with temperature.

However, the high correlation coefficients between ozone and the solar irradiance throughout the upper stratosphere and lower mesosphere at subtropical and mid-latitudes in the 90-day period of strong 27-day variability (Figure 7.6b and c) can be explained by an out-of-phase response of temperature in the summer stratopause region (Figure 7.8b and 7.8c). This was also observed by a Lidar at the Observatory of Haute Provence in southern France (Keckhut and Chanin, 1992). A lower temperature reduces the rates of ozone-depleting reactions and, thus, tends to increase the ozone response.

## 7.4 Mean ozone response

The motivation for this study was, as mentioned in section 7.1, to assess the importance of the solar rotational period for transient long term simulations as proposed by the SPARC CCMVal initiative. The 27-day solar rotation period which is close to one month might introduce interfering effects when considering monthly means and might also play a non-negligible role in some regions of the middle atmosphere.

To estimate the net effect of an individual rotational cycle on ozone mean values over two individual cycles, a strong and a weak one, were computed. These cycles were defined on the basis of the Lyman-$\alpha$ time series. The strong cycle occurs from 4 February to 7 March (max to max) while the weak cycle is running from 29 June to 24 July (min to min) in each year of the CY simulation. Time averages of ozone over the selected strong and weak cycles of the CY simulation were computed and, subsequently, averaged to four-year mean values. These were then compared with four-year mean results of the corresponding periods of the CO simulation, i.e., with constant solar irradiance.

The strong and weak cycle four-year mean ozone differences (CY-CO) are displayed in Figure 7.9a and 7.9b. In both the strong and weak cycle case there are common vertical structures in the tropics. In the low-latitude mesosphere reduced ozone volume mixing ratios of the order of 1% to 3% are found in the CY experiment compared with the CO simulation. This is due to a quadratic component in the main odd oxygen sink reaction O+OH since both reactants change in the same direction with the UV-change. Towards the lower mesosphere the ozone abundance is enhanced in the CY experiment. In the tropical middle and upper stratosphere (10 hPa to 1 hPa) there are again negative ozone differences indicating lower ozone volume mixing ratios in the experiment with daily varying irradiances. Only the strong cycle equatorial mesospheric signal and the weak cycle lower mesospheric response are statistically significant. In the lower stratosphere transport processes dominate. The large difference of up to -10% in the polar lower stratosphere in Figure 7.9a is, e.g., not a result of solar irradiance variability. It is most likely due to interannual variations in the break-up date of the southern polar vortex in

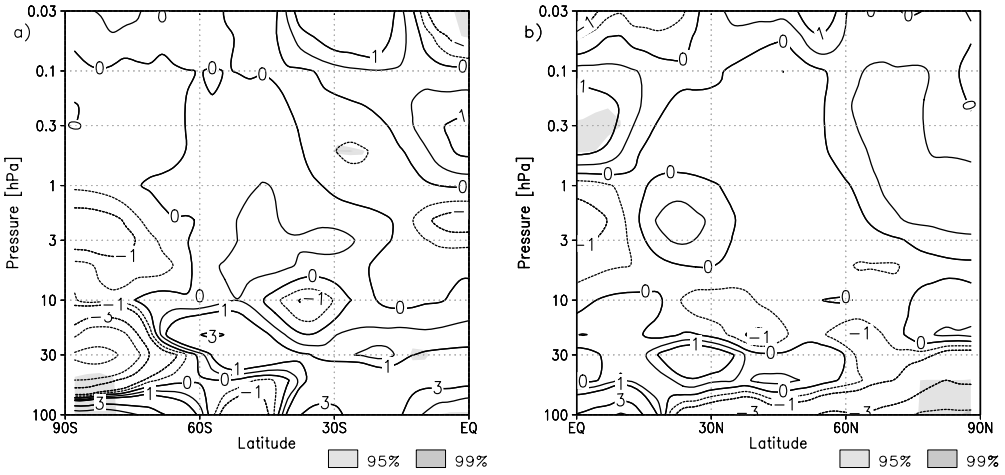


**Figure 7.9:** Mean relative ozone differences CY-CO in percent. a) Strong cycle, southern summer. b) Weak cycle, northern summer. Contours are drawn at 0, ±0.5, ±1, ±3, ±5, ±10%, respectively. Shaded regions indicate statistically significant differences at the 95% and 99% level.

both experiments and the associated mixing of ozone-poor air into the surrounding air masses, as dicussed by Fioletov and Shepherd (2005).

To gain more confidence in the above analysis it is tested whether the standard deviations of the four-year mean ozone anomalies in the CY and the CO experiment are significantly different from each other, using a Fisher-test. Figure 7.10a shows that for the strong cycle case there are nearly no statistically significant differences between the standard deviations. For the weak cycle case, there is a significant difference between the standard deviations of the two experiments in the mid- to high-latitude mesosphere and in the low-latitude middle and lower stratosphere (Figure 7.10b). The standard deviation

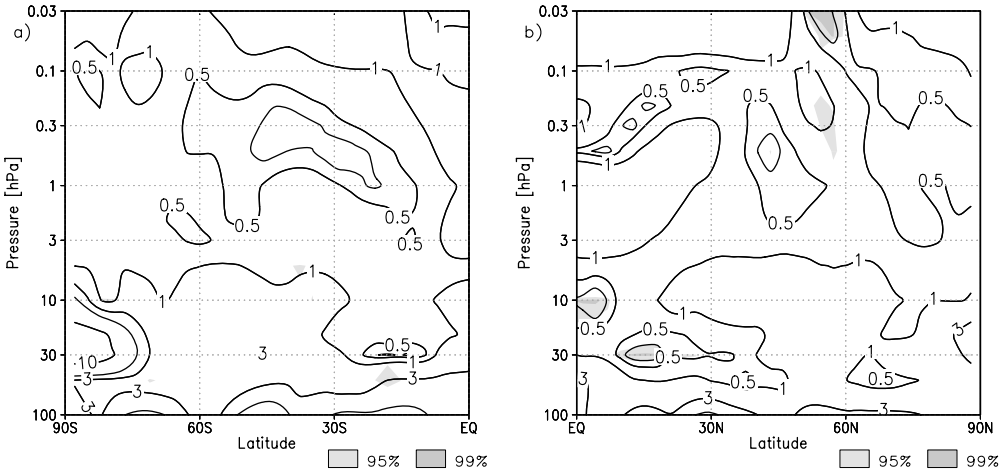


**Figure 7.10:** Results from a Fisher-test on the standard deviations of the CY and the CO experiment. Contours depict the relative standard deviation of the CY experiment in %. Shaded regions indicate statistically significant differences at the 95% and 99% level. a) Strong cycle, SH summer; b) Weak cycle, NH summer.

of the CO experiment is higher than that of the CY experiment in the stratosphere as well as in the mesosphere (not shown). This shows that adding a systematic source of variability to one of the experiments did in most regions not lead to significantly different standard deviations.

## 7.5 Results from the winter hemisphere

It is possible that the solar variability on the rotational time scale of 27 days, which is most prominent during 11-year cycle maxima, influences the excitation of planetary waves or the propagation conditions for these waves. As planetary waves can only propagate to the stratosphere in the winter season, it is appropriate to focus on the winter hemisphere. There is observational evidence for a 27-day signal in temperature in the winter hemisphere stratosphere from, e.g., an empirical mode decomposition analysis of MLS temperature data from the declinig phase of solar cycle 23 (Ruzmaikin et al., 2007).

The following analysis focuses now on the first 90 days of the year, i.e., the winter period in the northern hemisphere and, simultaneously, the period with strong 27-day solar irradiance variability. The planetary wave amplitudes in winter are the highest at 1 hPa and in a latitude belt between 55-75 °N. An average over the wave amplitudes in this latitude belt and at this level is computed and spectrally analysed.

The geopotential height wave with the zonal wavenumber 1 and the temperature wave 1 both show higher amplitudes at the 27-day period in the experiment with 27-day solar forcing compared to the experiment with constant solar forcing (Figure 7.11a and 7.11c). The geopotential height wave with zonal wavenumber 2 (Figure 7.11b) exhibits a lower amplitude in the cyclic experiment than in the constant experiment. This indicates a shift towards more frequent wave 1 disturbances in the cyclic experiment. In the temperature wave 2 spectrum there is no notable difference between the amplitudes obtained from both experiments (Figure 7.11d).

In an earlier study Soukharev and Labitzke (2001) found higher planetary wave amplitudes on the 27-day and 54-day (two times 27 days) time scale during solar maximum periods at mid-latitudes in the middle stratosphere. These dynamical patterns might be caused by periodically varying propagation conditions for planetary waves.

The EP-flux divergence time series, which provides a quantitative measure for the interaction of transient waves with the zonal mean flow was likewise spectrally analysed. The results are displayed in Figure 7.12. It is seen that in the CY experiment there is more energy present at periods of 27 days than in the CO simulation. This is another indication for an influence of the solar rotational cycle on the dynamics in the winter hemisphere. The propagation and breaking of planetary waves in the upper stratosphere is, thus, periodically altered. A conceivable mechanism might work as follows: The meridional temperature gradient is enhanced with a period of 27 days. This affects via the thermal

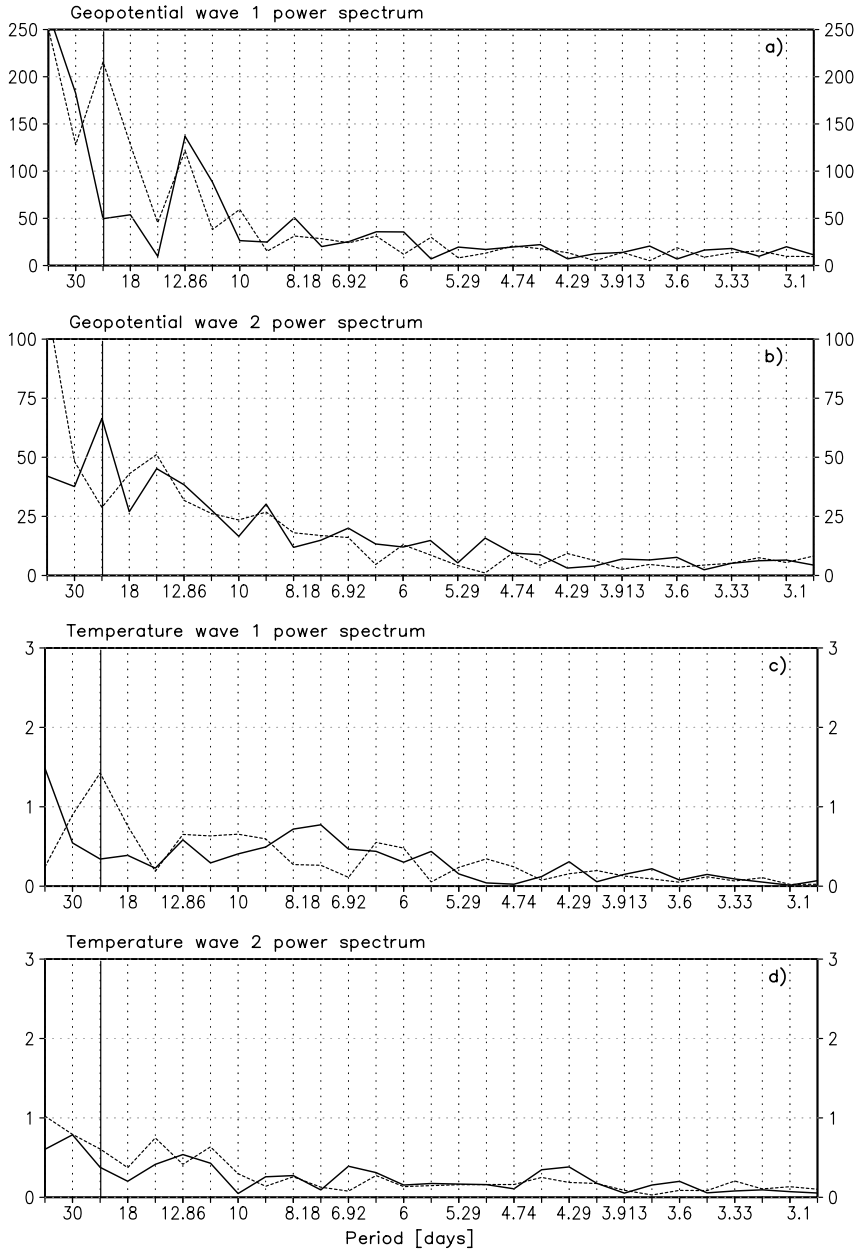


**Figure 7.11:** Spectra of geopotential height and temperature waves with wavenumbers 1 and 2 at 1 hPa averaged over the latitude belt 55 °N to 75 °N for the first 90 days, i.e., northern winter. Geopotential height amplitudes are given in gpm, temperature amplitudes in K. Solid lines: constant experiment, dashed lines: cyclic experiment. The period of approximately 27 days is highlighted by a vertical line.

wind relationship the vertical shear of the zonal wind. The strength of the polar night jet determines in turn the propagation conditions for planetary waves according to the Charney-Drazin criterion (waves can propagate in a westerly mean flow below a certain threshold wind velocity which depends on the wavenumber, the higher the wavenumber the lower the critical wind velocity, Charney and Drazin (1961)). Ultimately, this may shift the regions of wave breaking.

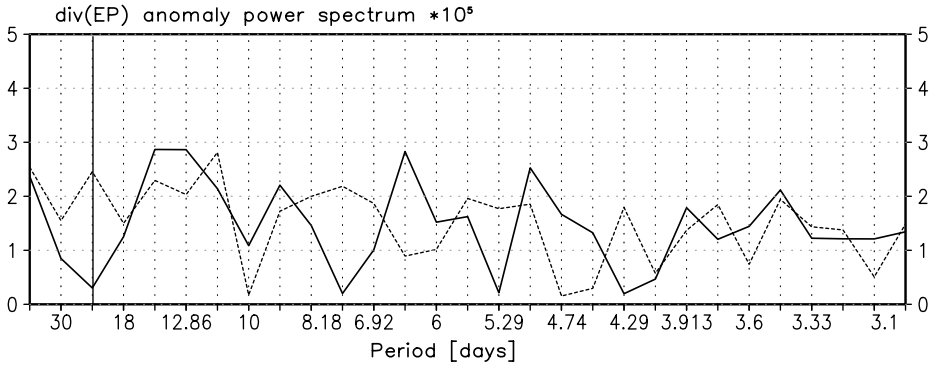


**Figure 7.12:** Same as Figure 7.11 but for the EP-flux divergence at 1 hPa averaged over the latitude belt 55 °N to 75 °N.

Since breaking planetary waves drive the mean meridional circulation there should also be a 27-day signal in the residual vertical and meridional velocities $\overline{w}^*$ and $\overline{v}^*$. This is indeed the case as the spectra of $\overline{w}^*$ and $\overline{v}^*$ which are displayed in Figure 7.13 show. The vertical velocity $\overline{w}^*$ is directed downward in northern winter at high latitudes. The spectra are computed from time series in the lower mesosphere at 0.5 hPa and averaged over a latitude belt from 65 °N to 75 °N which is a region where strong downward motion is found in the model. It is seen that there is more energy at periods about 27 days in the experiment with the 27-day cycle explicitly resolved compared to the constant experi-

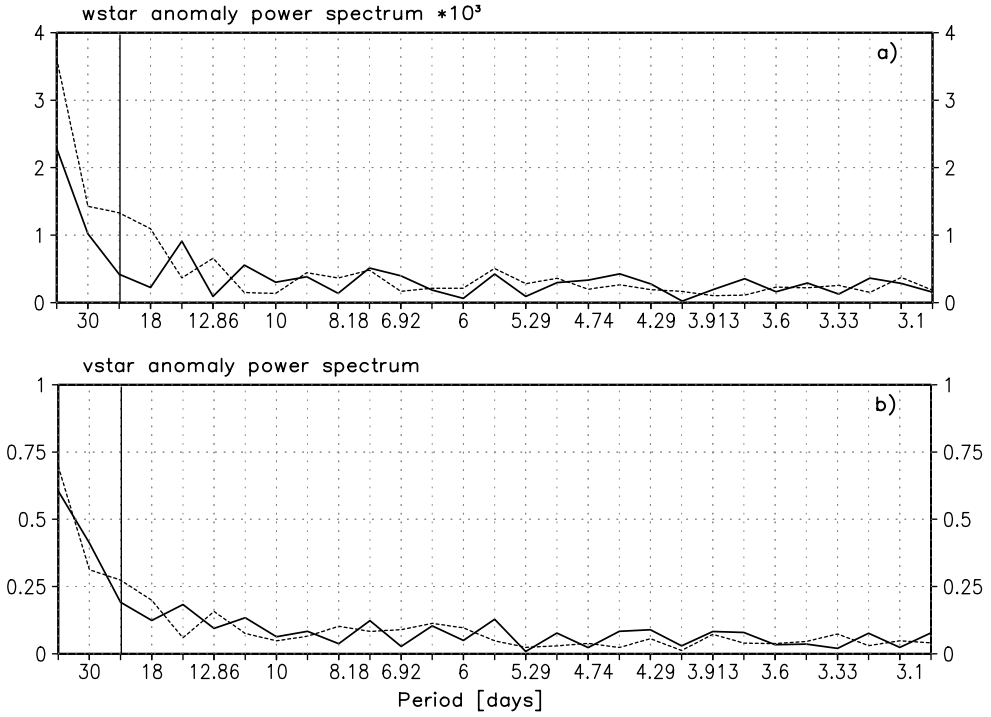


**Figure 7.13:** Same as Figure 7.11 but for the residual mean meridional circulation components a) $\overline{w}^*$ at 0.5 hPa averaged over the latitude belt 65 °N to 75 °N and b) $\overline{v}^*$ at 0.2 hPa averaged over 45 °N to 55 °N.

ment which supports the hypothesis of a periodically varying intensity in the wave-mean flow interaction. The spectra of the meridional velocity $\overline{v}^*$ which is directed northward in northern winter, are likewise analysed in a region where strong poleward transport occurs (at 0.2 hPa and averaged over 45 °N to 55 °N). Figure 7.13b shows a slightly higher amplitude in the cyclic experiment at a period of about 27 days than in the constant experiment but it is not as pronounced as for the vertical velocity.

Via the mean meridional circulation the periodic influence may feed back on the tropics, especially, on the lower stratosphere, and on the summer hemisphere where the response to 27-day irradiance variability is mainly photochemically controlled (Hood, 2003).

## 7.6 Summary and Discussion

In this CCM case study the influence of the 27-day solar rotational cycle on the atmosphere has been investigated using observed daily varying spectrally resolved irradiances including a variable amplitude and period of the solar forcing. Relevant photochemical mechanisms as absorption of the Lyman-$\alpha$-wavelength in the mesosphere are taken into account, and the 27-day variability was included in both the radiative heating and the photolysis schemes of the model.

EMAC-FUB simulates an ozone response to 27-day solar irradiance variability that is in agreement with observations concerning the upper stratospheric and lower mesospheric correlation between ozone and the solar UV flux which is positive where enhanced photolysis of $O_2$ enforces ozone formation. Ozone is negatively correlated with UV in the upper mesosphere which is due to enhanced ozone loss as a consequence of increased photolytic production of OH from water vapour at the Lyman-$\alpha$ wavelength. However, the modelled upper mesospheric response deviates from observations but is in line with other model studies.

The magnitude and phase lag of the ozone response to UV changes in the stratosphere are in good agreement with observations and other model studies when the full irradiance time series is considered. For two sub-periods of 90 days each representing strong and weak and more irregular 27-day irradiance variability a likewise realistic phase relation was simulated. The strength of the correlation between ozone and the solar flux is time dependent as was noticed in earlier observational studies. The temperature response to daily varying irradiances shows phase lags that are consistent with the ozone response (Keating et al., 1987) and with observations from the mid-latitudes (Keckhut and Chanin, 1992). The magnitude of the observed temperature response is, however, underestimated by the model.

It has been shown that ozone in the summer hemisphere upper stratosphere does not respond uniformly to 27-day solar variability of different intensity. Ozone is most

sensitive to changes in the solar flux in the mesosphere at 0.03 hPa and at about 3 hPa in the stratosphere. The derived sensitivity in the tropical stratosphere from a period of strong 27-day variability is in good agreement with values found in the literature. In the extratropics a lower ozone sensitivity was derived for a lower amplitude of the 27-day solar forcing and a dominant 13.5-day period. This is possibly a reversal of the relation that Fioletov (2009) found in the tropical upper stratosphere, i.e., ozone being more sensitive to UV irradiance changes at the 13.5-day period than at the 27-day period.

The analysis of cycle mean ozone differences yielded for a strong and a weak 27-day cycle a similar vertical tripole structure of the anomalies in the equatorial mesosphere and upper stratosphere. A negative signal of about 3% which is statistically significant in the strong cycle case, is found in the upper mesosphere above a positive anomaly of the order of 1 to 2% in the lower mesosphere, which is statistically significant in the weak 27-day cycle case. In the upper stratosphere a negative ozone response is found which is most likely related to the non-linear response of photolytic ozone production to the overhead ozone columns and to the altitude dependent different phase lag for temperature and ozone. There are weak and insignificant anomalies in the stratosphere and mesosphere of the respective summer hemisphere.

As a result one can infer from this study that resolving the short term UV variability associated with the solar rotational cycle does not alter the mean ozone response in the extratropical summer stratosphere significantly. However, the difference between neglecting and considering the 27-day cycle may be as high as 3% in the upper mesosphere. Hence, from a photochemical and radiative point of view our results suggest that resolving the daily solar irradiance variability has only a low relevance for the mean ozone signal in the stratosphere.

However, potential dynamical effects of the 27-day solar irradiance variability in the winter stratosphere may play a non-negligible role for the distribution of ozone in the stratosphere. An indication for the susceptibility of the winter hemisphere circulation to 27-day irradiance variability was obtained from a spectral analysis of geopotential and temperature wave amplitudes as well as of the EP-flux divergence which is a measure for the interaction of waves with the mean flow. As the wave-mean flow interaction governs the mean meridional circulation and hence the transport of trace species this may affect the ozone abundance in the lower stratosphere. With regard to the 11-year cycle these results imply the possibility of a contribution from the 27-day solar rotational cycle to the 11-year solar signal since the rotational cycle is strongest at 11-year cycle maxima.

Parts of this chapter have been submitted for publication to the Journal of Geophysical Research (Kubin et al., 2011).

# Chapter 8

# The 11-year Solar Signal in the Stratosphere and Troposphere

In the previous chapters results from two sensitivity studies were presented and discussed. These pre-studies dealt with an analogy of the dynamical part of the 11-year solar influence and with the effect of solar irradiance variability on the 27-day solar rotational time scale which is most pronounced during 11-year solar cycle maxima. Thus, the 11-year solar cycle was indirectly involved in the investigations.

In the present chapter the 11-year solar signal in the stratosphere and troposphere as it appears in various GCM and CCM simulations is analysed. The focus is on the tropospheric signal as well as on the solar induced changes in the tropical lower stratosphere.

In section 4.3.3 several open questions were posed. The analyses in this chapter shall contribute to answer, e.g. the question for the appearance of the 11-year solar signal in the troposphere and the question in which way natural modes of climate variability are affected by the solar influence. To this end, a transient simulation which aims to reproduce the last half century as realistically as possible is chosen as a reference. The 11-year solar signal in the stratosphere and troposphere is described in detail for this simulation (section 8.1). In the following, the influence of a number of factors on the simulated 11-year solar signal is investigated involving the model's vertical resolution (section 8.2) as well as the use of equilibrium perpetual solar maximum and minimum simulations versus a transient simulation (section 8.3). Moreover, it is investigated in which way the use of prescribed ozone changes in a GCM compared to interactively modelled atmospheric chemistry in a CCM influences the 11-year solar signal (section 8.4). Finally, the role of sea surface temperatures and sea ice data, which are prescribed at the lower boundary of the model, for the appearance of the solar signal is analysed (section 8.5). At the end of each section, the findings are briefly summarised and discussed.

## 8.1 The 11-year solar signal in a transient simulation of the period 1960-2005

The 11-year solar signal in the stratosphere and in the troposphere shall be described using a transient CCM simulation of the recent past as a reference. The intention with this simulation was to model the period from 1960 to 2005, i.e., 46 years, as realistically as possible (see section 5.3.1 for details of the experimental set-up). On the basis of this simulation the ability of the EMAC-FUB CCM to model the solar influence on the atmosphere shall be assessed. By definition of the experiment with prescribed observed SSTs and sea ice conditions the indirect top-down effect can be studied. For the analysis of the simulation results a multiple linear regression approach is used (see section 5.4, equation 5.2) in order to separate the influence of the different forcing factors that were active in the model. The observed F10.7 cm solar radio flux, the Nino3.4 index as calculated from the observed SSTs and the modelled equatorial wind at 50 hPa representing the QBO were used as regressors together with three terms representing the major volcanic eruptions in 1963, 1982 and 1991. Generally, a linear trend term is incorporated in the regression analysis. Only in the cases of ozone and southern hemisphere geopotential height effective stratospheric chlorine (ESC) is used as a regressor instead of the linear trend. The reason therefor is the strong destructive influence of chlorofluorocarbons (CFCs) on ozone and the influence of the CFC induced ozone depletion on radiative heating and temperature. All solar regression results are given per 100 units of the F10.7 cm solar radio flux.

### 8.1.1 The annual mean solar signal

In the transient simulation of the past the spectral solar irradiance has been prescribed at the top of the model atmosphere on a daily basis. The highest percentaged differences between solar maximum and minimum occur in the ultraviolet spectral region (cf. Figure 2.9). As incoming solar radiation in this spectral region is absorbed in the middle and upper atmosphere by molecular oxygen and ozone one would expect associated differences in the short-wave heating rates in the stratosphere and mesosphere.

The short-wave heating due to the absorption in the Hartley, Huggins and Chappuis bands of ozone is closely linked to the ozone distribution which in this simulation is determined interactively. Therefore, the SW heating is, on the one hand, influenced by in-situ production and destruction of ozone which depends in the middle and upper atmosphere mainly on the photolysis of $O_2$ and the presence of ozone depleting substances. On the other hand, it is influenced by transport of ozone into a particular region which is slow compared to the time scale of photochemical reactions in the middle and upper atmosphere but which gains importance in the lower stratosphere. The SW heating associated with molecular oxygen is barely affected by transport since molecular oxygen is a well-mixed constituent of the atmosphere.

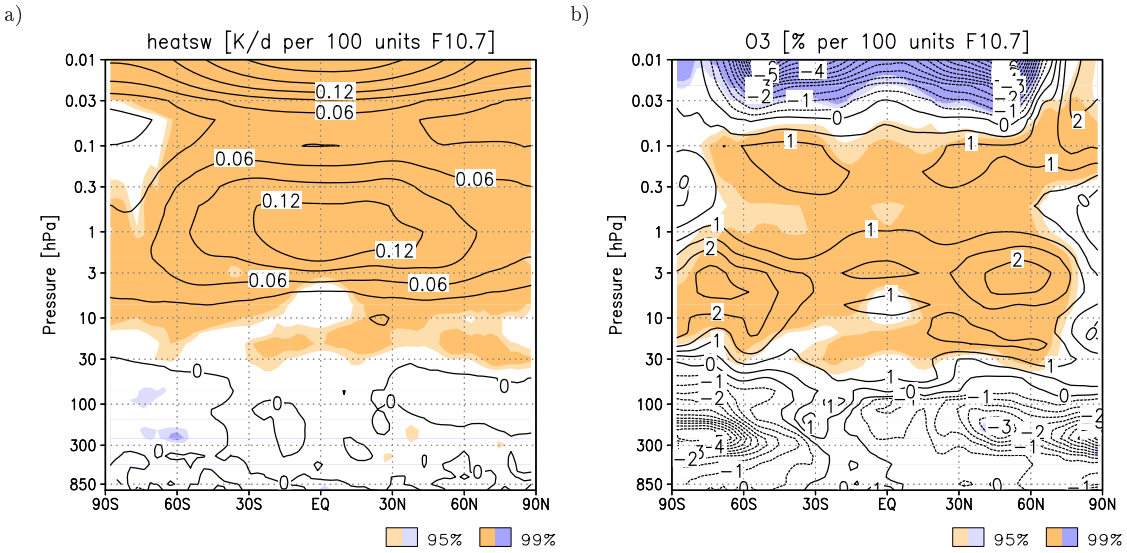


**Figure 8.1:** a) Zonal mean annual mean solar regression coefficient of short-wave heating rates in K/day, contour interval is 0.03 K/day per 100 units of F10.7 and b) Zonal mean annual mean solar coefficient of ozone in % (coefficient/mean), contour interval is 0.5 % per 100 units of F10.7. Light (heavy) shading indicates statistically significant changes at the 95(99) % level.

This stated, the annual mean solar regression pattern which is depicted in Figure 8.1a can be understood. Short-wave heating is enhanced at higher solar activity (i.e., solar maximum) throughout the middle atmosphere. This signal is statistically highly significant. In the stratosphere the regression coefficient is highest close to the stratopause at about 1 hPa with values of 0.14 K/d per 100 units of F10.7 cm radio flux. However, in the mesosphere there is a second maximum of about 0.18 K/d which is due to the strong solar cycle dependence of solar irradiance at the Lyman-$\alpha$ wavelength. The presence of this second maximum is an improvement compared to the study of Matthes et al. (2004) who used an earlier version of the short-wave heating scheme. Compared to other CCMs and to a line-by-line reference scheme the EMAC-FUB radiation code performance regarding 11-year solar cycle influence is very good (Chapter 3 of SPARC CCMVal, 2010).

The ozone response is given as percentaged anomaly (coefficient*100/46-year mean). Since the absolute ozone abundance in the stratosphere varies over one order of magnitude this is a convenient way to highlight important changes. Ozone reacts to the imposed solar irradiance with a positive anomaly of about 1.5 to 2 % in both the southern and northern hemisphere mid-latitudes at about 5 hPa. In terms of absolute values the ozone change amounts to 0.14 to 0.16 ppm per 100 units F10.7. The mesospheric response is of opposite sign, i.e., the ozone volume mixing ratio decreases as solar activity increases, and this is due to the enhanced abundance of OH as a consequence of increased water vapour photolysis at the Lyman-$\alpha$ wavelength. OH depletes ozone in a catalytic cycle and leads, thus, to the negative ozone anomaly.

The spatial distribution of the stratospheric ozone changes resembles the one de-

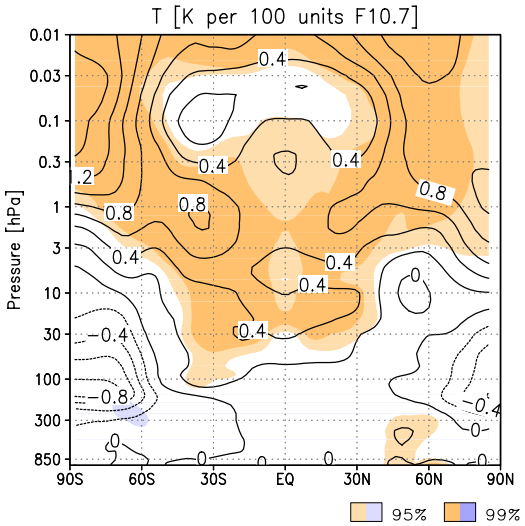


**Figure 8.2:** Zonal mean annual mean solar regression coefficient of temperature in K, contour interval is 0.2 K per 100 units of F10.7. Light (heavy) shading indicates statistically significant changes at the 95(99) % level.

scribed by Haigh (1994) and Haigh (1999) which was obtained from a two-dimensional chemistry-transport model. More importantly, it also resembles the pattern that Randel and Wu (2007) derived by multiple linear regression from an observed data set (SAGE I 1979-1981 and SAGE II 1984-2005) which shows significant ozone increases between 10 and 3 hPa in the mid-latitudes. Soukharev and Hood (2006) report a similar latitudinal structure with two maxima at mid-latitudes in the middle and upper stratosphere from other satellite ozone data sets (SBUV/2 1979-2003 and UARS HALOE 1992-2003). However, the model results disagree with the observations in the tropical lower stratosphere where Soukharev and Hood (2006) and Randel and Wu (2007) report a secondary maximum of ozone response of about half of the magnitude that was seen in the upper stratosphere.

The fact that the solar signals in ozone and short-wave heating rates in the upper stratosphere do not coincide can be understood when it is considered that not only the higher ozone leads to increased absorption of short-wave solar irradiance but that it is irradiance with shorter wavelenghts, and hence with higher energy, that is absorbed higher up in the atmosphere. Thus, the combination of higher ozone and higher solar irradiance produces the depicted response in the short-wave heating rates which peaks above the level of highest ozone changes.

The temperature response at mid-latitudes shows significantly higher temperatures at higher solar activity of the order of 0.8 K per 100 units of F10.7 at the stratopause (Figure 8.2). Compared with observations (Randel et al., 2009) there is agreement but also a discrepancy in the shape and strength of the solar signal in temperature. A similar structure is seen in Figure 8.2 and Randel et al. (2009) (their Figure 25) with significantly higher temperatures equatorward of 30 °N and S and weak and insignificant changes

poleward of about 40 °N and S, respectively, in the altitude range of 25 to 40 km (≈ 30 to 3 hPa). Above about 3 hPa the positive temperature anomaly is even found at mid- and high latitudes in accord with the observations. However, the modelled response disagrees qualitatively with the observed one with respect to the vertical profile. The solar signal in temperature as found in observations is strongest at low latitudes at the stratopause and decreases towards the lower stratosphere whereas the modelled signal shows a local minimum at the equatorial stratopause and is weak throughout the tropical stratosphere. The solar signal in Randel et al. (2009) is given as approximate difference between solar maximum (max) and minimum (min). Assuming the average solar cycle difference (max-min) in the F10.7 cm radio flux as 130 units the scaled results from the transient simulation read as 0.65 K between 30 °N and S and ≈1 K at mid-latitudes at the stratopause. Thus, in the tropics the modelled temperature response in particular in the middle and upper stratosphere is weaker than the observed one.

In the mesosphere towards the top of the model domain the temperature sensitivity to changes in solar irrandiance increases again to about 1.0 to 1.2 K per 100 units F10.7 at mid- to high latitudes which is higher than the stratopause maximum. The annual mean response at high northern latitudes is dominated by the winter signal with lower temperatures in the lower stratosphere at solar maximum and higher values in the upper stratosphere and lower mesosphere, as shall be discussed in the next section. The cooling signal in the northern high-latitude lower stratosphere is not statistically significant which reflects the high interannual variability in the northern hemisphere polar region. The corresponding signal in the southern hemisphere is statistically significant only in a limited region and in agreement with the results of Randel et al. (2009).

It is seen that the ozone and the temperature response in the stratosphere close to the equator are not (in the lower stratosphere) or only marginal (in the middle and upper stratosphere) statistically significant. This is due to the variability associated with the QBO. It is also possible that the QBO which was assimilated from observations in this simulation is itself influenced by the 11-year solar cycle. This will be discussed in chapter 9.

### 8.1.2 The stratospheric solar signal in winter and its downward transfer

#### Northern winter

Having seen the annual mean response it is interesting to analyse monthly mean data, in particular, in the dynamically active winter season on the northern hemisphere. Composite analyses of observations have shown an initial intensification of the zonal mean zonal wind in the subtropical lower mesosphere in November. This signal is amplified and moves poleward and downward in December and January. It is replaced by a downward moving easterly zonal wind anomaly in February and March. Simultaneously, a dipole anomaly pattern in the zonal mean temperature poleward of 60 °N with higher temperatures in the

upper stratosphere and a cooling anomaly below moves downward over the course of the winter from December to February (Kodera and Kuroda, 2002). When forming composits according to solar activity it is likely that both phases of the QBO are present in the solar max and min composits, respectively. Therefore, it is not possible to extract the "pure" solar signal. For the best possible comparison the results of a multiple linear regression analysis of the ERA-40 data from 1980 to 2001 is shown in the first two columns of Figure 8.3. The period was selected from the ERA-40 data set since satellite observations have become available for assimilation into the reanalysis since 1979. The temporal and spatial coverage of these satellite data provides an important improvement compared to the sparse ground-based observations that were before available to constrain the reanalysis model in the middle atmosphere. The regression approach is the same that was used for the EMAC-FUB data. However, the ERA-40 and EMAC-FUB results are not completely comparable since the ERA-40 time series from 1980 to 2001 is much shorter than the EMAC-FUB time series from 1960 to 2005.

The multiple linear regression solar coefficients for the months of November to February are shown in the third and fourth column of Figure 8.3. The temperature dipole signal is situated rather stationary with the significant positive anomaly in the upper stratosphere and lower mesosphere and the likewise significant negative anomaly in the lower stratosphere during November and December. The signal is displaced downwards in January but the negative anomaly in the lower stratosphere is no longer statistically significant. The temperature signal proceeds downward in February when the positive anomaly is now centred at about 5 hPa and the negative anomaly below has almost vanished. Overall in the ERA-40 data set there is a similar structure with higher temperatures at solar maximum in the upper stratosphere and a negative anomaly below.

The solar signal in zonal mean zonal wind in EMAC-FUB shows a positive anomaly, i.e., an enhanced westerly wind in the upper stratosphere in November. A similar spatial structure is seen in the solar regression pattern obtained from the 1980s and 1990s ERA-40 data. In December the westerly anomaly in EMAC-FUB has moved downward and is now strongest in the middle stratosphere at about 10 hPa. The downward transfer of the westerly anomaly continues in January and is accompanied by a weakening of the signal. However, in January a statistically significant region appears in the mid-latitude troposphere. This is an indication for a poleward shift of the jet stream. In this mid-winter month there is good agreement between the EMAC-FUB solar signal in zonal mean zonal wind and the signal in the reanalyses. In February the westerly anomaly is confined to the lowermost stratosphere and troposphere where it is weak but significant and again evidence for a poleward shifted tropospheric jet. In the high-latitude middle and upper stratosphere a negative, i.e., easterly anomaly has replaced the positive wind signal. Since the absolute zonal mean zonal wind field in February is dominated by the strong westerly polar night jet an easterly anomaly implies a weakening of the westerly wind. A similar signal is seen in the ERA-40 data. Through all winter months a positive (westerly) zonal wind anomaly in the subtropical lower mesosphere is visible in the ERA-40 results. In

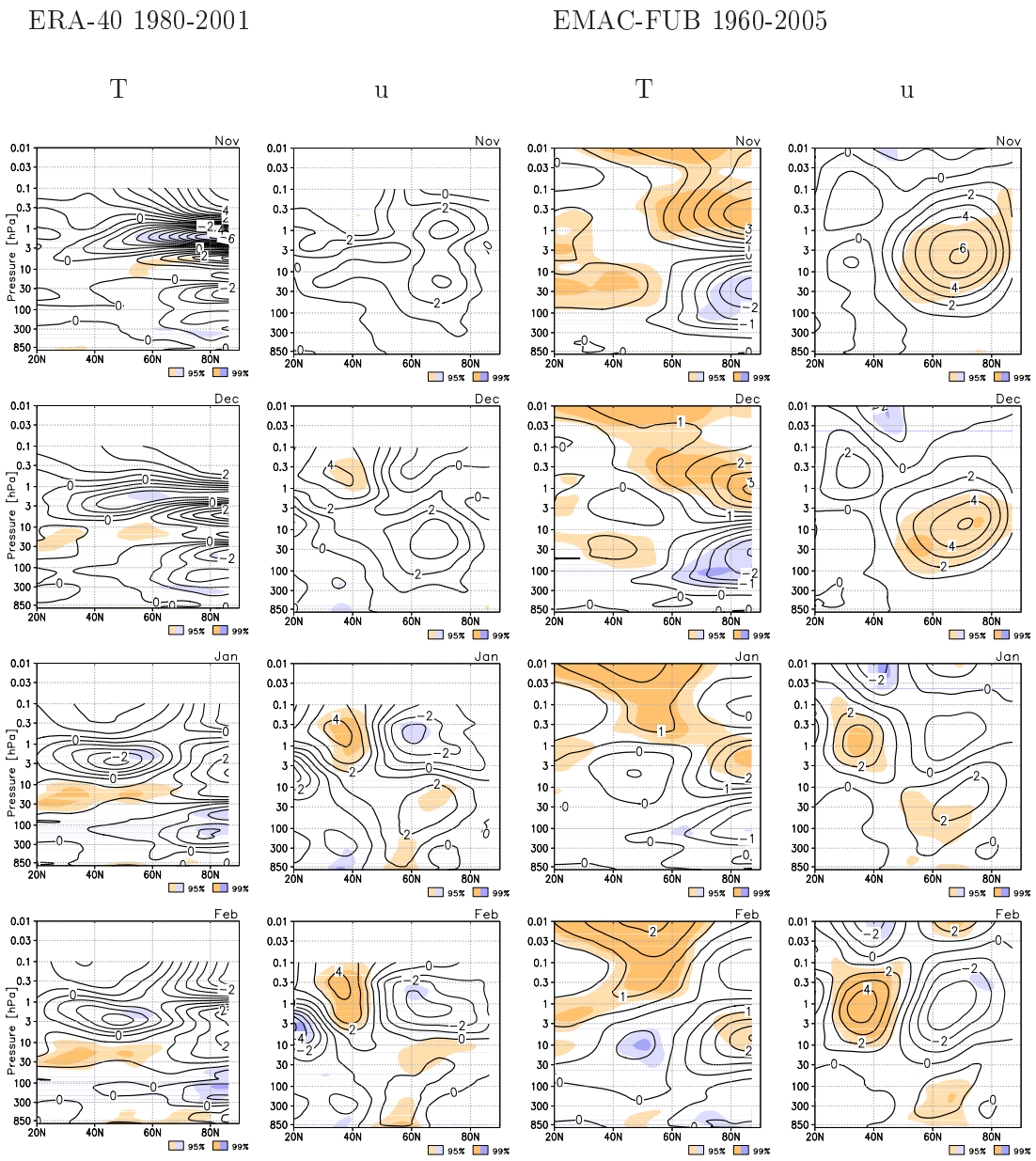


**Figure 8.3:** Monthly mean solar regression coefficient of zonal mean temperature and zonal mean zonal wind in the northern hemisphere from November to February (top to bottom). Left two columns: ERA-40 data from 1980 to 2001. Right two columns: EMAC-FUB REF-B1 simulation from 1960 to 2005. Contour interval is 0.5 K (1 m/s) per 100 units of F10.7, respectively. Light (heavy) shading indicates statistically significant changes at the 95(99) % level.

EMAC-FUB this signal is present as well but it becomes statistically significant first in January and is slowly displaced downward towards February. A solar influence on the mesospheric subtropical jet was reported by Kodera and Kuroda (2002) and Kodera et al. (2003) who found a longer lasting increase and ultimately higher maximum wind speeds of the westerlies in this region in solar maximum years, whereas, the increase of wind speed is interrupted and transformed into a decay in solar minimum winters. Compared with earlier GCM simulations (Kodera et al., 2003) the results obtained with EMAC-FUB

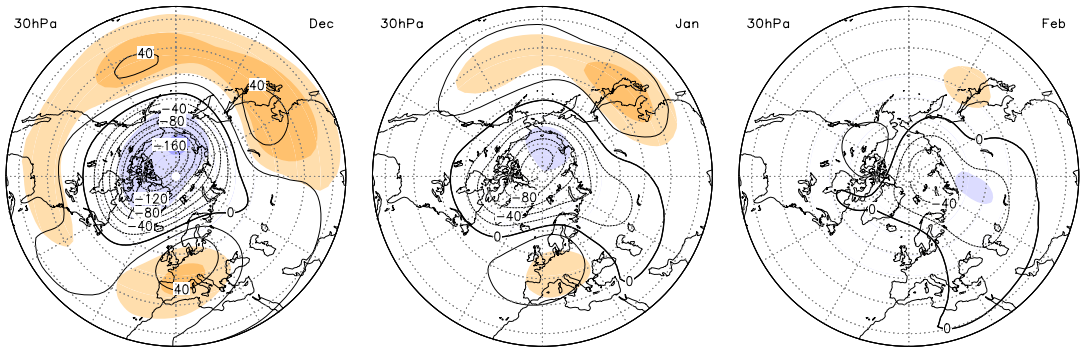


**Figure 8.4:** Monthly mean solar regression coefficient of geopotential height from 20 °N to 90 °N at 30 hPa in gpm per 100 units of F10.7, contour interval is 20 gpm. Light (heavy) shading indicates statistical significance at the 95(99) % level.

are an improvement.

However, when compared with the observational composits of Kodera and Kuroda (2002) the modelled zonal wind signal in early winter is situated too far north in EMAC-FUB and ERA-40. While the anomalies in Figure 8.3 propagate downward Kodera and Kuroda (2002) report a simultaneuos poleward and downward displacement. A possible reason for this discrepancy may lie in the different analysis approaches, multiple linear regression versus composite differences.

The described solar signal in the zonal mean zonal wind suggests the existence of a coherent signal in geopotential height. Figure 8.4 displays the solar term from the regression results for the 30 hPa-level in the lower stratosphere and the 500 hPa-level in the mid-troposphere. A clear and persistent signal is visible in the lower stratosphere. The region in vicinity of the pole shows lower geopotential height at higher solar activity in all three winter months. This region is surrounded by a belt of positive anomalies, i.e., the 30 hPa-level is situated higher at solar maximum than at solar minimum. The statistical significance of both the negative and positive anomalies is strongest in early winter and declines towards February. In December and January two regions with positive anomalies can be identified. One is over western and central Europe and the adjacent North Atlantic Ocean and another one over the North Pacific and Japan. The latter is still present in February.

The solar signal in geopotential height shows the spatial structure of the Northern Annular Mode (NAM) in its positive phase which is characterised by lower than average geopotential heights near the pole surrounded by greater than average heights at mid-latitudes. A manifestation of the solar signal with this positive NAM pattern has been found in observations (Kuroda and Kodera, 2002) as well as in CCM (Tourpali et al., 2005) and GCM (Matthes et al., 2006) studies. In particular, the decay of the pattern in February agrees with the composite analyses of observational data by Kuroda and Kodera (2002).

*Planetary wave activity*

The hitherto shown 11-year solar cycle influence on the stratospheric geopotential height, zonal wind and temperature may lead to the anticipation that also the propagation of planetary waves is affected by the solar irradiance changes. This is investigated with the help of the Eliassen-Palm-Flux (EP-flux) which is a useful diagnostic tool for the propagation of plantary waves in the latitude-height-plane. The vertical component of the EP-flux is associated with the northward eddy heat transport and the horizontal component with the northward eddy momentum flux. It should be mentioned that the TEM variables are computed on a 6-hourly basis and, subsequently, averaged to monthly means.

The 11-year solar cycle induced EP-flux anomalies for the months of December, January and February are displayed in the top row of Figure 8.5. Throughout the winter an anomalously downward directed EP-flux is seen at high latitudes from the lower stratosphere up to the mesosphere. This implies a weaker than average northward heat transport. This is consistent with the negative geopotential height anomalies at high latitudes (cf. Figure 8.4) which are evidence of cooler than average air columns below the considered pressure level. The horizontal component of the EP-flux which is in the climatological mean directed towards the equator is reduced at higher solar activity. Together

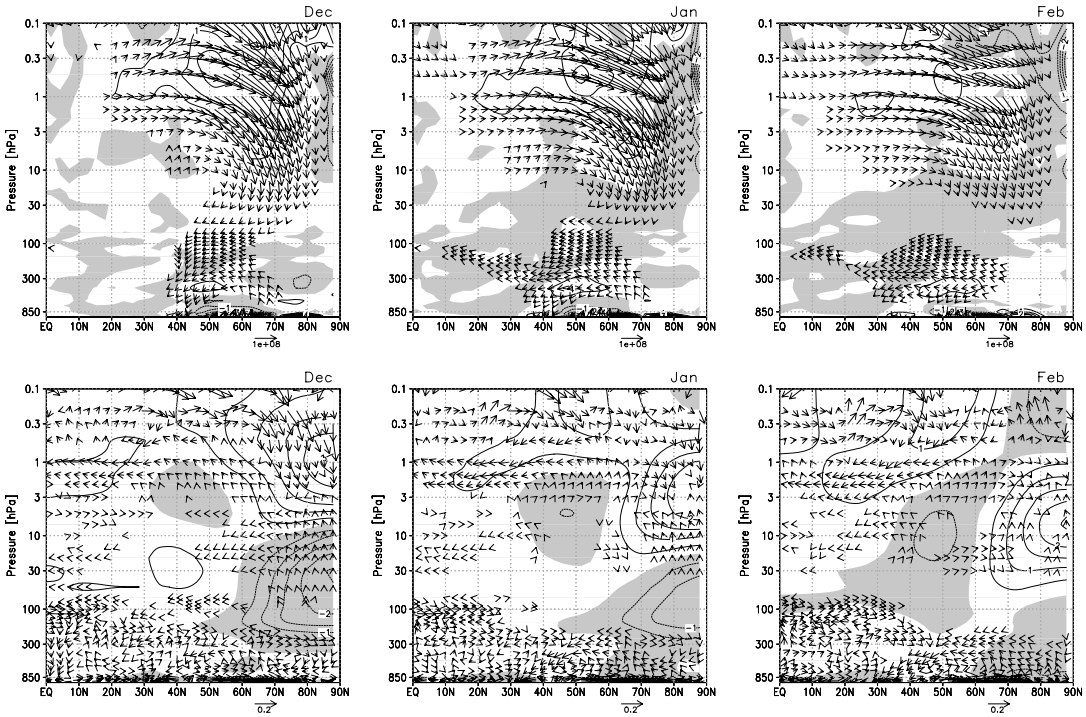


**Figure 8.5:** Top: Northern hemisphere monthly mean solar regression coefficient of the EP-flux in m/s$^2$ (arrows) and the EP-flux divergence (contours, anomalous convergence is shaded). Bottom: Monthly mean solar regression coefficient of the residual mean meridional circulation $\overline{v}^*$ and $\overline{w}^*$ (arrows) and the zonal mean temperature (contours, negative temperature anomalies are shaded).

this indicates weaker than average wave activity in the winter hemisphere which is also consistent with the stronger zonal mean zonal wind in early and mid winter (Figure 8.3). Compared with solar induced EP-flux anomalies that were derived from observational data (Kuroda and Kodera, 2002) there is general agreement.

The EP-flux divergence is a measure for the interaction of planetary waves with the mean flow. Climatologically there is a convergence of EP-flux in the mid-latitude mesosphere throughout the winter with a decreasing tendency towards late winter. According to 3.9 a convergence implies a weakening of the mean flow. The contours in the top panels of Figure 8.5 show an anomalous divergence in the mid- to high latitude upper stratosphere and mesosphere in December and January, i.e., an absolute weaker convergence at higher solar activity. This is consistent with the reduced wave activity in the stratosphere and the accelerated zonal mean zonal wind. The signal looses strength in February. An increasing region of anomalous divergence is seen at mid-latitudes in the middle and upper troposphere. To the south of it, i.e., in the subtropics an anomalous convergence develops in January and February. This reflects the downward propagation of the stratospheric zonal wind anomalies and the poleward shift of the tropospheric jet that was already seen in Figure 8.3.

The interaction of planetary waves with the mean flow drives the residual mean meridional circulation (MMC) in order to re-establish thermal wind balance. During northern winter the climatological MMC has its main upwelling branch in the tropics and in the southern hemisphere. The air is then transported northward in the upper stratosphere and mesosphere and the descending branch is found over the winter pole. Apart from this main branch there is northward transport and subsidence taking place at lower altitudes and at mid-latitudes. Against this background state the solar signal as displayed in the bottom row of Figure 8.5 implies a weakening of the MMC in the stratosphere which manifests itself in a reversed anomalous circulation. This is particularly pronounced in early winter. The weaker MMC is, moreover, consistent with the solar signal in zonal mean temperature which is indicated by grey shading (anomalous cooling) and contours in the Figure. Regions of anomalous cooling coincide with upward directed anomalies in the MMC and vice versa, regions that are warmer than average at high solar activity are characterised by an anomalous downwelling of the MMC. The negative temperature anomaly emerges, thus, by reduced downwelling, and the positive temperature anomaly develops as a consequence of enhanced downwelling. The temperature anomaly pattern moves downward as the winter proceeds.

**Southern winter and spring**

In observations, there is a significant solar signal in zonal mean zonal wind and zonal mean temperature in southern winter and spring from June to September (see the first two columns of Figure 8.6). At higher solar activity the westerly winds at mid-latitudes are strengthened and poleward of about 60 °S there is an easterly anomaly, indicating

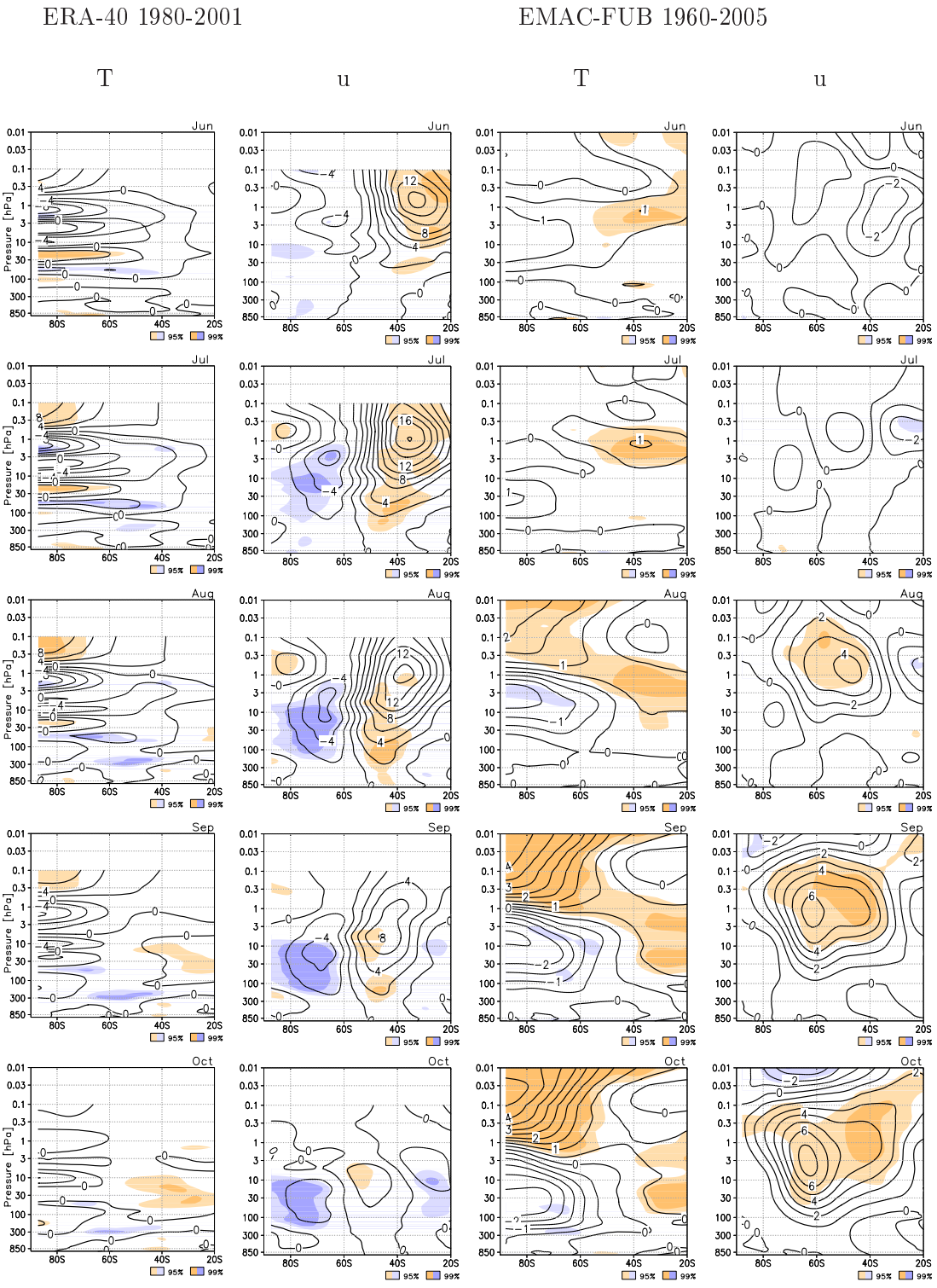


**Figure 8.6:** Monthly mean solar regression coefficient of zonal mean temperature and zonal mean zonal wind in the southern hemisphere from June to October (top to bottom). Left two columns: ERA-40 data from 1980 to 2001. Contour interval is 2 K (2 m/s) per 100 units of F10.7 flux, respectively. Right two columns: EMAC-FUB from 1960 to 2005. Contour interval is 0.5 K (1 m/s) per 100 units of F10.7, respectively. Light (heavy) shading indicates statistical significance at the 95(99) % level.

weaker absolute zonal mean zonal winds. The modelled solar signal in the southern hemisphere is most pronounced in late winter and spring, about two months later than in the observations. The modelled response is, furthermore, weaker (cf. the last two columns of Figure 8.6). The initial significant westerly zonal mean zonal wind anomaly appears in the model in August as compared to May (not shown) and June in the ERA-40 data. The anomaly intensifies and propagates poleward and downward with time. Similarly does the dipole temperature anomaly pattern intensify and descend from August to October. The anomalies of zonal mean temperature and zonal wind are also present in the troposphere down to the surface in September and October but without being statistically significant. The observations show a stronger and statistically significant westerly zonal wind solar signal in the troposphere all the way down to the surface in August, i.e., in late winter.

The appearance of the strongest solar induced anomalies in late winter and spring is also different from the northern hemisphere where the signal is strongest in early and mid winter in the stratosphere and in mid and late winter in the troposphere.

The solar signal in southern hemisphere geopotential height is qualitatively similar to its northern hemisphere analogue, but it is more intense, as can be seen from Figure 8.7, in particular in October and November. The polar vortex in the stratosphere is significantly deeper during solar maxima than during solar minima from September to December (not shown). The negative geopotential height anomaly near the south pole is surrounded by likewise significant positive anomalies at lower latitudes. This resembles the spatial pattern of the Southern Annular Mode (SAM). Kuroda and Kodera (2002) performing a composite analysis, i.e., solar max-min differences, of southern hemispheric geopotential height from observations (NCEP-CPC data from 1979 to 1999), report a similar positive SAM pattern in response to higher solar activity in the southern hemisphere stratosphere in September and October. In November the observed positive SAM anomaly is replaced by a negative SAM signal. This is not seen in the EMAC-FUB results which may be due to the delayed development of the solar signal in the model.

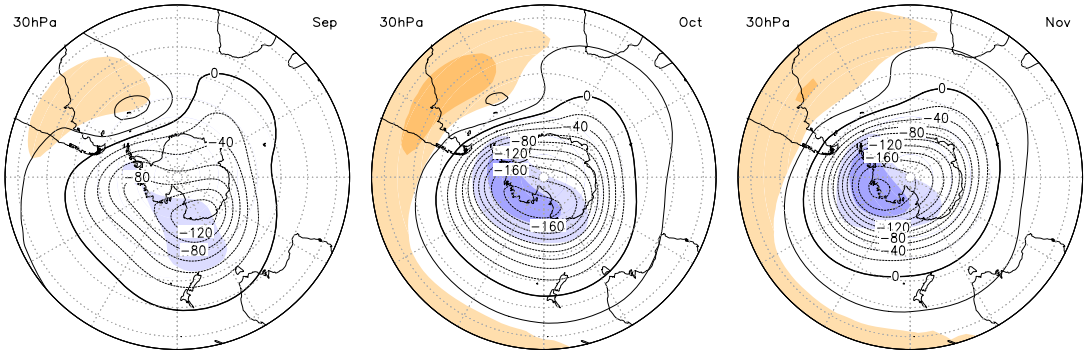


**Figure 8.7:** Monthly mean solar regression coefficient of geopotential height from 20 °S to 90 °S in September, October and November at 30 hPa in gpm per 100 units of F10.7, contour interval is 20 gpm. Light (heavy) shading indicates statistical significance at the 95(99) % level.

### 8.1.3 The solar signal in the troposphere

The solar cycle induced anomalies of zonal mean zonal wind and temperature as well as in geopotential height are all consistent with the indirect mechanism for solar influence on the atmosphere as proposed by Kodera and Kuroda (2002). The initial signal is transferred from the upper to the lower stratosphere by means of dynamical interactions involving changes in the propagation of planetary waves and the wave-driven mean meridional circulation. The focus in the current section is on the manifestation of 11-year solar cycle induced changes in the troposphere.

#### The signal in northern winter

As was seen in Figure 8.3 there is a significant zonal mean zonal wind signal in the troposphere in January and February which is relatively weak. It is possible that stronger statistically significant changes appear in the latitude-longitude plane. The lower panel of Figure 8.8 shows the solar signal in zonal wind at 500 hPa, a level in the middle troposphere at about 5.5 km. It is seen that already in December when the zonal mean signal is insignificant (Figure 8.3) there are statistically significant changes over Europe and the Mediterranean. More precisely, these changes imply an extension and northward shift of

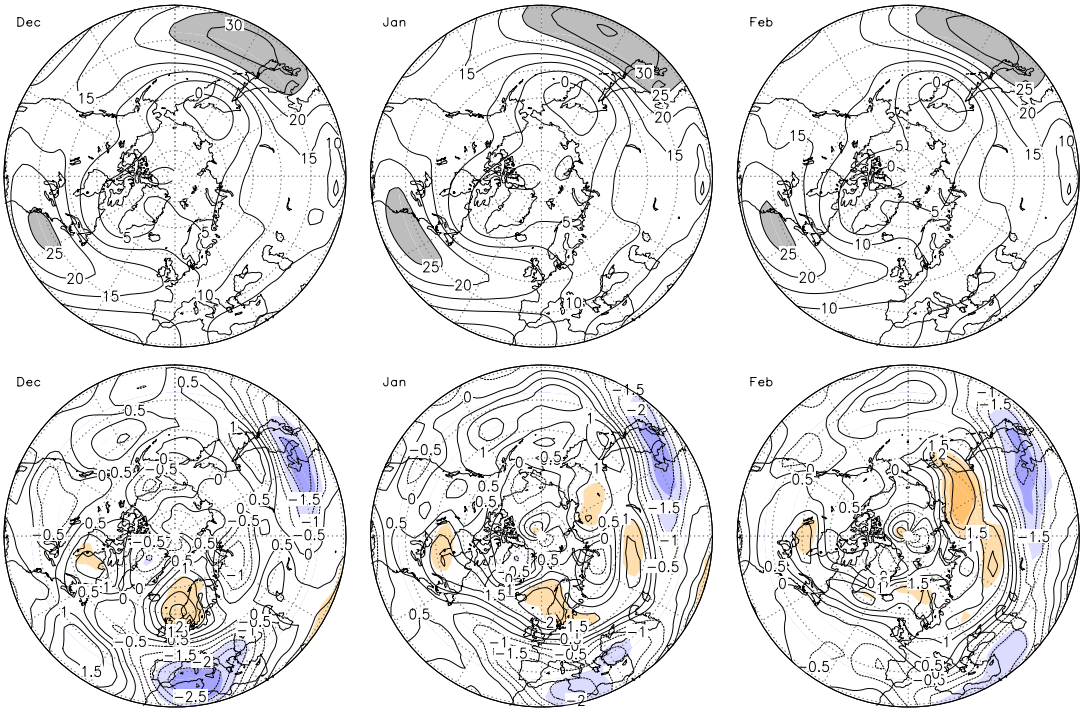


**Figure 8.8:** Top: Monthly mean long term mean zonal wind from 30 °N to 90 °N at 500 hPa in December (left), January (middle) and February (right). Velocities exceeding 25 m/s are shaded. Bottom: Monthly mean solar regression coefficient of zonal wind at 500 hPa in m/s per 100 units of F10.7, contour interval is 0.5 m/s. Light (heavy) shading indicates statistically significant changes at the 95(99) % level.

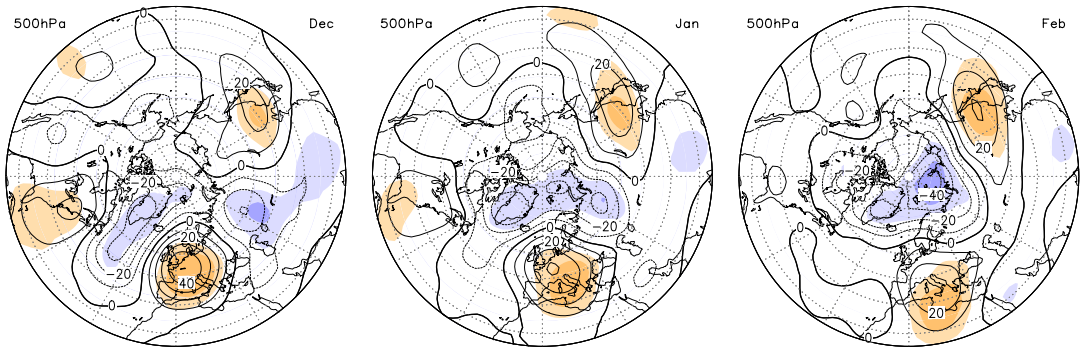


**Figure 8.9:** Monthly mean solar regression coefficient of geopotential height from 20 °N to 90 °N at 500 hPa in gpm per 100 units of F10.7, contour interval is 10 gpm. Light (heavy) shading indicates statistical significance at the 95(99) % level.

the strong westerly tongue associated with the North Atlantic polar jet stream (upper panel of Figure 8.8). Furthermore, the jet downstream of the Central Asian highlands is significantly weakened and, simultaneously, shifted polewards. Both the North Atlantic and the eastern Asian signal persist in January and February. While the North Atlantic signal looses strength the eastern Asian anomaly intensifies and is more pronounced in February.

The solar signal in geopotential height at 500 hPa (Figure 8.9) shows an evolution from a pattern with strong meridionally arranged positive and negative anomalies in December towards a state with more zonally arranged anomalies in February. The European anomaly that was seen in the geopotential height solar signal at the 30 hPa-level (Figure 8.4) is also present in the mid-troposphere. It persists in February when the stratospheric signal has deteriorated. Furthermore, it is seen that the tropospheric pattern in February has a similarity to the stratospheric signal one month earlier in January. The time lag of one month until a stratospheric anomaly has propagated to the troposphere was noted earlier by Kuroda (2008), Matthes et al. (2006) and Kuroda and Kodera (2002). A comparison with the zonal wind changes (Figure 8.8) reveals that it is the strong and significant positive anomaly in geopotential height over Europe that shifts the storm tracks northward. The Asian anomaly over Japan and the Japanese Sea intensifies from December to February which coincides with the northward shift of the polar jet that was seen in the same region and that likewise undergoes an intensification over the course of the winter. The tropospheric geopotential height anomalies in January and, in particular, in February can be interpreted as a positive NAM phase with lower than normal heights over the pole and higher than normal values over Europe and eastern Asia.

The solar cycle induced changes in the geopotential height and zonal wind suggest significant changes in lower tropospheric temperature. The analysis of the zonal mean fields (Figure 8.3) already yielded a statistically significant signal in the near-surface temperature in February. The longitudinally resolved solar signal in near-surface temperature is shown in Figure 8.10. In December a statistically significant positive temperature

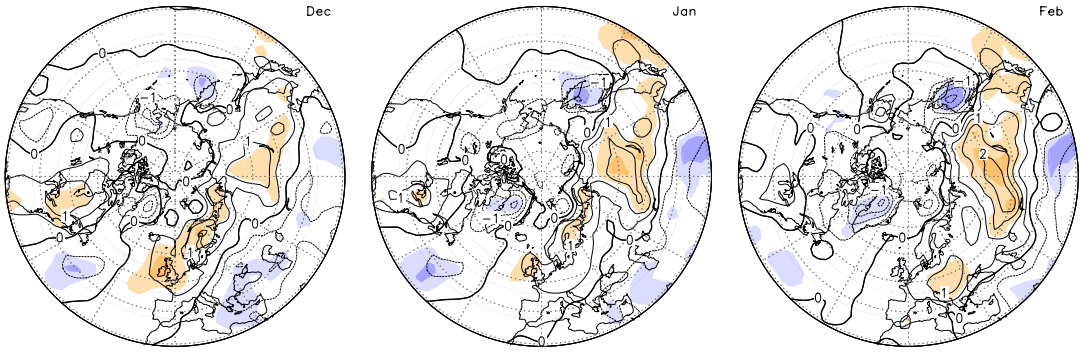


**Figure 8.10:** Monthly mean solar regression coefficient of temperature from 30 °N to 90 °N at 1000 hPa in K per 100 units of F10.7, contour interval is 0.5 K. Light (heavy) shading indicates statistical significance at the 95(99) % level.

anomaly is seen over north western Europe. This is the region where the zonal winds increase under solar maximum conditions indicating a northward deflection of the North Atlantic cyclone track. Cyclones tend to transport relatively warm marine airmasses from the ocean towards the continent and that precisely is seen in the December panel of Figure 8.10. Other regions with significantly higher temperatures at higher solar activity are central Asia and eastern North America. Lower temperatures are found downstream of the Asian and North American land masses as well as over the eastern Mediterranean and the Black Sea. This pattern remains basically unchanged in January but the significance of some anomalies declines. In February the significant positive anomaly from north western Europe has moved southwards being now situated over central and (south) eastern Europe. The central and eastern Asian anomaly pattern persists largely at the same position as in January.

The transfer of the solar signal from the stratosphere to the troposphere and the presence of a statistically significant signal in the troposphere in late northern winter in observational data was reported by Kuroda and Kodera (2002). Matthes et al. (2006) obtained a corresponding tropospheric signal in geopotential height and near-surface temperature in perpetual solar maximum and minimum GCM simulations. The new results from the more realistic transient EMAC-FUB CCM simulation confirm the earlier GCM results and are in general agreement with observations.

*Blocking frequency*

In consideration of the persistent positive geopotential height anomalies during periods of elevated solar activity in the mid-troposphere (see the lower panel of Figure 8.4) and the shifted cyclone track the question arises whether the solar cycle induced anomalies imply a change in the occurrence frequency of blockings. This issue has been discussed using observational data (Barriopedro et al., 2008) but never on the basis of a transient CCM simulation. The definition of blockings in this analysis is done according to Tibaldi and Molteni (1990). Instantaneous 12 UTC 500 hPa-gepotential height data from three

latitude belts are tested for a southern and a northern geopotential height gradient to fulfill certain conditions:

$$GHGS = \frac{Z(\varphi_0) - Z(\varphi_S)}{\varphi_0 - \varphi_S} > 0,$$

$$GHGN = \frac{Z(\varphi_N) - Z(\varphi_0)}{\varphi_N - \varphi_0} < -10 \frac{m/s}{\text{deg lat.}}.$$

The latitudes used for this analysis are $\varphi_N = 80\,°\text{N} + \Delta$, $\varphi_0 = 60\,°\text{N} + \Delta$ and $\varphi_S = 40\,°\text{N} + \Delta$, with $\Delta$ = -5 °, 0 °, +5 °. A blocking is detected at a given longitude if the criteria are fulfilled for at least one value of $\Delta$. The evaluation of observational data shows that blockings occur most frequently over the eastern North Atlantic and Europe as well as over the eastern and western North Pacific (Tibaldi and Molteni, 1990; Croci-Maspoli et al., 2007).

For the analysis of a possible solar influence only blocking episodes that last for at least 5 consecutive days and that cover a longitude range of at least 11.25 ° were taken into account. In this study only the winter season from December to March is considered. The blocking frequency is then defined as the number of blocked days relative to the total number of days per winter and is expressed in per cent. Solar maximum and minimum composites are formed by selecting winters with a DJFM-average F10.7 cm radio flux above (below) 150 (80) solar flux units. This results in 14 (11) winters in each group.

Figure 8.11a shows the longitudinal distributions of the solar maximum and minimum blocking freqency. The largest differences are found in the Pacific sector east of the date line as well as over the western Atlantic. However, the year-to-year variability of the blocking frequency is high. Therefore, the differences are statistically not significant. A comparison with the results Barriopedro et al. (2008) who analysed 44 winters based on NCEP/NCAR reanalysis data reveals a generally lower frequency of persistent blockings in EMAC-FUB. Furthermore, the Pacific peak exceeds the maximum over the Atlantic while the opposite is seen in the reanalyses. The tendency of blockings to occur farther east under solar maximum conditions than under solar minimum conditions that was shown by Barriopedro et al. (2008) can be retrieved in the model only in the eastern Pacific region near 150 °W. EMAC-FUB does not simulate an increase in blocking frequency when the solar activity is low. This is possibly due to the lower number of solar minimum winters in the model analysis.

The QBO phase determines the propagation region of planetary waves in the stratosphere. The waves emanating from the northern hemisphere mid-latitudes can cross the equator during QBO west phases but are confined to the northern hemisphere during QBO east phases. This may lead to a cold and undisturbed stratospheric polar vortex (QBO west) or to a relatively warm and disturbed vortex (QBO east). The 11-year solar cycle modulates this relationship, known as Holton-and-Tan relationship (Holton and Tan, 1980). It is, thus, conceivable that the solar influence on the blocking frequency

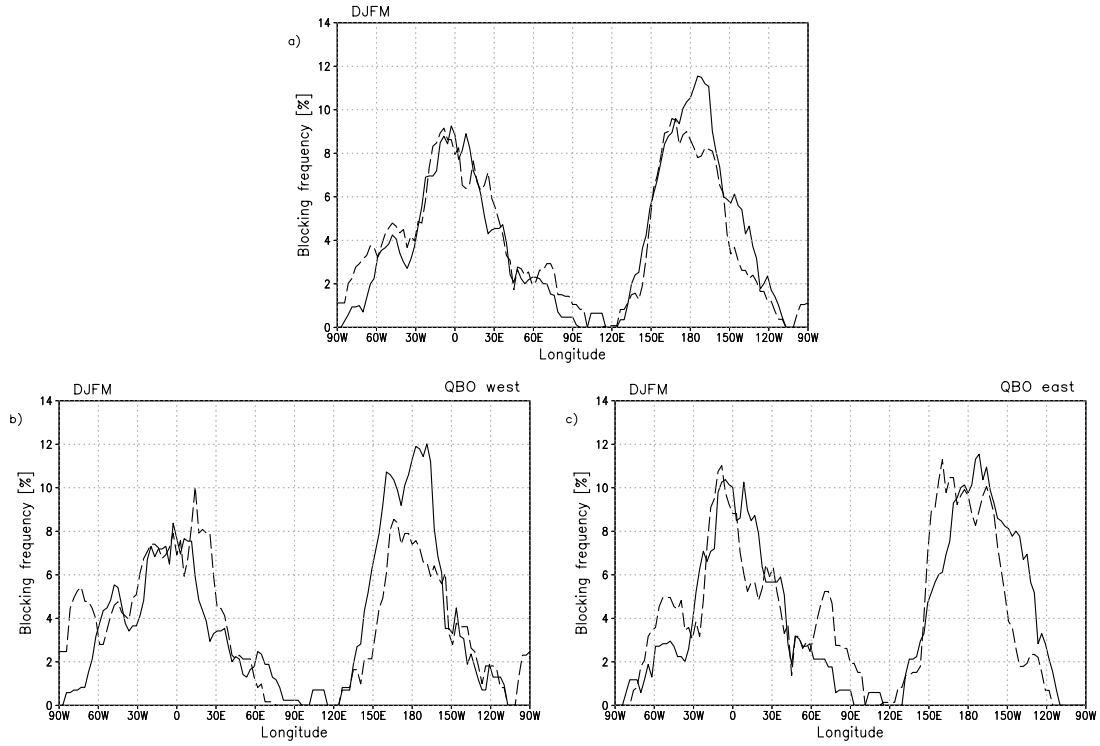


**Figure 8.11:** Blocking frequency for the extended winter period from December to March at 500 hPa in %. Solid lines: Solar maximum, dashed lines: Solar minimum. a) Without QBO stratification, b) QBO west phase, c) QBO east phase.

becomes more pronounced when the data are stratified according to the QBO phase. The stratification criterion used here is the DJFM zonal mean zonal wind at the equator at 50 hPa. This yields 7 (5) QBO west solar maximum (minimum) winters and 7 (6) QBO east solar maximum (minimum) winters.

The composite mean blocking frequencies are depicted in Figures 8.11b and 8.11c. In comparison to the unstratified distributions (Figure 8.11a) there is an eastward shift of the maximum blocking frequency in the Atlantic/European sector when solar activity is low and the QBO is westerly. The opposite is seen when the solar activity is low and the QBO is easterly, i.e., blockings over western Europe occur more frequently under solar maximum conditions and QBO east phases. The location of the Pacific peak under solar maximum conditions is essentially unaffected by the QBO. However, the solar minimum response of blocking frequency is different when the QBO is westerly or easterly. It is a reduction compared to solar maximum at QBO west and a westward shift at a comparable level in QBO east winters. Due to the additional QBO stratification the number of years in each class is further reduced. Nevertheless, some regions can be found where the differences between the solar maximum and minimum blocking frequency distributions are marginally statistically significant on the 90 %-level, e.g., near 150 °W (not shown). The location of the Pacific maximum farther to the east during winters characterised by high solar activity compared to winters in solar minimum periods when the QBO is in

its westerly phase is in qualitative agreement with the reanalysis results of Barriopedro et al. (2008). The solar signal in blocking frequency over the Atlantic and western Europe under QBO west conditions is also similar to the findings by Barriopedro et al. (2008) who report the strongest signal in late winter. For the QBO east phase Barriopedro et al. (2008) notice a response that resembles the solar signal regardless of the QBO. In comparison EMAC-FUB simulates more frequent blockings in the Atlantic/European sector when the QBO is easterly than when it is westerly or not considered at all.

*Excitation and propagation of planetary waves*

In the stratosphere in the latitude-height plane significant changes of variables associated with the propagation and the dissipation of planetary waves were noted (cf. Figure 8.5). The 11-year solar cycle influence on the tropospheric geopotential height and blocking frequency shown above likely also affects the excitation and propagation of planetary waves in the troposphere. This is investigated with the help of the Plumb-flux which is a generalisation of the EP-flux and is a useful diagnostic tool for the propagation of stationary waves in three dimensions (see section 3.3 for details). The Plumb-flux was computed using daily data and, subsequently, analysed on a monthly basis.

In northern winter the climatological horizontal Plumb-flux in the mid-troposphere is largest over the eastern North Pacific as well as over the North Atlantic and Europe, in general downstream of the strongest zonal winds (left column of Figure 8.12). The flux is directed upwards basically everywhere in the northern hemisphere. The strongest upward directed wave activity is found over the North Pacific and the North Atlantic, as indicated by the contours in Figure 8.12 (left column). The solar signal in the horizontal Plumb-flux (right column of Figure 8.12) shows changes over the eastern North Atlantic and Europe. In their location and strength they are closely related with the geopotential height anomalies at 500 hPa (cf. Figure 8.9) which are likewise strong in December and January and decrease in strength in February.

The Plumb-flux anomalies over the North Atlantic and European sector in December and January are directed upward and southeastward. The horizontal anomaly implies an extension of the climatological Plumb-flux source region towards the northeast. The region of strongest upward directed wave activity is shifted from the central to the eastern North Atlantic. In contrast, the signal over the North Pacific becomes stronger towards February. The west-southwest-ward directed anomaly from the climatologically east-southeast-ward pointing Plumb-flux vector indicates a shift towards a more southward directed wave activity. Simultaneously, a negative anomaly of the Plumb-flux' vertical component implies less upward propagation and, thus, a decrease in stationary wave activity over the eastern North Pacific in mid- and late winter. On the other hand, there is enhanced upward directed wave activity over the North American continent and over north eastern Asia. All of the mentioned changes are statistically significant at least at the 95%-confidence level (not shown). According to McDaniel and Black (2005) these

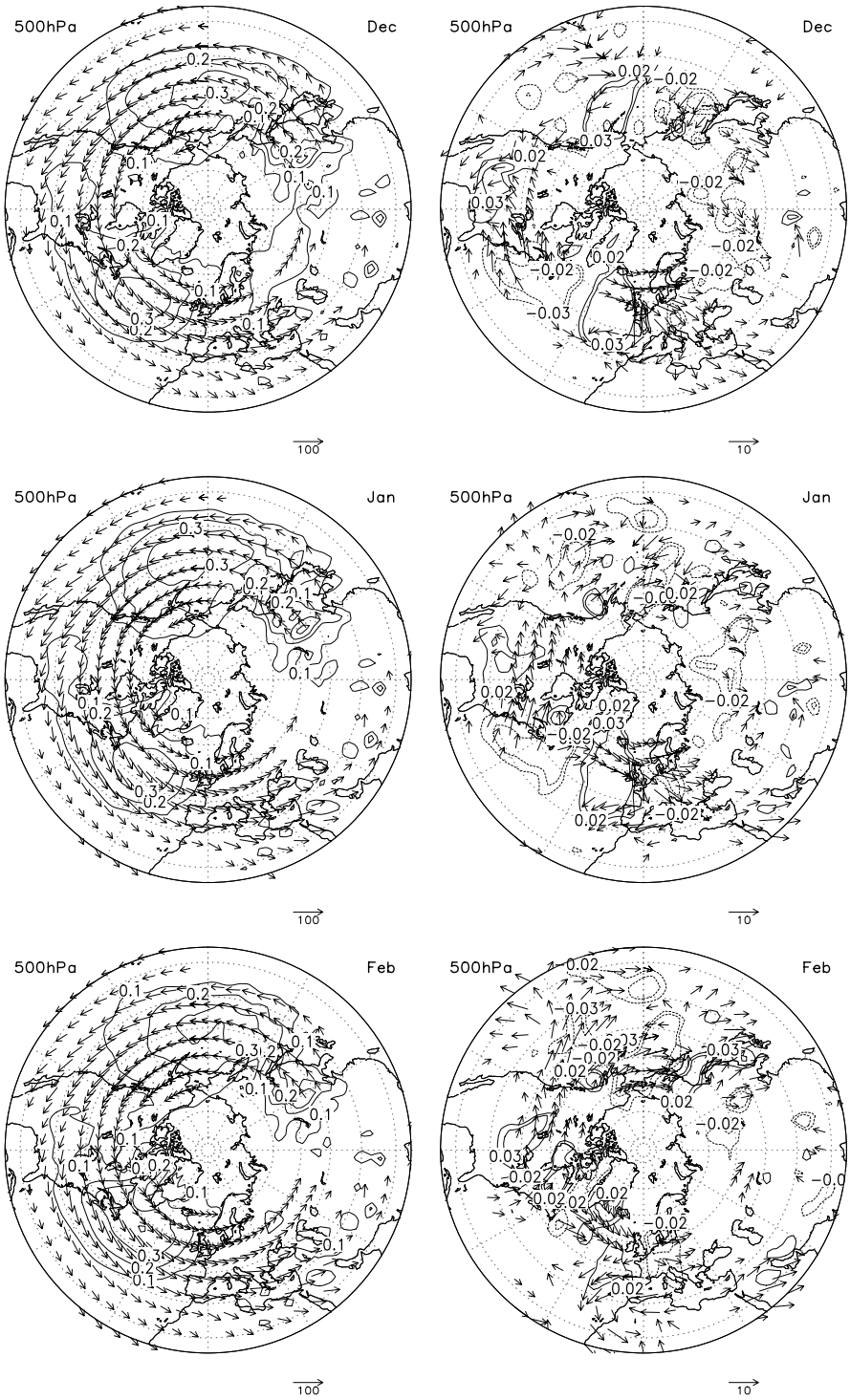


**Figure 8.12:** Monthly mean Plumb-flux from 20 °N to 90 °N at 500 hPa in m/s$^2$. Arrows: horizontal components, contours: vertical component. Left: long term mean field, right: Solar regression coefficient per 100 units of F10.7.

changes are typical during positive Northern Annular Mode (NAM) events. The geopotential height anomalies exhibit the spatial pattern of a positive NAM phase. Earlier, Kuroda and Kodera (2002) found very similar horizontal Plumb-flux anomalies in Jan-

uary and February at 500 hPa in their composite analysis of observed data from solar maximum and minimum.

From the polar stereographic plots in the left panel of Figure 8.12 it is visible that the climatological wave activity is directed upwards virtually everywhere in the mid troposphere. This is confirmed also for other tropospheric levels by the climatology of the vertical Plumb-flux in the longitude-height plane with latitude fixed at 51.5 °N (i.e., a latitude where distinct anomalies are seen in the right panel of Figure 8.12) which is displayed on the left hand side of Figure 8.13. The regions with the strongest upward directed wave activity are the Atlantic (0 °W to 70 °W) as well as eastern Asia and the Pacific (90 °E to 120 °W). However, the strong upward propagation of waves in the

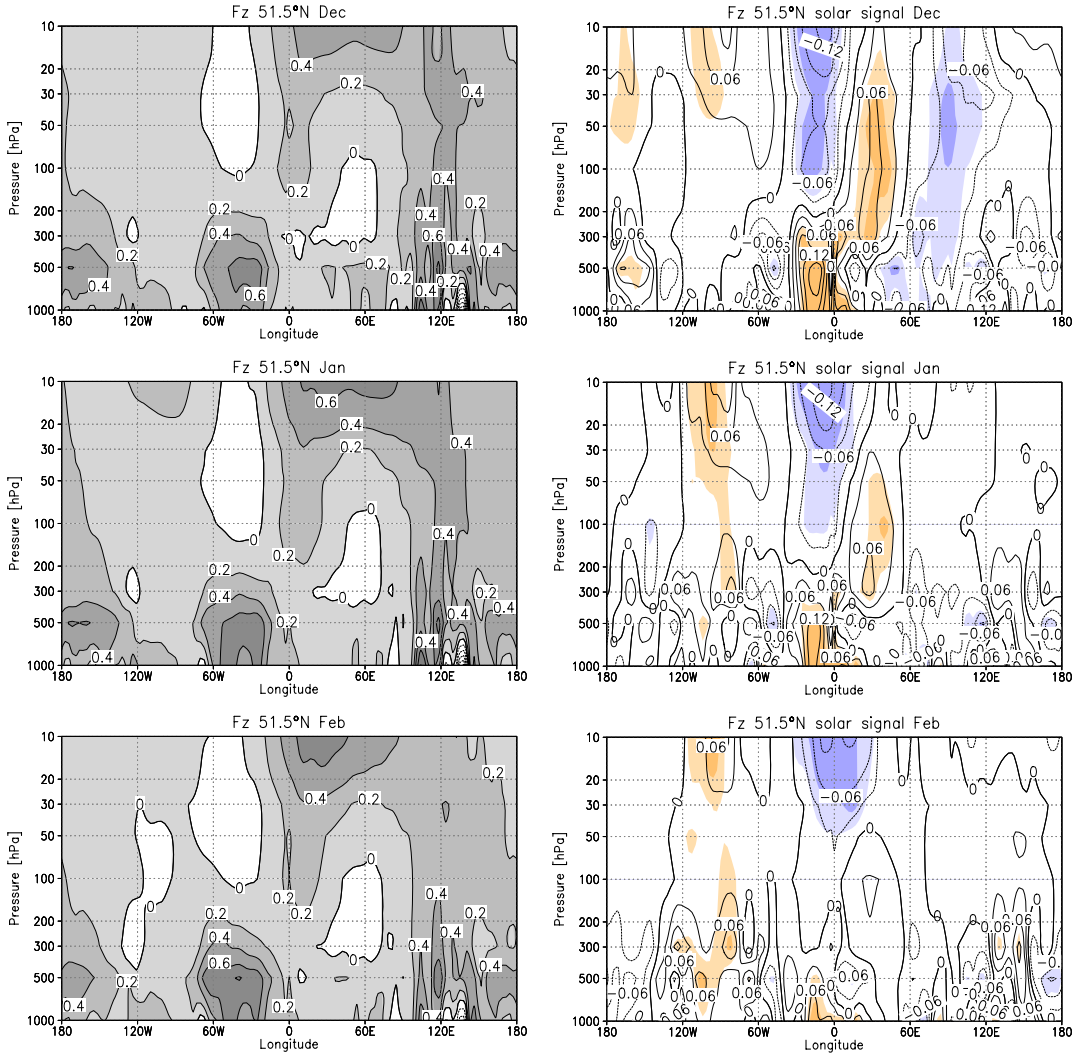


**Figure 8.13:** Longitude-height section of the Plumb-flux vertical component at 51.5 °N from December to February (top to bottom). Left: Monthly mean long term mean. The values are scaled by the inverse of pressure to highlight stratospheric patterns and are multiplied by 1000. Contour interval is 0.2, upward directed (positive) flux is shaded. Right: Monthly mean solar regression coefficient per 100 units of F10.7. Contour interval is 0.03. Light (heavy) shading indicates statistical significance at the 95 (99) % level.

Atlantic sector is confined to the troposphere. Waves emanating from this source region do not propagate directly upwards but enter the stratosphere farther east over western and central Europe. This configuration remains almost unchanged in December and January. In February a distinctly weaker upward propagation in the Pacific sector is noted and the waves are prevented from entering the upper troposphere and the stratosphere at about 120 °W, i.e., at the west coast of North America. The overall climatological patterns agree well with Plumb (1985).

The solar cycle induced changes in the upward Plumb-flux are presented on the right hand side of Figure 8.13. In early and mid-winter (December and January) the whole pattern of sources and upward propagation channels is shifted eastward at higher solar activity, in particular, this is true for the Atlantic and European sector where the changes are statistically highly significant. In late winter (February) the Atlantic/European signal looses strength as was already seen in the geopotential height anomalies (Figure 8.9) and in the Plumb-flux anomalies at 500 hPa (right panel of Figure 8.12). Conversely the solar signal in the Pacific sector increases in late winter, showing enhanced upward directed wave activity in the troposphere over north east Asia and the North American continent and a reduction of upward propagating waves over the Pacific. Significantly more waves can propagate upwards into the stratosphere over the North American continent where in the climatological mean a region without upward directed wave activity was seen.

Some features of the solar signal agree qualitatively with the picture shown by McDaniel and Black (2005) for positive NAM events, e.g., the significant downward anomaly over central Asia and the upward anomaly over the eastern Atlantic and the European continent in December. This fits well with the positive NAM-like pattern in the solar induced geopotential height anomalies in December (Figure 8.9).

*Upwelling in the tropics*

The solar signal in zonal mean monthly mean vertical velocity at 300 hPa does only show very weak and insignificant changes during northern winter indicating less upwelling to the south of the equator at higher solar activity, i.e., in the region of strongest upward motion in northern winter (not shown). Despite the weak signal in the zonal mean it is possible to find locally stronger signals which may cancel each other when averaged over latitude. Figure 8.14 presents the longitudinally resolved vertical velocity anomalies for December, January and February. Note that it is pressure velocity in Pa/s which is displayed in the figure, thus, absolute upwelling is represented by negative values and a positive anomaly implies a weaker upwelling whereas a negative anomaly stands for increased upwelling. The region of strongest upwelling follows the Sun's zenith point and is situated at about 15 °N and S during the solstice seasons (not shown) with distinct maxima over the South American, the African and the maritime continent. The solar signal in tropical upwelling manifests as a persistent tripole pattern over the Indian Ocean, the maritime continent and the western Pacific Ocean with significantly weaker than average updrafts over the Philippines and north eastern Australia. This is flanked by significantly

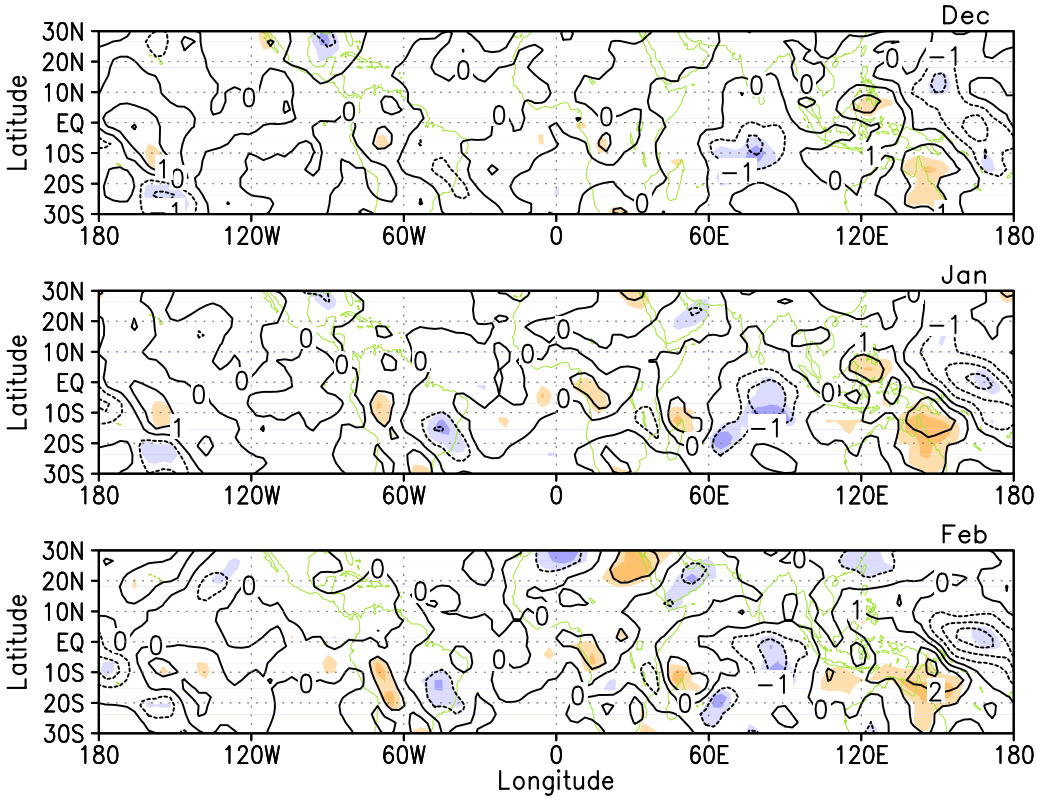


**Figure 8.14:** Monthly mean solar regression coefficient of vertical velocity at 300 hPa in Pa/s per 100 units of F10.7 multiplied by 100, contour interval is 1.0. Light (heavy) shading indicates statistical significance at the 95(99) % level.

stronger than average updrafts over the western Pacific and the Indian Ocean. The signals over the South American and African continent intensify from December to February. An intensification of tropospheric solar cycle manifestations was already noted in, e.g., the zonal mean zonal wind (Figure 8.3) or the near-surface temperature (Figure 8.10).

Closely connected with upwelling is the formation of convective precipitation so that one might expect to see a solar signal also in this quantity. Figure 8.15 shows the monthly mean solar regression coefficient along with the ENSO regression coefficient for January. In the same regions where upwelling is decelerated at solar maximum a reduction is seen in convective precipitation. Vice versa do areas with enhanced upwelling show an increase of convective rainfall at higher solar activity. The patterns persist throughout the three winter months as did the vertical velocity anomalies. The solar signal over the Indian Ocean, the Philippines, northern Australia and the western Pacific resembles in some aspects qualitatively the ENSO signal. For instance, there is more convective rainfall during ENSO warm events over the Indian Ocean and the equatorial western Pacific and reduced convective rainfall over Indonesia and east of the Philippines. However, the enhanced precipitation during warm ENSO phases stretches out all the way to the eastern Pacific and the coast of South America which is not seen in the solar signal. In contrast to the ENSO signal, the solar signal is in most regions statistically not significant, possibly

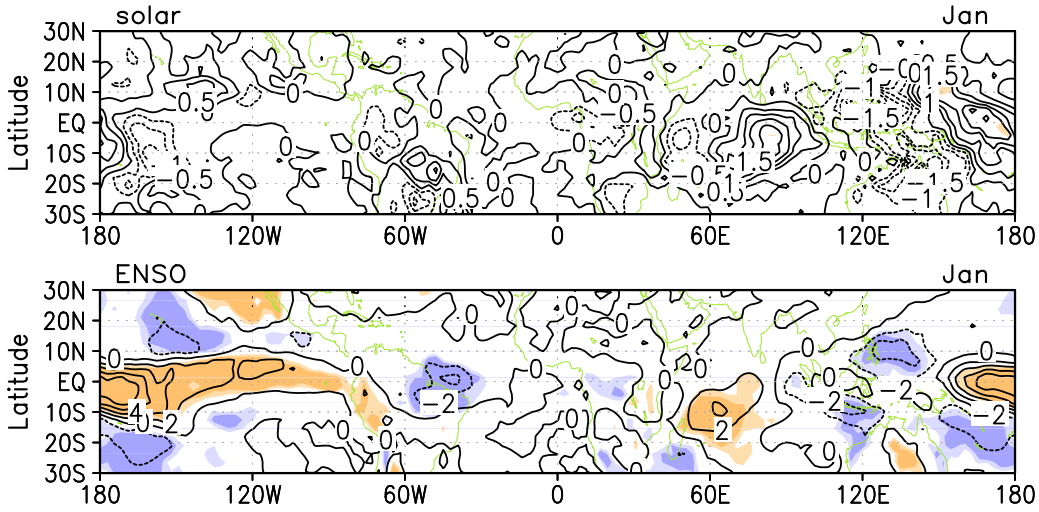


**Figure 8.15:** January monthly mean regression coefficient of convective precipitation. Top: solar term in mm/day per 100 units of F10.7, contour interval is 0.5 mm/day, Bottom: ENSO term in mm/day per 2 units Niño3.4 index, contour interval is 1 mm/day. Light (heavy) shading indicates statistical significance at the 95(99) % level.

due to the few 11-year solar cycles (4 1/2) that occurred in the considered period from 1960 to 2005.

### The high-latitude signal in southern winter

From September and forward significant SAM-like geopotential height anomalies were found at 30 hPa (cf. Figure 8.7). The pattern penetrates from the middle stratosphere down to the middle troposphere within about one month (Figure 8.16), i.e., the SAM-like anomalies appear one month later at 500 hPa in October and persist in November. In December the pattern decays in the stratosphere but persists in the troposphere (not shown). Kuroda and Kodera (2002) found a solar signal which consists of a negative anomaly surrounded by positive anomalies, i.e., a SAM pattern in the positive phase

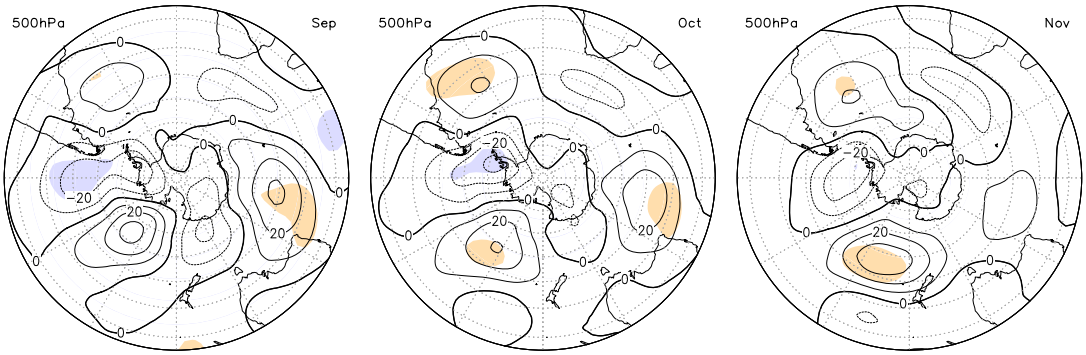


**Figure 8.16:** Monthly mean solar regression coefficient of geopotential height in September, October and November at 500 hPa in gpm per 100 units of F10.7, contour interval is 10 gpm. Light (heavy) shading indicates statistical significance at the 95(99) % level.

of the annular mode. The depression was found to be connected from the troposphere (500 hPa) to the upper stratosphere in October. This result is very similar to the one seen in the October panels of Figures 8.7 and 8.16 obtained from the CCM simulation. Moreover, Kuroda and Kodera (2002) found the negative signal in the mid-troposphere in vicinity to the Antarctic Peninsula with positive anomalies to the east and to the west and persistent also in November. A similar pattern is seen in Figure 8.16 in October and November. The persistence of the tropospheric signal when the stratospheric signal has disappeared is comparable in the simulation and in the reanalyses.

### The tropical signal in northern summer

In late northern summer (August) there is a reduction in upwelling north of the equator and an enhanced upwelling at the equator. This signal is zonally symmetric and, therefore, also found in the zonal mean (not shown). The longitudinally resolved pressure velocity anomalies are displayed in Figure 8.17. Note that absolute upwelling is represented by negative values and a positive anomaly implies a weaker upwelling whereas a negative anomaly stands for increased upwelling. Over the Indian Ocean, Southeast Asia and the Pacific Ocean there is in terms of absolute values a wide region of upward motion which reaches from about 20 °N to 10 °S, i.e., unusually far south in view of the solar zenith being situated north of the equator in August and also compared to other regions of upwelling.

The solar signal in upwelling and convective precipitation over the Indian Ocean sector in August is displayed in more detail in Figure 8.18. It implies an enhanced upward motion at higher solar activity at the equator which is statistically significant. There is a significant upward anomaly over the southern edge of the Arabian peninsula and the Red Sea. Another upward anomaly, but statistically insignificant, is found over the Indian subcontinent. This pattern is overall consistent with the results of Kodera (2004) who analysed the solar influence on the Indian Ocean Monsoon using NCEP/NCAR reanalysis data. Coincident with the positive upwelling anomalies there is enhanced rainfall during periods of higher solar activity along the Arabian peninsula's south-western coast which

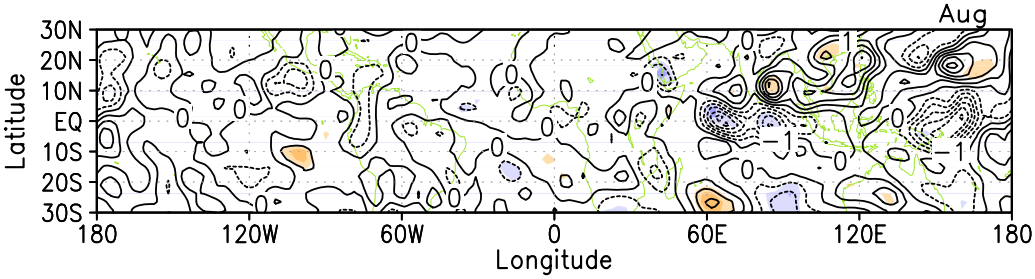


**Figure 8.17:** Monthly mean solar regression coefficient of vertical velocity at 300 hPa in Pa/s per 100 units of F10.7 multiplied by 100, contour interval is 0.5. Light (heavy) shading indicates statistical significance at the 95(99) % level.

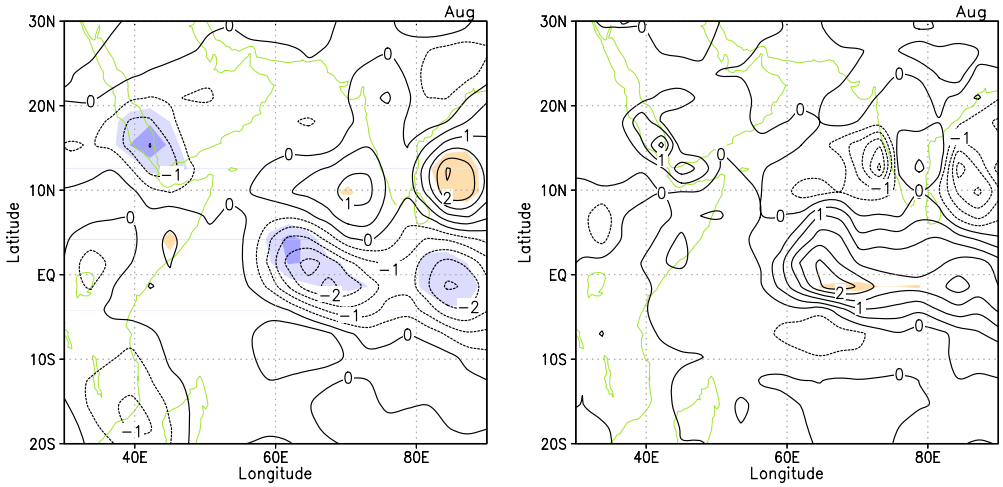


**Figure 8.18:** Monthly mean solar regression coefficient in August of vertical velocity at 300 hPa in Pa/s per 100 units of F10.7 multiplied by 100 (left) and convective precipitation in mm/day per 100 units of F10.7 flux (right), contour interval is 0.5. Light (heavy) shading indicates statistical significance at the 95(99) % level.

agrees with paleoclimatic records in this region (Kodera, 2004). However, the modelled signal in this region is statistically not significant. The only significant positive convective precipitation anomaly is found near the equator. The solar influence on the Indian summer monsoon and the role of the SSTs for the appearance and the strength of the signal is further investigated in section 8.5.

Beyond the signal over the Indian Ocean there are significant changes in upwelling seen over Central America and near the international date line in July (not shown). Both signals are present in August as well, but they have lost there significance. The meridional dipole pattern near the date line in Figure 8.17 is evidence for a northward shift of the strongest upwelling.

### 8.1.4 Summary and Discussion

In the above sections the ability of the EMAC-FUB CCM to simulate an 11-year solar signal which is overall consistent with observations has been demonstrated. Annual mean short-wave heating rates are enhanced by up to 0.14 K/day per 100 units F10.7 cm solar radio flux in the stratopause region. The ozone response with maxima of about 2 to 2.5% per 100 units F10.7 cm solar radio flux at mid-latitudes in the upper stratosphere is of reasonable magnitude. However, a secondary ozone response maximum in the tropical lower stratosphere is not simulated by EMAC-FUB. Temperature responds to the solar irradiance changes with an increase of about 0.8 K per 100 units F10.7 cm solar radio flux in the mid-latitude stratopause region. In the tropical stratosphere the model underestimates the solar cycle induced temperature change which may be related to interactions between the 11-year solar cycle and the QBO which are difficult to separate.

During the dynamically active winter seasons on both the northern and the southern hemisphere when troposphere-stratosphere coupling allows a two-way interaction between the layers, the 11-year solar signal can propagate from the lower mesosphere and upper stratosphere down to the troposphere and to the Earth's surface. In the transient EMAC-FUB simulation the tropospheric signal peaks in late winter, typically one month after the maximum response in the stratosphere. This confirms the results of Matthes et al. (2006) that were obtained for the northern hemisphere from GCM equilibrium simulations. Matthes et al. (2010) report a similar result for the southern hemisphere from equilibrium CCM simulations.

In the EMAC-FUB CCM simulation an initial westerly zonal wind anomaly in the upper stratosphere which is ultimately caused by stronger differential heating under solar maximum conditions moves downward over the course of the winter. It is accompanied by consistent temperature anomalies. This progress is in overall agreement with observational results as was shown in a comparison with the solar signal in ERA-40 data. The stronger westerlies of the polar night jet and the cooling in the polar lower stratosphere are associated with a positive annular mode-like anomaly pattern in the geopotential height which is charaterised by lower than average heights over the pole and higher than average values at mid- and low latitudes. Eventually, this implies a stronger polar vortex during periods of high solar activity.

The 11-year solar signal is present in the troposphere in all northern hemispheric winter months. It is intensified towards the late winter and becomes then also manifest in the zonal mean. The tropospheric jet is weakened and displaced polewards in solar maximum winters, in accordance with the mechanism that was proposed by Haigh et al. (2005). The crucial factor for this is a negative meridional temperature gradient in the lower stratosphere and upper troposphere. In the model this negative meridional temperature gradient does not appear so much because of a warming of the tropical lower stratosphere but rather due to a cooling of the polar lower stratosphere. The consequence is in any case a weakening and a poleward displacement of the jet and EMAC-FUB is able to simulate that. Compared with equilibrium CCM simulation results published by Schmidt et al. (2010) EMAC-FUB simulates a solar signal in the troposphere which is closer to observations.

In the longitudinally resolved picture it is evident that the zonal wind is most strongly affected by the solar influence in two regions: over western Europe and eastern Asia. The European anomaly implies a shift of the cyclone tracks towards higher latitudes in early winter at solar maximum. This has to be seen in conjunction with the appearance of a region of greater than average geopotential height over central Europe which is but one feature of the large scale changes associated with the descending positive Northern Annular Mode anomaly. The combination of shifted cyclone tracks and the greater than normal geopotential height leads to an anomalous upward directed stationary wave activity as indicated by the Plumb-flux. According to McDaniel and Black (2005) this is typical

for a positive phase of the Northern Annular Mode. The anomalous horizontal Plumb-flux in the mid-troposphere and the solar signal in the 500 hPa-geopotential height resemble the signal that was obtained from observations by Kuroda and Kodera (2002) with the difference of an eastward shift of the positive geopotential height anomaly over Europe in EMAC-FUB. Moreover, the solar signal in the 500 hPa-geopotential height confirms the (general circulation) model results of Matthes et al. (2006). The latter authors showed consistent near-surface temperature changes induced by the solar variability with significantly higher temperatures over northern Eurasia. These results can also be confirmed by the current EMAC-FUB simulation, especially in early winter. In connection with the persistent positive geopotential height anomaly over western and central Europe during solar cycle maxima winters an influence on the occurrence frequency of blockings may be conjecturable. However, this is difficult to detect due to high interannual variability. A stratification of the winters according to the QBO phase yielded, though, a shift in the preferred longitudinal location of blockings at solar maximum with more such events farther east during QBO east phases and a lower number of blockings over Europe during QBO west phases. These results are similar to those obtained from reanalysis data by Barriopedro et al. (2008).

The 11-year solar signal in the southern hemispheric winter months develops analogue to the signal in the northern hemisphere. Compared with observations the stratospheric solar signal in southern winter and spring is delayed by one to two months in the model. Despite this discrepancy there is a deep barotropic structure of geopotential height anomalies from the stratosphere to the troposphere in October in the model. A similar response was found in observations by Kuroda and Kodera (2002). The solar induced zonal wind changes at mid- to high latitudes affect the propagation conditions for planetary waves and, thereby, the mean meridional circulation in southern winter (not shown) in a similar way as they do during northern winter. In this way, the solar signal is conveyed to the tropical lower stratosphere. The presence of the tropospheric solar signal in EMAC-FUB in southern winter is an improvement compared to earlier (GCM) studies (Matthes, 2003) where an unrealistically strong southern polar night jet suppressed the weak solar signal in zonal wind and, thereby, also the modulation of the MMC and an effect on the tropical troposphere.

The tropical tropospheric response is particularly pronounced in the upwelling pattern associated with the Indian monsoon. Consistent with the observational analysis of Kodera (2004) a significantly enhanced upward motion is found over the Arabian peninsula and near the equator over the Indian Ocean while the upwelling is weaker over southern India which implies a weaker than average Hadley circulation during solar maxima. Other model studies with an AO-CCM (Shindell et al., 2006; Lee et al., 2009) arrived at a similar conclusion from analyses of lower tropospheric integrated specific humidity and upwelling in the tropics.

It has, thus, been shown that an 11-year solar signal may emerge in the tropsophere

as an indirect consequence of short-wave solar irradiance changes which affect primarily the stratosphere and initiate stratospheric circulation changes which in turn are transferred downward to the troposphere on a time scale of about one month.

## 8.2 The influence of the vertical resolution

A comparison of the 11-year solar signal in tropical stratospheric ozone and temperature in the reference simulation (Figures 8.1b and 8.2) with observational results (Figures 4.1, Randel and Wu (2007) and 4.2, Randel et al. (2009)) revealed a discrepancy in the vertical structure of the response. While the observed solar signal shows a statistically significant secondary peak in the tropical lower stratosphere the simulated response does not show such an increase in the lower stratosphere. Besides interactions between the solar influence and the QBO (Matthes et al., 2010) or the SSTs (Marsh and Garcia, 2007) a possible reason for the absence of the secondary peak in the model may be an insufficient vertical resolution in the lower stratosphere. Hence, it is an interesting question whether a simulation with an increased vertical resolution would yield an ozone and temperature response in the tropical lower stratosphere that is closer to observations.

Within the framework of the German Research Foundation's priority program "Climate And Weather of the Sun-Earth System (CAWSES)" the "Project on Solar Effects on Chemistry and Climate including Ocean interactions (ProSECCO)" is funded. It investigates the solar influence on the Earth's atmosphere, its composition and the circulation at time scales ranging from decades to centuries. It is driven by researchers at the Institut für Meteorologie at Freie Universität Berlin in co-operation with researchers at the Max-Planck-Institut für Chemie in Mainz, where the EMAC model and in particular the coupling tool MESSy was developed. The project partners in Mainz performed a CCMVal Reference B1 simulation (Eyring et al., 2008) with EMAC at a higher vertical resolution (90 layers instead of 39) covering the period from 1960 to 2000.

The 90-layer version has a more than doubled number of layers compared to the standard L39 version referred to as EMAC-FUB (These names, EMAC for the L90 version and EMAC-FUB for the L39 version are also used in the literature to distinguish both configurations, e.g., Austin et al., 2010.). The refinement of the vertical coordinate is most prominent from the troposphere up to the lower and middle stratosphere, as was shown in Figure 5.1. However, possible differences that appear between the EMAC simulation (L90) and the EMAC-FUB reference simulation (L39) cannot be ascribed solely to the higher vertical resolution. The reason is that EMAC uses two submodels to simulate the influence of precipitating charged particels on ozone which were not used in EMAC-FUB (see section 5.3.2 for details of the experimental set-up). Although, the strongest influence of particle precipitation is expected at high altitudes and at polar latitudes a propagation of the signal to lower latitudes or even to the lower atmosphere cannot be ruled out (Langematz et al., 2005).

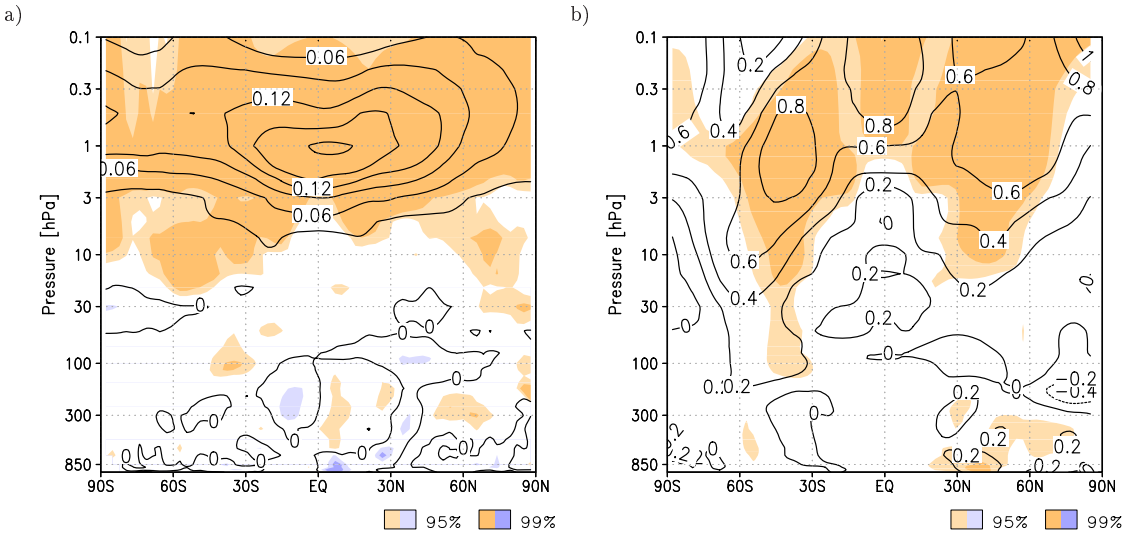


**Figure 8.19:** a) Zonal mean annual mean solar regression coefficient of short-wave heating rates in K/day, contour interval is 0.03 K/day per 100 units of F10.7 and b) Zonal mean annual mean solar coefficient of temperature in K, contour interval is 0.2 K per 100 units of F10.7. Light (heavy) shading indicates statistically significant changes at the 95(99) % level.

The SW heating rate, the temperature and the ozone response to the imposed irradiance changes in the simulation with higher vertical resolution are different from the signals in the reference simulation. The L90 simulation results are shown between the surface and the lower mesosphere (0.1 hPa). This limitation is due to an unrealistic ozone response in the mesosphere of the L90 simulation which is most probably caused by the usage of outdated rate constants for the reaction $H + HO_2$, depleting $HO_x$ by yielding $H_2$ instead of OH (Hack et al., 1978). The resulting underestimation of the OH abundance yields too much ozone in the upper mesosphere. Figure 8.19a shows the zonal mean annual mean response in short-wave heating which peaks at a value of about 0.18 K/day at the equatorial stratopause. This signal is statistically highly significant. Compared to the signal obtained from the reference simulation which comprises five more years (Figure 8.1) this value is higher. Even if the analysed period of the reference simulation is restricted to the years 1960 to 2000 the value from the L90 version is still higher (not shown). A reason therefor may be the equator-centred ozone response (Figure 8.20a) as discussed below.

The temperature response to the 11-year solar variability in the stratopause region at mid-latitudes is in the L90 simulation (Figure 8.19b) similar to the response in the L39 version. As was the case with the SW heating rates the solar signal in temperature in the L39 reference simulation remains qualitatively and to a large extent even quantitatively unchanged when the analysis period is limited to 41 years (1960 to 2000, not shown).

Stratospheric ozone reacts to an increase in spectral solar irradiance in the annual mean with a positive anomaly of about 2% per 100 units F10.7 flux in the tropical upper stratosphere at about 5 hPa (Figure 8.20a). The response decreases towards mid-

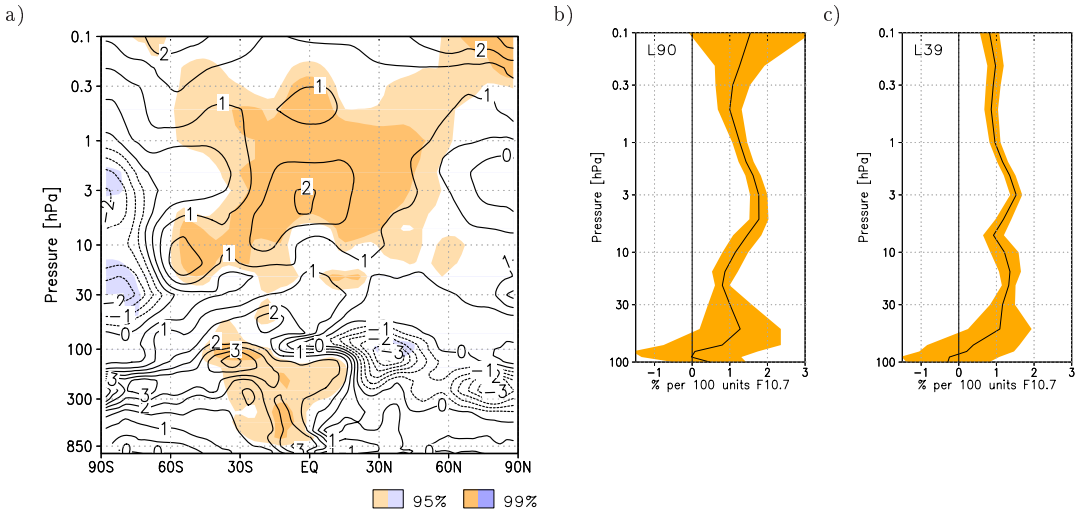


**Figure 8.20:** a) Zonal mean annual mean solar regression coefficient of ozone in % per 100 units of F10.7, contour interval is 0.5%. Light (heavy) shading indicates statistically significant changes at the 95(99) % level. b) and c) Zonal mean annual mean ozone change profile in the stratosphere and lower mesosphere in % per 100 units of F10.7, averaged over the tropics (25 °N to 25 °S) in the L90 simulation (b) and in the L39 simulation (c). Shading denotes uncertainty associated with the fit.

latitudes. Compared with the L39 reference simulation and with observations there is a clear discrepancy in the location of the strongest positive ozone response which is found at mid-latitudes in observations and in EMAC-FUB instead of in the tropics.

However, the tropical ozone change profile, shown in Figure 8.20b, exhibits a secondary maximum of solar induced ozone increase in the lower stratosphere which is significant within the range of uncertainty. The analogue profile from the EMAC-FUB (L39) simulation is shown in Figure 8.20c. There is only a rudiment of a secondary maximum in the tropical lower stratosphere. Because of the better, though not perfect, agreement of the L90 solar ozone change profile with observations (Soukharev and Hood, 2006) a detailed analysis of the phenomenon is done using the results obtained by the higher vertical resolution model version (EMAC).

The EMAC tropical regression profile is shown once more in Figure 8.21a where it is compared with the QBO and ENSO induced ozone changes (Figure 8.21b and 8.21c). In the lower stratosphere, i.e., the region between 100 hPa and 30 hPa, it is seen that higher solar activity leads to a higher abundance of ozone. A westerly QBO phase at 50 hPa acts into the same direction, that is towards more ozone. The reaction of ozone to sea surface temperature anomalies in the tropical Pacific, expressed by means of the Niño3.4 index, is such that a higher Niño3.4 index (i.e., an ENSO warm event) leads to less ozone in the tropical lower stratosphere. Vice versa does an ENSO cold event (a lower Niño3.4 index) yield more ozone in the tropical lower stratosphere. From these regression profiles it could be inferred that the simultaneous occurrence of QBO westerlies and an ENSO cold event during a period of high solar activity may support the solar signal in ozone. Since observations show an opposite QBO influence on the solar signal

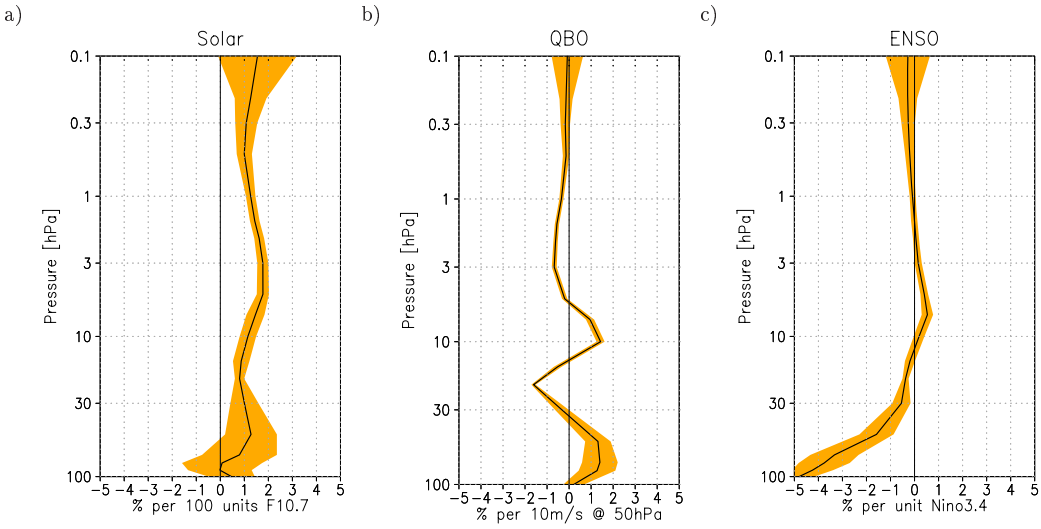


**Figure 8.21:** Zonal mean annual mean ozone change profile in the stratosphere and lower mesosphere in %, averaged over the tropics (25 °N to 25 °S). Shading denotes uncertainty associated with the fit. a) Solar regression coefficient in % per 100 units F10.7, b) QBO regression coefficient in % per 10 m/s at 50 hPa, c) ENSO regression coefficient in % per unit Niño3.4 index.

a more profound examination is needed and done below. On the other hand, an ENSO warm event coincident with solar maximum can offset the solar signal in the tropical lower stratosphere due to the strength of the ENSO signal (-2% per unit Niño3.4 index compared to +1.3% per 100 units F10.7 flux at 50 hPa). At the same time it should be noted that the uncertainty range associated with the fit is larger for the solar signal than for the QBO and ENSO influence. These results refer to the signal in the annual mean.

An analysis of monthly mean profiles yields different ozone sensitivities in late northern and southern winter, respectively. Figure 8.22a1 and 8.22d1 show the 11-year solar cycle induced ozone change in February and August, respectively. While the ozone abundance is enhanced everywhere in the stratosphere at higher solar activity in February it is decreased in the lowermost stratosphere in August. The positive ozone response peaks in February at 70 hPa and in August at 50 hPa. As the uncertainty range in both months includes the zero change line these signals are statistically not significant. The QBO signal in ozone is rather constant during the year, as Figure 8.22b1 and 8.22e1 show. The more westerly the wind at 50 hPa the higher the ozone abundance in the tropical lower stratosphere. The ENSO signal in February is similar to the annual mean (Figure 8.22c1). It implies a significantly higher ozone abundance in the tropical lower stratosphere during ENSO cold events. The signal changes sign in southern summer at 50 hPa, but it is then weak and statistically insignificant (Figure 8.22f1). This may be due to the fact that ENSO usually peaks in northern winter which is a favourable season for the upward propagation of the signal by means of planetary waves (García-Herrera et al., 2006).

Figure 8.22a2 to c2 and 8.22d2 to f2 show the temperature anomaly profiles due to the respective regressor. In general, the temperature anomalies are consistent with the

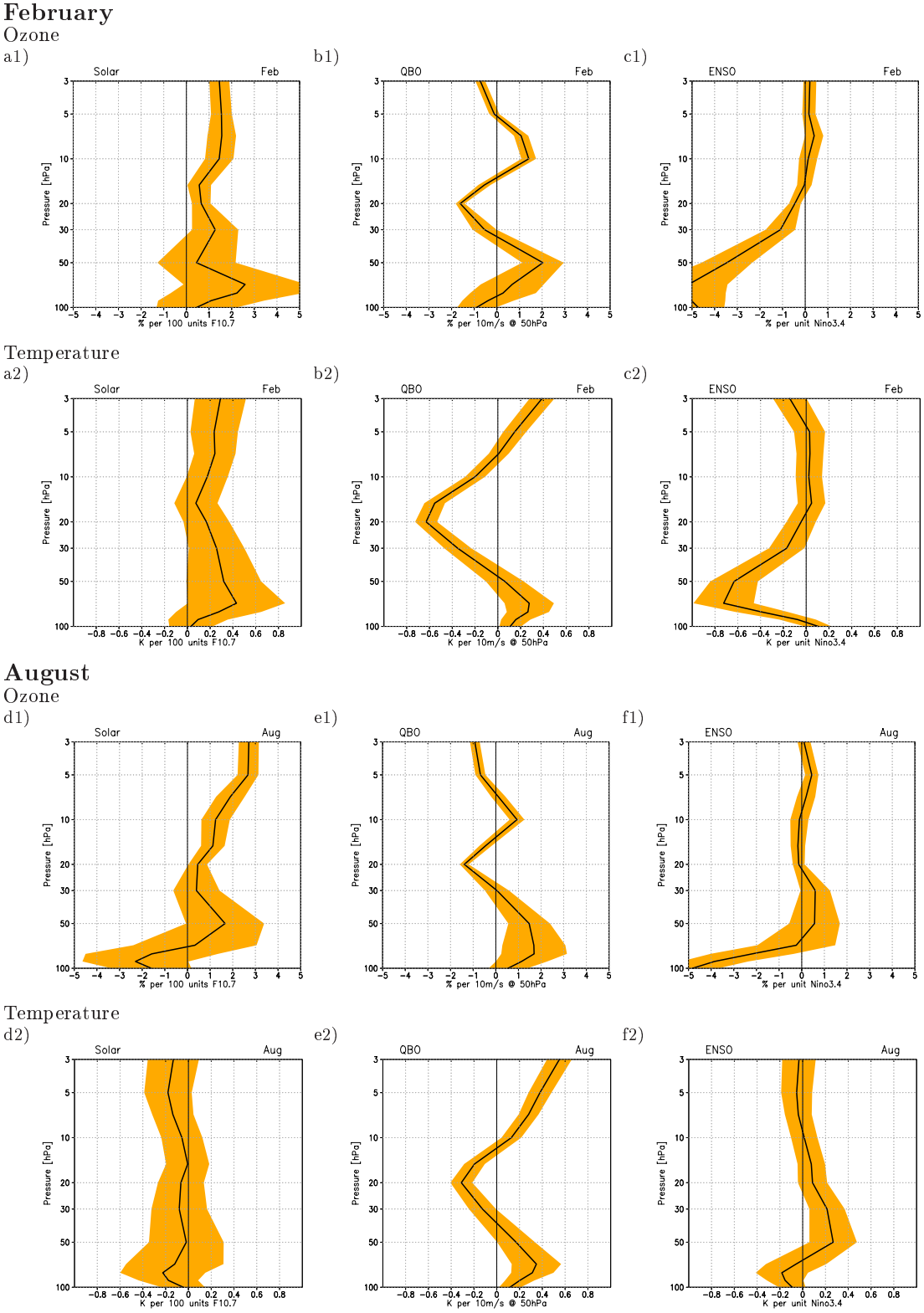


**Figure 8.22:** Zonal mean monthly mean ozone change profile in the stratosphere in % for February (top) and August (bottom), averaged over the tropics (25 °N to 25 °S). Shading denotes uncertainty associated with the fit. a) and d) Solar regression coefficient in % per 100 units F10.7, b) and e) QBO regression coefficient in % per 10 m/s at 50 km, c) and f) ENSO regression coefficient in % per unit Niño3.4 index.

ozone anomalies. Altitude regions with positive ozone anomalies coincide with regions of higher temperatures. However, there is one exception. The solar cycle induced temperature anomaly in August is weakly negative throughout the stratosphere whereas the ozone anomaly is positive above about 70 hPa. With the high uncertainty associated with the temperature profile in Figure 8.22e2 this discrepancy should not be overemphasised.

These tendencies are the result of a purely statistical multiple linear regression model. The physical reason for the respective response is discussed in the following. Under solar maximum conditions a weaker upwelling in the region of the maritime continent was noted (cf. Figure 8.14). As this is the region with the in terms of absolute values strongest upward motion it dominates the transport of tropospheric ozone poor air into the lower stratosphere by deep convection. A deceleration of the upwelling there implies a decrease in the amount of tropospheric ozone poor air that reaches the lower stratosphere which may explain the relative increase of ozone in this altitude domain.

During ENSO warm phases warmer than average water is found in the eastern Pacific off the coast of equatorial South America. Related with this is an eastward shift of the deep convection zone. As a consequence the tropopause rises and cools. This mechanism is supported via stratospheric pathways. ENSO usually peaks in northern winter when the strong westerly polar night jet allows Rossby waves to propagate into the stratosphere. There, they dissipate weakening the polar night jet and reinforcing the mean meridional circulation which in turn leads to a cooling in the tropical lower stratosphere. Thus, more ozone poor air from the troposphere reaches the lower stratosphere (Sassi et al., 2004; García-Herrera et al., 2006; Manzini et al., 2006; Calvo et al., 2010) associated with decreasing amounts of ozone there.

In connection with the QBO and in particular with its vertical structure with westerly winds above easterly winds or vice versa strong shear zones are present between the individual regimes. For example, there is a positive shear zone between westerly winds that prevail on top of easterlies. North and south of the equator at low latitudes the thermal wind balance requires in this case a poleward decreasing positive temperature anomaly which can only be created and maintained by an adiabatic secondary circulation with downwelling at the equator and upwelling off the equator (Plumb and Bell, 1982). Thus, the positive temperature anomaly peaks in the shear zone but not at the altitude of the maximum easterly or westerly winds. Westerly winds at 50 hPa are associated with easterlies above, i.e., there is a negative shear zone which according to the thermal wind relationship produces an anomalous cooling at the altitude of maximum shear. In the lowermost stratosphere (50 hPa and below) a westerly QBO phase is associated with a positive temperature anomaly (Marquardt, 1997). This can also be understood when it is considered that a westerly QBO allows planetary waves emerging at northern mid-latitudes to propagate towards and, even, across the equator in the lower stratosphere. According to the Holton-and-Tan relationship (Holton and Tan, 1980) this causes a strong and stable polar night jet. A strong jet in connection with a lower rate of plan-

etary wave breaking creates a weaker than average mean meridional circulation which in turn is the reason for a relative warming (a weaker absolute cooling) of the tropical lower stratosphere.

From the above discussion about the annual mean signal as well as the signal in individual months one can infer that a westerly QBO phase coincident with a solar maximum leads to a secondary maximum in the tropical lower stratosphere in ozone and temperature. However, this is not what observations show (Labitzke and Kunze, 2009). In the real atmosphere there is a positive correlation between the solar radio flux and temperature in the tropical lower stratosphere during QBO east phases. The correlation is weakly negative during QBO west phases. To test the model against this observational result the monthly mean zonal mean temperature data for February have been stratified according to the QBO phase. The criterion used for the classification is the zonal mean zonal wind in the preceding December being in the monthly mean greater than 6 m/s or less than -2 m/s for the winter being regarded as QBO west or east, respectively. The relatively high threshold value of 6 m/s for the westerly QBO phase was chosen in order to ensure that westerly winds prevail also in January and February. As the winds at the QBO east phase tend to be stronger and as the onset of the west phase in the lower stratosphere happens very seldom in mid-winter (Marquardt, 1997) the threshold of -2 m/s is sufficient. Winters following a major volcanic eruption have been excluded from the analysis as such an eruption influences both the downward propagation of the QBO which is delayed (Marquardt, 1997) and the temperature in the tropical lower stratosphere which is higher than prior to the eruption (Randel et al., 2009).

Figure 8.23 shows the results of the correlation analysis which is performed for both EMAC and EMAC-FUB. Tropical lower stratospheric temperature is indeed positively correlated with the solar flux during QBO east phases. The correlation in the L90 model version is strongest between 80 and 70 hPa at the equator. In the L39 version there is a wider region with statistically significant positive correlations of the order of 0.5. During QBO west phases the correlation in the tropical lower stratosphere is very weakly positive in the L90 model but in general too low to draw a definite conclusion. EMAC-FUB shows, however, an anti-correlation between temperature and the solar flux everywhere in the tropical lower stratosphere up to 30 hPa when the QBO is westerly.

At high northern latitudes a discrepancy in the responses of the L90 and the L39 model version is apparent. While EMAC-FUB (L39) shows in qualitative agreement with observations (Labitzke and Kunze, 2009) a positive correlation between temperature and the solar flux in QBO west winters and vice versa in QBO east winters, the opposite is seen in EMAC (L90). Labitzke and Kunze (2009) find an anti-correlation between the solar activity and the lower stratospheric temperatures at high northern latitudes indicating that the polar vortex is stronger when solar activity is high. The opposite is observed during QBO west phases. Polar temperature is positively correlated with the solar F10.7 radio flux, i.e., the polar vortex is weak and disturbed in those winters. Hence,

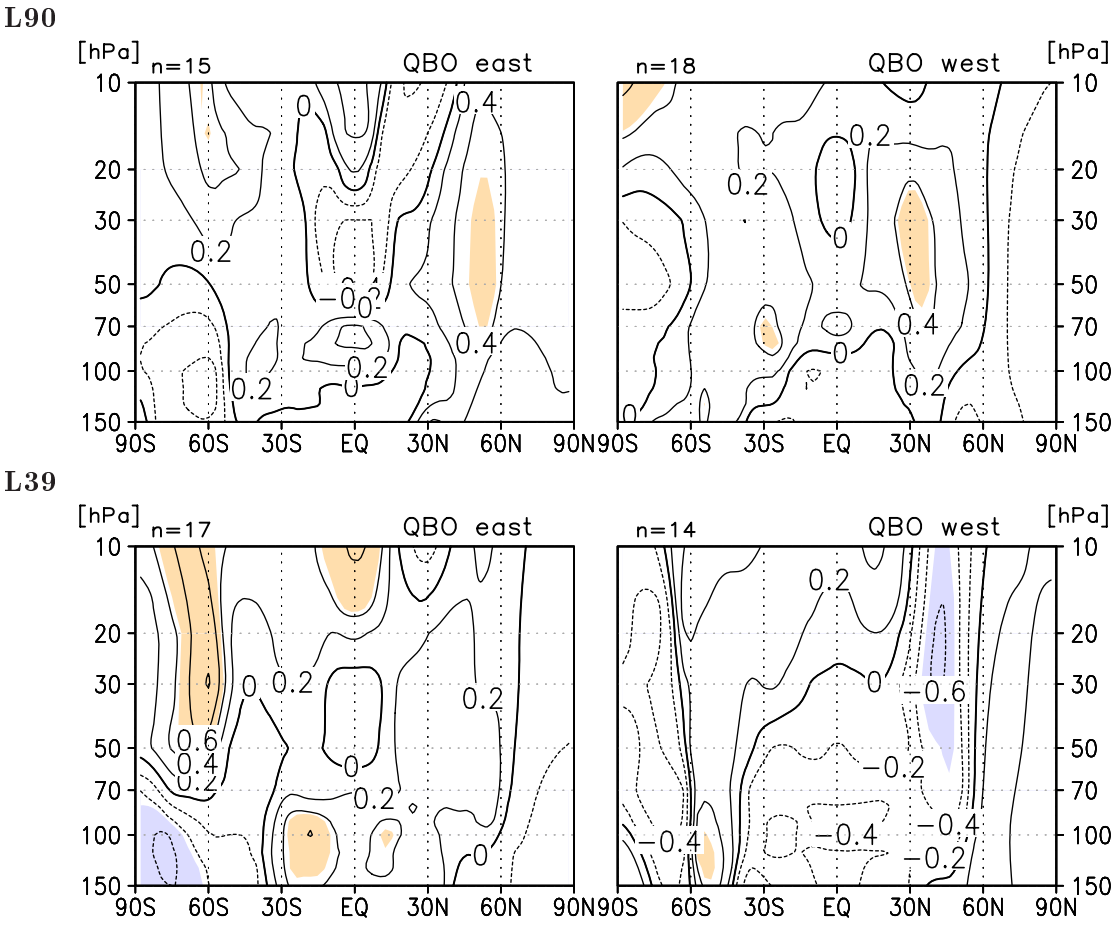


**Figure 8.23:** Correlation between the solar F10.7 cm solar radio flux and zonal mean monthly mean temperature in February in the upper troposphere and lower and middle stratosphere. Contour interval is 0.2. Statistically significant (90%) correlation coefficients are shaded. Top: EMAC with 90 levels and bottom: EMAC-FUB with 39 levels. Left: During QBO east phases and right: During QBO west phases. The number of years included in the analysis is given above each panel.

EMAC fails to reproduce this observed relationship. It is not known to what extent the effects of precipitating particles which were accounted for in the EMAC simulation but not in EMAC-FUB contribute to this unrealistic behaviour.

The explanation for the occurrence of the tropical lower stratospheric warming in solar maximum/QBO east winters given by, e.g., Labitzke and Kunze (2009) involves the MMC which is weaker in those winters due to the strong polar night jet and the decreased wave-mean flow interaction. As a strong polar night jet is directly connected to the strength of the polar vortex this explanation does not work for the EMAC (L90) model results that indicate a weaker vortex in solar maximum/QBO east winters. A disturbed polar vortex along with a weaker polar night jet at solar maximum/QBO east conditions cannot be the reason for the tropical lower stratospheric warming as this would reinforce the MMC which in turn would cause a cooling in the equatorial lower stratosphere. Vice versa does a negative correlation at high latitudes under QBO west conditions imply a

cooler pole at solar maximum. A weaker MMC associated with the cooler pole should, therefore, cause a more pronounced warming; also as the westerly QBO itself acts to increase the temperature in the tropical lower stratosphere.

In fact the tropical residual vertical velocity is in the L90 simulation in the lowermost stratosphere positively correlated with the solar flux in QBO east winters whereas the correlation is weakly negative in QBO west cases (not shown). EMAC-FUB (L39) simulates an anti-correlation between the residual vertical velocity and the solar flux in the QBO east phase. During QBO west winters the response is somewhat heterogeneous with enhanced upward motion over the equator and a weaker upward velocity at northern and southern tropical latitudes (not shown). Thus, at least the EMAC-FUB QBO east signal in tropical upwelling is consistent with the high latitude response and with the suggested mechanism which was derived from observations (Labitzke and Kunze, 2009). However, the correlation coefficients are small in all cases (L90, L39, QBO east and west) and only locally statistically significant. From this result it is difficult to deduce the consequences for the upward transport of ozone. The correlation coefficients of ozone and the solar flux are likewise small and insignificant everywhere in the tropical lower stratosphere (not shown) which further complicates the diagnosis of a clear ozone transport tendency.

From the above consideration of the EMAC (L90) results the question arises as to what else can cause the tropical lower stratospheric warming when dynamically induced heating via a modulated MMC fails. A possible mechanism is radiative heating. To answer this question an experiment with the stand-alone offline FUBRad radiative heating model was performed. The abundances of radiatively active trace gases were prescribed to the model as was the temperature field. The calculated radiative heating does not feed back on the temperature field in the offline FUBRad version. The offline code was run in the same configuration that was used for the CCMVal2 radiation code intercomparison (Chapter 3 of SPARC CCMVal, 2010; case A).

For a first test experiment the ozone volume mixing ratio in the lower tropical stratosphere was increased according to the ozone change profile in Figure 8.24a that resembles the lower stratospheric anomaly simulated by EMAC in February (see Figure 8.22a1). The results are compared with the heating rates obtained from a control experiment. Both the control and the test experiments were run under intermediate solar activity conditions, i.e., the results reflect the pure ozone contribution to heating rate changes.

Figure 8.24b shows the relative change profile in the equatorial SW heating rate. It is seen that the distinctive ozone increase in the tropical lower stratosphere (67 hPa) of about 2.3 % yields an SW heating rate that is about 0.6 % higher than in the control experiment. At the same altitude there is a reduced long-wave (LW) cooling (by up to 6 %) as is evident in Figure 8.24c. The increase in SW radiative heating together with the reduced LW cooling leads to a positive anomaly in total radiative heating in the tropical lower stratosphere.

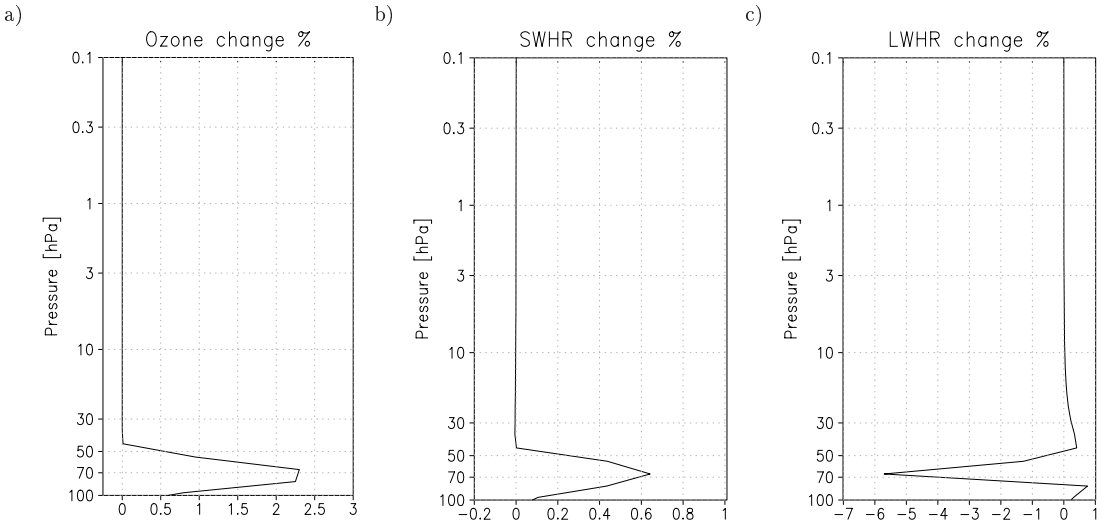


**Figure 8.24:** Profiles of a) relative ozone change in %, b) relative change in the SW heating rate in % and c) relative change in the LW heating rate in % obtained at the equator from the stand-alone offline FUBRad code.

In a second test experiment the February EMAC ozone change profile was prescribed to the offline code over the depth of the stratosphere. Thus, the ozone increase in the upper stratosphere is included which may shield the lower stratosphere from UV irradiance. This effect reduces the lower stratospheric SW heating response to a value of approximately 0.5 % (not shown). The LW signal is virtually unaffected by the presence of the upper stratospheric ozone increase (not shown).

Hence, radiative heating may play a role for the higher temperature at higher solar activity in the absence of dynamically induced heating provided that more ozone is found in the tropical lower stratosphere. However, it is difficult to assess whether the latter requirement is satisfied owing to the low correlation between tropical lower stratospheric ozone and the solar radio flux.

Aspects of a possible misattribution or aliasing due to the presence of 11-year solar cycle periods in the QBO and the SSTs are further discussed in chapter 9.

### Summary and Discussion

It has been shown that the EMAC model with a higher vertical resolution, i.e., 90 levels instead of 39 as implemented in EMAC-FUB simulates a solar signal in the stratosphere which is to a certain extent qualitatively similar to the EMAC-FUB results but which differs in some important aspects. The latitudinal structure of the solar cycle induced upper stratospheric ozone increase is centred over the equator whereas EMAC-FUB simulates the maximum ozone increase at mid-latitudes which is overall consistent with observations. The equator-centred ozone signal may be responsible for the stronger solar signal in SW heating rates in EMAC compared with EMAC-FUB.

Another important difference is the appearance of secondary maxima in the annual tropical lower stratospheric ozone and temperature responses. In this regard the EMAC results are closer to observations than the results obtained with the L39 model version. A closer inspection shows that the maxima are most pronounced during late northern hemisphere winter. They are, however, statistically not significant due to low correlations between ozone or temperature and the solar flux. The observed relationship of a stronger solar induced temperature increase in the lower stratosphere during QBO east winters (Labitzke and Kunze, 2009) cannot be reproduced with EMAC. This is most probably connected with the unrealistic tendency towards a warm and disturbed polar vortex under solar maximum/QBO east conditions in EMAC where observations show the opposite. The lower resolved EMAC-FUB shows a similar behaviour as is known from observations: At least under QBO east conditions there is a coherent picture of a cooler polar vortex at higher solar activity which implies a stronger polar night jet, a reduced wave-mean flow interaction and in turn a weaker mean meridional circulation. However, since the correlation between the residual vertical velocity and the solar activity proxy is low, probably owing to the length of the time series (four solar cycles) which is further reduced by the QBO stratification, this result should not be overemphasised. Anyway, it can be stated that the solar influence which is relatively weak compared with the QBO influence can invert the intrinsic QBO effect on temperature and upward motion in the tropical lower stratosphere. The involved processes leading to this inversion remain, however, unclear. Yet, it is not possible to ascribe all the differences between the results from the two model versions to the higher vertical resolution of EMAC since the EMAC set-up included the effects of precipitating particles.

Moreover, it has been shown that the presence of the tropical lower stratospheric ozone maximum may contribute to the development of the secondary temperature maximum via radiative heating, in particular, by reduced LW cooling.

## 8.3 Transient versus equilibrium simulations

Solar maximum and minimum equilibrium simulations are a widely used method to study the solar influence on the atmosphere. The imposed irradiance changes force the model into a permanent state of maximum and minimum, respectively. On the one hand, this is unrealistic since it neglects the temporal evolution of the solar irradiance with its natural 11-year cycle. On the other hand, it is an effective way to simulate the state of the atmosphere during peculiar phases of solar activity in a computationally inexpensive manner which allows longer model integrations and, hence, raises the probability to obtain statistically significant signals. It has been suggested that a time-varying solar forcing is necessary to reproduce the observed solar signal, in particular, in the tropical lower stratosphere (Austin et al., 2007). However, from some equilibrium studies a vertical structure of the tropical ozone and temperature response consistent with the observed

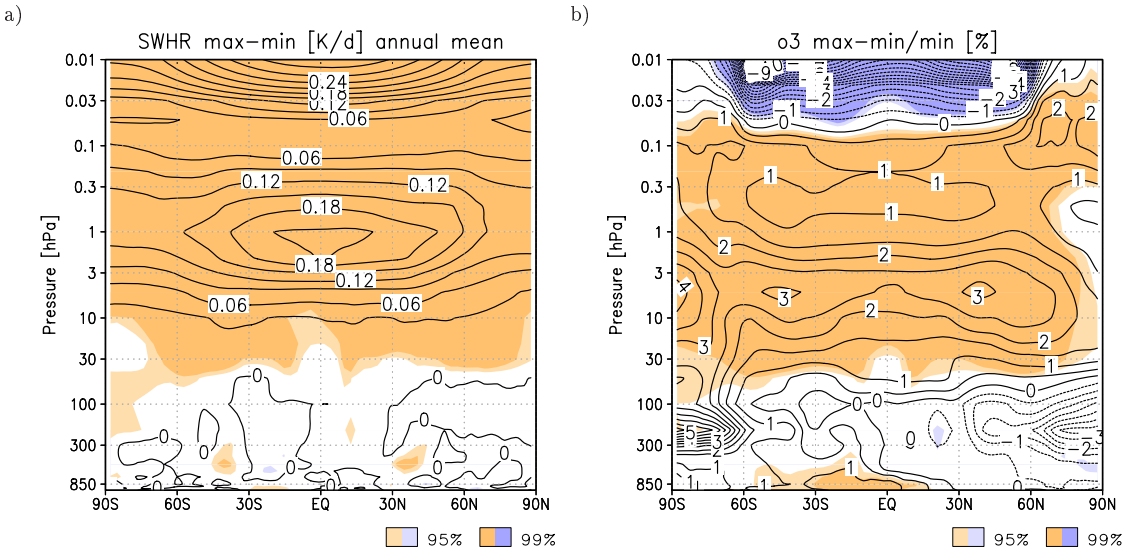


**Figure 8.25:** a) Zonal mean annual mean difference (max-min) of short-wave heating rates in K/day, contour interval is 0.03 K/day and b) Zonal mean annual mean difference (max-min)/min of ozone in %, contour interval is 0.5 %. Light (heavy) shading indicates statistical significance at the 95(99) % level.

profile has been reported (Schmidt and Brasseur, 2006; Schmidt et al., 2010; Matthes et al., 2010).

In the solar maximum and minimum equilibrium experiments with EMAC-FUB the spectral solar irradiance has been adjusted to the respective conditions using the values of November 1989 for solar maximum and of September 1986 for solar minimum from solar cycle 22. For a detailed description of the experimental set-up see section 5.3.3. The results are analysed by maximum-minimum differences. The actual difference in the F10.7 cm radio flux for the two extrema of solar activity is 166 units. For comparison with results from the transient simulation (section 8.1) the latter have to be scaled by a factor 1.66.

The difference pattern between the solar maximum and solar minimum (max-min) in the annual mean short-wave heating rates is depicted in Figure 8.25a. Similar to the results of the transient simulation (Figure 8.1) the short-wave heating is enhanced under solar maximum conditions compared to solar minimum conditions everywhere in the middle atmosphere. The difference is statistically highly significant. In the stratosphere the differences are the highest close to the stratopause at about 1 hPa with values of 0.21 K/d. Compared with the values in Figure 8.1a) scaled by 1.66 which yields a maximum stratospheric response of about 0.2 K/day this is in very good agreement. The secondary maximum in the mesosphere of about 0.3 K/d which is due to the variability at the Lyman-$\alpha$ wavelength is also similar to the values obtained from the transient simulation (0.18 K/day $\cdot$ 1.66 $\approx$ 0.3 K/day).

The ozone response from the maximum and minimum equilibrium simulations shows a positive anomaly, i.e., there is more ozone during solar max, of about 3 % in both the

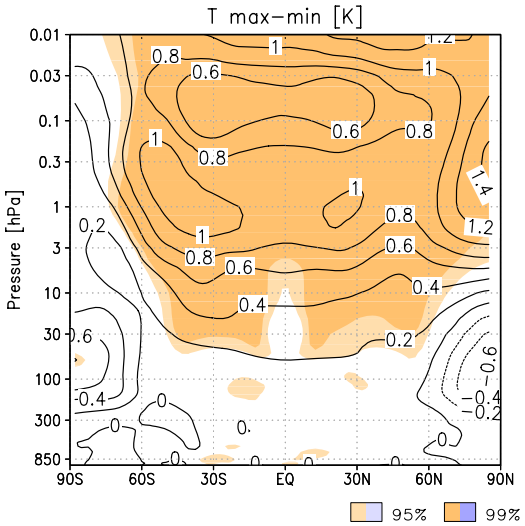


**Figure 8.26:** Zonal mean annual mean temperature difference (max-min) in K, contour interval is 0.2 K. Light (heavy) shading indicates statistical significance at the 95(99) % level.

southern and northern hemisphere mid-latitudes at about 5 hPa. The mesospheric response is negative due to the ozone depleting effect of OH as was seen in the transient simulation in section 8.1. The distribution of the ozone signal in the latitude-height plane is similar in the equilibrium and in the transient simulations with EMAC-FUB (cf. Figure 8.1b). Note that the relative difference between the two equilibrium simulations was calculated as (max-min)/min which is not the same as the regression coeffient divided by the long term mean which was shown in Figure 8.1b. When comparing absolute values the upper stratospheric ozone signal is somewhat stronger in the transient simulation (0.25 ppmv/166 units of the F10.7 cm solar radio flux) than in the equilibrium simulation (0.21 ppmv). The tropical ozone change does not show a secondary maximum in the lower stratosphere. However, when analysing a subset of the 30 years the tropical secondary maximum does appear. This indicates that the signal is not robust. Possibly it could reappear if the simulation was continued. Since EMAC-FUB does not simulate the tropical secondary ozone maximum neither in the transient nor in the equilibrium runs it is not possible to support the statement made by Austin et al. (2007) that the use of time-varying forcings leads to an improved vertical structure of the solar signal.

The temperature response at mid and low latitudes (Figure 8.26) is a more direct reaction to the altered SW heating rates, i.e., the highest temperature anomalies are found in the same regions as the strongest SW heating response. This is a bit different from the transient simulation (Figure 8.1a and 8.2) where the highest temperature response is seen in the extratropics while the transient SW heating response peaks in the tropics and subtropics. From the equilibrium simulations higher temperatures of the order of 0.9 K are found at the stratopause level at all latitudes between 60 °S and 60 °N. This resembles the observational results of Randel et al. (2009). However, the strongest observed

temperature changes reach farther down to about 30 hPa whereas the simulated signal decreases faster towards the lower stratosphere. The equilibrium simulation results do not show the secondary maximum in the tropical lower stratosphere that is found in the observations of Randel et al. (2009). The magnitude of the signal is lower than the scaled transient results in the extratropics suggest ($0.8\,\mathrm{K} \cdot 1.66 \approx 1.32\,\mathrm{K/day}$). Towards higher altitudes the signal shows a local minimum and increases again in the upper mesosphere which is similar to the response to the transient forcing. At high northern latitudes the annual mean signal is again dominated by the winter signal with lower temperatures in the lower stratosphere and higher values in the upper stratosphere and lower mesosphere at solar maximum. As was already noted in connection with the transient simulation (section 8.1) this gives an indication for a weaker mean meridional circulation.

Matthes et al. (2010) showed from equilibrium simulations with prescribed fixed solar irradiance and fixed QBO phases that the QBO east phase supports the development of the tropical lower stratospheric maximum. The balance between ozone production and the vertical advection of ozone was found to be crucially influenced by the solar signal in the residual vertical velocity which is reduced during QBO east phases and slightly enhanced during QBO west phases. This renders the vertical advection ineffective in balancing a stronger ozone production at solar maximum/QBO east which leads to an ozone increase in the tropical lower stratosphere. Under QBO west conditions, however, the vertical advection cancels the ozone production in the lower stratosphere and, hence, suppresses the development of a positive ozone anomaly.

It is difficult to perform a comparable analysis on the contributions of advection, production and ozone loss as Matthes et al. (2010) involving the whole year since the QBO phase was not fixed in the EMAC-FUB equilibrium simulations. However, it is possible to stratify particular months or seasons by the QBO phase and look at the difference between solar maximum and minimum. This is individually done for the southern hemisphere late winter and spring months of September and October. Profiles of the ozone difference, the residual upward velocity difference and the temperature difference averaged over the tropics (25 °S to 25 °N) are shown in Figure 8.27.

In the ozone change profiles there is a tendency for an ozone increase to appear during QBO east winter and spring months. This is qualitatively overall consistent with the annual mean results of Matthes et al. (2010). The magnitude of the ozone increase is weaker in the individual months at QBO east in Figure 8.27a (between 1 and 1.5 %) compared to the annual mean values (approximately 3 %). Moreover, there is no real secondary maximum in the EMAC-FUB ozone signal at QBO east phases. During QBO west winter and spring seasons there is, in contrast, a negative response to the solar irradiance forcing.

The residual upward velocity differences between solar maximum and minimum in the lower stratosphere (Figure 8.27b) show a tendency towards stronger upward motion in solar maximum/QBO west winter/spring months as opposed to QBO east winter/spring

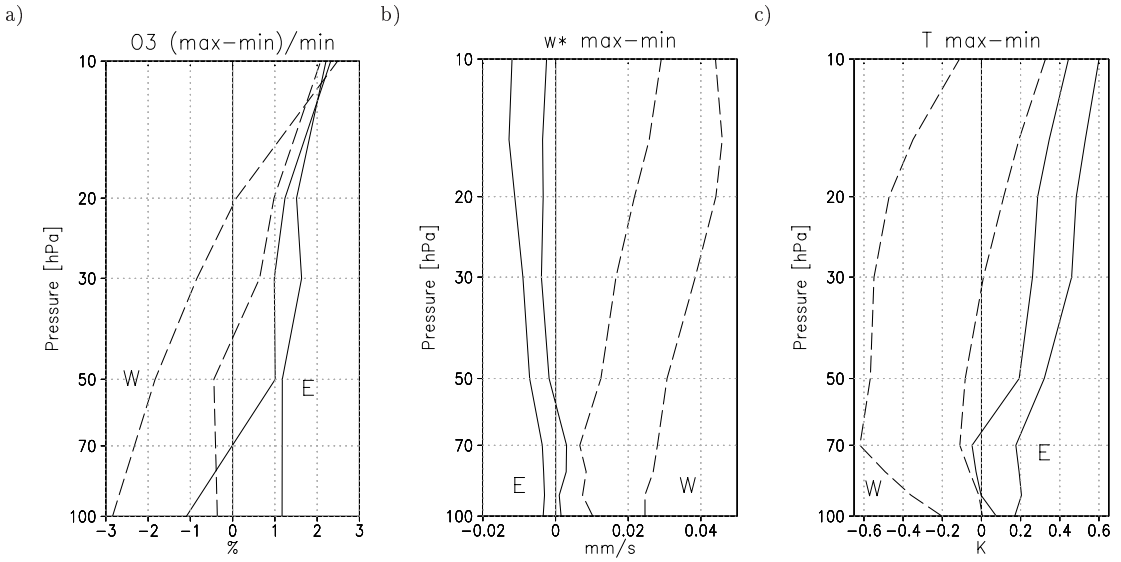


**Figure 8.27:** Profiles of September and October a) relative ozone difference (max-min)/min in %, b) residual vertical velocity difference in mm/s and c) temperature difference in K during QBO east (solid lines) and QBO west (dashed lines) phases. Average over the tropics from 25 °S to 25 °N.

months in which higher solar irradiance tends to cause a reduced upwelling. This result is also in general agreement with the findings of Matthes et al. (2010). It can be interpreted as follows: The reduced upwelling in solar maximum/QBO east implies less ozone-poor air from below entering the lower stratosphere. Thus, according to Matthes et al. (2010), the in-situ production of ozone is not attenuated by advection and produces the lower stratospheric maximum. On the other hand, the increased upward transport of ozone-poor tropospheric air during solar maximum/QBO west does quite effectively cancel (and even outbalance) the local ozone production in the lower stratosphere. Hence, the lower stratospheric ozone maximum does not appear.

Furthermore, it is seen that the QBO phase looses its importance for the ozone solar signal in the middle stratosphere at about 10 hPa whereas the signal in the residual upward velocity is influenced by the QBO throughout the depth of the lower and middle stratosphere. This is due to ozone being photochemically determined in the middle and upper stratosphere as opposed to the lower stratosphere where transport phenomena dominate the distribution of ozone.

Temperature reacts to the increase in solar irradiance in a consistent manner with higher temperatures during solar maximum and QBO east seasons (Figure 8.27c) due to the enhanced ozone volume mixing ratio and the reduced upwelling. Under QBO west conditions lower temperatures are found in accordance with lower ozone abundances and increased residual upward velocities. In the temperature profiles a recessive influence of the vertical velocity towards higher altitudes is also noticeable, i.e., solar induced temperature anomalies tend to become positive at higher altitudes regardless of the QBO phase. However, this effect is not as strong as in the case of ozone.

The QBO influence on the solar signal is less pronounced in EMAC-FUB results compared to the results of Matthes et al. (2010). This has to be seen in connection with the experimental set-up. While EMAC-FUB was integrated for 30 years with a time-varying QBO under solar maximum and minimum conditions, respectively, the experiments conducted by Matthes et al. (2010) were 20-year fixed solar fixed QBO runs for each case. The QBO stratification of the EMAC-FUB model output further reduces the number of years in each class which is, finally, of the order of 10. Because of the low number of years none of the above results is statistically significant. However, the tendency towards higher temperatures and more ozone in the tropical lower stratosphere during QBO east phases is visible. The temperature signal is qualitatively consistent with observations (Labitzke, 2004a).

### The tropospheric solar signal in southern winter and spring

The above discussed different appearance of the solar signal in the tropical lower stratosphere during QBO east or west phases is supposed to determine the characteristics of the solar signal in zonal mean zonal wind in the troposphere. Based on the results of Haigh et al. (2005) the lower stratospheric meridional temperature gradient is important for the sign of the influence on the tropospheric subtropical jet. A warming at low latitudes in conjunction with a high-latitude cooling leads to a weakening and a poleward shift of the jet stream. Vice versa, a cooling at low latitudes combined with a warming at polar latitudes yields an equatorward shift of the jet. The former mechanism (weaker and poleward shifted jet) was found in the mechanistic momentum study (see chapter 6) as well as in the transient EMAC-FUB simulation of the past (see section 8.1.3). On the basis of the negative temperature anomaly in the tropical lower stratosphere in southern spring during QBO west phases it is expected that the opposite effect should occur.

Figure 8.28 shows in the top panels the temperature difference between solar maximum and minimum from the south pole to the equator in October. When the QBO is easterly there is a weakly positive temperature difference at low latitudes. The polar temperature difference is stronger positive, though. The resulting influence on the tropospheric zonal mean zonal wind is weak and somewhat heterogeneous. On the other hand, there is a negative temperature difference between solar maximum and minimum when the QBO is westerly. In combination with the warming at high latitudes this yields a positive anomalous equator-to-pole temperature gradient. The tropospheric jet is in response to this forcing strengthened at its equatorward flank and weakened on the poleward side. Ultimately, this implies an equatorward displacement of the jet in agreement with the mechanism proposed by Haigh et al. (2005). Due to the relatively low number of years in each class (QBO west and solar maximum, etc.) the signal is statistically not significant.

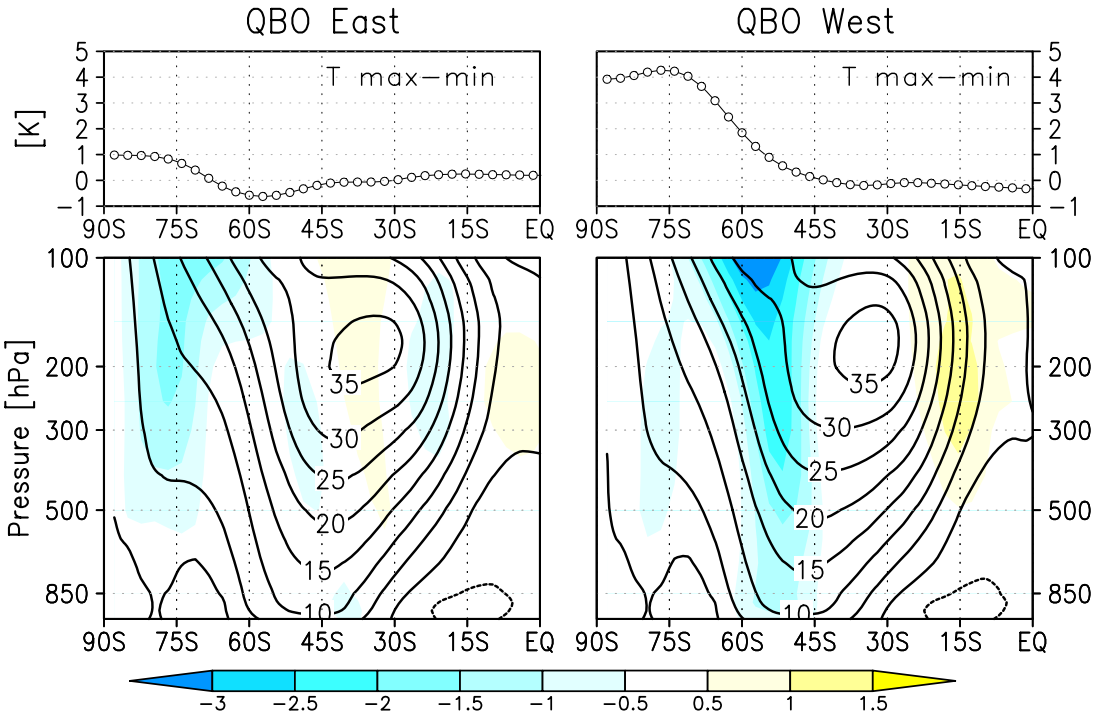


**Figure 8.28:** October monthly mean differences of zonal mean temperature in the upper troposphere/lower stratosphere at 100 hPa in K (top) and differences of zonal mean zonal wind in m/s in the troposphere (below, shaded) during QBO east (left) and west phases (right). Solid contours depict the zonal mean zonal wind at solar minimum in m/s.

*The solar signal in the Indian monsoon*

In the transient reference simulation a solar influence on the Indian summer monsoon was detected which was qualitatively in agreement with observational results (Kodera, 2004). During periods of solar maximum there is an enhanced upward motion of air from the southern Red Sea and the southern Arabian peninsula to the equatorial Indian Ocean. Simultaneously, there is anomalous downwelling south of the equator and over southern India.

This signal can be partly retrieved in the equilibrium simulations. Figure 8.29 shows the difference in vertical pressure velocity between solar maximum and minimum. The anomalies over the Indian Ocean north of the equator are negative, indicating stronger upwelling at solar maximum. South of the equator there is anomalous downwelling which is also found over the Indian Ocean north of about 10 °N. However, the signal over the southern Arabian peninsula has vanished. A quantitative comparison with the transient reference simulation result (Figure 8.18) reveals a considerable weaker solar signal in the equilibrium simulations. The difference is particularly large when it is recalled that the transient reference simulation result is given per 100 units of the F10.7 cm solar radio flux whereas the actual difference between the equilibrium maximum and minimum set-up is 166 units. A possible reason for the weaker monsoon solar signal in the equilibrium simulations may be the specification of the SSTs. In contrast to the transient simulation

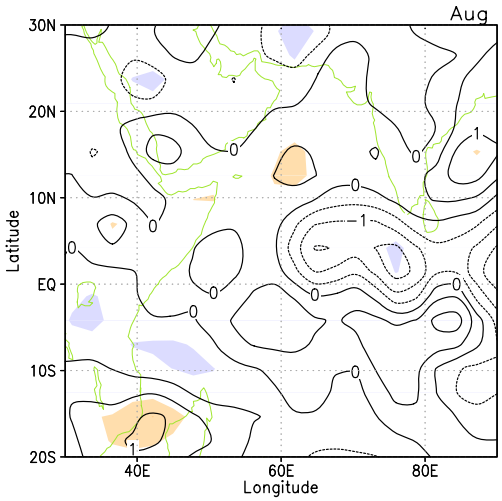


**Figure 8.29:** Monthly mean difference in August of vertical velocity at 300 hPa in Pa/s multiplied by 100. Contour interval is 0.5. Light (heavy) shading indicates statistical significance at the 95(99) % level.

which had observed SSTs prescribed as lower boundary condition fixed climatological SSTs were used in the equilibrium simulation (for details see section 5.3.3).

However, it is conceivable that the variable observed SSTs are themselves subject to 11-year solar irradiance variations and, thus, contribute to the solar signal in the transient reference simulation. The multiple linear regression method that is used to analyse the transient simulation results relies on the linear independence of the regressors. If this requirement is not fulfiled, the regression will not work properly. This may result in the attribution of decadal variability in the SSTs to the solar irradiance basis function. In principle, this is not a mistake when it is assumed that the decadal variability in the SSTs originates from the 11-year solar cycle. As there is no temporal evolution in the SSTs used for the equilibrium simulations other than the annual cycle, and as the SSTs are identical for the perpetual solar maximum and minimum run an SST contribution to the solar signal can be excluded.

Moreover, it is possible that the QBO modulates the solar influence on the monsoon as it did with the tropospheric subtropical jet. The difference shown in Figure 8.29 has been computed regardless of the QBO phase. When the model results are stratified by the phase of the QBO an influence of the lower stratospheric zonal wind becomes visible. From Figure 8.30a and 8.30b it is seen that the spatial distribution of the upwelling anomalies is similar in both QBO phases. However, during QBO east phases the signal is much more pronounced than during QBO west phases. This is consistent with the "pure" QBO effect on the monsoon circulation as described by Giorgetta et al. (1999) in a GCM model study and by Mukherjee et al. (1985) in an observational study. Giorgetta et al. (1999) propose a mechanism for the enhanced upwelling during QBO east phases: The secondary circulation associated with easterly winds in the lower stratosphere leads to a

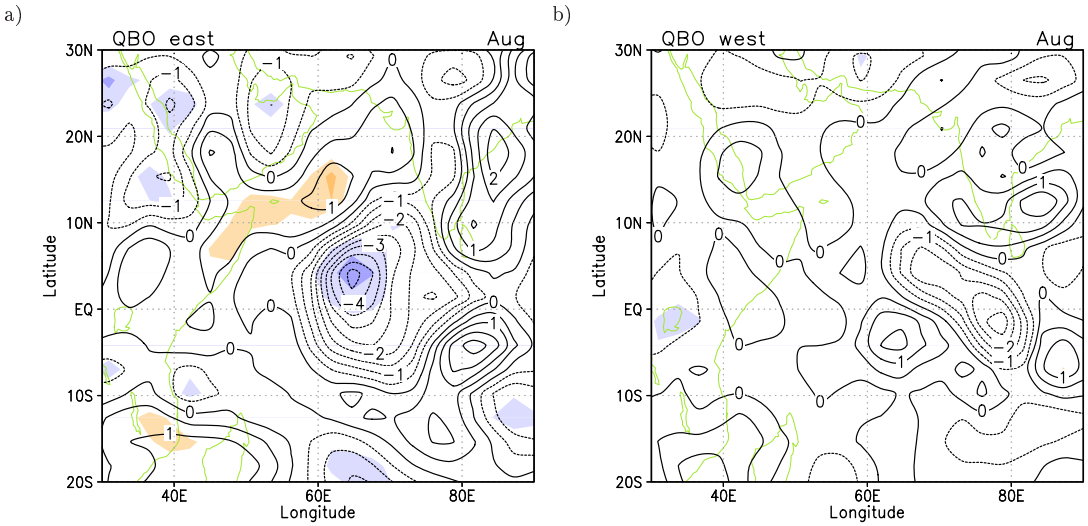


**Figure 8.30:** Monthly mean difference in August of vertical velocity at 300 hPa in Pa/s multiplied by 100 from the **equilibrium simulations**. a) During QBO east phases and b) during QBO west phases. Contour interval is 0.5. Light (heavy) shading indicates statistical significance at the 95(99) % level.

cooling in the tropopause region. This decreases the static stability which allows more vigorous deep convection. The enhanced upwelling in the upper troposphere is reflected in Figure 8.30a. On the other hand, during QBO west phases the static stability is increased due to the QBO induced warming in the lowermost stratosphere. In this case, the solar influence on the circulation is weak, leading to a slight enhancement of upwelling over the equatorial Indian Ocean east of 60 °E (Figure 8.30b). The fact that the difference between solar maximum and solar minimum involving all years (Figure 8.29) is relatively weak is due to a slight bias in the number of years in each class towards a westerly QBO (QBO east: 10 years max, 10 years min; QBO west: 12 years max, 11 years min).

A similar analysis of the transient reference simulation, i.e., the months being grouped according to solar activity and QBO phase instead of a multiple linear regression, yields a comparable result. The threshold values for solar maximum and minimum were 140 units and 100 units of the solar F10.7 cm radio flux, respectively. The QBO phase was determined using the JJA mean wind at 50 hPa. In general, Figure 8.31a and 8.31b show congruent areas of enhanced upwelling or anomalous downwelling with stronger differences in the QBO east phase. Thus, it can be stated that the easterly phase of the QBO supports the solar signal in the monsoon circulation. Due to the smaller number of years in each class compared with the analysis of the equilibrium simulations (QBO east: 7 years max, 8 years min; QBO west: 11 years max, 9 years min) only some parts of the signal are statistically significant.

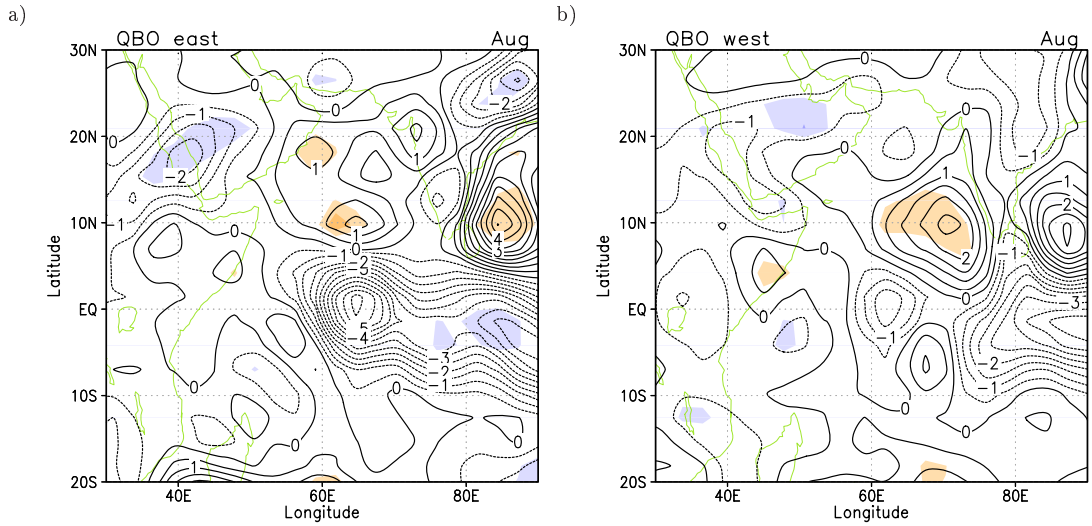


**Figure 8.31:** Monthly mean difference in August of vertical velocity at 300 hPa in Pa/s multiplied by 100 from the **transient reference simulation**. a) During QBO east phases and b) during QBO west phases. Contour interval is 0.5. Light (heavy) shading indicates statistical significance at the 95(99) % level.

### Summary and Discussion

It has been shown that the main characteristics of the annual mean 11-year solar signal in the upper stratosphere obtained with a pair of solar maximum and minimum equilibrium simulations are comparable to those obtained from the transient reference simulation. This is in line with other recent equilibrium CCM studies (Schmidt et al., 2010; Matthes et al., 2010). In the tropical lower stratosphere EMAC-FUB does not simulate a secondary peak in ozone or temperature increase whether the model is driven by a transient 11-year solar cycle or by fixed extrema of the solar irradiance. On the basis of these model experiments it is, hence, not possible to confirm the assumption of Austin et al. (2007) that a time-varying irradiance forcing will improve the vertical structure of the ozone and temperature response.

However, a difference is noted in the tropical lower stratospheric response to the solar irradiance forcing in individual months of the equilibrium simulations when the results are stratified by the QBO phase. EMAC-FUB simulates a positive ozone and temperature change in the lower stratosphere at solar maximum when the QBO is easterly and a negative anomaly when the QBO is westerly in late southern hemisphere winter and spring. These changes are part of a consistent picture with reduced upwelling during QBO east phases and enhanced upward motion during QBO west phases. The change in the upwelling response to the solar forcing between QBO east and west is, according to Matthes et al. (2010) the crucial factor for the determination of the ozone and temperature anomalies' sign as it renders vertical advection of ozone ineffective in balancing the ozone production when the upwelling is reduced (QBO east) and amplifies the vertical advection of ozone-poor air from the troposphere when the upwelling is enhanced (QBO west). The

above results are in general agreement with the findings of Matthes et al. (2010), although, it has to be taken into account that the modulating effect of the QBO is present in EMAC-FUB only in some months. This is due to a different experimental set-up. Furthermore, the QBO effect is limited to the lower stratosphere (below about 28 km or 15 hPa) where ozone is determined by transport whereas its behaviour at higher altitudes is dominated by photochemistry.

In connection with the different low-latitude zonal mean temperature response in late southern hemisphere winter under different QBO conditions it could be shown that EMAC-FUB is able to simulate the equatorward shift of the tropospheric subtropical jet when the equator-to-pole temperature gradient in the lower stratosphere is positive. This is in accordance with Haigh et al. (2005). It is the opposite effect from the one shown in chapter 6 and in section 8.1.3 in response to negative equator-to-pole temperature gradients.

The solar signal in the monsoon circulation is qualitatively similar but weaker in the equilibrium simulation compared with the transient reference simulation. This is probably due to the identical fixed SSTs that were specified to both equilibrium experiments. A modulating QBO influence on the solar signal in the Indian summer monsoon circulation becomes visible when the data are stratified according to the QBO phase. Easterly winds in the tropical lower stratosphere have a supporting effect on the solar signal whereas westerlies tend to counteract the solar signal in the Indian monsoon in agreement with observations (Mukherjee et al., 1985) and GCM results (Giorgetta et al., 1999). This effect is also found in the transient reference simulation when composites are formed similar to the analysis of the equilibrium simulations.

## 8.4 Interactive chemistry versus prescribed ozone changes

In this section results of the perpetual solar maximum and minimum simulations with prescribed ozone changes, i.e., EMAC-FUB in GCM mode, are compared with the results from the solar maximum and minimum equilibrium simulations with interactive chemistry (previous section) and, moreover, with the results of the transient reference simulation (section 8.1). 25 years of perpetual solar maximum and minimum are available for the analysis.

Figure 8.32 shows the long term annual mean difference between solar maximum and minimum (max-min) of zonal mean short-wave heating rates and zonal mean temperature. The SW heating rate peaks just below the stratopause level (1 hPa) at a value of about 0.21 K/d. A secondary stronger maximum is found at the top of the model domain with about 0.30 K/d which is due to heating at the Lyman-$\alpha$ wavelength. Temperature reacts to the altered radiative heating in a very similar way as was seen in the equilibrium simulations including interactive chemistry (cf. Figure 8.26). The temperature response in the upper stratosphere and lower mesosphere is comparable in magnitude to the CCM

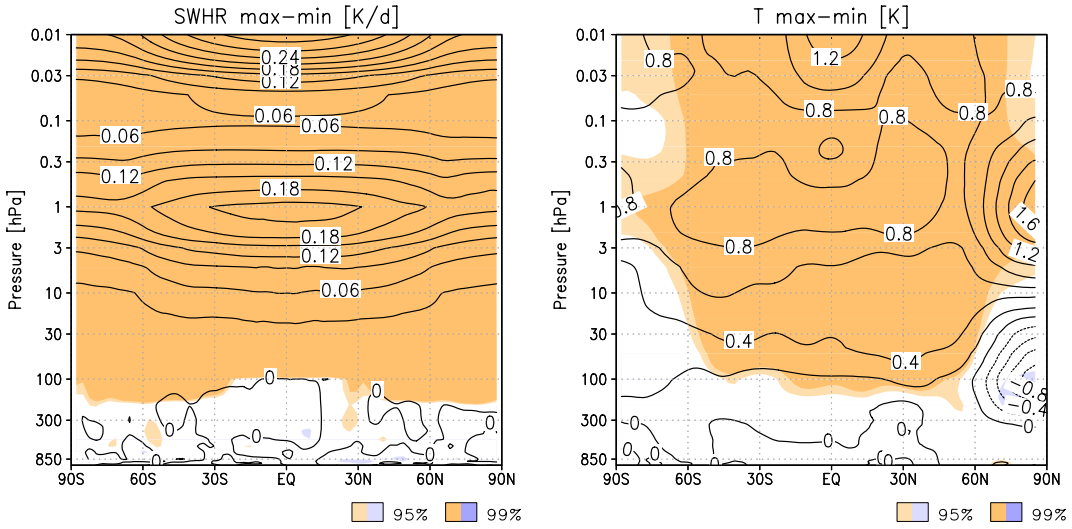


**Figure 8.32:** Annual mean short-wave heating rate difference (max-min, left). Contour interval is 0.03 K/d. Annual mean temperature difference (right). Contour interval is 0.2 K. Light (heavy) shading indicates statistical significance at the 95(99) % level.

results (0.9 K in Figure 8.32 right vs. 1 K in Figure 8.26). Higher up, in the mesosphere, the temperature response decreases reaching 0.6 K in the tropics and increases again towards the upper mesosphere reaching higher values (1.2 K) than at the mid-latitude stratopause. The solar signal in temperature at high northern latitudes is of comparable magnitude as in the equilibrium CCM simulations, too. Again the strong winter signal dominates the annual mean at high northern latitudes. The temperature response is statistically highly significant almost everywhere in the tropical and mid-latitude stratosphere and mesosphere and also at high northern latitudes. In comparison to the analogous Figure 8.26 it is conspicuous that the domain of statistical significance even comprises the tropical middle and lower stratosphere. This is due to the fact that no observed equatorial winds were assimilated into EMAC-FUB in GCM mode, hence, the variability associated with the QBO is absent in the present simulations.

### The northern hemisphere winter signal

The solar signal in zonal mean zonal wind during northern winter (bottom row of Figure 8.33) is well captured in comparison to the reanalysis data since 1980 (Figure 8.3). A westerly zonal wind anomaly moves downward from December to January and is replaced by an easterly anomaly in February. Then, in late winter, a significant zonal mean zonal wind change appears at mid-latitudes in the troposhere. The easterly anomaly on the equatorward side of the subtropical jet stream implies in connection with the westerly anomaly on the jet's northern flank a poleward shift of the zonal wind maximum. This is the response to the anomalous negative equator-to-pole temperature gradient in the tropical lower stratosphere in January and February. The tropospheric jet was shown to react to such a forcing in precisely that manner in chapter 6 and in sections 8.1.3

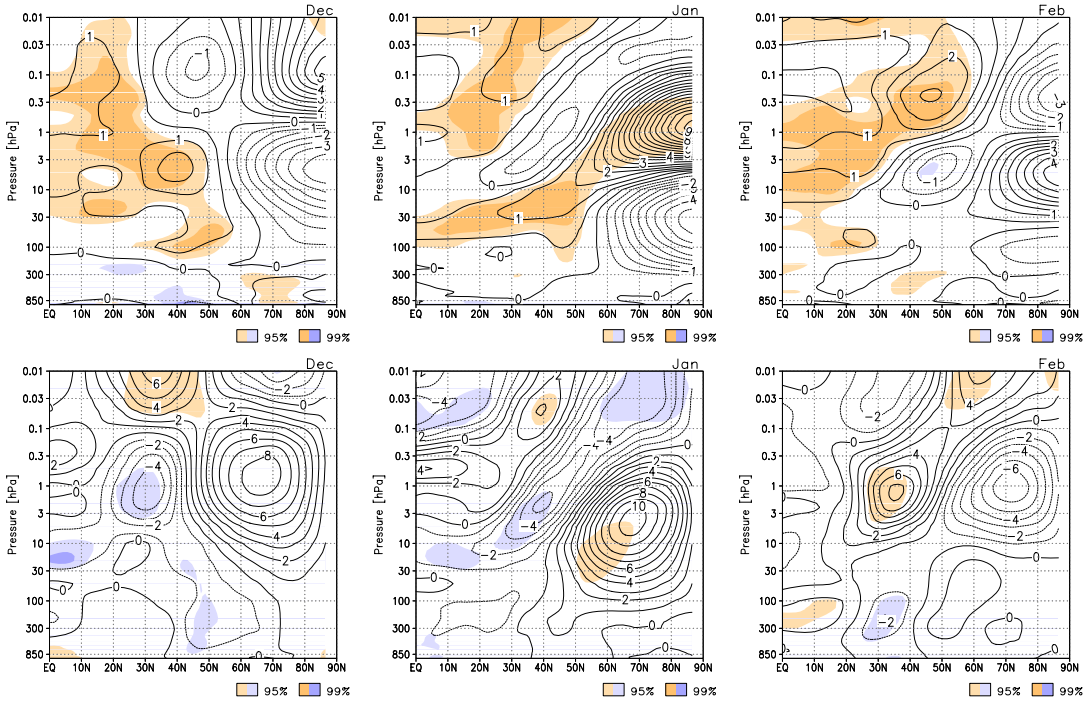


**Figure 8.33:** Monthly mean differences (max-min) of zonal mean temperature (top) and zonal mean zonal wind (bottom) from December to February. Contour interval is 0.5 K and 1 m/s, respectively. Light (heavy) shading indicates statistical significance at the 95(99) % level.

and 8.3 in agreement with the results of Haigh et al. (2005). The accompanying high-latitude temperature signal (top row of Figure 8.33) consists of a warm anomaly above a cold anomaly which descends from December to February, meanwhile, intensifying and becoming statistically significant in January.

The longitudinally resolved geopotential height differences for a stratospheric level (30 hPa) and near the surface (1000 hPa) for January are displayed in Figure 8.34 along with the 1000 hPa-temperature difference. It is seen that the 30 hPa-level is situated at significantly lower altitudes during solar maximum in vicinity of the pole. A similar signal is seen at 1000 hPa. In the transient reference simulation results for northern winter there is a time lag of about one month between the strongest signal in the middle and lower stratosphere and the maximum anomalies in the troposphere. No such delay is seen in the present equilibrium simulations with prescribed ozone climatology, indicating a consistent barotropic change at all altitudes from the middle stratosphere to the surface. As is found in the transient reference simulation the geopotential height differences show an AO-like pattern with the two characteristic positive anomalies over the Atlantic and the Pacific Ocean. Associated with this AO-like pattern in heights is a warming over central Europe of about 1.5 K which is statistically significant. The reason for this positive temperature anomaly is, as discussed before (cf. section 8.1.3), an enhanced transport of maritime air masses to the European continent by stronger westerlies that form due to the higher than average pressure in the Azores region and the lower than average pressure near Iceland.

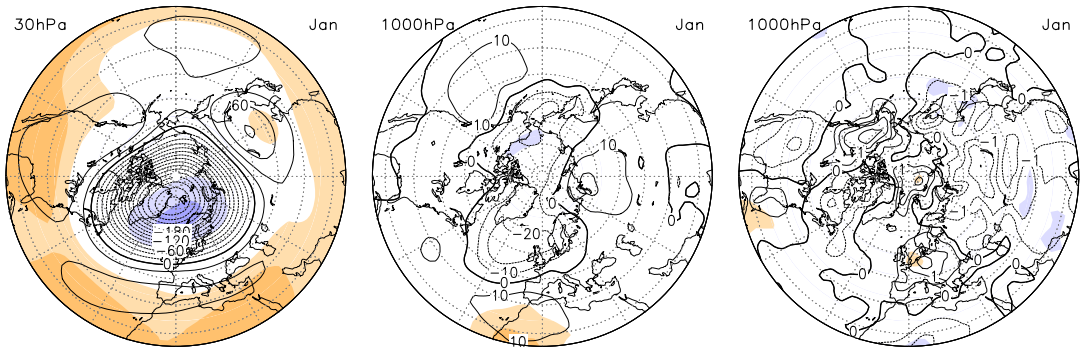


**Figure 8.34:** Monthly mean differences for January of left: Geopotential height at 30 hPa, contour interval is 20 gpm; Middle: Geopotential height at 1000 hPa, contour interval is 10 gpm; Right: Temperature at 1000 hPa, contour interval is 0.5 K. Light (heavy) shading indicates statistical significance at the 95(99) % level.

In summary, it can be stated that EMAC-FUB in GCM mode simulates a reasonable 11-year solar signal in the stratosphere, a likewise reasonable downward transfer of the signal and a tropospheric solar signal that resembles the one obtained from the transient reference simulation. This is interesting in view of the low level of scientific understanding that was stated in IPCC (2007) with respect to the solar influence on climate. If a GCM under certain prerequisites is able to simulate a consistent 11-year solar signal this opens the possibility to incorporate the solar cycle in the ensembles of scenario runs that form the basis of an IPCC report with a manageable effort of computing time. However, some important prerequisites have to be fulfiled: 1) The model must have a fully resolved stratosphere. 2) Since the 11-year solar signal is relatively weak, a realistic model climatology is necessary in order to obtain expedient results. 3) An ozone climatology needs to be prescribed to the model that accounts for the 11-year solar cycle ozone changes as well as for the (time-dependent) CFC-induced ozone depletion at southern polar latitudes in spring. 4) A suffiently high resolved short-wave heating scheme is absolutely essential when simulating the solar influence (cf. Chapter 3 of SPARC CCMVal, 2010). As EMAC-FUB with the ozone climatology based on Haigh (1994) meets these requirements it can be used in GCM mode to simulate the solar signal.

## 8.5 The influence of different SST and sea ice data sets

At present the majority of CCMs is not coupled to an interactive ocean model. For this reason SSTs and sea ice coverage have to be prescribed to the models as lower boundary condition. Depending on the focus of the respective study it might be appropriate or even necessary to use SSTs and sea ice data that were pre-calculated by an Atmosphere-Ocean-GCM. Garny et al. (2009) found in a comparative study significant differences in the climatologies of ozone and temperature in simulations with prescribed either observed or modelled SSTs and sea ice data. Furthermore, tropical upwelling and the Brewer-Dobson-Circulation and the trends in these quantities were affected by the choice of the SSTs

and sea ice. It is, therefore, conceivable that different SSTs may lead to different 11-year solar signals in the respective simulations.

In this section results from a transient simulation to which modelled SSTs were prescribed as lower boundary conditions are compared with results of the reference simulation that used observed SSTs at the lower boundary. Additionally, a transient simulation with fixed SSTs and fixed GHGs, a so-called "No-Climate-Change" simulation, is incorporated in the comparison. For details of the respective experimental setup see section 5.3.5 and 5.3.1 as well as section 5.3.6. To facilitate the comparison the same period from 1960 to 2005, i.e., 46 years, was analysed from all three simulations.

### 8.5.1 The annual mean signal

The annual mean solar regression coefficients for ozone and temperature from the experiment with modelled SSTs are displayed in Figure 8.35a and 8.35b. The ozone response to the 11-year solar variability in the upper stratosphere and lower mesosphere is similar to the response in the reference experiment (cf. Figure 8.1b). The maximum ozone increase at higher solar activity of about 2.5 % per 100 units F10.7 cm radio flux is found at mid-latitudes in the upper stratosphere at 5 to 3 hPa. The ozone sensitivity reaches a second maximum in the mesosphere of about 1 % between 0.3 and 0.1 hPa. Tropical lower stratospheric ozone increases by up to 5 % which is more than in the upper stratosphere. The signal ist statistically significant in a region between 20 and 40 ° on each hemisphere. The use of a different SST and sea ice data set, thus, yielded the secondary ozone change maximum in the tropical lower stratosphere that is seen in observations.

The temperature response to 11-year solar cycle irradiance changes is of the same order of magnitude of about 0.7 K per 100 units F10.7 cm radio flux at mid-latitudes at the stratopause as it is in the reference simulation with the observed SSTs (cf. Figure 8.2). Towards higher altitudes the temperature sensitivity decreases attaining a local minimum in the lower and middle mesosphere. Consistent with the secondary maximum in tropical lower stratospheric ozone a secondary maximum also appears in the temperature response pattern which is statistically marginally significant.

In the simulation with fixed SSTs the ozone response (Figure 8.35c) in the mid-latitude upper stratosphere is reduced compared to the reference simulation (cf. Figure 8.1b). The temperature signal (Figure 8.35d) is of comparable magnitude. The secondary maxima in the tropical lower stratospheric ozone and temperature have disappeared in the simulations with climatological SSTs.

These results emphasise the importance of the interplay between the 11-year solar cycle, the ENSO variability in the lower boundary condition and the QBO. The observed SSTs may be subject to 11-solar cycle changes. On the other hand, the modelled SSTs may be influenced by the 11-year solar cycle as it was prescribed to the atmospheric model. Furthermore, the intrinsic ENSO characteristics are different between the two

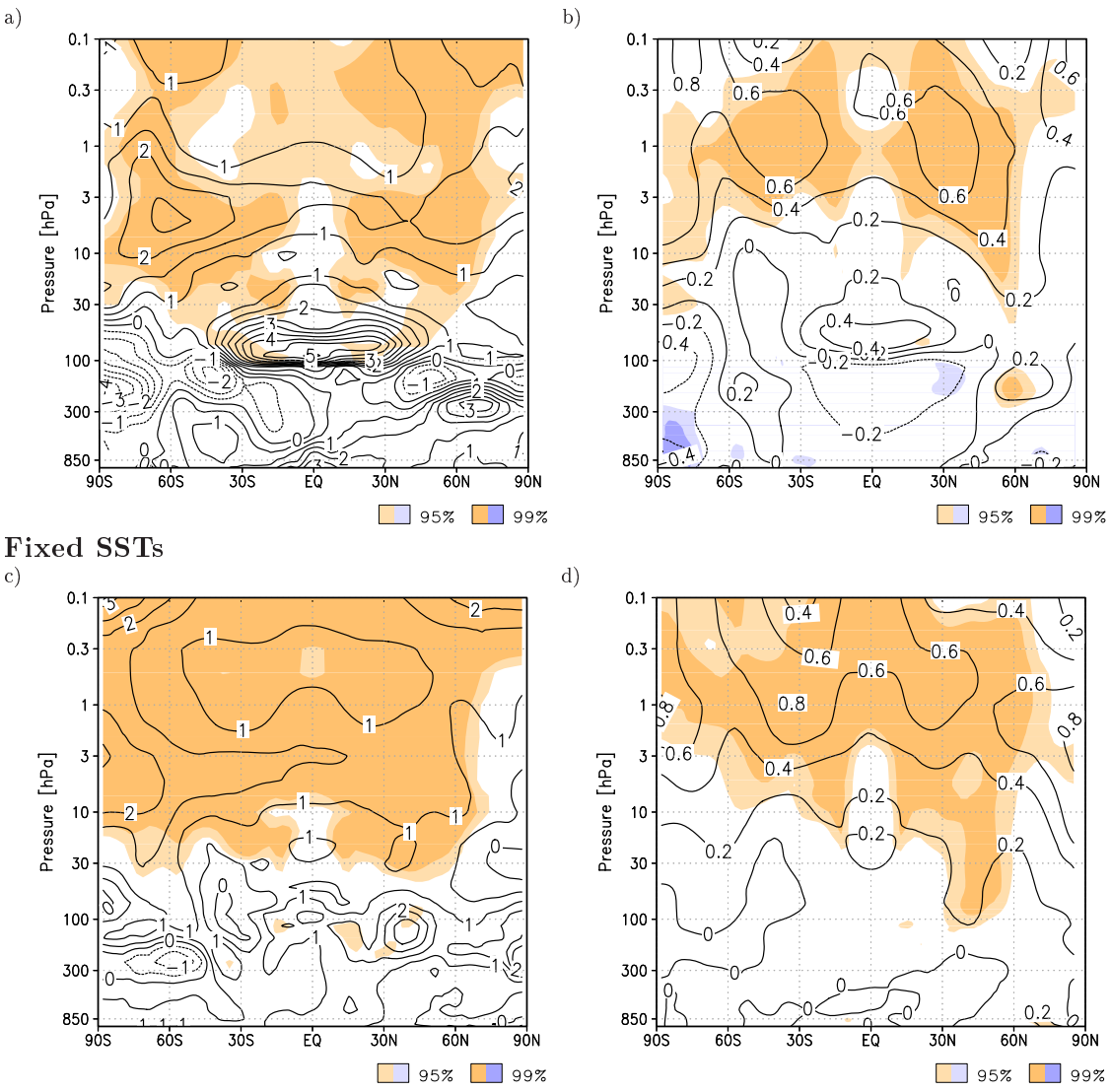


**Figure 8.35:** Annual mean solar regression coefficient of a and c) zonal mean ozone in % per 100 units of F10.7, contour interval is 0.5 % and b and d) Zonal mean temperature in K per 100 units of F10.7, contour interval is 0.2 K. Light (heavy) shading indicates statistical significance at the 95(99) % level.

data sets as is seen in Figure 8.36. The most striking difference is the higher amplitude of the modelled SST variability compared with the observed data. Especially, the intensity of ENSO cold events is overestimated in the modelled SSTs. This may contribute to the occurrence of the lower stratospheric ozone and temperature maximum in the solar signal since an ENSO cold event supports a positive ozone and temperature anomaly (cf. Figure 8.21). It is also seen, that the modelled SST anomalies have a different timing of warm and cold events. For example, the strong ENSO warm event that was observed in 1972 is not simulated by the Atmosphere-Ocean-GCM.

From the presence of the secondary maxima in ozone and temperature in the tropical lower stratosphere in the annual mean when modelled SSTs are used an influence on

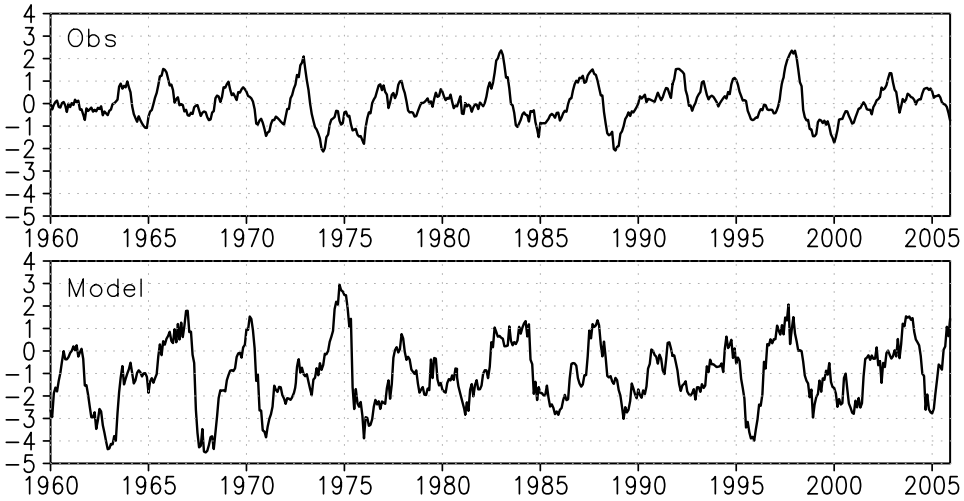


**Figure 8.36:** Niño3.4 index of the observed SSTs (top) and of the modelled SSTs (bottom).

the tropospheric circulation may be expected. Figure 8.37 shows the long term monthly mean tropical upwelling $\overline{w}^*$ at 300 hPa together with the 11-year solar cycle induced changes of $\overline{w}^*$ over the course of the year. In northern winter (December and January), when the region of strongest upwelling is situated south of the equator following the solar zenith there is a statistically significant reduction at 10 °S and a likewise significant increase at 20 °S. This implies a weakening of the updraft at its equatorward side and a strengthening at its poleward side. In southern winter (July and August) a similar signal is found at 10 °N. There, in the region of strongest upwelling, a reduced upward motion is found during periods of higher solar activity. The positive anomaly south of the equator indicates a decelerated downwelling.

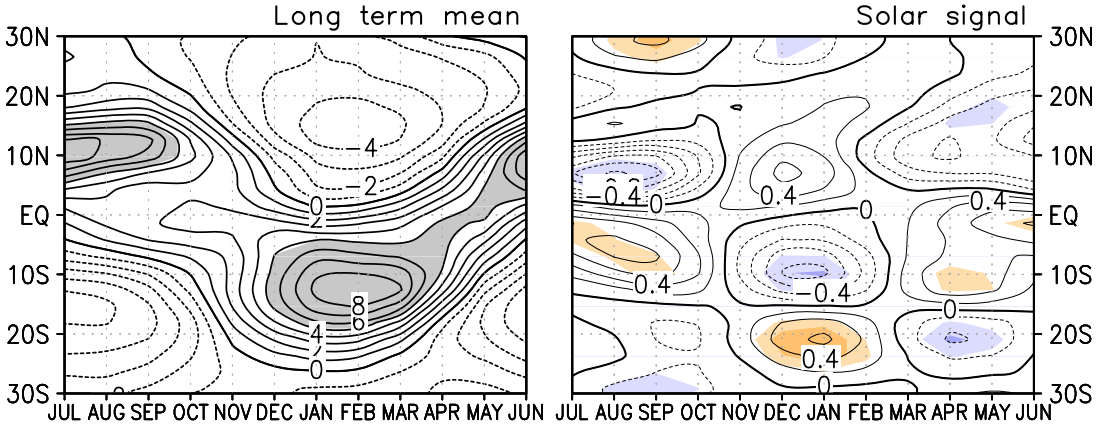


**Figure 8.37:** Left: Long term monthly mean of zonal mean residual vertical velocity $\overline{w}^*$ at 300 hPa in mm/s, contour interval is 1 mm/s, values exceeding 5 mm/s are shaded; Right: Monthly mean solar regression coefficient of zonal mean $\overline{w}^*$ at 300 hPa in mm/s per 100 units of F10.7, contour interval is 0.2 mm/s. Light (heavy) shading indicates statistical significance at the 95(99) % level.

The strong and significant signal in the zonal mean upper tropospheric upwelling may likewise imply strong changes in the longitudinally resolved data. The focus is on the solar signal in the Indian summer monsoon which is simulated by EMAC-FUB using observed SSTs as lower boundary condition.

### 8.5.2 The solar signal in the Indian summer monsoon

On the basis of the reference simulation it could be shown that the 11-year solar cycle influences the summer monsoon circulation in the Indian Ocean sector in a similar way as was described by Kodera (2004) (see Figure 8.17). It is interesting to re-examine this aspect now with modelled and also with fixed SSTs as lower boundary conditions.

Displayed in Figure 8.38 is the pressure velocity $\omega$ at 300 hPa in August, as long term monthly mean (left hand side) along with the solar regression coefficients (right hand side). Note that an upward directed $\omega$ is by definition negative. In the long term mean strong upward motion is basically seen over the African continent, the Red Sea and parts of the Arabian Peninsula as well as over the Indian Ocean near the equator and the land mass of north-eastern India. A closer inspection reveals a significant difference along the Indian west coast where a strong upward motion is present when observed SSTs are prescribed to the model which cannot be retrieved in the simulation using modelled SSTs nor in the one using fixed climatological SSTs. Moreover, the upwelling is weaker in the region of the Red Sea and the Arabian Peninsula when modelled or fixed SSTs are prescribed as lower boundary conditions.

The solar signal in the simulation with modelled SSTs is considerably weaker than in the experiment with observed SSTs. The latter exhibits an enhanced upwelling over the Red Sea which is statistically significant. Likewise significant is the stronger upwelling over the Indian Ocean in vicinity of the equator, as well as a reduction in upwelling at about 10 °N to the east and west of the Indian sub-continent. These changes are largely consistent with the correlation analysis of Kodera (2004) who considered an average over the months of July and August.

Only the negative Red Sea signal is statistically significant in the experiment with modelled SSTs. The anomaly near the equator is very weak and has changed sign. In the simulation with fixed SSTs there are only two regions with marginally statistically significant changes. A reduced upwelling is seen over north-eastern India and a stronger upward motion over eastern Africa.

These results show the strong effect of the SSTs on the tropospheric circulation and its sensitivity to natural climate variability. Only with observed SSTs a solar signal in the monsoon circulation similar to observations is obtained. This is an indication for an 11-year solar influence being included in the observed SSTs.

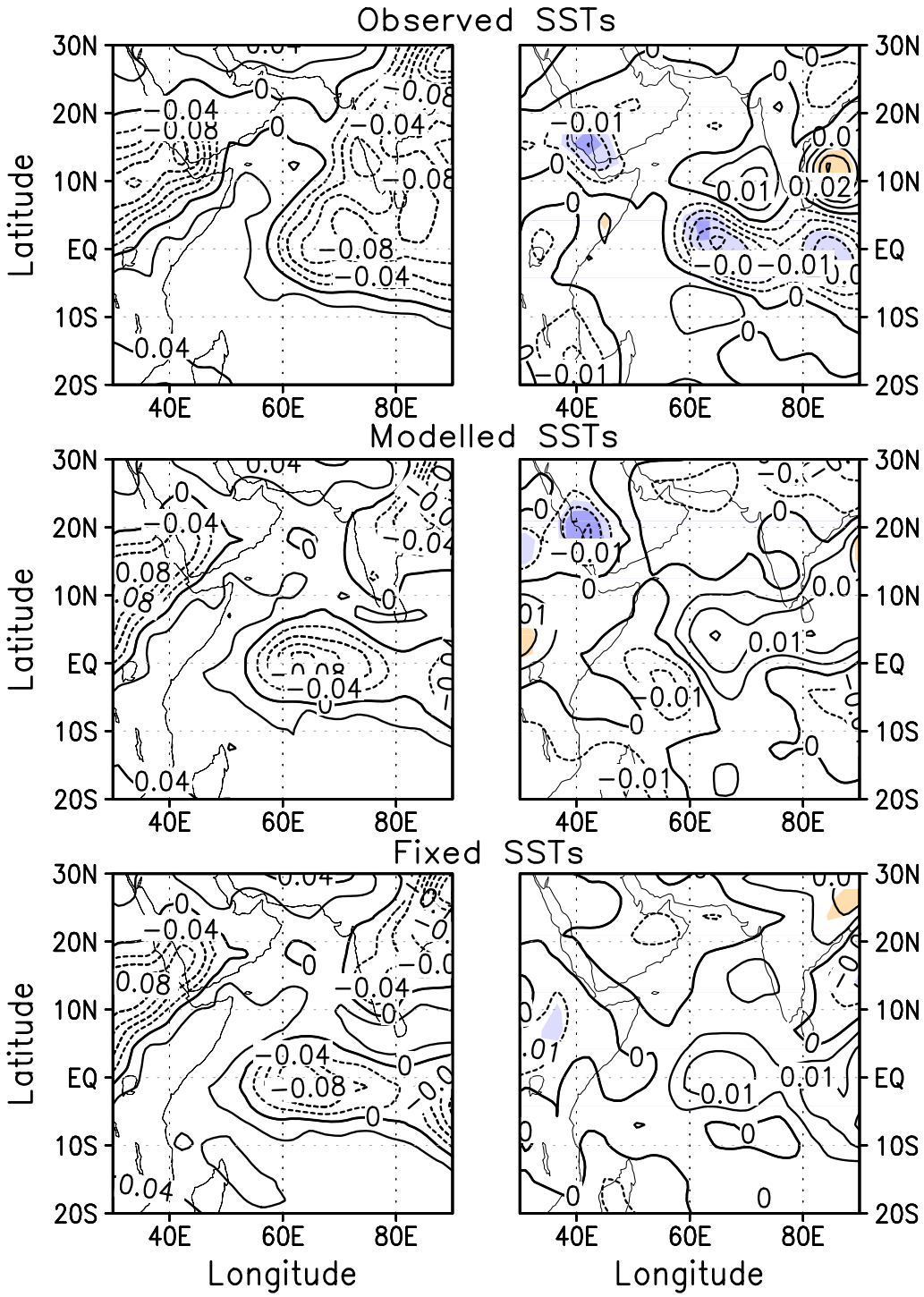


**Figure 8.38:** Monthly mean vertical pressure velocity $\omega$ at 300 hPa in Pa/s for August. Left: Long term mean absolute values, contour interval is 0.02 Pa/s. Note that upward velocities are negative. Right: Solar regression coefficient in Pa/s per 100 units of F10.7, contour interval is 0.005 Pa/s. Light (heavy) shading indicates statistical significance at the 95(99) % level.

The different ENSO variability in the modelled SSTs may also contribute to the change in the background climatology. As is seen from Figure 8.36 there seems to be a bias towards stronger and longer lasting ENSO cold periods in the modelled data set. Thus, the results confirm the importance of a realistic background climatology for solar influence simulations. The long term mean upwelling obtained with the observed SSTs is in this regard in general agreement with the NCEP data (Kalnay et al., 1996; Kistler et al., 2001) averaged from 1979 to 2001 (not shown) which are themselves the output of a reanalysis model since the vertical velocity is difficult to measure.

In the absence of SST variability the signal has virtually disappeared. In comparison with the weak solar signal that occurred in the solar maximum and minimum equilibrium experiments (Figure 8.29) this rises the question whether the equilibrium simulation result is actually not a real solar signal but a mere QBO influence. An argument against this interpretation is the consistent spatial structure of the QBO modulated solar signal (Figures 8.30a and 8.30b) However, the perpetual constant solar maximum and minimum simulations do by definition not contain a temporal evolution of the solar irradiance. This may yield a more distinct signal than obtained from the multiple linear regression analysis of a simulation with time-varying solar irradiance forcing.

### 8.5.3 The solar signal in a changed climate in the second half of the 21st century

The period from 1960 to 2100 covered by the SCN2d simulation allows to investigate whether the solar signal changes under a changing climate. By the end of the 21st century the $CO_2$ concentration has more than doubled compared to the 1960 values. Polar stratospheric ozone is projected to have returned to 1980 values but not to have fully recovered from the influence of chlorofluorocarbons whereas tropical ozone continuously declines due to a projected increase in tropical upwelling (Eyring et al., 2010).

To facilitate the comparison the period in the second half of the 21st century spans 46 years, from 2055 to 2100. This is the same number of years as in the past period from 1960 to 2005. The same regression approach is used for the past and the future, except that no volcanic eruptions are considered in the simulation and in the regression model due to the episodic and unpredictable character of such events.

The annual mean ozone response to 11-year solar variability in the future is in its main features similar to the response in the past. The ozone volume mixing ratio increases by about 2 to 2.4 % in the extratropical upper stratosphere at about 5 hPa (Figure 8.39a). It is interesting to note the absence of a signal in the lower mesosphere between about 1 hPa and 0.1 hPa (50 to 65 km). Another difference can be noted in the tropical lower stratosphere. Where in the past period a strong and significant secondary maximum is seen there is a very weak and insignificant response in the future period.

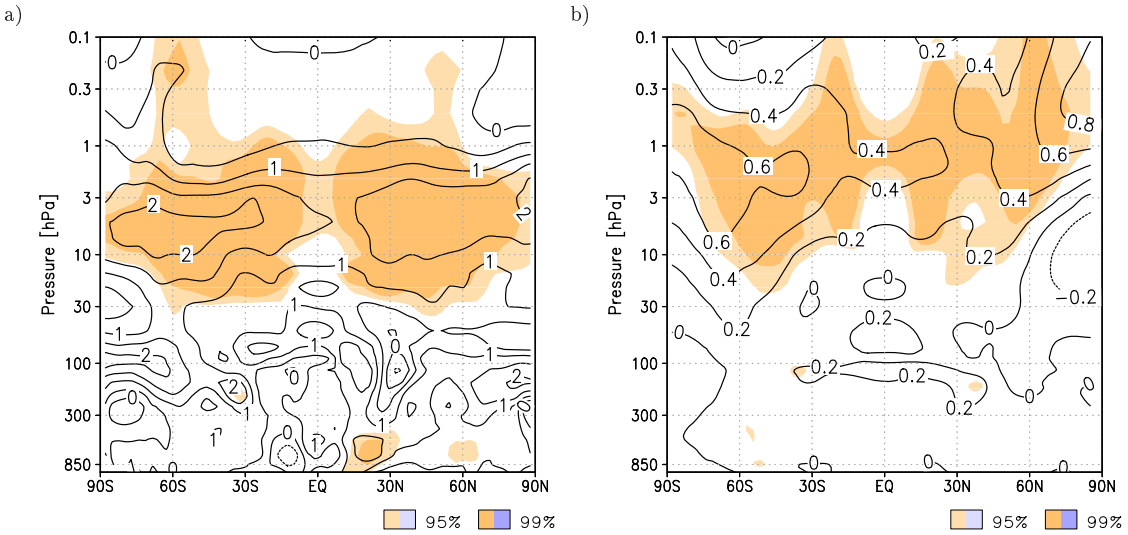


**Figure 8.39:** Annual mean solar regression coefficient of a) zonal mean ozone in % per 100 units of F10.7, contour interval is 0.5 % and b) Zonal mean temperature in K per 100 units of F10.7, contour interval is 0.2 K. Light (heavy) shading indicates statistical significance at the 95(99) % level.

The temperature signal near the stratopause is comparable in magnitude to the signal in the past, but it is situated at a lower altitude. The changes are highly significant in the extratropics (Figure 8.39b). At high northern latitudes a dipole pattern with a significant warming at the stratopause and in the lower mesosphere and a cooling in the middle stratosphere appears. This signal was absent in the past analysis period, but was also seen in the reference simulation of the past with observed SSTs (Figure 8.2a). The secondary maximum in the tropical lower stratosphere that was found in the past period is weaker in the future period. However, due to a large internal variability in this region the signals in both the past and the future period are statistically not significant.

It is also noted that the area with statistically significant changes has shrinked from the past to the future period. This points towards an increased variability in the atmosphere in a warming climate.

However, these results are subject to a substantial uncertainty associated with the imposed solar irradiance changes. The solar cycles 20 to 23 (1962-2004) were repeated several times to continue the solar irradiance time series for the model input. As the solar activity will not necessarily remain on the present relatively high level this assumption may be unrealistic, particularly, since there are indications for a decrease of solar activity in the future (Solanki et al., 2004; Abreu et al., 2008).

### 8.5.4 Summary and Discussion

It has been shown that the annual mean 11-year solar signal in ozone and temperature depends on the sea surface temperatures that are prescribed to the model as lower

boundary conditions. A data set of modelled SSTs obtained from a coupled Atmosphere-Ocean-GCM shows a bias towards ENSO cold events. This may be responsible for the appearance of secondary maxima in the ozone and temperature solar signals in the tropical lower stratosphere since it had previously been shown that the Niño3.4 index describing ENSO activity is anti-correlated with temperature and ozone in the tropical lower stratosphere in the sense that ENSO cold events favour higher ozone abundances and higher temperatures (cf. section 8.2). The use of fixed SSTs reduces the solar signal in the tropical lower stratosphere.

Furthermore, the specified SSTs affect the upwelling climatology which deviates from observations when modelled or fixed SSTs are used. This, combined with the absence of an intrinsic 11-year solar variability in the modelled SSTs (and of course in the fixed SSTs) reduces the response of the Indian summer monsoon circulation to the solar influence.

Finally, it has been shown that the annual mean 11-year solar signal in ozone and temperature will likely remain unaffected in its main characteristics in a changing climate. However, this statement is only valid if it is assumed that solar activity itself will remain on the relatively high level which was observed in recent decades.

# Chapter 9

# The SOLARIS Comparison

In this chapter the questions related to the appearance of the secondary maxima in ozone and temperature in the tropical lower stratosphere in response to the 11-year solar cycle are addressed. The interactions of 11-year solar forcing, the QBO and ENSO are examined by means of a comparison. The reference simulation (see section 8.1) is compared to a similar simulation in which band-pass filtered QBO and SST forcings were used. The motivation for these experiments is the fact that most CCMs still need prescribed SSTs and equatorial zonal winds. Observed time series are used for this purpose which may, however, be themselves influenced by the 11-year solar cycle and may, thus, contain an 11-year periodicity. It is suspected that (non-)linear interactions of the solar irradiance variability with the QBO and the SST-variability associated with ENSO produce secondary maxima in the temperature and ozone responses to the 11-year solar cycle (Marsh and Garcia, 2007; Smith and Matthes, 2008). The removal of the 11-year period from the other two observed forcing time series as well as the suppression of mutual influences between the QBO and the SSTs should, hence, minimise the possibility for linear interactions.

The simulations with filtered forcings were defined and performed within the framework of the Solar Influence for SPARC (SOLARIS) initiative (Kunihiko Kodera and Katja Matthes, SPARC conference, Bologna, 2008). The intention of the filtering is to remove possible solar induced periodicities from the other two forcing time series as well as to remove mutual influences of, e.g. the ENSO phenomenon on the QBO or vice versa. In this way, the forcing time series become linearly independent. The applied filter retained periods between 0.75 and 4 years for the QBO time series. From the SST and sea ice data all periods between 2 and 3 years as well as periods greater than 7 years were removed. Hence, the annual cycle is still contained in the time series (cf. section 5.3.7). If the secondary maxima in ozone and temperature emerge in the simulation with filtered forcings this could be an indication for either a purely solar origin or for non-linear interactions being operative, since linear interactions are suppressed by the band-pass filtering of the forcing time series.

**Table 9.1:** Some basic features of the three models that performed the SOLARIS simulations.

| | **EMAC-FUB** | **MRI-CCM** | **WACCM** |
|---|---|---|---|
| Model type | spectral | spectral | finite volume |
| Horizontal resolution | 2.8° × 2.8° | 2.8° × 2.8° | 1.9° × 2.75° |
| Vertical extension | 0-80 km | 0-80 km | 0-140 km |
| Vertical resolution | 39 levels | 68 levels | 66 levels |
| Self-consistent QBO | no | yes | no |

## 9.1 Transient simulations with filtered forcings

Apart from EMAC-FUB, the same simulations with filtered forcings were performed with the MRI-CCM of the Japanese Meteorological Research Insitute in Tsukuba (Japan) and with the Whole Atmosphere Community Climate Model (WACCM) of NCAR in Boulder, Colorado. Kiyotaka Shibata at MRI and Katja Matthes at Deutsches GeoForschungsZentrum Potsdam (Germany) conducted the simulations and kindly provided the data for this novel analysis. Results from the simulations with filtered forcings with the three models are incorporated into the comparison along with results from the reference simulations that were performed with the very models in the framework of the SPARC CCMVal-2 intercomparison. Table 9.1 gives an overview of the most important features of the participating models. Details about the MRI-CCM can be found in Shibata and Deushi (2008) and about WACCM in Garcia et al. (2007) and Richter et al. (2010). The MRI-CCM has a sufficient vertical resolution to simulate a self-consistent QBO. For the present analysis this implies that for this particular model a solar influence on the QBO and an influence of the SSTs on the QBO cannot be ruled out.

Model output data from the SPARC CCMVal-2 REF-B1 simulations forced with unfiltered time series have been obtained from the British Atmospheric Data Centre (BADC) where the results of all models participating in the SPARC CCMVal-2 intercomparison are stored. The coverage of CCMVal-2 simulation results is limited to the altitude range from 0 to 65 km (1000 to 0.1 hPa) in accordance with the CCMVal data request[1].

## 9.2 The annual mean solar signal

The analysis of the transient simulation with filtered forcings starts with a correlation analysis to gain a qualitative impression of the individual forcing factors' impact. The time series of detrended zonal mean short-wave heating rates, ozone, and temperature at each gridpoint are correlated with the time series of the F10.7 cm-solar radio flux, the Nino3.4-index calculated from the observed filtered SST fields, and the QBO at 50 hPa

[1]The SPARC CCMVal-2 data request is available online at `http://www.pa.op.dlr.de/CCMVal/DataRequests/CCMVal-2_Datarequest_FINAL.pdf`.

as it was used for the assimilation of the equatorial zonal wind, respectively. For MRI-CCM results the simulated zonal mean zonal wind at 50 hPa is used for correlation. At a later stage a multiple linear regression model is applied to analyse the contribution of the individual forcings in a more quantitative way (section 9.2.2).

### 9.2.1 Correlation analysis

Both the simulations with filtered forcings and with observed forcings cover the period 1960 to 2005, i.e., 46 years. For the correlation analysis this implies that absolute values of the correlation coefficient exceeding 0.3 are statistically significant on the 95 %-level, and those exceeding 0.4 on the 99 %-level. Results are shown in the altitude range 0 to 65 km (1000 to 0.1 hPa).

The correlation of short-wave heating rates with the 10.7 cm-solar radio flux is strongly positive in the stratosphere and lower mesosphere in EMAC-FUB, the MRI-CCM and WACCM (Figure 9.1a-c). It is seen from Figure 9.1a-9.1c that the correlation coefficients exceed 0.7 in a wide latitude range above the stratopause in all models. This can be interpreted as that the variation of solar output explains more than 49 % of the variation of short-wave heating rates in this region using the square of the correlation coefficient as coefficient of determination. For EMAC-FUB the correlation peaks at values larger than 0.8 in the lower mesosphere. The response in WACCM is not as strong as in the other two models. The correlation maximum in the WACCM results is located somewhat lower than in EMAC-FUB and the MRI-CCM. Simultaneously, the area with significant changes is smaller in WACCM than in the other two models. It reaches from the top of the considered domain down to about 5 to 10 hPa whereas its lower boundary in located between 10 and 30 hPa in EMAC-FUB and the MRI-CCM. A comparison with results of the reference simulations which are depicted in Figure 9.2a-9.2c shows similar distributions of the significant correlation areas in the upper stratosphere and mesosphere.

The correlation of temperature with the 10.7 cm-solar radio flux (Figure 9.1d-9.1f) in general follows the signal in the short-wave heating rates with the exception of the equatorial latitudes where the variability associated with the QBO degrades the correlation. However, in the tropical upper stratosphere the correlation is still statistically significant. This is different from the simulations with unfiltered forcings (Figure 9.2d-9.2f) where the correlation drops below the significance level in a wide altitude range near the equator. The higher correlation coefficients in the simulations using filtered forcings indicate an improved similarity of temperature and solar flux variations with time when linear solar cycle-QBO interactions are suppressed.

Ozone volume mixing ratio is closely correlated with the 10.7 cm-solar radio flux, in particular, in two regions: in the altitude range of the absolute maximum of ozone volume mixing ratio at about 10 hPa and above the stratopause (Figure 9.1g-9.1i). The

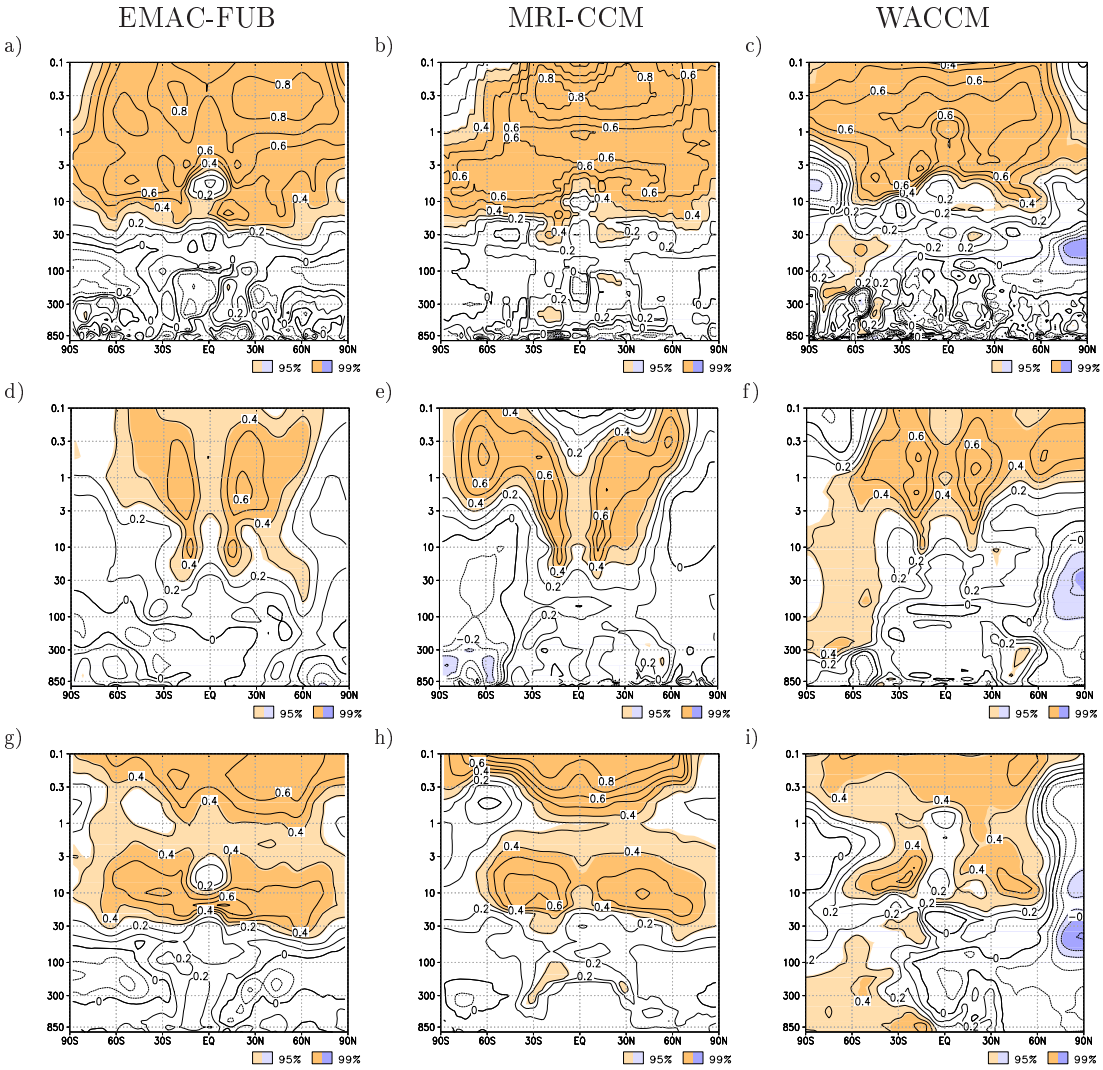


**Figure 9.1:** Annual mean correlation of zonal mean short-wave heating rates (top), temperature (middle) and ozone (bottom) with the F10.7 cm solar radio flux from **SOLARIS** simulations using filtered forcings with EMAC-FUB (left), the MRI-CCM (middle) and WACCM (right). Contour interval is 0.1. Light (heavier) shading indicates statistical significance on the 95 %(99 %)-level.

signal near 10 hPa shows a structure with two maxima at mid-latitudes. This structure is comparable to observations (Randel and Wu, 2007) and to the results of the reference simulations (Figure 9.2g-9.2i). In both WACCM runs, i.e., with filtered and unfiltered forcing time series, the maximum correlation between ozone and the solar flux is located at somewhat higher altitudes than in the other two models. The correlation of lower mesospheric ozone with the solar activity proxy is strongest for the MRI-CCM in both the SOLARIS and the reference simulations.

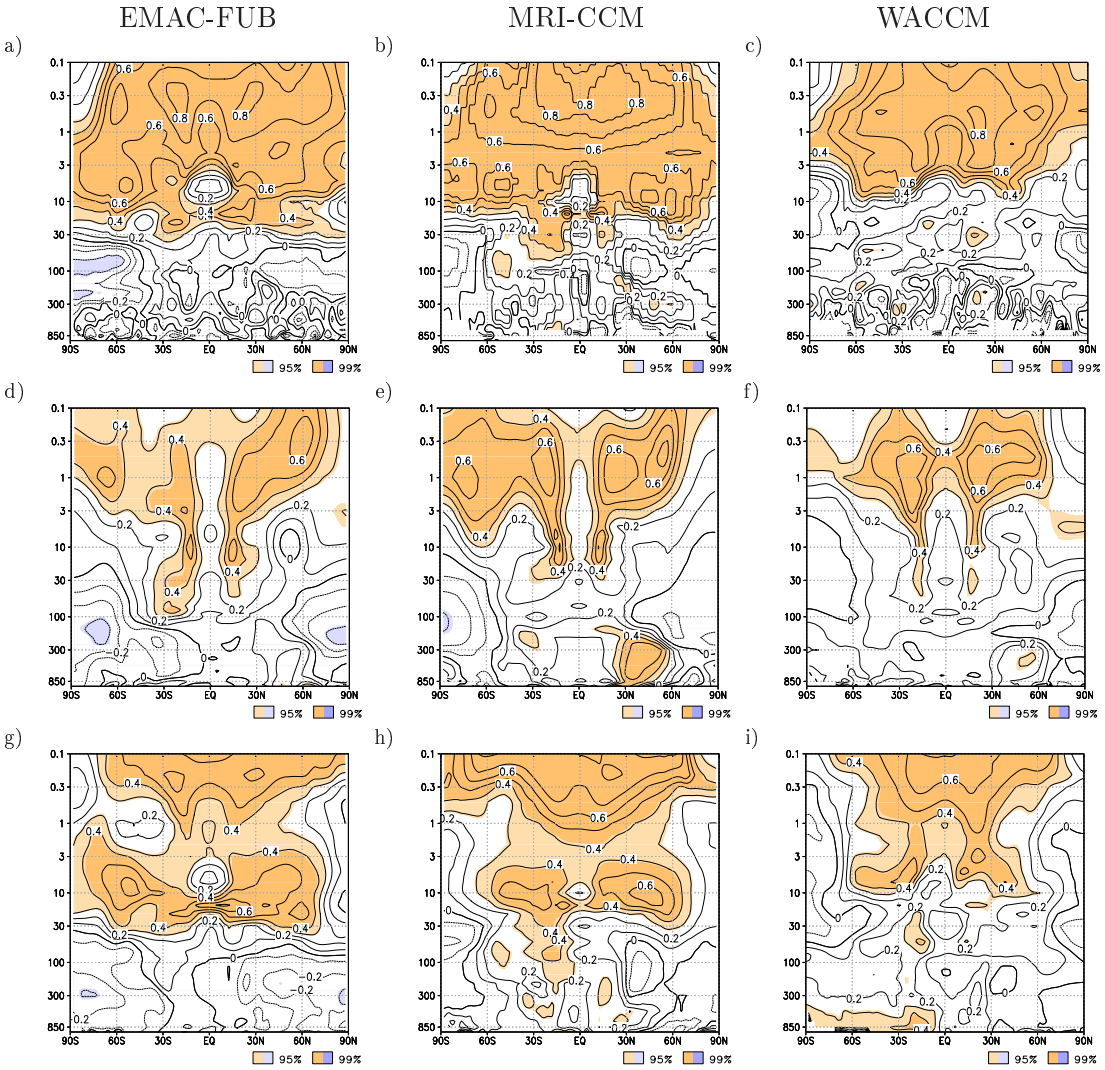


**Figure 9.2:** Annual mean correlation of zonal mean short-wave heating rates (top), temperature (middle) and ozone (bottom) with the F10.7 cm solar radio flux from **CCM-Val REF-B1** simulations with EMAC-FUB (left), the MRI-CCM (middle) and WACCM (right). Contour interval is 0.1. Light (heavier) shading indicates statistical significance on the 95 %(99 %)-level.

### 9.2.2 Multiple linear regression analysis

The above correlation analysis provides a qualitative impression about the uniformity of variations of two quantities, in this case, e.g., ozone and the F10.7 cm radio flux as indicator for solar irradiance variability. A more quantitative view of the response to the 11-year solar variability is provided by the following multiple linear regression analysis. The results from the SOLARIS runs with filtered forcings are shown in Figure 9.3 and from the reference simulations with observed forcings, for comparison, in Figure 9.4.

EMAC-FUB simulates a solar signal in SW heating in the stratopause region of about 0.13 K/d per 100 units F10.7 solar radio flux. WACCM and the MRI-CCM both exhibit a somewhat stronger signal of about 0.15 K/d per 100 units F10.7 solar radio flux

(Figure 9.3a-c). Compared to the results from the reference simulations using unfiltered observed QBO and SST forcings (Figure 9.4a-c) there is good agreement for EMAC-FUB and WACCM. The MRI-CCM, however, shows a stronger SW heating response in the reference simulation of up to 0.21 K/d per 100 units F10.7 solar radio flux. Since the solar forcing was identical in the simulations with filtered and unfiltered simulations this may be due to the multiple linear regression analysis which weights the influence of the respective basis functions in order to fulfil the least-squares requirement.

The temperature signals from the SOLARIS simulations with the three models agree in the order of magnitude but differ with respect to the region where the maximum re-

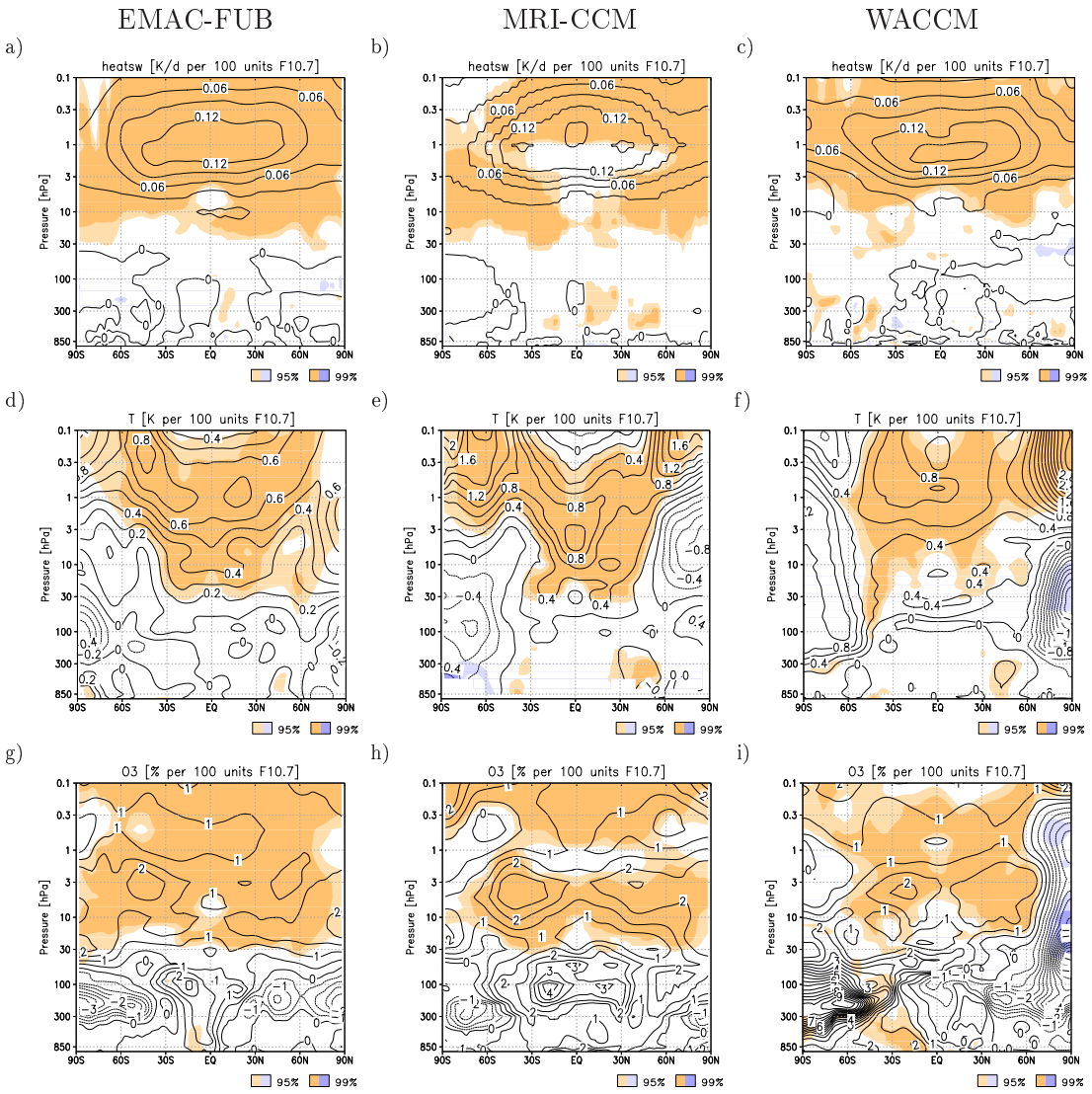


**Figure 9.3:** Annual mean solar regression coefficient per 100 units of F10.7 from **SOLARIS** simulations using filtered forcings with EMAC-FUB (left), the MRI-CCM (middle) and WACCM (right). Top: Zonal mean short-wave heating rates in K/day, contour interval is 0.03, middle: Temperature in K, contour interval is 0.1 for EMAC-FUB and 0.2 for the MRI-CCM and WACCM, and bottom: Ozone in percent, contour interval is 0.5. Light (heavier) shading indicates statistical significance on the 95 %(99 %)-level.

sponse is found (Figure 9.3d-f). The MRI-CCM shows a temperature increase above the equator in the upper stratosphere at about 5 to 3 hPa. The signals in EMAC-FUB and WACCM have their tropical maxima at higher altitudes at or slightly above 1 hPa. From southern to northern mid-latitudes EMAC-FUB and WACCM show a qualitatively similar temperature signal in the mesosphere with the signal being stronger in WACCM. The responses at both northern and southern polar latitudes are very different in the three models. In comparison to the results from the reference simulations with unfiltered observed forcings (Figure 9.4d-9.4f) there is an interesting change: The latitudinal distribution of the solar signal in temperature has lost its hemispheric structure with maxima in the subtropics on either hemisphere. Instead it has become more equatorially cen-

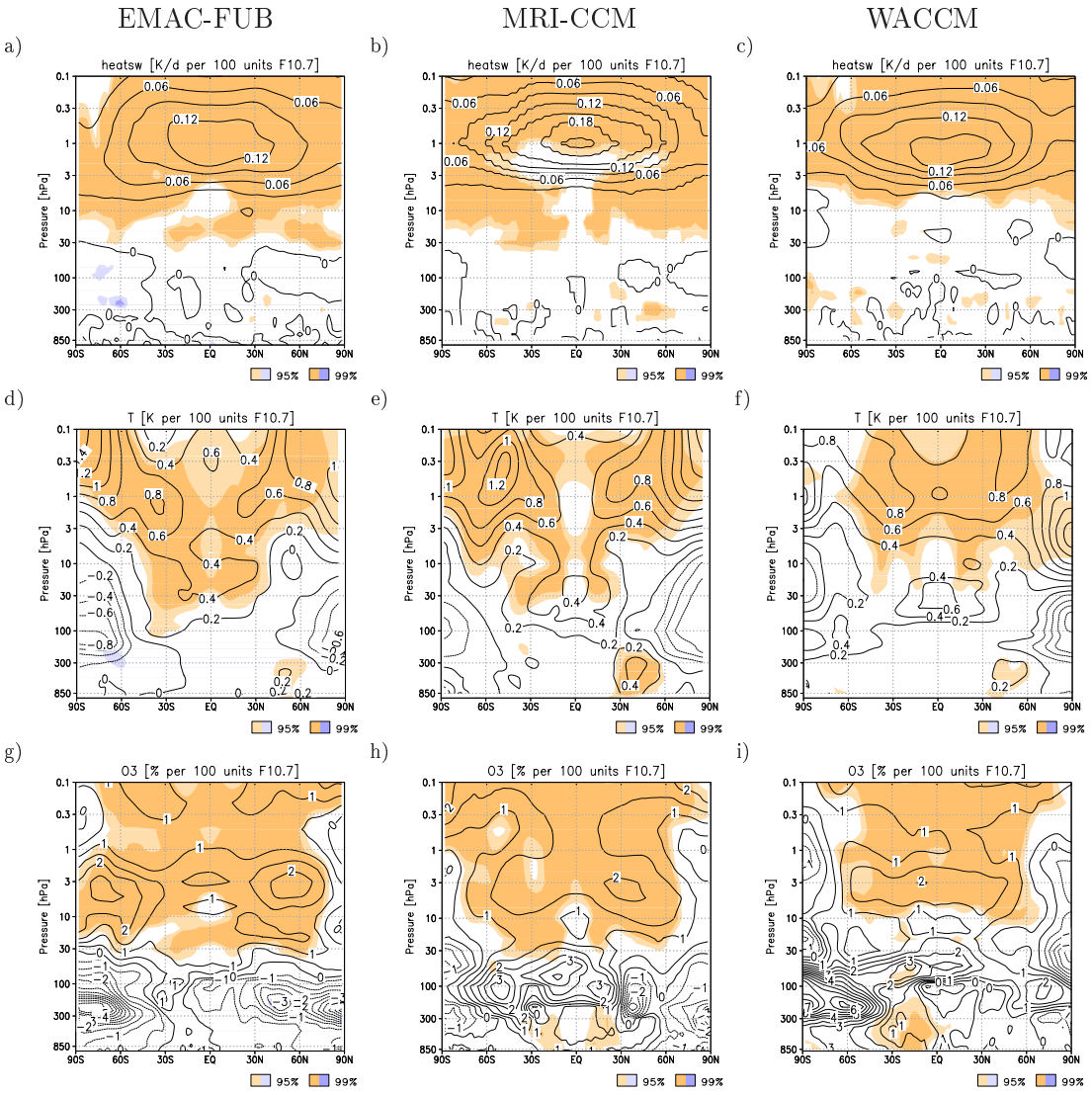


**Figure 9.4:** Annual mean solar regression coefficient per 100 units of F10.7 from **CCM-Val REF-B1** simulations with EMAC-FUB (left), the MRI-CCM (middle) and WACCM (right). Top: Zonal mean short-wave heating rates in K/day, contour interval is 0.03, middle: Temperature in K, contour interval is 0.2, and bottom: Ozone in percent, contour interval is 0.5. Light (heavier) shading indicates statistical significance on the 95 %(99 %)-level.

tred. A similar equator-centred latitudinal distribution is seen in observations (Randel et al., 2009). The MRI-CCM and WACCM show a tendency towards a slight secondary increase of the temperature change in the tropical lower stratosphere below about 30 hPa in both the simulations with filtered and unfiltered forcings. The signal in this region is statistically not significant due to the variability that is introduced by the QBO. In the EMAC-FUB results no such increase can be found. In the troposphere the three models simulate a statistically significant annual mean warming in the subtropics and at mid-latitudes which is particularly pronounced in the MRI-CCM and in WACCM. This is found in the SOLARIS simulation results as well as in the reference simulations.

There is general agreement among the models about the ozone response to increased solar irradiance (Figure 9.3g-9.3i). About 1.5 to 2.5 % per 100 units F10.7 solar radio flux more ozone are found at mid-latitudes in the altitude region between about 5 hPa and 3 hPa. Compared with the solar signal obtained from the reference simulations with unfiltered observed forcings (Figure 9.4g-9.4i) it is seen that the latitudinal structure has changed in all three models when the filtered forcings are used. This is an improvement when compared with observations as these show a structure with two maxima at mid-latitudes (Randel and Wu, 2007). Furthermore, the ozone sensitivity in the MRI-CCM and in WACCM is higher in the SOLARIS simulations than in the reference simulations. In the tropical lower stratosphere between about 50 and 30 hPa the ozone response increases again in the MRI-CCM and in WACCM in both the reference and the SOLARIS simulations. In EMAC-FUB an increase does occur only below 50 hPa and only in the simulation using filtered forcings (Figure 9.3g). None of these secondary signals is statistically significant.

Figure 9.5 shows the profiles of 11-year solar cycle induced ozone and temperature changes from the simulations using filtered forcings together with the reference simulations using unfiltered observed forcings.

The ozone change profiles in Figure 9.5a confirm the general agreement between the models about the upper stratospheric ozone response. At about 3 hPa the profiles of the respective filtered and unfiltered simulation are located close to each other. This is a strong indication for the upper stratospheric solar signal being independent from the specification of the filtered or unfiltered QBO or from the prescribed tropical SSTs. This supports earlier results reported by Rind et al. (2008) or in SPARC CCMVal (2010). In the tropical lower stratosphere there is a considerable spread of the signals. The two EMAC-FUB profiles show no secondary peak in ozone change. At about 30 hPa the solar signal in ozone is reduced in the simulation with filtered forcings compared to the reference simulation. The EMAC-FUB profiles diverge strongly below about 50 hPa. While the profile obtained with filtered forcings shows an ozone increase towards lower levels ozone behaves inversely in the reference simulation. It is difficult to draw any conclusion from these results. The difference between the two curves representing the MRI-CCM is small from about 2 hPa in the upper stratosphere down to about 80 hPa

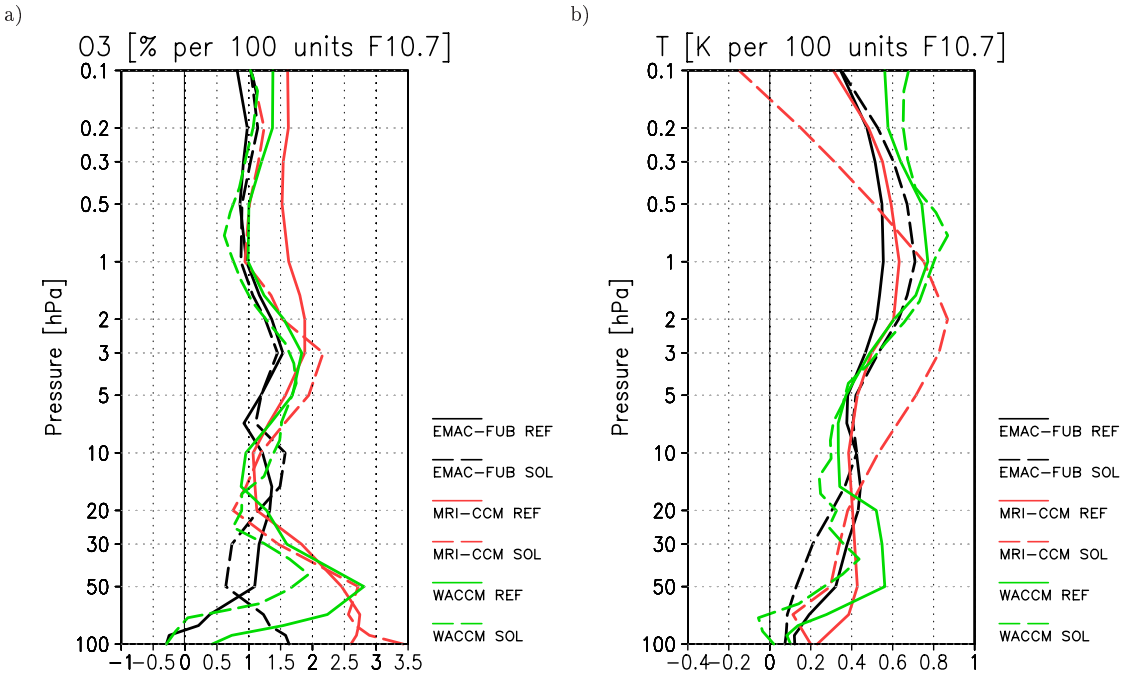


**Figure 9.5:** Profiles of the tropical mean (25 °S-25 °N) annual mean solar regression coefficient of a) Ozone in percent per 100 units of F10.7 and b) Temperature in K per 100 units of F10.7. Solid lines depict results from simulations with unfiltered input time series, dashed lines from simulations using filtered forcings.

in the lower stratosphere. Keeping the fact in mind that the MRI-CCM simulates its own QBO this leads to the inference that a possible solar influence on the QBO is still contained in the filtered MRI-CCM simulation. Between the two WACCM profiles there is a noticeable difference in the lower stratosphere. The solar induced ozone change decreases when the 11-year component is removed from the QBO and the SST time series. The response from the simulation using filtered forcings can be interpreted as the "pure" solar signal. Hence, the tropical lower stratospheric ozone maximum in the solar signal would have a component that is indeed solar-cycle induced but it has, furthermore, a fraction which emerges from the linear interaction of the 11-year solar cycle with the QBO and the SSTs. Another interpretation is also possible: The maximum may be the result of non-linear interactions between the QBO and SST time series at their own frequencies with the 11-year solar forcing which then produces variability on the 11-year time scale. However, the profile from the reference simulation and from the simulation with filtered forcings are enclosed in large uncertainty ranges (not shown) because of the correlation between ozone and solar irradiance being weak in this region, only about 0.15. This implies that neither of the secondary maxima is statistically significant nor is the difference between the two profiles statistically significant.

The temperature profiles from the reference simulations with unfiltered observed forcings and the simulations with filtered forcings are seen in Figure 9.5b. The reference simulation profiles (solid lines) all show the maximum temperature response to changes

in solar activity in the stratopause region at values ranging from 0.5 to 0.8 K per 100 units F10.7 cm solar radio flux. Towards lower altitudes temperature is less sensitive to solar irradiance changes before the signal increases again below about 7 hPa. WACCM and to a weaker extent also the MRI-CCM show a secondary peak in the temperature response in the tropical lower stratosphere. EMAC-FUB has no such secondary peak, instead there is a slight increase in the middle stratosphere and a monotonic decrease below. When the filtered forcings are applied EMAC-FUB simulates a stronger temperature response in the stratopause region compared to the unfiltered forcings and so does WACCM. The MRI-CCM's temperature change profile from the simulation with filtered forcings has a very different shape compared to the reference simulation result. This is due to the equator-centred temperature response in the simulation with filtered forcings (cf. Figure 9.3e) and the response pattern of the reference simulation which exhibits maxima at subtropical and mid-latitudes (cf. Figure 9.4e). In the lower stratosphere the temperature response is reduced in all three models when the filtered forcings are applied. However, the differences between the respective profiles are statistically not significant as the uncertainty of the fits is large below about 50 hPa. Thus, the same caveat concerning the uncertainty that was expressed in the context of the ozone profiles is valid for the temperature profiles.

Figure 9.6a shows the ozone change profiles due to the ENSO associated SST variability. In the upper stratosphere and lower mesosphere there is very little influence of ENSO on ozone. However, in the middle and lower stratosphere ENSO has a non-negligible effect on ozone in the sense that the ozone abundance decreases during ENSO warm events expressed as positive anomalies of the Niño3.4 index. This is most pronounced in the reference simulations with EMAC-FUB and WACCM. When filtered forcings are used, in particular, filtered SST time series, the response decreases markedly below about 50 hPa in these two models. The MRI-CCM shows an ozone decrease in ENSO warm years which is comparable to the one in WACCM and EMAC-FUB when filtered SSTs are prescribed to the model. However, since the signal from the reference simulation is weak and insignificant an assessment of the relevance of this change is not possible.

Ozone also reacts strongly to changes in the lower stratospheric zonal mean zonal wind associated with the QBO. The profiles in Figure 9.6b all show an S-shaped structure from the upper stratosphere down to about the tropopause level. A remarkable feature is the close proximity of the ozone change profiles obtained from the SOLARIS and the reference simulations with WACCM and EMAC-FUB at all altitudes above about 30 hPa (WACCM) or 50 hPa (EMAC-FUB). This is not the case for the two MRI-CCM runs which is due to the internally generated QBO in the Japanese model. Apart from the MRI-CCM this agreement of the profiles at higher altitudes implies that the ozone response to the QBO is not influenced by the use of filtered or unfiltered observed forcings. The filtered equatorial zonal wind that was assimilated, e.g., into EMAC-FUB covers the altitude range from 90 to 8 hPa (cf. Table 5.1). The almost identical ozone response above 50 hPa, thus, suggests that the QBO is affected by the 11-year solar cycle mostly at lower

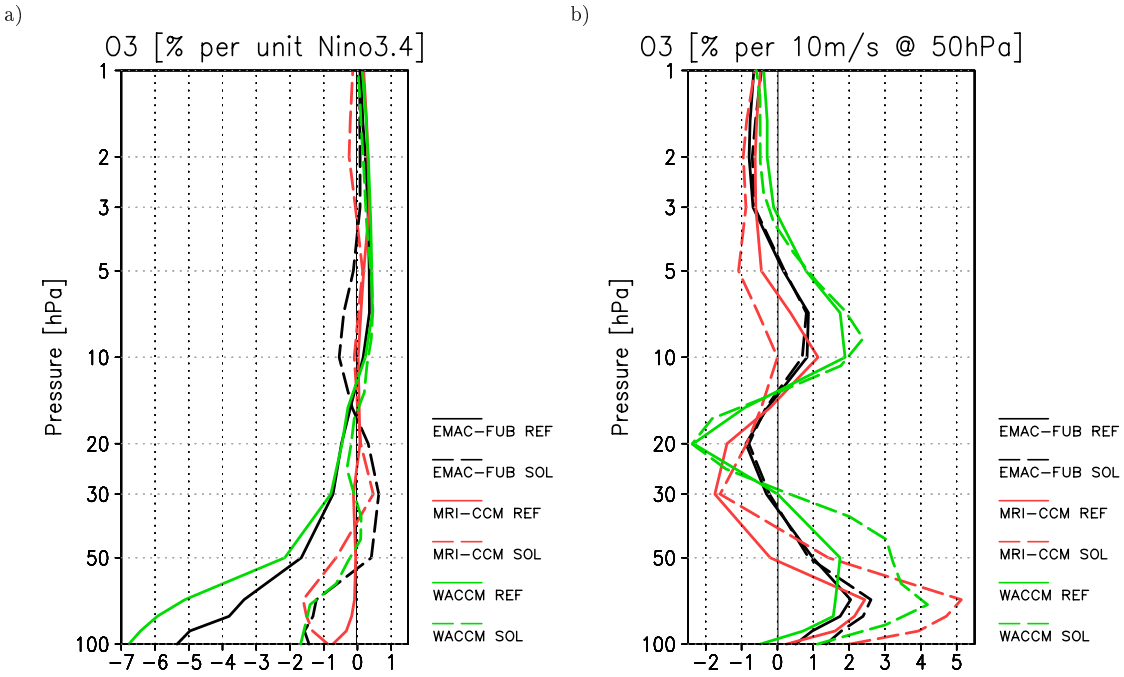


**Figure 9.6:** Profiles of the tropical mean (25 °S-25 °N) annual mean a) ENSO and b) QBO regression coefficient of ozone in percent per unit of the Niño3.4 index (a) and percent per 10 m/s at 50 hPa (b), respectively. Solid lines depict results from simulations with unfiltered input time series, dashed lines from simulations using filtered forcings.

levels. There is, however, an increase of the ozone response to stronger westerlies in the lower stratosphere when the filtered forcing time series are used. The three models agree in this tendency.

## 9.3 The solar signal in northern winter

The annual mean correlations of ozone or temperature with the F10.7 solar radio flux in the tropical lower stratosphere are very low in both the simulations using filtered or observed forcings. It is, however, possible that there is a substantial correlation between ozone or temperature and solar activity during individual seasons. To that end, seasonal means over the three months December, January and February (DJF) have been calculated from the time series of zonal mean ozone and temperature from the SOLARIS and the reference simulations and have, subsequently, been correlated with the F10.7 cm solar radio flux, likewise seasonally averaged. The results are shown in the Figures 9.7 and 9.8.

Temperature is positively correlated with the 10.7 cm solar radio flux in the middle and upper stratosphere as well as in the lower mesosphere in the tropics and on the summer hemisphere with maxima of about 0.6 to 0.7. It is negatively correlated at high northern latitudes in the middle and upper stratosphere in EMAC-FUB and in WACCM. Although, the correlation in EMAC-FUB is weak and insignificant in the seasonal mean it becomes significant in individual months (not shown). The tendency to higher correlation

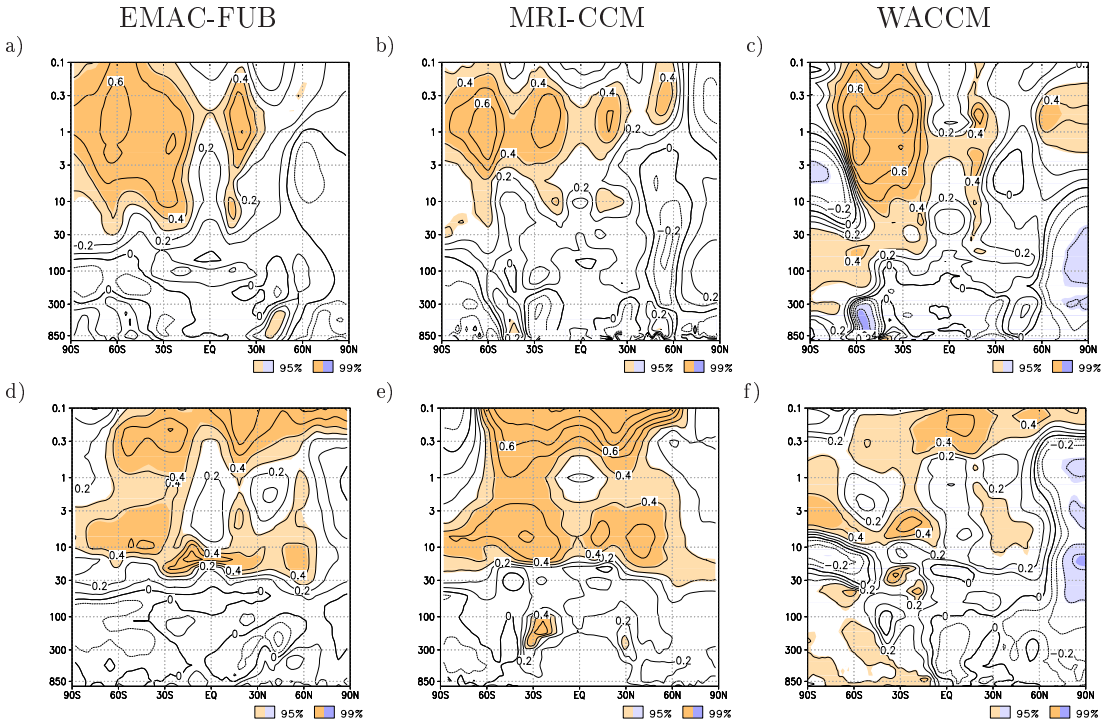


**Figure 9.7:** Winter (DJF) mean correlation of zonal mean temperature (top) and ozone (bottom) with the F10.7 cm solar radio flux from **SOLARIS** simulations using filtered forcings with EMAC-FUB (left), the MRI-CCM (middle) and WACCM (right). Contour interval is 0.1. Light (heavier) shading indicates statistical significance on the 95 %(99 %)-level.

coefficients in the equatorial stratopause region in the simulations using filtered forcings compared to the reference simulations that was first noticed in the annual mean signals is also visible for the winter temperature-solar flux correlation (Figures 9.7a-c and 9.8a-c). However, in the tropical lower stratosphere only the WACCM SOLARIS simulation and the EMAC-FUB and MRI-CCM reference simulations show rudimentary signs of a significant positive correlation.

The correlations of ozone with the 10.7 cm-solar radio flux (Figures 9.7d-f and 9.8d-f) are generally positive in the stratosphere and lower mesosphere as they used to be in the annual mean. However, the QBO-associated variability leaves its imprint in the lower correlation coefficients near the equator. Again, there tend to be higher correlation coefficients in the equatorial region in the simulations using filtered forcings (Figure 9.7a-c) compared to the reference simulations with unfiltered observed forcings (Figure 9.8a-c). The correlations in the tropical lower stratosphere are weak and insignificant in all models and set-ups except in the MRI-CCM reference simulation (Figure 9.8b).

When DJF seasonal mean ozone and temperature are averaged over the tropics and correlated with the solar radio flux in order to quantify the above impression, this results in low and insignificant correlation coefficients in the lower stratosphere below about 30 hPa (Figure 9.9a and 9.9d). Only in the MRI-CCM reference simulation results there is a statistically significant correlation between ozone and the solar flux at about 50 hPa.

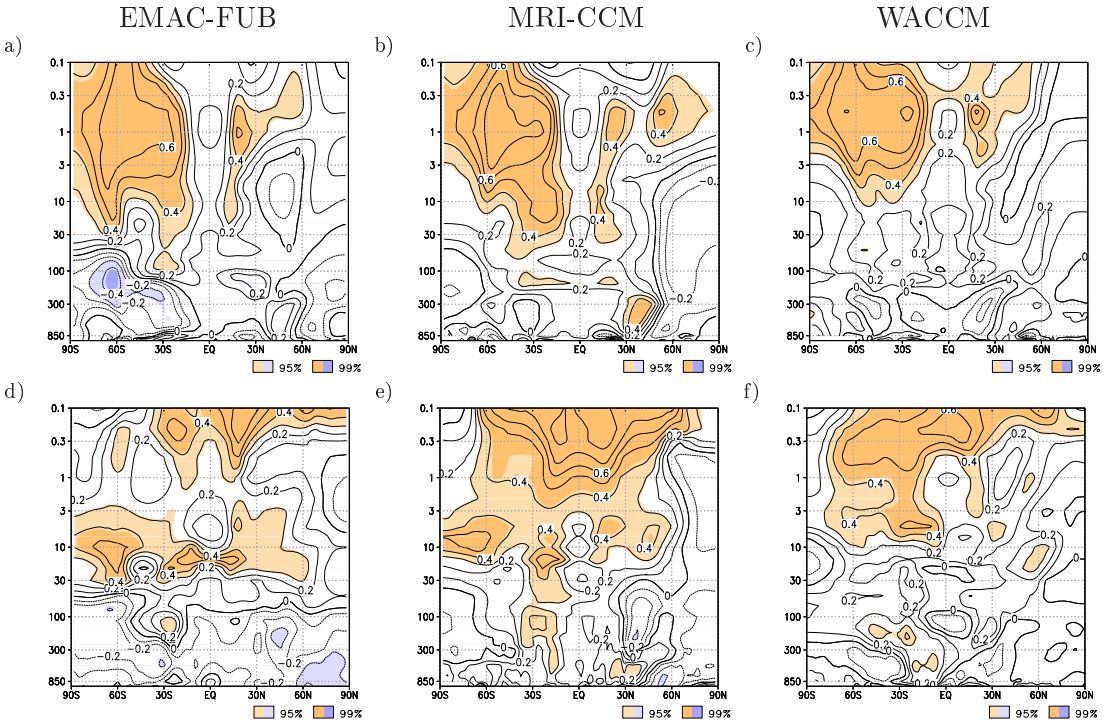


**Figure 9.8:** Winter (DJF) mean correlation of zonal mean temperature (top) and ozone (bottom) with the F10.7 cm solar radio flux from **CCMVal REF-B1** simulations with EMAC-FUB (left), the MRI-CCM (middle) and WACCM (right). Contour interval is 0.1. Light (heavier) shading indicates statistical significance on the 95 %(99 %)-level.

The ozone(temperature)-solar flux correlation coefficients in the MRI-CCM and EMAC-FUB SOLARIS simulations with filtered forcings tend to be lower than in the reference simulations. No such trend is found in the WACCM results. The value of this finding is, however, limited due to the low correlations.

The insufficient correlation also complicates the multiple linear regression analysis. Figure 9.9b and 9.9e shows the coefficients for solar influence. The profiles from EMAC-FUB and the MRI-CCM show the tendency towards a lower ozone and temperature sensitivity to changes in the F10.7 solar flux when filtered forcings are applied. This tendency has already been seen in the EMAC-FUB and WACCM annual mean profiles (Figure 9.5). In the winter season, however, WACCM shows a stronger ozone and temperature increase in the simulation with filtered forcings than in the reference simulation. Although, the uncertainty associated with the regression profiles in the lower stratosphere is large due to the low correlation coefficients (Figure 9.9c and 9.9f) the common tendency in two of three models may be an indication for a real reduction of the secondary ozone and temperature sensitivity peaks in the tropical lower stratosphere when the linear interaction between the solar, the SST and the QBO forcings is suppressed.

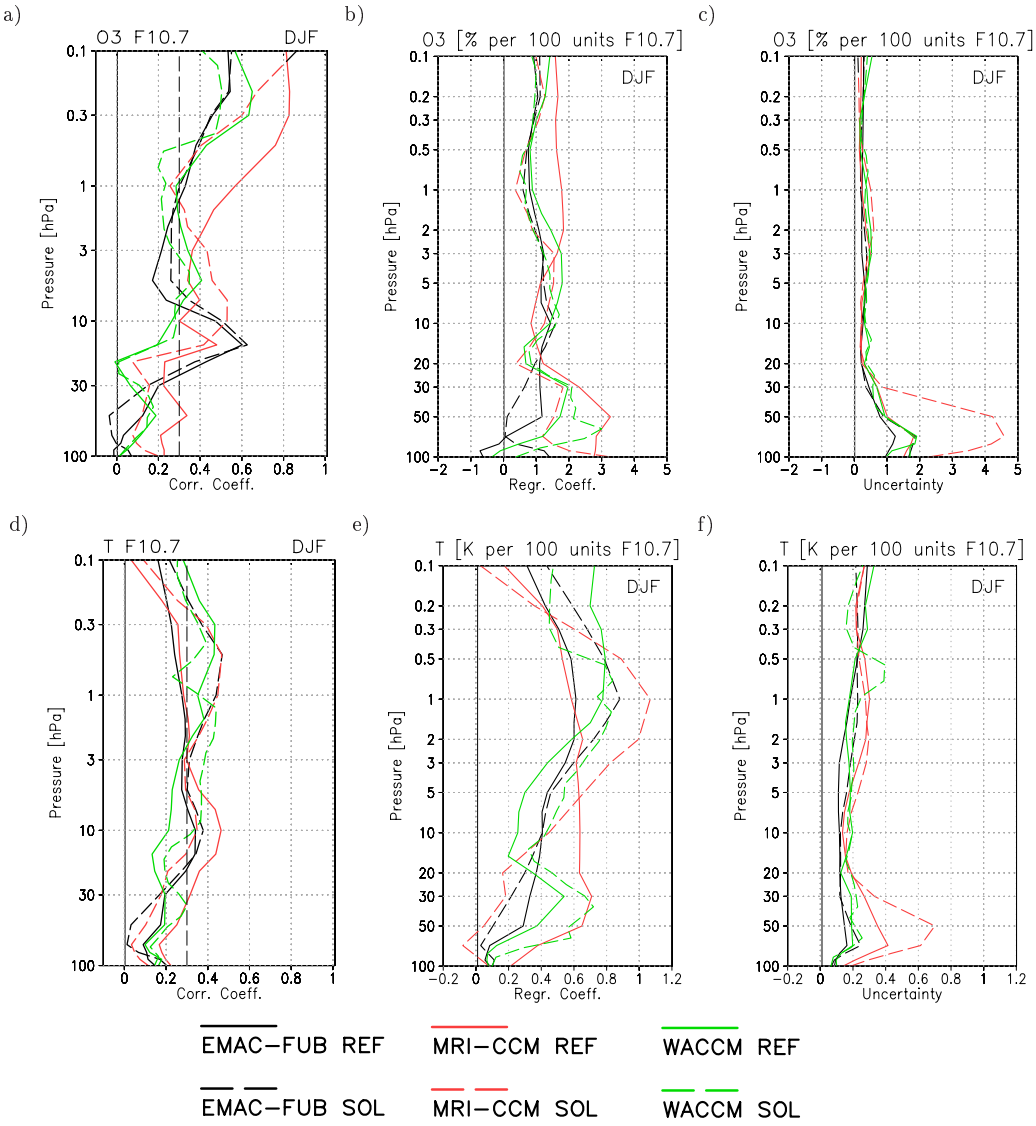


**Figure 9.9:** Profiles of the tropical mean (25 °S-25 °N) DJF seasonal mean a) Correlation coefficient between ozone and the F10.7 cm solar radio flux, b) Regression coefficient of ozone in percent per 100 units of F10.7, c) Uncertainty of the ozone regression coefficient in percent per 100 units F10.7 solar radio flux, d) Correlation coefficient between temperature and the F10.7 solar radio flux, e) Regression coefficient of temperature in K per 100 units of F10.7 and f) Uncertainty of the temperature regression coefficient in K per 100 units of F10.7. Solid lines depict results from simulations with unfiltered input time series, dashed lines from simulations using filtered forcings. The dashed vertical black lines in a) and d) mark the threshold of 0.3 for statistical significance at the 95 %-level.

## 9.4 Comparison of the solar signal with the QBO and ENSO signals

To further pursue the interaction of solar influence, SST variability and the QBO in the tropical lower stratosphere and their respective effect on temperature and the ozone volume mixing ratio tropical (25 °S-25 °N) averages of the latter quantities are considered

at several pressure levels in the lower stratosphere (50 hPa, 70 hPa and 90 hPa) on a monthly basis. For the calculation of the correlation coefficients of ozone or temperature with the equatorial QBO the filtered data were used for the SOLARIS simulations and the observed winds for the reference runs with unfiltered forcings. The Niño3.4 index was computed from the observed SSTs or from the filtered SSTs for the respective correlation with ozone or temperature from the reference simulations or the SOLARIS simulations using filtered forcings. The correlation of ozone and temperature with the F10.7 solar radio flux, the Niño3.4 index and the QBO at 50 hPa yielded similar results at the three levels. As an example the results for the 70 hPa-level are shown in Figure 9.10 for EMAC-FUB and WACCM. The MRI-CCM is not considered in this analysis since this model generates the QBO internally also in the simulation with filtered forcings which implies a possible solar or SST influence on the QBO.

Moreover, in the EMAC-FUB simulation with filtered forcings no significant correlation between tropical mean temperature or ozone and the solar activity appears (see the dashed curves in Figure 9.10a). In comparison with the correlation obtained from the reference simulation using unfiltered observed forcings (solid lines in Figure 9.10a) the correlation of temperature with F10.7 only improves in July. The ozone-solar flux correlation coefficients are higher when the filtered forcings are used from May to August. However, since none of the correlation coefficients exceeds 0.3, the result is statistically not significant and the correlation may be accidental. Possibly, the time series of 46 years is too short to obtain a significant correlation with the 11-year solar activity proxy. In the reference simulation with WACCM the tropical lower stratospheric temperature and ozone are weakly positively correlated with the F10.7 solar radio flux (solid curves in Figure 9.10b). When the filtered forcings are applied, the correlation improves in February and March but degrades from May to December switching occasionally to an anti-correlation. Since neither the positive nor the negative values from May to December reach the level of statistical significance a definitive assessment about the sign of the correlation cannot be made. However, in February the correlation coefficients of temperature (ozone) with F10.7 are enhanced by about 0.15 when the filtered forcings are prescribed to the model. Hence, at least the temperature-solar activity correlation is elevated to a statistically significant level.

Regarding the middle panels of Figure 9.10 it is seen that the correlation between the tropical lower stratospheric ozone or temperature and the QBO at 50 hPa is considerably higher than the correlation with the solar radio flux. Whereas the ozone-solar activity and temperature-solar activity correlation coefficients were very similar there are systematically higher correlation coefficients between temperature and the QBO than between ozone and the QBO. This is true for both the EMAC-FUB and the WACCM results with WACCM showing generally higher correlations between ozone or temperature and the QBO. The strong and in most months statistically significant correlation can be interpreted as the QBO being a very important forcing which explains between 16 % and 25 % of the ozone (temperature) variability in the tropical lower stratosphere using

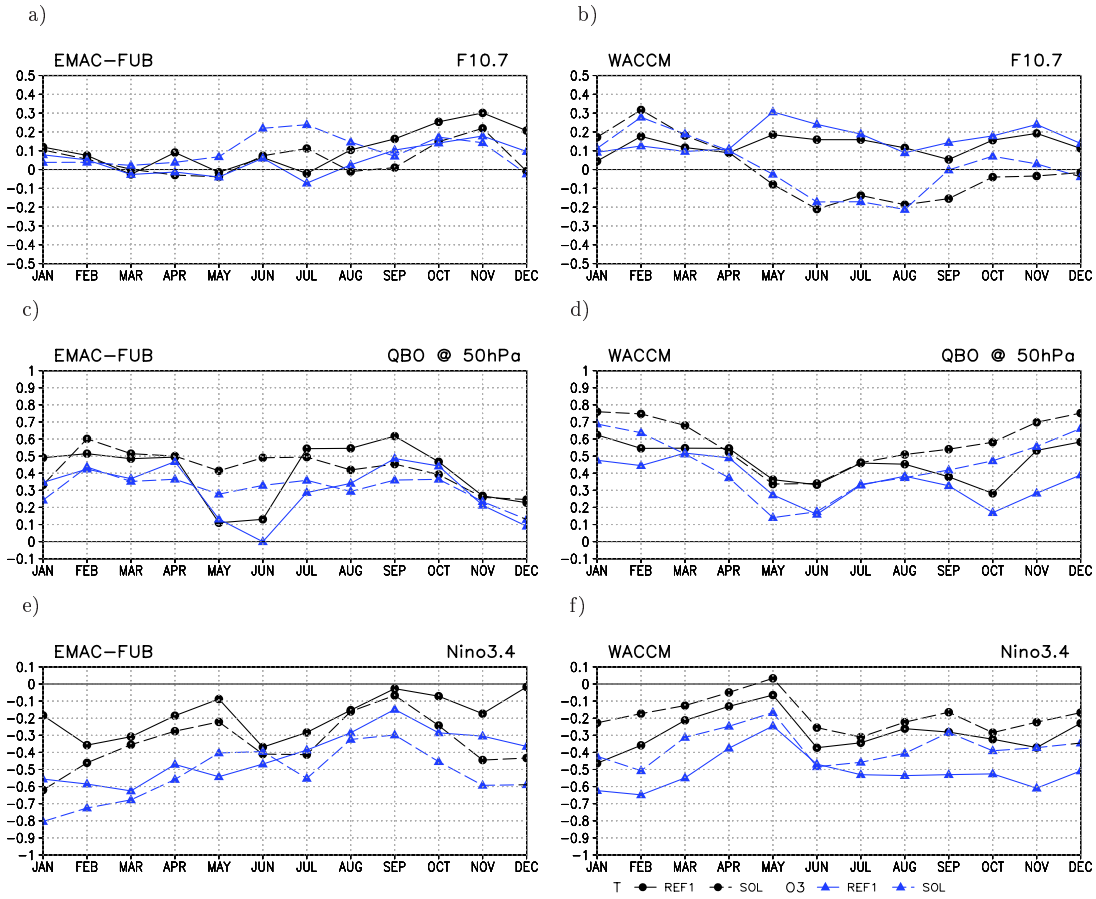


**Figure 9.10:** Correlation coefficients of the tropical mean (25 °S-25 °N) monthly mean temperature (black, circles) and ozone (blue, triangles) at 70 hPa as simulated by EMAC-FUB (left) and WACCM (right). Top: Correlation with the F10.7 cm solar radio flux. Middle: Correlation with the QBO at 50 hPa. Bottom: Correlation with the Niño3.4 index. Correlation coefficients with absolute values exceeding 0.3 (0.4) are statistically significant at the 95 %(99 %)-level. Solid lines depict results from the simulation with unfiltered input time series, dashed lines from the simulation using filtered forcings.

the square of the correlation coefficient as coefficient of determination. When the filtered forcing time series are prescribed to EMAC-FUB the temperature-QBO correlation is enhanced in February, May and June compared to the reference simulation with unfiltered forcings. The ozone-QBO correlation is elevated from May to July. In the same season the ozone-solar activity correlation was improved in EMAC-FUB when filtered forcings were applied. In WACCM the temperature-QBO correlation is strengthened from August to March as is the ozone-QBO correlation from September to February. The difference between the temperature-QBO correlation coefficients obtained from the reference simulation and from the SOLARIS simulation with filtered forcings is largest in February and October. The ozone-QBO correlation from the SOLARIS run differs most strongly from the reference simulation result in October. However, the difference remains large throughout the northern hemisphere winter season. The month of February was the month where the temperature(ozone)-solar correlation was enhanced when filtered forcings were pre-

scribed to WACCM. This may indicate that WACCM is most susceptible to interferences between the forcing time series in late northern winter.

In contrast to the correlation between tropical lower stratospheric ozone or temperature and the QBO, the correlation of these quantities with the Niño3.4 index is generally negative (see Figure 9.10e and 9.10f). This implies a lower temperature and a reduced ozone volume mixing ratio at high values of the Niño3.4 index which represents an El Niño warm event. It is furthermore seen, that ozone is more closely correlated with the Niño3.4 index than temperature. The application of filtered forcings leads to a somewhat inconsistent reaction in EMAC-FUB and in WACCM. The ozone-Niño3.4 correlation is strengthened when filtered forcings are used in EMAC-FUB in all months except May and June. The temperature-Niño3.4 correlation is found to be stronger in all months without any exception. However, even the stronger correlation remains below the threshold for statistical significance (0.3) in northern spring and autumn. The WACCM results show a weaker ozone(temperature)-Niño3.4 correlation throughout the year when the filtered forcings are used compared to the reference simulation with unfiltered forcings which drops below the level of statistical significance in some months.

From the previously described changes a common tendency emerges, at least in EMAC-FUB: It appears that ozone and temperature in the tropical lower stratosphere are particularly susceptible to the (linear) interaction of solar, QBO and ENSO forcing in the period May to August. In the simulation with filtered QBO and SSTs and, thereby, suppressed interference of the forcings, the correlation between ozone and temperature with the solar radio flux and with the QBO is improved. Simultaneously, the correlation between ozone and the Niño3.4 index is reduced. In WACCM the susceptible season seems to be limited to the months of January and February. In these months improved ozone(temperature)-solar(QBO) correlations coincide with reduced ozone(temperature)-ENSO correlations. However, the picture is not as consistent as in EMAC-FUB.

The improvement of the ozone and temperature correlation with the solar flux and the QBO during some months is an indication for less interference between the forcing time series in the filtered SOLARIS simulations. It implies a more uniform temporal development of ozone(temperature) and the solar cycle or the QBO in the absence of an 11-year component in the QBO. On the other hand, the reduction of the ozone-ENSO correlation cannot be explained in a similar manner. It could be accidental since the temperature-ENSO correlation is improved in all months. This, in turn, suggests the successful removal of an 11-year periodicity from the SST time series.

From observations it is known that the correlation of, e.g., temperature with the solar radio flux is weak and insignificant as long as both phases of the QBO are included in the analysis (Labitzke, 2004a). Prior stratification according to the phase of the QBO yields especially under QBO east conditions significant correlations between low-latitude temperature and the solar radio flux. Because of this the correlation analysis of ozone and temperature with the solar flux (Figure 9.10a and 9.10b) is repeated separately for

the east and west phases of the filtered and observed QBO, respectively. The criterion for a month to belong to the QBO east (west) group was the monthly mean zonal wind at 50 hPa being less (greater) than zero. The correlation results are shown in Figure 9.11.

Looking first at the EMAC-FUB results (Figure 9.11a and 9.11c) a clear differentiation is seen between the two QBO phases from August until December. Ozone and temperature are positively correlated with the F10.7 solar radio flux in the QBO east phase while the correlation of the two quantities with the solar activity proxy is weak and often negative in the QBO west phase. This is in agreement with Labitzke (2004a). During the first half of the year it is rather the temperature(ozone)-solar flux correlation under QBO west conditions that yields positive values, also in agreement with Labitzke (2004a). During the northern summer months there is again an improvement of the correlation in the SOLARIS simulation with filtered forcings in July (QBO west, ozone and temperature) and August (QBO east, ozone).

In WACCM the differentiation between the ozone or temperature correlation with solar flux under either QBO east or west conditions in the second half of the year is not as obvious as in EMAC-FUB (Figure 9.11b and 9.11d). In the first half, however, in the QBO west cases there are higher correlation coefficients for ozone and the solar flux compared to the QBO east cases. The month which shows the greatest enhancement of the correlation when filtered forcings are applied and both QBO phases included is February (cf. Figure 9.10b). This improvement is retrieved for temperature during QBO

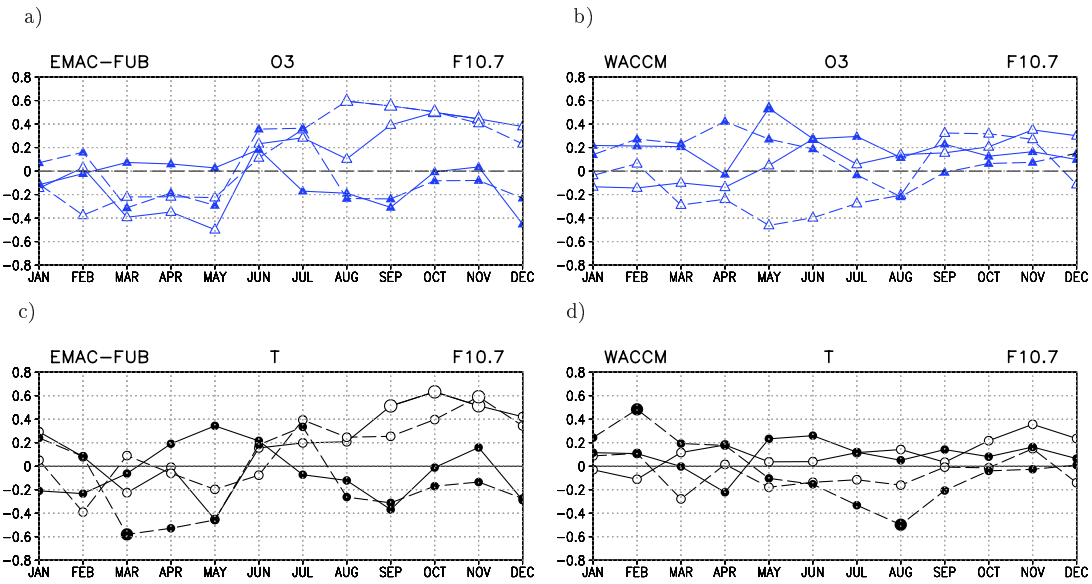


**Figure 9.11:** Correlation coefficients of the tropical mean (25 °S-25 °N) monthly mean ozone (top, blue, triangles) and temperature (bottom, black, circles) at 70 hPa as simulated by EMAC-FUB (left) and WACCM (right) with the F10.7 cm solar radio flux. Open symbols: Correlation during QBO east phase; Closed symbols: Correlation during QBO west phase. Solid lines depict results from the simulation with unfiltered input time series, dashed lines from the simulation using filtered forcings. Larger symbols indicate statistically significant correlations at the 95 %-level.

west phases. For ozone a similar improvement is seen in April under QBO west conditions which was not detectable without the QBO stratification. However, in April there is no enhancement of the ozone-QBO correlation, but a reduction when the filtered forcings are prescribed to the model.

## 9.5 Summary and Discussion

As mentioned in this chapter's introduction the motivation for these analyses was the necessity to prescribe SSTs and equatorial zonal winds to most CCMs. For that purpose observed time series are used which may, however, be themselves influenced by the 11-year solar cycle. The role of possible (non-)linear interactions between the solar irradiance variability and the QBO and the SST-variability associated with ENSO for the appearance of secondary maxima in the temperature and ozone responses to the 11-year solar cycle was investigated. CCMVal-2 REF-B1 simulation results from three CCMs (EMAC-FUB, the MRI-CCM and WACCM) were compared with results obtained with the same models from REF-B1-like simulations that used band-pass filtered QBO and SST input. The intention of the filtering was primarily to remove possible solar induced periodicities from the other two forcing time series. In this way, the forcing time series became linearly independent. This approach is a novelty and such simulations have never been performed before.

In comparison with reference simulations that used the observed forcing time series the most important changes were, however, not found in the tropical lower stratosphere but in the middle stratosphere and in the stratopause region.

The annual mean 11-year solar signal in upper stratospheric temperature is improved in the simulations with filtered forcings compared to the reference simulations using the observed forcings. The solar induced changes appear centred over the equator and, hence, closer to observations (Randel et al., 2009). The annual mean solar induced ozone changes in the middle stratosphere exhibit an improved latitudinal structure and a higher amplitude in the SOLARIS simulations. Thus, the modelled signal bears closer resemblance to the observed signal (Randel and Wu, 2007). In the dynamically active northern winter season strengthened correlations between temperature or ozone and the solar radio flux were found, in particular, in the low-latitude middle and upper stratosphere. The three CCMs participating in the SOLARIS comparison generally agree with regard to these results. This does not necessarily imply that the CCMs failed to simulate a solar signal close to reality with the observed forcings. It rather illustrates the challenge to identify and to correctly attribute the solar signal with a multiple linear regression approach when the forcing time series are linearly not completely independent.

There is a tendency towards a reduction of the secondary peaks in the ozone and temperature responses to the 11-year solar variability in the tropical lower stratosphere in the annual mean when the band-pass filtered QBO and SST data sets are used to

force the models instead of the observed (or internally generated) forcings. Due to low correlation coefficients between ozone or temperature and the solar activity proxy in the tropical lower stratosphere region the reduction tendency is statistically not significant and should not be overemphasised. Four solar cycles are possibly not sufficient to establish a statistically significant solar signal in tropical lower stratospheric ozone and temperature in current CCMs. Ensemble simulations might yield a more reliable result than individual realisations of an experiment (Gabriel Chiodo, 2010, personal communication).

# Chapter 10

# Summary

In this study different aspects of the influence of the 11-year solar cycle on the stratosphere and troposphere have been shown by means of simulations with the coupled chemistry-climate model EMAC-FUB. Spectrally resolved as well as total solar irradiance data were used to force the model. A series of model simulations have been performed to investigate the atmospheric response to a realistically varying solar irradiance forcing. The lower boundary conditions have been systematically varied in order to learn more about their influence on the appearance of the solar signal. The CCM was also run in a higher vertical resolution to test the possible effect of the model resolution on the vertical structure of the response. In addition, equilibrium simulations have been conducted in order to analyse the influence of the temporal evolution of the irradiance forcing on the solar signal. Within the framework of the SPARC SOLARIS initiative a comparative study involving three CCMs addressed aspects of linear and non-linear interactions between the 11-year solar forcing, the SSTs and the QBO. Results from model simulations with observed forcings are compared to results obtained from simulations with filtered linearly independent forcings.

The focus of the analyses was on the solar signal in the troposphere which has been comprehensively analysed and on the vertical structure of the solar signal in the tropical stratosphere. The results presented in this report shall be summarised by picking up the actual scientific questions that were also posed in section 4.3.3.

- Which forcings are necessary to let the secondary maximum of ozone and temperature in the tropical lower stratosphere emerge?
- How do these forcings interact to produce the observed response?

The EMAC-FUB model does not simulate the secondary maxima in ozone and temperature increase that are seen in observations, neither with fixed solar cycle phases nor using a time-varying solar irradiance forcing. In this context, the interaction between the solar influence and the QBO becomes important. Although, the QBO is the considerably stronger source of variability in the tropical lower stratosphere compared wih the 11-year solar cycle the solar cycle may invert the sign of QBO influence on vertical velocity, ozone and temperature. However, the precise chain of involved processes remains unknown.

The secondary ozone and temperature maxima in the 11-year solar signal appear in a simulation that used modelled SSTs as lower boundary conditions. The modelled SSTs were, however, biased towards cool anomalies in the tropical Pacific, i.e., La Niña conditions, which favours the emergence of the secondary maxima. Since the El Niño-Southern Oscillation has a strong influence on the tropical lower stratosphere it may outbalance the 11-year solar influence. This emphasises the importance of a realistic SST variability for transient simulations, although, the secondary maxima in ozone and temperature did not occur in the simulation with observed SSTs.

In a transient model simulation with an enhanced vertical resolution (90 layers instead of 39 layers) and observed SSTs the secondary maxima in solar induced ozone and temperature increase could be obtained. It is, however, not possible to ascribe this result to the higher vertical resolution alone since the simulation included also the effects of precipitating particles and descending thermospheric $NO_x$ anomalies which were not represented in the experiment with the lower resolved model version.

- How important is the presence of the tropical lower stratospheric signals, in particular, of the temperature signal, for the solar signal in the troposphere?

The crucial factor for the appearance of the solar signal in the troposphere is the equator-to-pole temperature gradient rather than the temperature anomaly in the equatorial lower stratosphere, in agreement with the results of Haigh et al. (2005). In particular, a negative meridional temperature gradient does not necessarily presuppose a warming in the tropical lower stratosphere. Constant temperatures in the tropics and a simultaneous cooling at high latitudes set up a negative equator-to-pole temperature gradient in the lower stratosphere. The tropospheric circulation reacts to this forcing with a weakening and poleward shift of the subtropical jet stream. The opposite forcing, i.e., warming in the polar lower stratosphere and cooling in the tropics, leads to an equatorward shift of the jet. Both reactions are in line with Haigh et al. (2005) and could be demonstrated by means of EMAC-FUB simulations. Thus, it was possible to confirm the GCM results of Haigh et al. (2005) with a CCM. Furthermore, the transient EMAC-FUB simulation results imply an improvement compared to a recent equilibrium CCM study by Schmidt et al. (2010). A negative equator-to-pole temperature gradient in the lower stratosphere along with the poleward shift of the tropospheric jet is also the result of a mechanistic momentum forcing study with an artificially enhanced polar night jet which is considered to be an analogue to the initial dynamical solar signal in the stratosphere. Since the solar irradiance conditions were unchanged in all simulations of the mechanistic forcing study and the lower boundary conditions were identical the resulting signal in the troposphere can be ascribed solely to the imposed dynamical forcing.

- How does the solar signal in the troposphere look like?
- How much of the stratospheric solar signal is transferred downward to the troposphere and by which mechanisms?
- In which way are natural modes of climate variability affected by the solar influence?

The 11-year solar signal in the troposphere in the global and annual mean is weak. However, on a hemispheric or regional spatial scale and on a monthly and seasonal time scale it is detectable. The solar influence on the troposphere as it is investigated in this study is primarily indirect by definition of the experiments. It originates in the upper stratosphere where direct radiative and photochemical changes associated with the 11-year UV irradiance variability affect the ozone abundance, the radiative heating and the meridional temperature gradient. From the upper stratosphere the signal is transferred downward by wave-mean flow interactions during the dynamically active winter seasons on each hemisphere. The 11-year solar influence is most pronounced in the troposphere in the late solstice seasons, i.e., about one month after the peak signal in the stratosphere. It leads to positive anomalies of tropospheric modes of variability, in particular, of the Northern and Southern Annular Mode and, hence, modifies the circulation throughout the depth of the troposphere. The solar irradiance variability does also affect the tropical circulation by suppression and redistribution of the regions of strongest upwelling. This could be demonstrated, in particular, for the summer monsoon circulation over the Indian Ocean and the adjacent land masses.

- Which factors such as lower boundary conditions or temporal evolution of the forcings influence the tropospheric solar signal?

An 11-year solar signal in the Indian Ocean monsoon circulation as it is seen in observations (Kodera, 2004) has for the first time been retrieved with a CCM. However, it does only appear in EMAC-FUB when transient observed SSTs are prescribed to the model as lower boundary conditions. The use of modelled SSTs leads to a considerably weaker signal and the signal is suppressed when the SSTs are fixed. This demonstrates the importance of 11-year solar cycle-SST interactions for the emergence of the observed signal in the Indian Ocean monsoon circulation which is a novel finding. The observed SSTs most likely bear an 11-year solar cycle influence (Roy and Haigh, 2010) and convey it to the troposphere, thus, supporting the development of the observed atmospheric circulation changes in response to the 11-year solar cycle.

Readdressing the question on how different forcings interact to produce the observed stratospheric response the possible linear dependence of the model forcings (11-year solar cycle, QBO, SSTs) and the effect on the detection of the 11-year solar signal are investigated. To that end simulations using observed forcings are compared with simulations that used filtered QBO and SST forcings. The band-pass filtering procedure intended to remove the 11-year period from the other two observed forcing time series as well as to suppress mutual influences between the QBO and the SSTs. The forcings became,

thus, linearly independent. Hence, only non-linear interactions of the 11-year solar irradiance variability with the QBO and the SST-variability may occur in the simulations with the prescribed filtered forcings. The filtered forcing simulations were performed with EMAC-FUB and, in addition, with the Japanese MRI-CCM and with WACCM.

In comparison with reference simulations that used the observed forcing time series the most important changes were found in the middle stratosphere and in the stratopause region. The annual mean 11-year solar signal in ozone and temperature is improved in the simulations with filtered forcings compared to the reference simulations using the observed forcings. In particular, the latitudinal distribution of the solar induced changes becomes more similar to the observed signal. This is especially important in the low-latitude middle and upper stratosphere where it indicates less interference between the solar influence and the QBO in the simulations with filtered forcings. The three CCMs participating in the comparison agree with regard to these results. This does not necessarily imply that the CCMs failed to simulate a solar signal close to reality with the observed forcings. It rather illustrates the challenge to identify and to correctly attribute the solar signal with a multiple linear regression approach when the forcing time series are linearly not completely independent.

There is a tendency towards a reduction of the secondary peaks in the annual mean ozone and temperature responses to the 11-year solar variability in the tropical lower stratosphere when the band-pass filtered QBO and SST data sets are used to force the models instead of the observed (or internally generated) forcings. This can be interpreted as they are either of solar origin or appear due to non-linear interactions of the 11-year solar irradiance variability with the QBO and the SST-variability. If they were of solar origin they should also appear in a simulation with only solar forcing.

In view of the GCM scenario simulations that are performed in support of an IPCC report it can be stated that some important prerequisites have to be fulfiled in order to properly include the natural climate forcing due to 11-year solar variability: 1) The GCM must have a fully resolved stratosphere. 2) Since the 11-year solar signal is relatively weak, a realistic model climatology is necessary in order to obtain expedient results. 3) An ozone climatology needs to be prescribed to the model that accounts for the 11-year solar cycle ozone changes as well as for the (time-dependent) CFC-induced ozone depletion at southern polar latitudes in spring. 4) A suffiently high resolved short-wave heating scheme is absolutely essential when simulating the solar influence (cf. Chapter 3 of SPARC CCMVal, 2010).

As an additional aspect of solar variability the ozone response to the 27-day solar rotational cycle which is most pronounced during periods of high 11-year solar activity was investigated. The analysis of cycle mean ozone differences yielded for a strong and a weak 27-day cycle a similar vertical tripole structure of the anomalies in the equatorial mesosphere and upper stratosphere. The mean ozone response in the extratropical summer stratosphere is not significantly altered when short term UV variability associated

with the solar rotational cycle is resolved. Hence, from a photochemical and radiative point of view the results suggest that resolving the daily solar irradiance variability has only a low relevance for the mean ozone signal in the stratosphere. However, potential dynamical effects of the 27-day solar irradiance variability in the winter stratosphere may play a non-negligible role for the distribution of ozone in the stratosphere. An indication for the susceptibility of the winter hemisphere circulation to 27-day irradiance variability was obtained from a spectral analysis of several quantities associated with the mean meridional circulation and, hence, the transport of trace species.

Recapitulating the above results it might be an advantage to take a step backwards and reduce the complexity of the experimental set-up when studying the processes involved in the formation of the 11-year solar signal. This can help to reduce the possible interactions and overlaps between individual forcings. This is particularly important considering the trend towards the development of so-called Earth System Models that include interactive chemistry, an ocean model, and even involve land-use changes.

Finally, it must be stated that the investigation of the 11-year solar cycle influence on the Earth's atmosphere is a long-term task. It is of great importance to have continuous measurements of the total and spectral solar irradiance as well as of chemical and physical atmospheric quantities. In this context a recent study published by Haigh et al. (2010) has to be mentioned in which the authors report a stronger spectral irradiance change with solar activity than was previously assumed (Lean, 2000; Lean et al., 2005).

## Outlook

When looking at the new findings about the spectral solar irradiance change over the course of the 11-year solar cycle (Haigh et al., 2010) it is interesting to perform new modelling studies to test the atmospheric response to the stronger spectral irradiance forcing. The EMAC-FUB CCM has been shown to be an appropriate tool for this type of simulations.

At present, efforts are made to couple EMAC-FUB to an interactive deep-ocean model. With the coupled Atmosphere-Ocean-CCM the 11-year solar cycle influence on the Earth's atmosphere can be studied in a more comprehensive way including direct effects at the surface which involve the reaction of sea surface temperatures to the solar forcing (Meehl et al., 2009).

To further pursue the investigations on the interactions between solar irradiance variability, the QBO and ENSO and their role for the appearance of the 11-year solar signal, in particular, the ozone and temperature signal in the tropical lower stratosphere three additional simulations with EMAC-FUB are currently being performed or have just been completed. In these experiments the three important forcings act separately, i.e., (1) only solar forcing, no QBO and no SST variability, (2) only band-pass filtered SSTs,

no QBO, intermediate solar irradiance and (3) only band-pass filtered assimilated QBO, intermediate solar irradiance, no SST variability. It is expected that the evaluation of these simulations will help to gain more insight into the processes that led to the qualitative improvement of the solar signal in the SOLARIS simulation with the combined filtered forcings (SSTs and QBO).

With regard to the solar signal in a warming climate and the uncertainty associated with solar activity in the future which will possibly decline (Abreu et al., 2008) it would be interesting to perform a sensitivity study using solar irradiance data from a period of exceptionally low solar activity, e.g., the Maunder Minimum (1645-1715) in combination with greenhouse gas levels projected for the end of the 21st century.

# Bibliography


Abreu, J., J. Beer, F. Steinhilber, S. Tobias and N. Weiss, 2008. For how long will the current grand maximum of solar activity persist? *Geophys. Res. Lett.*, **35**, L20109.

Andrews, D., J. Holton and C. Leovy, 1987. *Middle atmosphere dynamics*, Volume 40 of *International Geophysics Series*. Academic Press, Orlando, Florida.

Andrews, D. and M. McIntyre, 1976. Planetary Waves in Horizontal and Vertical Shear: The Generalized Eliassen-Palm Relation and the Mean Zonal Acceleration. *J. Atmos. Sci.*, **33**(11), 2031–2048.

Austin, J., L. Hood and B. Soukharev, 2007. Solar cycle variations of stratospheric ozone and temperature in simulations of a coupled chemistry-climate model. *Atmos. Chem. Phys.*, **7**, 1693–1706.

Austin, J., H. Struthers, J. Scinocca, D. Plummer, H. Akiyoshi, A. Baumgaertner, S. Bekki, G. Bodeker, P. Braesicke, C. Brühl, N. Butchart, M. Chipperfield, D. Cugnet, M. Dameris, S. Dohmse, S. Frith, H. Garny, A. Gettelman, S. Hardiman, P. Jöckel, D. Kinnison, A. Kubin, J. Lamarque, U. Langematz, E. Mancini, M. Marchand, M. Michou, O. Morgenstern, T. Nakamura, J. Nielsen, G. Pitari, J. Pyle, E. Rozanov, T. Shepherd, K. Shibata, D. Smale, H. Teyssedre and Y. Yamashita, 2010. Chemistry-climate model simulations of spring Antarctic ozone. *J. Geophys. Res.*, **115**, D00M11.

Austin, J., K. Tourpali, E. Rozanov, H. Akiyoshi, S. Bekki, G. Bodeker, C. Brühl, N. Butchart, M. Chipperfield, M. Deushi, V. Fomichev, M. Giorgetta, L. Gray, K. Kodera, F. Lott, E. Manzini, D. Marsh, K. Matthes, T. Nagashima, K. Shibata, R. Stolarski and W. Tian, 2008. Coupled chemistry climate model simulations of the solar cycle in ozone and temperature. *J. Geophys. Res.*, **113**, D11306.

Barriopedro, D., R. García-Herrera and R. Huth, 2008. Solar modulation of Northern Hemisphere winter blocking. *J. Geophys. Res.*, **113**, D14118.

Barriopedro, D., R. García-Herrera, P. Lionello and C. Pino, 2010. A discussion of the links between solar variability and high-storm-surge events in Venice. *J. Geophys. Res.*, **115**, D13101.

Baumgaertner, A. J. G., P. Jöckel and C. Brühl, 2009. Energetic particle precipitation in ECHAM5/MESSy1 - Part 1: Downward transport of upper atmospheric NOx produced by low energy electrons. *Atmos. Chem. Phys.*, **9**, 2729–2740.

Baumgaertner, A. J. G., P. Jöckel, H. Riede, G. Stiller and B. Funke, 2010. Energetic particle precipitation in ECHAM5/MESSy - Part 2: Solar Proton Events. *Atmos. Chem. Phys.*, **10**, 7285–7302.

Berggren, A.-M., A. Aldahan, G. Possnert, E. Haltia-Hovi and T. Saarinen, 2010. 10Be and solar activity cycles in varved lake sediments, AD 1900-2006. *J. Paleolimnol.*, **44**, 559–569.

Bhattacharyya, S. and R. Narasimha, 2005. Possible association between Indian monsoon rainfall and solar activity. *Geophys. Res. Lett.*, **32**, L05813.

Bodeker, G., I. Boyd and W. Matthews, 1998. Trends and variability in vertical ozone and temperature profiles measured by ozonesondes at Lauder, New Zealand: 1986-1996. *J. Geophys. Res.*, **103**(D22), 28661–28681.

Brasseur, G., A. D. Rudder, G. Keating and M. Pitts, 1987. Response of Middle Atmosphere to Short-Term Solar Ultraviolet Variations: 2. Theory. *J. Geophys. Res.*, **92**(D1), 903–914.

Brasseur, G. and S. Solomon, 2005. *Aeronomy of the Middle Atmosphere.* Springer, Dordrecht, 3rd edition.

Brühl, C., B. Steil, G. Stiller, B. Funke and P. Jöckel, 2007. Nitrogen compounds and ozone in the stratosphere: comparison of MIPAS satellite data with the chemistry climate model ECHAM5/MESSy1. *Atmos. Chem. Phys.*, **7**, 5585–5598.

Buchholz, J., 2005. *Simulations of physics and chemistry of polar stratospheric clouds with a general circulation model.* PhD thesis, University of Mainz.

Calvo, N., R. Garcia, W. Randel and D. Marsh, 2010. Dynamical mechanism for the increase in tropical upwelling in the lowermost tropical stratosphere during warm ENSO events. *J. Atmos. Sci.*, **67**, 2331–2340.

Camp, C. and K. Tung, 2007a. Surface Warming by the Solar Cycle as Revealed the Composite Mean Difference Projection. *Geophys. Res. Lett.*, **34**, L14703.

Chandra, S., 1991. The solar UV related changes in total ozone from a solar rotation to a solar cycle. *Geophys. Res. Lett.*, **18**(5), 837–840.

Charlton, A., L. Polvani, J. Perlwitz, F. Sassi, E. Manzinin, S. Pawson, J. Nielsen, K. Shibata and D. Rind, 2007. A new look at stratospheric sudden warmings. Part II. Evaluation of numerical model simulations. *J. Clim.*, **20**(3), 470–488.

Charney, J. and P. Drazin, 1961. Propagation of Planetary-Scale Disturbances from the Lower into the Upper Atmosphere. *J. Geophys. Res.*, **6**(1), 83–109.

Croci-Maspoli, M., C. Schwierz and H. Davies, 2007. A multifaceted climatology of atmospheric blocking and its recent linear trend. *J. Clim.*, **20**(4), 633–649.

Crooks, S. A. and L. J. Gray, 2005. Characterization of the 11-Year Solar Signal Using a Multiple Regression Analysis of the ERA-40 Dataset. *J. Clim.*, **18**(7), 996–1015.

Dikty, S., M. Weber, C. von Savigny, T. Sonkaew, A. Rozanov and J. Burrows, 2010. Modulations of the 27 day solar rotation signal in stratospheric ozone from Scanning Imaging Absorption Spectrometer for Atmospheric Cartography (SCIAMACHY) (2003-2008). *J. Geophys. Res.*, **115**, D00I15.

Egorova, T., E. Rozanov, E. Manzini, M. Haberreiter, W. Schmutz, V. Zubov and T. Peter, 2004. Chemical and dynamical response to the 11-year variability of the solar irradiance simulated with a chemistry-climate model. *Geophys. Res. Lett.*, **31**, L06119.

Etling, D., 2002. *Theoretische Meteorologie. Eine Einführung.* Springer, Berlin, 2nd edition.

Eyring, V., M. Chipperfield, M. Giorgetta, D. Kinnison, E. Manzini, K. Matthes, P. Newman, S. Pawson, T. Shepherd and D. Waugh, 2008. Overview of the New CCMVal reference and sensitivity simulations in support of upcoming Ozone and Climate Assessments and the Planned SPARC CCMVal Report. *SPARC Newsletter*, **30**, 20–26.

Eyring, V., I. Cionni, G. Bodeker, A. Charlton-Perez, D. Kinnison, J. Scinocca, D. Waugh,

H. Akiyoshi, S. Bekki, M. Chipperfield, M. Dameris, S. Dhomse, S. Frith, H. Garny, A. Gettelman, A. Kubin, U. Langematz, E. Mancini, M. Marchand, T. Nakamura, L. Oman, S. Pawson, G. Pitari, D. Plummer, E. Rozanov, T. Shepherd, K. Shibata, W. Tian, P. Braesicke, S. Hardiman, J. Lamarque, O. Morgenstern, J. Pyle, D. Smale and Y. Yamashita, 2010. Multi-model assessment of stratospheric ozone return dates and ozone recovery in CCMVal-2 models. *Atmos. Chem. Phys.*, **10**, 9451–9472.

Eyring, V., D. Kinnison and T. Shepherd, 2005. Overview of planned coupled chemistry-climate simulations to support upcoming ozone and climate assesments. *SPARC Newsletter*, **25**, 11–17.

Fioletov, V., 2009. Estimating the 27-day and 11-year solar cycle variations in tropical upper stratospheric ozone. *J. Geophys. Res.*, **114**, D02302.

Fioletov, V., G. Bodeker, A. Miller, R. McPeters and R. Stolarski, 2002. Global and zonal total ozone variations estimated from ground-based and satellite measurements: 1964-2000. *J. Geophys. Res.*, **107**(D22), 4647.

Fioletov, V. and T. Shepherd, 2005. Summertime total ozone variations over middle and polar latitudes. *Geophys. Res. Lett.*, **32**, L04807.

Fischer, P. and K. Tung, 2008. A reexamination of the QBO period modulation by the solar cycle. *J. Geophys. Res.*, **113**, D07114.

Fortuin, J. and U. Langematz, 1995. An update on the global ozone climatology and on concurrent ozone and temperature trends. *Proceedings SPIE Atmospheric Sensing and Modeling*, **2311**, 207–216.

Fouquart, Y. and B. Bonnel, 1980. Computations of solar heating of the earth's atmosphere: A new parametrization. *Beitr. Phys. Atmos.*, **53**, 35–62.

Frame, T. H. A. and L. J. Gray, 2010. The 11-year solar cycle in ERA-40 data: an update to 2008. *J. Clim.*, **23**, 2213–2222.

Fröhlich, C., 2004. Solar Irradiance Variability. In: *Solar Variability and its Effects on Climate*, edited by J. Pap and P. Fox, Volume 141 of *Geophysical Monograph Series*, pp. 97–110. American Geophysical Union.

Fröhlich, C. and J. Lean, 2004. Solar radiative output and its variability: evidence and mechanisms. *Astron. Astrophys. Rev.*, **12**, 273–320.

Garcia, R., T. Dunkerton, R. Lieberman and R. Vincent, 1997. Climatology of the semiannual oscillation of the tropical middle atmosphere. *J. Geophys. Res.*, **102**(D22), 26019–26032.

Garcia, R., D. R. Marsh, D. E. Kinnison, B. A. Boville and F. Sassi, 2007. Simulation of secular trends in the middle atmosphere, 1950-2003. *J. Geophys. Res.*, **112**, D09301.

García-Herrera, R., N. Calvo, R. Garcia and M. Giorgetta, 2006. Propagation of ENSO temperature signals into the middle atmosphere: A comparison of two general circulation models and ERA-40 reanalysis data. *J. Geophys. Res.*, **111**, D06101.

Garny, H., M. Dameris and A. Stenke, 2009. Impact of prescribed SSTs on climatologies and long-term trends in CCM simulations. *Atmos. Chem. Phys.*, **9**, 6017–6031.

Giorgetta, M. A., L. Bengtsson and K. Arpe, 1999. An investigation of QBO signals in the east Asian and Indian monsoon in GCM experiments. *Climate Dynamics*, **15**, 435–450.

Giorgetta, M. A., E. Manzini, E. Roeckner, M. Esch and L. Bengtsson, 2006. Climatology and Forcing of the Quasi-Biennial Oscillation in the MAECHAM5 Model. *J. Climate*,

**19**, 3882–3901.

Gleisner, H. and P. Thejll, 2003. Patterns of tropospheric response to solar variability. *Geophys. Res. Lett.*, **30**, 1711.

Gondolatsch, F., S. Steinacker and O. Zimmermann, 1990. *Astronomie Grundkurs*. Klett, Stuttgart.

Gray, L., J. Beer, M. Geller, J. Haigh, M. Lockwood, K. Matthes, U. Cubasch, D. Fleitmann, G. Harrison, L. Hood, J. Luterbacher, G. Meehl, D. Shindell, B. van Geel and W. White, 2010. Solar Influences on Climate. *Reviews of Geophysics*, **48**(RG4001).

Gray, L., P. S. J, T. Dunkerton, M. Baldwin, E. Drysdale and M. Allen, 2001. A data study of the influence of the equatorial upper stratosphere on northern hemisphere stratospheric sudden warmings. *Q. J. R. Meteorol. Soc.*, **127**(576), 1985–2003.

Grenfell, J., M. Kunze, U. Langematz, P. Mieth and B. Steil, 2010. The 27-day solar rotational cycle in the Freie Universität Berlin Climate Middle Atmosphere Model with interactive Chemistry (FUB CMAM CHEM). *Journal of Atmospheric and Solar-Terrestrial Physics*, **72**, 705–712.

Gruzdev, A., H. Schmidt and G. Brasseur, 2009. The effect of the solar rotational irradiance variation on the middle and upper atmosphere calculated by a three-dimensional chemistry-climate model. *Atmos. Chem. Phys.*, **9**, 595–614.

Hack, W., H. Wagner and K. Hoyermann, 1978. Reaktionen von Wasserstoffatomen mit Hydroperoxylradikalen I. Bestimmung der spezifischen Geschwindigkeitskonstanten der Reaktionskanäle. *Ber. Bunsenges. Phys. Chem.*, **82**, 713–719.

Haigh, J., 1994. The role of stratospheric ozone in modulating the solar radiative forcing of climate. *Nature*, **370**, 544–546.

Haigh, J., 1996. The Impact of Solar Variability on Climate. *Science*, **272**, 981–984.

Haigh, J., 1999. A GCM study of climate change in response to the 11-year solar cycle. *Q. J. R. Meteorol. Soc.*, **125**, 871–892.

Haigh, J., 2003. The effects of solar variability on the Earth's climate. *Philos. Trans. R. Soc. Lond. A*, **361**, 95–111.

Haigh, J., 2004. Fundamentals of the Earth's Atmosphere and Climate. In: *Solar Variability and its Effects on Climate*, edited by J. Pap and P. Fox, Volume 141 of *Geophysical Monograph Series*, pp. 97–110. American Geophysical Union.

Haigh, J., M. Blackburn and R. Day, 2005. The Response of Tropospheric Circulation to Perturbations in Lower-Stratospheric Temperature. *J. Clim.*, **18**, 3672–3691.

Haigh, J. and H. Roscoe, 2009. The final warming date of the antarctic polar vortex and influences on its interannual variability. *J. Clim.*, **22**, 5809–5819.

Haigh, J., A. Winning, R. Toumi and J. Harder, 2010. An influence of spectral variations on radiative forcing of climate. *Nature*, **467**, 696–699.

Hale, G. and S. Nicholson, 1925. The Law of Sun-Spot Polarity. *Ap.J.*, **62**, 270–300.

Hegerl, G., F. W. Zwiers, P. Braconnot, N. Gillett, Y. Luo, J. M. Orsini, N. Nicholls, J. Penner and P. Stott, 2007. Understanding and Attributing Climate Change. In: IPCC (2007).

Hines, C., 1974. A possible mechanism for the production of Sun-weather correlations. *J. Atmos. Sci.*, **31**, 589–591.

Hines, C., 1997a. Doppler-spread parameterization of gravity wave momentum deposition in the middle atmosphere. Part I: Basic formulation. *Journal of Atmospheric and Solar-*

*Terrestrial Physics*, **59**, 371–386.

Hines, C., 1997b. Doppler-spread parameterization of gravity wave momentum deposition in the middle atmosphere. Part II: Broad and quasi-monochromatic spectra, and implementation. *Journal of Atmospheric and Solar-Terrestrial Physics*, **59**, 387–400.

Holton, J., 1992. *An Introduction to Dynamic Meteorology*, Volume 48 of *International Geophysics Series*. Academic Press, San Diego, 3rd edition.

Holton, J. and H.-C. Tan, 1980. The Influence of the Equatorial Quasi Biennial Oscillation on the Global Circulation at 50 mb. *Journal of the Atmospheric Sciences*, **37**, 220–2208.

Hood, L., 1997. The solar cycle variation of total ozone: Dynamical forcing in the lower stratosphere. *J. Geophys. Res.*, **102**(D1), 1355–1370.

Hood, L., 2003. Thermal response of the tropical tropopause region to solar ultraviolet variations. *Geophys. Res. Lett.*, **30**, 2215.

Hood, L., Z. Huang and S. Bougher, 1991. Mesospheric Effects of Solar Ultraviolet Variations: Further Analysis of SME IRonal Ozone and Nimbus 7 SAMS Temperature Data. *J. Geophys. Res.*, **96**(D7), 12989–13002.

Hood, L. and S. Zhou, 1998. Stratospheric effects of 27-day solar ultraviolet variations: An analysis of UARS MLS ozone and temperature data. *J. Geophys. Res.*, **103**(D3), 3629–3638.

Hoyt, D. and K. Schatten, 1997. *The Role of the Sun in Climate Change*. Oxford University Press.

Hupfer, P. and W. Kuttler (editors), 1998. *Witterung und Klima*. Teubner, Stuttgart, 10th edition.

Huth, R., J. Kyselý, J. Bochníček and P. Hejda, 2008. Solar activity affects the occurrence of synoptic types over Europe. *Annales Geophysicae*, **26**, 1999–2004.

IPCC, 2007. *Synthesis Report. Contribution of Working Groups I, II and III to the Fourth Assessment Report of the Intergovernmental Panel on Climate Change*. IPCC, Geneva, Switzerland.

Jöckel, P., R. Sander, A. Kerkweg, H. Tost and J. Lelieveld, 2005. Technical Note: The Modular Earth Submodel System (MESSy) - a new approach towards Earth System Modeling. *Atmos. Chem. Phys.*, **5**, 433–444.

Jöckel, P., H. Tost, A. Pozzer, C. Brühl, J. Buchholz, L. Ganzeveld, P. Hoor, A. Kerkweg, M. G. Lawrence, R. Sander, B. Steil, G. Stiller, M. Tanarhteand, D. Taraborrelli, J. van Aardenne and J. Lelieveld, 2006. The atmospheric chemistry general circulation model ECHAM5/MESSy1: consistent simulation of ozone from the surface to the mesosphere. *Atmos. Chem. Phys.*, **6**, 5067–5104.

Kalnay, E., M. Kanamitsu, R. Kistler, W. Collins, D. Deaven, L. Gandin, M. Iredell, S. Saha, G. White, J. Woollen, Y. Zhu, M. Chelliah, W. Ebizusaki, W. Higgins, J. Janowiak, K. Mo, C. Ropelewski, J. Wang, A. Leetmaa, R. Reynolds, R. Jenne and D. Joseph, 1996. The NCEP/NCAR 40-year reanalysis project. *Bull. Americ. Meteor. Soc.*, **77**, 437–471.

Keating, G., M. Pitts, G. Brasseur and A. DeRudder, 1987. Response of Middle Atmosphere to Short-Term Solar Ultraviolet Variations: 1. Observations. *J. Geophys. Res.*, **92**(D1), 889–902.

Keckhut, P. and M. Chanin, 1992. Middle Atmosphere Response to the 27-day Solar Rotation as observed by Lidar. *Geophys. Res. Lett.*, **19**, 809–812.

Kerkweg, A., J. Buchholz, L. Ganzeveld, A. Pozzer, H. Tost and P. Jöckel, 2006a. Technical Note: An implementation of the dry removal processes DRY DEPosition and SEDImentation in the Modular Earth Submodel System (MESSy). *Atmos. Chem. Phys.*, **6**, 4617–4632.

Kerkweg, A., R. Sander, H. Tost and P. Jöckel, 2006b. Implementation of prescribed (OFFLEM), calculated (ONLEM), and pseudo-emissions (TNUDGE) of chemical species in the Modular Earth Submodel System (MESSy). *Atmos. Chem. Phys.*, **6**, 3603–3609.

Kiepenheuer, K. O., 1954. Solar Activity. In: *The Sun*, edited by G. P. Kuiper, Chapter 6. University of Chicago Press, Chicago.

Kistler, R., W. Collins, S. Saha, G. White, J. Woollen, E. Kalnay, M. Chelliah, W. Ebizusaki, M. Kanamitsu, V. Kousky, H. van den Dool and R. J. ad M .Fiorino, 2001. The NCEP/NCAR 50-year reanalysis project. *Bull. Americ. Meteor. Soc.*, **82**, 247–267.

Kodera, K., 2002. Solar cycle modulation of the North Atlantic Oscillation: Implications for the spatial structure of the NAO. *Geophys. Res. Lett.*, **29**(8).

Kodera, K., 2003. Solar influence on the spatial structure of the NAO during the winter 1900-1999. *Geophys. Res. Lett.*, **30**(4).

Kodera, K., 2004. Solar influence on the Indian Ocean Monsoon through dynamical processes. *Geophys. Res. Lett.*, **31**, L24209.

Kodera, K., 2005. Possible solar modulation of the ENSO cycle. *Papers in Meteorology and Geophysics*, **55**(21-33).

Kodera, K. and Y. Kuroda, 2002. Dynamical response to the solar cycle. *J. Geophys. Res.*, **107**(D24).

Kodera, K., K. Matthes, K. Shibata, U. Langematz and Y. Kuroda, 2003. Solar impact on the lower mesospheric subtropical jet: A comparative study with general circulation model simulations. *Geophys. Res. Lett.*, **30**(6).

Kodera, K. and K. Shibata, 2006. Solar influence on the tropical stratosphere and troposphere in the northern summer. *Geophys. Res. Lett.*, **33**(L19704).

Krivova, N., S. Solanki, M. Fligge and Y. Unruh, 2003. Reconstruction of solar irradiance variations in cycle 23: Is solar surface magnetism the cause? *Astron. Astrophys.*, **399**, L1–L4.

Kuai, L., R.-L. Shia, X. Jiang, K. Tung and Y. Yung, 2009. Modulation of the Period of the Quasi-Biennial Oscillation by the Solar Cycle. *J. Atmos. Sci.*, **66**, 2418–2428.

Kubin, A., U. Langematz and C. Brühl, 2011. CCM simulations of the effect of the 27-day solar rotational cycle on ozone. *J. Geophys. Res.*, **submitted**.

Kuroda, Y., 2007. Effect of QBO and ENSO on the Solar Cycle Modulation of Winter North Atlantic Oscillation. *J. Met. Soc. Japan*, **85**(6), 889–898.

Kuroda, Y., 2008. Effect of stratospheric sudden warming and vortex intensification on the troposperic climate. *J. Geophys. Res.*, **110**, D15110.

Kuroda, Y., M. Deushi and K. Shibata, 2007. Role of solar activity in the troposphere-stratosphere coupling in the southern hemisphere winter. *Geophys. Res. Lett.*, **34**, L21704.

Kuroda, Y. and K. Kodera, 2002. Effect of Solar Activity on the Polar-night Jet Oscillation in the Northern and Southern Hemisphere Winter. *J. Meteorol. Soc. Japan*, **80**(4B), 973–984.

Kuroda, Y. and K. Kodera, 2005. Solar cycle modulation of the Southern Annular Mode. *Geophys. Res. Lett.*, **32**, L13802.

Kuroda, Y. and K. Shibata, 2006. Simulation of solar-cycle modulation of the Southern Annular Mode using a chemistry-climate model. *Geophys. Res. Lett.*, **33**, L05703.

Kuroda, Y. and K. Yamazaki, 2010. Influence of the solar cycle and QBO modulation on the Southern Annular Mode. *Geophys. Res. Lett.*, **37**, L12703.

Kuroda, Y., K. Yamazaki and K. Shibata, 2008. Role of ozone in the solar cycle modulation of the North Atlantic Oscillation. *J. Geophys. Res.*, **113**, D14122.

Labitzke, K., 1987. Suspots, the QBO and the stratospheric temperature in the north polar region. *Geophys. Res. Lett.*, **14**(5), 535–537.

Labitzke, K., 1999. *Die Stratosphäre.* Springer.

Labitzke, K., 2003. The global signal of the 11-year sunspot cycle in the atmosphere: When do we need the QBO? *Met. Zeitschr.*, **12**(4), 209–216.

Labitzke, K., 2004a. On the Signal of the 11-Year Sunspot Cycle in the Stratosphere and its Modulation by the Quasi-Biennial Oscillation (QBO). *Journal of Atmospheric and Solar-Terrestrial Physics*, **66**(13-14), 1151–1157.

Labitzke, K., 2004b. On the Signal of the 11-Year Sunspot Cycle in the Stratosphere over the Antarctic and its Modulation by the Quasi-Biennial Oscillation (QBO). *Met. Zeitschr.*, **13**(4), 263–270.

Labitzke, K., J. Austin, N. Butchart, J. Knight, M. Takahashi, M. Nakamoto, T. Nagashima, J. Haigh and V. Williams, 2002. The global signal of the 11-year solar cycle in the stratosphere: Observations and models. *J. Atmos. Solar-Terr. Phys.*, **64**, 203–210.

Labitzke, K. and M. Kunze, 2009. Variability in the stratosphere: The sun and the QBO. In: *Climate and Weather of the Sun-Earth System (CAWSES): Selected Papers from the 2007 Kyoto Symposium*, edited by T. Tsuda, R. Fujii, K. Shibata and M. A. Geller, pp. 257–278. TERRAPUB, Tokyo.

Labitzke, K., B. Naujokat and C. Marquardt, 1996. The Quasi-Biennial Oscillation. In: *Encyclopedia of climate and weather*, pp. 622–626. Oxford University Press, New York.

Labitzke, K. and H. van Loon, 1988. Association between the 11-year solar cycle, the QBO and the atmosphere. Part I: The troposphere and stratosphere in the northern hemisphere in winter. *Journal of Atmospheric and Solar-Terrestrial Physics*, **50**, 197–206.

Labitzke, K. and H. van Loon, 1995. Association between the 11-year solar cycle, the QBO and the atmosphere. Part I: The troposphere and stratosphere in the northern hemisphere in winter. *Tellus*, **47A**(2), 275–286.

Labitzke, K. and H. van Loon, 1997a. Total ozone and the 11-yr suspot cycle. *Journal of Atmospheric and Solar-Terrestrial Physics*, **59**(1), 9–19.

Landgraf, J. and P. J. Crutzen, 1998. An efficient method for online calculations of photolysis and heating rates. *J. Atmos. Sci.*, **55**, 863–878.

Langematz, U., J. Grenfell, K. Matthes, P. Mieth, M. Kunze, B. Steil and C. Brühl, 2005. Chemical effects in 11-year solar cycle simulations with the Freie Universität Berlin Climate Middle Atmosphere Model with online chemistry (FUB-CMAM-CHEM). *Geophys. Res. Lett.*, **32**, L13803.

Lean, J., 1997. The Sun's variable Radiation and its Relevance for Earth. *Annu. Rev. Astron. Astrophys.*, **35**, 33–67.

Lean, J., 2000. Evolution of the Sun's Spectral Irradiance Since the Maunder Minimum. *Geophys. Res. Lett.*, **27**(16), 2425–2428.

Lean, J., J. Cook, W. Marquette and A. Johannesson, 1998. Magnetic sources of the solar irradiance cycle. *Astrophys. J.*, **492**, 390–401.

Lean, J., G. Rottman, J. Harder and G. Kopp, 2005. SORCE contributions to new understanding of global change and solar variability. *Solar Phys.*, **230**, 27–53.

Lean, J., G. Rottman, H. Kyle, T. Woods, J. Hickey and L. Puga, 1997. Detection and parameterizations of variations in solar mid- and near-ultraviolet radiation (200-400nm). *J. Geophys. Res.*, **102**(D25), 29939–29956.

Lee, H. and A. Smith, 2003. Simulation of the combined effects of solar cycle, quasi-biennial oscillation and volcanic forcing on stratospheric ozone changes in recent decades. *J. Geophys. Res.*, **108**(D2), 4049.

Lee, J. and S. Hameed, 2007. Northern Hemisphere annular mode in summer: Its physical significance and its relation to solar activity variations. *J. Geophys. Res.*, **112**, D15111.

Lee, J., S. Hameed and D. Shindell, 2008. The northern annular mode in summer and its relation to solar activity variations in the GISS ModelE. *Journal of Atmospheric and Solar-Terrestrial Physics*, **70**, 730–741.

Lee, J., D. Shindell and S. Hameed, 2009. The Influence of Solar Forcing on Tropical Circulation. *J. Clim.*, **22**, 5870–5885.

Lelieveld, J., C. Brühl, P. Jöckel, B. Steil, P. J. Crutzen, H. Fischer, M. A. Giorgetta, P. Hoor, M. G. Lawrence, R. Sausen and H. Tost, 2007. Stratospheric dryness: model simulations and satellite observations. *Atmos. Chem. Phys.*, **7**, 1313–1332.

Liou, K., 2002. *An Introduction to Atmospheric Radiation*, Volume 84 of *International Geophysics Series*. Harvard University Press, Amsterdam, 2nd edition.

London, J., 1980. Radiative Energy Sources and Sinks in the Stratosphere and Mesosphere. In: *Proceedings of the NATO Advanced Study Institute*, edited by M. Nicolet and A. Aikin. US Department of Transportation, Washington, DC.

Lott, F., 1999. Alleviation of stationary biases in a GCM through a mountain drag parameterization scheme and a simple representation of mountain lift forces. *Mon. Wea. Rev.*, **127**, 788–801.

Lott, F. and M. Miller, 1997. A new subgrid scale orographic drag parameterization: Its formulation and testing. *Q. J. R. Meteorol. Soc.*, **123**, 101–127.

Manzini, E., M. Giorgetta, M. Esch, L. Kornblueh and E. Roeckner, 2006. The influence of sea surface temperatures on the northern winter stratosphere: Ensemble simulations with the MAECHAM5 model. *J. Clim.*, **19**, 3863–3881.

Marquardt, C., 1997. *Die tropische QBO und dynamische Prozesse in der Stratosphäre.* PhD thesis, Freie Universität Berlin.

Marsh, D. and R. Garcia, 2007. Attribution of decadal variability in lower-stratospheric tropical ozone. *Geophys. Res. Lett.*, **34**, L21807.

Marsh, D., R. Garcia, D. Kinnison, B. A. Boville, F. Sassi, S. Solomon and K. Matthes, 2007. Modeling the whole atmosphere response to solar cycle changes in radiative and geomagnetic forcing. *J. Geophys. Res.*, **112**, D23306.

Matthes, K., 2003. *Der Einfluss des 11-jährigen Sonnenfleckenzyklus und der QBO auf die Atmosphäre*. PhD thesis, Freie Universität Berlin.

Matthes, K. and K. Kodera, 2011. Report on 2010 SOLARIS Activities and Future Plans. *SPARC-Newsletter*, **36**.

Matthes, K., K. Kodera, J. Haigh, D. T. Shindell, K. Shibata, U. Langematz, E. Rozanov and Y. Kuroda, 2003. GRIPS Solar Experiments Intercomparison Project: Initial Results. *Papers in Meteorol. and Geophys.*, **54**, 71–90.

Matthes, K., Y. Kuroda, K. Kodera and U. Langematz, 2006. Transfer of the solar signal from the stratosphere to the troposphere: Northern winter. *J. Geophys. Res.*, **111**, D06108.

Matthes, K., U. Langematz, L. Gray, K. Kodera and K. Labitzke, 2004. Improved 11-year solar signal in the Freie Universität Berlin Climate Middle Atmosphere Model (FUB-CMAM). *J. Geophys. Res.*, **109**(D06101).

Matthes, K., D. Marsh, R. Garcia, D. Kinnison, F. Sassi and S. Walters, 2010. Role of the QBO in modulating the influence of the 11 year solar cycle on the atmosphere using constant forcings. *J. Geophys. Res.*, **115**, D18110.

McDaniel, B. and R. Black, 2005. Intraseasonal Dynamical Evolution of the Northern Annular Mode. *J. Clim.*, **18**, 3820–3839.

Meehl, G., J. Arblaster, G. Branstator and H. van Loon, 2008. A coupled air-sea response mechanism to solar forcing in the Pacific region. *J. Clim.*, **21**, 2883–2897.

Meehl, G., J. Arblaster, K. Matthes, F. Sassi and H. van Loon, 2009. Amplifying the Pacific Climate System Response to a Small 11-Year Solar Cycle Forcing. *Science*, **325**, 1114.

Meehl, G., W. Washington, T. Wigley, J. Arblaster and A. Dai, 2003. Solar and Greenhouse Gas Forcing and Climate Response in the Twentieth Century. *J. Clim.*, **16**, 426–444.

Mukherjee, B., K. Indira, R. Reddy and B. R. Murty, 1985. Quasi-biennial oscillation in stratospheric zonal wind and Indian summer monsoon. *Mon. Weather Rev.*, **113**, 1421–1424.

Naujokat, B., 1986. An update of the observed Quasi-Biennial Oscillation of the stratospheric winds over the tropics. *J. Atmos. Sci.*, **43**, 1873–1877.

Newman, P., J. Daniel, D. Waugh and E. Nash, 2007. A new formulation of equivalent effective stratospheric chlorine (EESC). *Atmos. Chem. Phys.*, **7**, 4537–4552.

Nissen, K., K. Matthes, U. Langematz and B. Mayer, 2007. Towards a better representation of the solar cycle in general circulation models. *Atmos. Chem. Phys.*, **7**, 5391–5400.

Ogi, M., Y. Tachibana and K. Yamazaki, 2003a. Impact of the wintertime North Atlantic Oscillation (NAO) on the summertime atmospheric circulation. *Geophys. Res. Lett.*, **30**(13).

Ogi, M., K. Yamazaki and Y. Tachibana, 2003b. Solar cycle modulation of the seasonal linkage of the North Atlantic Oscillation (NAO). *Geophys. Res. Lett.*, **30**(22).

Pap, J. M. and P. Fox (editors), 2004. *Solar Variability and its Effects on Climate*, Volume 141 of *Geophysical Monograph Series*. American Geophysical Union.

Pascoe, C., L. Gray, S. Crooks, M. Juckes and M. Baldwin, 2005. The quasi biennial oscillation: Analysis using ERA-40 data. *J. Geophys. Res.*, **110**, D08105.

Plumb, R., 1985. On the Three-Dimensional Propagation of Planetary Waves. *Journal of the Atmospheric Sciences*, **42**(3).

Plumb, R. and R. Bell, 1982. A model of the quasi-biennial oscillation on an equatorial beta-plane. *Q. J. R. Meteorol. Soc.*, **108**, 335–352.

Raith, W. (editor), 2002. *Bergmann Schäfer Lehrbuch der Experimentalphysik.* de Gruyter, Berlin, 2nd edition.

Randel, W., E. Fleming, M. Geller, M. Gelman, K. Hamilton, D. Karoly, D. Ortland, S. Pawson, R. Swinbank, P. Udelhofen, F. Wu, M. Baldwin, M.-L. Chanin, P. Keckhut, K. Labitzke, E. Remsberg, A. Simmons and D. Wu, 2002. *The SPARC intercomparison of Middle Atmosphere Climatologies.* Technical report WMO/TD-No. 1142, SPARC Report, No. 3, WCRP - 116.

Randel, W., K. Shine, J. Austin, J. Barnett, C. Claud, N. Gillet, P. Keckhut, U. Langematz, R. Lin, C. Long, C. Mears, A. Miller, J. Nash, D. Seidel, D. Thompson, F. Wu and S. Yoden, 2009. An update of observed stratospheric temperature trends. *J. Geophys. Res.*, **114**, D02107.

Randel, W., P. Udelhofen, E. Fleming, M. Geller, M. Gelman, K. Hamilton, D. Karoly, D. Ortland, S. Pawson, R. Swinbank, F. Wu, M. Baldwin, M.-L. Chanin, P. Keckhut, K. Labitzke, E. Remsberg, A. Simmons and D. Wu, 2004. The SPARC intercomparison of middle-atmosphere climatologies. *J. Clim.*, **17**, 986–1003.

Randel, W. and F. Wu, 2007. A stratospheric ozone profile data set for 1979-2005: Variability, trends, and comparisons with column ozone data. *J. Geophys. Res.*, **112**, D06313.

Rayner, N., D. Parker, E. Horton, C. Folland, L. Alexander, D. Rowell, E. Kent and A. Kaplan, 2003. Globally complete analyses of sea surface temperature, sea ice and night marine air temperature, 1871-2000. *J. Geophys. Res.*, **108**, 4407.

Richter, J., F. Sassi and R. Garcia, 2010. Towards a physically based gravity wave source parameterization in a general circulation model. *J. Atmos. Sci.*, **67**, 136–156.

Rind, D., J. Lean, J. Lerner, P. Lonergan and A. Leboissitier, 2008. Exploring the stratospheric/tropospheric response to solar forcing. *J. Geophys. Res.*, **113**, D24103.

Roeckner, E., G. Bäuml, L. Bonaventura, R. Brokopf, M. Esch, M. Giorgetta, S. Hagemann, I. Kirchner, L. Kornblueh, E. Manzini, A. Rhodin, U. Schlese, U. Schulzweida and A. Tompkins, 2003. *The atmospheric general circulation model ECHAM 5. PART I: Model description.* Technical report, Max-Planck-Institut für Meteorologie.

Roeckner, E., R. Brokopf, M. Esch, M. Giorgetta, S. Hagemann, L. Kornblueh, E. Manzini, U. Schlese and U. Schulzweida, 2004. *The atmospheric general circulation model ECHAM 5. PART II: Sensitivity of Simulated Climate to Horizontal and Vertical Resolution.* Technical report, Max-Planck-Institut für Meteorologie.

Roeckner, E., R. Brokopf, M. Esch, M. Giorgetta, S. Hagemann, L. Kornblueh, E. Manzini, U. Schlese and U. Schulzweida, 2006. Sensitivity of Simulated Climate to Horizontal and Vertical Resolution in the ECHAM5 Atmosphere Model. *J. Climate*, **19**, 3771–3791.

Roy, I. and J. Haigh, 2010. Solar cycle signals in sea level pressure and sea surface temperatures. *Atmos. Chem. Phys.*, **10**, 3147–3153.

Rozanov, E., T. Egorova, W. Schmutz and T. Peter, 2006. Simulation of the stratospheric ozone and temperature response to the solar irradiance variability during sun rotation

cycle. *Journal of Atmospheric and Solar-Terrestrial Physics*, **68**, 2203–2213.

Rozanov, E., M. Schlesinger, T. Egorova, B. Li, N. Andronova and V. Zubov, 2004. Atmospheric response to the observed increase of solar UV radiation from solar minimum to solar maximum simulated by the University of Illinois at Urbana-Champaign climate-chemistry model. *J. Geophys. Res.*, **109**, D01110.

Ruzmaikin, A., M. Santee, M. Schwartz, L. Froidevaux and H. Pickett, 2007. The 27-day variations in stratospheric ozone and temperature: New MLS data. *Geophys. Res. Lett.*, **34**, L02819.

Salby, M. and P. Callaghan, 2000. Connection between the solar cycle and the QBO: The missing link. *J. Clim.*, **13**(14), 2652–2662.

Salby, M. and P. Callaghan, 2006. Relationship of the quasi-biennial oscillation to the stratospheric signature of the solar cycle. *J. Geophys. Res.*, **111**, D06110.

Sander, R., A. Kerkweg, P. Jöckel and J. Lelieveld, 2005. Technical Note: The new comprehensive atmospheric chemistry module MECCA. *Atmos. Chem. Phys.*, **5**, 445–450.

Sassi, F., D. Kinnison, B. Boville, R. Garcia and R. Roble, 2004. Effect of El Niño-Southern Oscillation on the dynamical, thermal and chemical structure of the middle atmosphere. *J. Geophys. Res.*, **109**, D17108.

Scheffler, H. and H. Elsässer, 1990. *Physik der Sterne und der Sonne*. Bibliographisches Institut, Mannheim.

Schmidt, H. and G. Brasseur, 2006. The response of the middle atmosphere to solar cycle forcing in the Hamburg Model of the Neutral and Ionized Atmosphere. *Space Sci. Rev.*, **125**, 345–356.

Schmidt, H., G. Brasseur and M. Giorgetta, 2010. Solar cycle signal in a general circulation and chemistry model with internally generated quasi-biennial oscillation. *J. Geophys. Res.*, **115**, D00I14.

Schultz, M., A. Heil, J. Hoelzemann, A. Spessa, K. Thonicke, J. Goldammer, A. Held, J. Pereira and M. van het Bolscher, 2008. Global Wildland Fire Emissions from 1960 to 2000. *Global Biogeochem. Cyc.*, **22**, GB2002.

Shibata, K. and M. Deushi, 2008. Long-term variations and trends in the simulation of the middle atmosphere 1980-2004 by the chemistry-climate model of the Meteorological Research Institute. *Ann. Geophys.*, **26**, 1299–1326.

Shindell, D., G. Faluvegi, R. Miller, G. Schmidt and J. Hansen, 2006. Solar and athropogenic forcing of tropical hydrology. *Geophys. Res. Lett.*, **33**, L24706.

Simmons, A., D. Burridge, M. Jarraud, C. Girard and W. Wergen, 1989. The ECMWF Medium-Range Prediction Models. Development of the Numerical Formulations and the Impact of Increased Resolution. *Meteor. Atmos. Phys.*, **40**(1-3), 28–60.

Simpson, I., M. Blackburn and J. Haigh, 2009. The Role of Eddies in Driving the Tropospheric Response to Stratospheric Heating Pertubations. *Journal of the Atmospheric Sciences*, **66**(5), 1347–1365.

Smith, A. and K. Matthes, 2008. Decadal-scale periodicities in the stratosphere associated with the solar cycle and the QBO. *J. Geophys. Res.*, **113**, D05311.

Solanki, S. and N. Krivova, 2003. Can solar variability explain global warming since 1970? *J. Geophys. Res.*, **108**(A5), 1200.

Solanki, S., I. Usoskin, B. K. B., M. Schüssler and J. Beer, 2004. Unusual Activity of

the Sun During Recent Decades Compared to the Previous 11,000 Years. *Nature*, **431**, 1084–1087.

Solanki, S. K., 2002. Solar Variability. In: *The Radiometric Calibration of SOHO*, edited by A. Pauluhn, M. C. E. Huber and R. von Steiger, pp. 1–19. ESA Publ. Div., Noordwijk.

Solanki, S. K., 2003. Sunspots. An Overview. *Astron. Astrophys. Rev.*, **11**, 153–286.

Soukharev, B. and L. Hood, 2006. Solar cycle variation of stratospheric ozone: Multiple regression analysis of long-term satellite data sets and comparisons with models. *J. Geophys. Res.*, **111**, D20314.

Soukharev, B. and K. Labitzke, 2001. The 11-year solar cycle, the Sun's rotation, and the middle stratosphere in winter. Part II: Response of planetary waves. *Journal of Atmospheric and Solar-Terrestrial Physics*, **63**(18), 1931–1939.

SPARC CCMVal, 2010. *SPARC Report on the Evaluation of Chemistry-Climate Models.* Technical report WMO/TD-No. 1526, SPARC Report, No. 5, WCRP - 132.

Thomas, M. A., M. A. Giorgetta, C. Timmreck, H.-F. Graf and G. Stenchikov, 2009. Simulation of the climate impact of Mt.Pinatubo eruption using ECHAM5 - Part 2: Sensitivity to the phase of the QBO and ENSO. *Atmos. Chem. Phys.*, **9**, 3001–3009.

Thuburn, J. and G. Craig, 2000. Stratospheric Influence on Tropopause Height: The Radiative Constraint. *Journal of the Atmospheric Sciences*, **57**, 17–28.

Tibaldi, S. and F. Molteni, 1990. On the operational predictability of blocking. *Tellus*, **42A**, 343–365.

Tost, H., P. Jöckel, A. Kerkweg, R. Sander and J. Lelieveld, 2006. Technical Note: A new comprehensive SCAVenging submodel for global atmospheric chemistry modelling. *Atmos. Chem. Phys.*, **6**, 565–574.

Tourpali, K., C. Schuurmans, R. van Dorland, B. Steil and C. Brühl, 2003. Stratospheric and tropospheric response to enhanced solar UV radiation: A model study. *Geophys. Res. Lett.*, **30**(5), 1231.

Tourpali, K., C. Schuurmans, R. van Dorland, B. Steil, C. Brühl and E. Manzini, 2005. Solar cycle modulation of the Arctic Oscillation in a chemistry-climate model. *Geophys. Res. Lett.*, **32**, L17803.

Trenberth, K., 1997. The Definition of El Niño. *Bull. Americ. Meteorol. Soc.*, **78**(12), 2771–2777.

Tung, K. and C. Camp, 2008. Solar Cycle Warming at the Earth's Surface in NCEP and ERA-40 data: A linear Discriminant Analysis. *J. Geophys. Res.*, **113**, D05114.

Uppala, S., P. Kållberg, A. Simmons, U. Andrae, V. da Costa Bechtold, M. Fiorino, J. K. Gibson, J. Haseler, A. Hernandez, G. A. Kelly, X. Li, K. Onogi, S. Saarinen, N. Sokka, R. P. Allan, E. Andersson, K. Arpe, M. A. Balmaseda, A. Beljaars, L. van de Berg, J. Bidlot, N. Bormann, S. Caires, F. Chevallier, A. Dethof, M. Dragosavac, M. Fisher, M. Fuentes, S. Hagemann, E. Hólm, B. J. Hoskins, L. Isaksen, P. Janssen, R. Jenne, A. McNally, J.-F. Mahfouf, J.-J. Morcrette, N. Rayner, R. Saunders, P. Simon, A. Sterl, K. Trenberth, A. Untch, D. Vasiljevic, P. Viterbo and J. Woollen, 2005. The ERA-40 re-analysis. *Quart. J. R. Meteorol. Soc.*, **131**, 2961–3012.

van Loon, H., G. Meehl and J. Arblaster, 2004. A Decadal Solar Effect in the Tropics in July-August. *Journal of Atmospheric and Solar-Terrestrial Physics*, **66**, 1767–1778.

van Loon, H., G. Meehl and D. Shea, 2007. Coupled air-sea response to solar forcing in the pacific region during northern winter. *J. Geophys. Res.*, **112**, D02108.

White, W., 2006. Response of tropical global ocean temperature to the Sun's quasi-decadal UV radiative forcing of the stratosphere. *J. Geophys. Res.*, **111**, C09020.

White, W., M. Dettinger and D. Cayan, 2003. Sources of global warming of the upper ocean on decadal period scales. *J. Geophys. Res.*, **108**(C8), 3248.

White, W., J. Lean, D. Cayan and M. Dettinger, 1997. Response of global upper ocean temperature to changing solar irradiance. *J. Geophys. Res.*, **102**(C2), 3255–3266.

Williams, V., J. Austin and J. Haigh, 2001. Model simulations of the impact of the 27-day solar rotational period on the stratospheric ozone and temperature. *Adv. Space Res.*, **27**(12), 1933–1942.

Willson, R., C. Duncan and J. Geist, 1980. Direct measurement of solar luminosity variation. *Science*, **207**, 177–179.

WMO, W., 1992. *International meteorological vocabulary*. WMO, Geneva, 2nd edition.

Yamashita, Y., K. Sakamoto, H. Akiyoshi, M. Takahashi, T. Nagashima and L. Zhou, 2010. Ozone and temperature response of a chemistry climate model to the solar cycle and sea surface temperature. *J. Geophys. Res.*, **115**, D00M05.

Yukimoto, S. and K. Kodera, 2007. Annular Modes Forced from the Stratosphere and Interactions with the Oceans. *J. Met Soc. Japan*, **85**, 943–952.

# List of abbreviations

| | |
|---|---|
| ACRIM | Active Cavity Radiometer Irradiance Monitor |
| AO | Artic Oscillation |
| BDC | Brewer-Dobson Circulation |
| CAWSES | Climate And Weather of the Sun Earth System |
| CCM | Chemistry Climate Model |
| CCMVal | Chemistry Climate Model VALidation for SPARC |
| CFC | Chlorofluorocarbons |
| DJF | December, January, February |
| ECHAM5 | European Center HAMburg model 5 |
| ECMWF | European Center for Medium Range Weather Forecast, Reading, UK |
| EMAC | ECHAM/MESSy Atmospheric Chemistry model |
| ENSO | El Niño Southern Oscillation |
| EP | Eliassen-Palm flux |
| ERA | ECMWF ReAnalysis |
| ERBE | Earth's Radiation Budget Experiment |
| ERBS | Earth's Radiation Budget Satellite |
| ESC | Effective Stratospheric Chlorine |
| F10.7 | 10.7 cm Solar Radio Flux |
| FUB | Freie Universität Berlin |
| GCM | General Circulation Model |
| GHG | Greenhouse Gas |
| HALOE | Halogene Occultation Experiment |
| IIASA | International Institute for Applied Systems Analysis, Laxenburg, Austria |
| IPCC | Intergovernmental Panel on Climate Change |
| ITCZ | Inter Tropical Convergence Zone |
| IR | Infrared |
| JJA | June, July, August |
| MESSy | Modular Earth Submodel System |
| MMC | Mean Meridional Circulation |
| MRI | Meteorological Research Institut, Tsukuba, Japan |
| MSU | Microwave Sounding Unit |
| NAM | Northen Annular Mode |

| | |
|---|---|
| NAO | North Atlantic Oscillation |
| NCAR | National Center for Atmospheric Research, Boulder, Colorado, USA |
| NCEP | National Center for Environmental Prediction |
| OBS | Observations |
| ODS | Ozone Depleting Substances |
| PNA | Pacific North American Pattern |
| PNJ | Polar Night Jet |
| ProSECCO | Project on Solar Effects on Chemistry and Climate including Ocean interactions |
| QBO | Quasi-biennial Oscillation |
| SAGE | Stratospheric Aerosol and Gas Experiment |
| SAM | Southern Annular Mode |
| SAO | Semi-Annual Oscillation |
| SBUV | Solar Backscattered Ultraviolet |
| SOLARIS | SOLAR Influence for SPARC |
| SOLSTICE | SOLar STellar Irradiance Comparison Experiment |
| SORCE | SOlar Radiation and Climate Experiment |
| SPARC | Stratospheric Processes And their Role in Climate |
| SRES | Special Report on Emission Scenarios |
| SST | Sea Surface Temperature |
| SSU | Stratospheric Sounding Unit |
| SW | Short-Wave |
| TOMS | Total Ozone Mapping Spectrometer |
| UARS | Upper Atmosphere Research Satellite |
| UV | Ultraviolet |
| VIRGO | Variability of solar IRradiance and Gravity Oscillations |
| VOC | Volatile Organic Compounds |
| WACCM | Whole Atmosphere Community Climate Model |
| WMO | World Meteorological Organisation |

# Appendix

Within the context of the mechanistic momentum study (Chapter 6) an artificial momentum forcing was implemented in the stratosphere of EMAC-FUB. The Fortran90 code was originally written by Anne Kubin, the MESSy-conform (Jöckel et al., 2005) implementation was done in collaboration with Patrick Jöckel. The below printed module

`messy_mmforce.f90`

contains the so called submodel core layer routines in which the actual computation of the momentum force is done. The coupling between the submodel mmforce and the base model is realised in the so called submodel interface layer in the module

`messy_mmforce_e5.f90`.

```
! ************************************************************************
MODULE messy_mmforce
! ************************************************************************

  ! ----------- >

  USE messy_main_constants_mem, ONLY: DP

  IMPLICIT NONE
  PRIVATE

  PUBLIC :: DP

  ! ----------- <

  CHARACTER(LEN=*), PARAMETER, PUBLIC :: modstr = 'mmforce'
  CHARACTER(LEN=*), PARAMETER, PUBLIC :: modver = '1.1'

  ! CTRL NAMELIST SWITCH(ES)
  INTEGER,  PUBLIC :: i_month = 1
  REAL(DP), PUBLIC :: r_dudt  = 2.0_dp

  REAL(DP), PUBLIC, SAVE :: dayno ! number of day in year (set in global_start)

  PUBLIC :: mmforce_read_nml_ctrl
  PUBLIC :: mmforce_physc_int
  !PRIVATE :: mforc_physct
  !PRIVATE :: mforc_physc1

CONTAINS

! ------------------------------------------------------------------------
  SUBROUTINE mmforce_physc_int(vom, press, philat, forc, hw)
```

```
    ! I/O
    REAL(DP), DIMENSION(:,:), INTENT(INOUT) :: vom
    REAL(DP), DIMENSION(:,:), INTENT(IN)    :: press
    REAL(DP), DIMENSION(:),   INTENT(IN)    :: philat
    REAL(DP), DIMENSION(:,:), INTENT(OUT)   :: forc
    REAL(DP), DIMENSION(:,:), INTENT(OUT)   :: hw

    SELECT CASE(i_month)
    CASE(0)
       CALL mforc_physct(vom, press, philat, forc, hw)
    CASE(1)
       CALL mforc_physc1(vom, press, philat, forc, hw)
    CASE(7)
       CALL mforc_physc1(vom, press, philat, forc, hw)
    CASE DEFAULT
       ! CANNOT BE REACHED
    END SELECT

  END SUBROUTINE mmforce_physc_int
! ------------------------------------------------------------------------

! ------------------------------------------------------------------------
  SUBROUTINE mmforce_read_nml_ctrl(status, iou)

    USE messy_main_tools, ONLY: read_nml_open, read_nml_check, read_nml_close

    IMPLICIT NONE

    ! I/O
    INTEGER, INTENT(IN)  :: iou    ! logical I/O unit
    INTEGER, INTENT(OUT) :: status ! error status

    ! LOCAL
    CHARACTER(LEN=*), PARAMETER  :: substr = 'mmforce_read_nml_ctrl'
    LOGICAL                      :: lex          ! file exists?
    INTEGER                      :: fstat        ! file status

    NAMELIST /CTRL/ i_month, r_dudt

    ! initialize
    status = 1 ! error

    CALL read_nml_open(lex, substr, iou, 'CTRL', modstr)
    IF (.NOT.lex) RETURN    ! <modstr>.nml does not exist

    READ(iou, NML = CTRL, IOSTAT = fstat)
    CALL read_nml_check(fstat, substr, iou, 'CTRL', modstr)
    IF (fstat /= 0) RETURN  ! error while reading namelist

    ! diagnose namelist and set global switches
    ! check namelist entries
    SELECT CASE(i_month)
    CASE(0)
       WRITE(*,*) substr,': ... TRANSIENT'
    CASE(1)
       WRITE(*,*) substr,': ... PERPETUAL JANUARY'
    CASE(7)
       WRITE(*,*) substr,': ... PERPETUAL JULY'
    CASE DEFAULT
       WRITE(*,*) substr,': ERROR: UNKNOWN SELECTION FOR i_month'
       RETURN
    END SELECT

    WRITE(*,*) substr,': FORCING TENDENCY = ',r_dudt,' m/s/day'

    CALL read_nml_close(substr, iou, modstr)

    status = 0 ! no error

  END SUBROUTINE mmforce_read_nml_ctrl
```

```
! ------------------------------------------------------------------------

! ------------------------------------------------------------------------
  SUBROUTINE mforc_physc1(vom, press, philat, forc, hw)

    IMPLICIT NONE

    INTRINSIC :: ASIN, SIN, SIZE

    ! I/O
    REAL(DP), DIMENSION(:,:), INTENT(INOUT) :: vom
    REAL(DP), DIMENSION(:,:), INTENT(IN)    :: press
    REAL(DP), DIMENSION(:),   INTENT(IN)    :: philat
    REAL(DP), DIMENSION(:,:), INTENT(OUT)   :: forc
    REAL(DP), DIMENSION(:,:), INTENT(OUT)   :: hw

    ! LOCAL
    REAL(DP) :: lati, latib, pi, dudtf
    INTEGER ::  jk, jp
    INTEGER :: nproma, nlev

    nproma = SIZE(vom,1)
    nlev   = SIZE(vom,2)

    pi=2.0_dp*asin(1.0_dp)

    dudtf=r_dudt/86400.0_dp   ! => 2.3148*10^-5 m/s^2 ,
    !                                       corresponds to 2 m/s /day

    DO  jp = 1, nproma    ! vector loop

       lati = philat(jp) ! degrees
       latib=lati*pi/180.0_dp    ! radian

       DO jk = 1, nlev    ! level loop

!
!     hw(p) = 1.0                    for p < 10 hPa
!             (100 hPa -p)/90 hPa    for 10 hPa < p < 100 hPa
!             0.                     for p > 100 hPa


          IF (press(jp,jk) > 10000._dp) THEN

             hw(jp,jk)=0.0_dp

          ELSE IF (press(jp,jk) <= 10000._dp .and. press(jp,jk) > 1000._dp) THEN

             hw(jp,jk)=(10000.0_dp - press(jp,jk))/9000.0_dp

          ELSE

             hw(jp,jk)=1.0_dp

          ENDIF


          ! calculate forcing
          ! for perpetual july runs set IF (lati >= 0.0_dp) THEN ...

          month: IF (i_month == 1) THEN

             IF (lati <= 0.0_dp) THEN   ! zero forcing on SH -> perp. january

                forc(jp,jk)=0.0_dp

             ELSE

                forc(jp,jk)=(sin(2.0_dp*latib))**2 * hw(jp,jk) * dudtf

             ENDIF
```

```
          ELSE

             IF (lati >= 0.0_dp) THEN   ! zero forcing on NH -> perp. july

                forc(jp,jk)=0.0_dp

             ELSE

                forc(jp,jk)=(sin(2.0_dp*latib))**2 * hw(jp,jk) * dudtf

             ENDIF

          END IF month

          vom(jp,jk) = vom(jp,jk) + forc(jp,jk)


       ENDDO   ! level loop


    ENDDO   ! vector loop

END SUBROUTINE mforc_physc1
! ----------------------------------------------------------------------

! ----------------------------------------------------------------------
  SUBROUTINE mforc_physct(vom, press, philat, forc, hw)

    ! this subroutine contains a time-dependent zonal wind forcing
    ! and should NOT be used in perpetual january runs

    IMPLICIT NONE

    INTRINSIC :: ASIN, SIN, SIZE

    ! I/O
    REAL(DP), DIMENSION(:,:), INTENT(INOUT) :: vom
    REAL(DP), DIMENSION(:,:), INTENT(IN)    :: press
    REAL(DP), DIMENSION(:),   INTENT(IN)    :: philat
    REAL(DP), DIMENSION(:,:), INTENT(OUT)   :: forc
    REAL(DP), DIMENSION(:,:), INTENT(OUT)   :: hw

    ! LOCAL
    REAL(DP) :: lati, latib, pi, dudtf
    REAL(DP) :: twnh, twsh, count
    INTEGER  :: jk, jp
    INTEGER  :: nproma, nlev

    nproma = SIZE(vom,1)
    nlev   = SIZE(vom,2)

    pi=2.0_dp*asin(1.0_dp)

    dudtf=r_dudt/86400.0_dp   ! => 2.3148*10^-5 m/s^2 ,
!                                      corresponds to 2 m/s /day

!      temporal weighting factors
!      forcing on northern hemisphere (twnh) starts on 15th october,
!      max on 15th january, end of forcing on 16th april
!      forcing on southern hemisphere (twsh) starts on 16th april,
!      max on 16th july, end of forcing on 15th october


    count = dayno - 288.75_dp

    IF (dayno .ge. 106.25_dp .and. dayno .le. 288.75_dp) THEN

       twnh = 0.0_dp
       twsh = sin(pi*(count-182.5_dp)/182.5_dp)
```

```
    ELSE

       twnh = sin(pi*count/182.5_dp)
       twsh = 0.0_dp

    ENDIF

    DO  jp = 1, nproma    ! vector loop

       lati = philat(jp) ! degrees
       latib=lati*pi/180.0_dp    ! radian

       DO jk = 1, nlev    ! level loop

!
!     hw(p) = 1.0                    for p < 10 hPa
!             (100 hPa -p)/90 hPa    for 10 hPa < p < 100 hPa
!             0.                     for p > 100 hPa


          IF (press(jp,jk) > 10000._dp) THEN

             hw(jp,jk)=0.0_dp

          ELSE IF (press(jp,jk) <= 10000._dp .and. press(jp,jk) > 1000._dp) THEN

             hw(jp,jk)=(10000.0_dp - press(jp,jk))/9000.0_dp

          ELSE

             hw(jp,jk)=1.0_dp

          ENDIF


          ! calculate forcing

          IF (lati <= 0.0_dp) THEN

             forc(jp,jk)= twsh*(sin(2.0_dp*latib))**2 * hw(jp,jk) * dudtf

          ELSE


             forc(jp,jk)= twnh*(sin(2.0_dp*latib))**2 * hw(jp,jk) * dudtf

          ENDIF


          vom(jp,jk) = vom(jp,jk) + forc(jp,jk)

       ENDDO   ! level loop

    ENDDO   ! vector loop

  END SUBROUTINE mforc_physct
! ------------------------------------------------------------------------

! ************************************************************************
END MODULE messy_mmforce
! ************************************************************************
```

```
! ************************************************************************
MODULE messy_mmforce_e5
! ************************************************************************

  USE messy_mmforce

  IMPLICIT NONE
  PRIVATE

  INTRINSIC :: NULL

  ! cpl namelist switches
  LOGICAL :: l_diag_out_force = .FALSE.
  LOGICAL :: l_diag_out_hw = .FALSE.

  ! WORKSPACE
  ! pointer to stream elements
  REAL(DP), DIMENSION (:,:,:), POINTER :: hw    => NULL()
  REAL(DP), DIMENSION (:,:,:), POINTER :: forc  => NULL()
  REAL(DP), DIMENSION (:,:,:), POINTER :: press  => NULL()

  ! PUBLIC INTERFACE ROUTINES
  PUBLIC :: mmforce_initialize
  PUBLIC :: mmforce_init_memory
  PUBLIC :: mmforce_init_coupling
  PUBLIC :: mmforce_global_start
  PUBLIC :: mmforce_physc
  !PRIVATE :: mmforce_read_nml_cpl

CONTAINS

! ------------------------------------------------------------------------
  SUBROUTINE mmforce_initialize

    ! ECHAM5/MESSy
    USE messy_main_mpi_bi,   ONLY: p_parallel_io, p_io, p_bcast, finish
    USE messy_main_tools_bi, ONLY: find_next_free_unit

    IMPLICIT NONE

    ! LOCAL
    CHARACTER(LEN=*), PARAMETER :: substr = 'mmforce_initialize'
    INTEGER         :: iou    ! I/O unit
    INTEGER         :: status ! error status

    ! INITIALIZE CTRL
    IF (p_parallel_io) THEN
       iou = find_next_free_unit(100,200)
       ! *** CALL SMCL ROUTINE:
       CALL mmforce_read_nml_ctrl(status, iou)
       IF (status /= 0) CALL finish(substr)
    END IF
    CALL p_bcast(i_month, p_io)
    CALL p_bcast(r_dudt, p_io)

    ! INITIALIZE CPL
    IF (p_parallel_io) THEN
       iou = find_next_free_unit(100,200)
       ! *** CALL SMIL ROUTINE:
       CALL mmforce_read_nml_cpl(status, iou)
       IF (status /= 0) CALL finish(substr)
    END IF
    CALL p_bcast(l_diag_out_force, p_io)
    CALL p_bcast(l_diag_out_hw, p_io)

  END SUBROUTINE mmforce_initialize
! ------------------------------------------------------------------------

! ------------------------------------------------------------------------
  SUBROUTINE mmforce_init_memory
```

```
    USE mo_memory_base,   ONLY: t_stream, new_stream, add_stream_element

    IMPLICIT NONE

    TYPE (t_stream),  POINTER :: sforc

    call new_stream(sforc, modstr)

    call add_stream_element(sforc, 'forc', forc, units='m/s^2' &
         , longname= 'momentum forcing', lpost = l_diag_out_force)

    call add_stream_element(sforc, 'hw', hw &
         , longname= 'weighting factor', lpost = l_diag_out_hw)

  END SUBROUTINE mmforce_init_memory
! ------------------------------------------------------------------------

! ------------------------------------------------------------------------
  SUBROUTINE mmforce_init_coupling

    USE mo_memory_base,   ONLY: get_stream, get_stream_element, t_stream

    IMPLICIT NONE

    TYPE (t_stream),  POINTER :: stream

    call get_stream(stream, 'messy')

    call get_stream_element(stream, 'press', press)

  END SUBROUTINE mmforce_init_coupling
! ------------------------------------------------------------------------

! ------------------------------------------------------------------------
  SUBROUTINE mmforce_global_start

    USE messy_main_bmluse_bi, ONLY: get_year_day, current_date
    USE messy_mmforce, ONLY: dayno

    IMPLICIT NONE

    dayno = get_year_day(current_date)

  END SUBROUTINE mmforce_global_start
! ------------------------------------------------------------------------

! ------------------------------------------------------------------------
  SUBROUTINE mmforce_physc

    USE messy_main_data_bi, ONLY: vom, philat_2d, jrow

    IMPLICIT NONE

    CALL mmforce_physc_int(vom(:,:), press(:,:,jrow), philat_2d(:,jrow) &
         , forc(:,:,jrow), hw(:,:,jrow))

  END SUBROUTINE mmforce_physc
! ------------------------------------------------------------------------

! ------
! PRIVATE
! ------------------------------------------------------------------------
  SUBROUTINE mmforce_read_nml_cpl(status, iou)

    USE messy_main_tools, ONLY: read_nml_open, read_nml_check, read_nml_close

    IMPLICIT NONE

    ! I/O
    INTEGER, INTENT(IN)  :: iou    ! logical I/O unit
    INTEGER, INTENT(OUT) :: status ! error status
```

```
    ! LOCAL
    CHARACTER(LEN=*), PARAMETER  :: substr = 'mmforce_read_nml_cpl'
    LOGICAL                      :: lex          ! file exists?
    INTEGER                      :: fstat        ! file status

    NAMELIST /CPL/ l_diag_out_force, l_diag_out_hw

    ! initialize
    status = 1 ! error

    CALL read_nml_open(lex, substr, iou, 'CPL', modstr)
    IF (.NOT.lex) RETURN    ! <modstr>.nml does not exist

    READ(iou, NML = CPL, IOSTAT = fstat)
    CALL read_nml_check(fstat, substr, iou, 'CPL', modstr)
    IF (fstat /= 0) RETURN  ! error while reading namelist

    CALL read_nml_close(substr, iou, modstr)

    status = 0 ! no error

  END SUBROUTINE mmforce_read_nml_cpl
! ------------------------------------------------------------------------

! ************************************************************************
END MODULE messy_mmforce_e5
! ************************************************************************
```

# Acknowledgment

Sincere thanks are given to

Professor Dr. Ulrike Langematz, my supervisor, for her constant guidance, support and encouragement. I appreciate very much the opportunities to work to a large extent independently and to attend international conferences as well as to get involved in teaching.

Professor Joanna Haigh at Imperial College London for being the second examiner of my dissertation and for encouraging discussions.

Professor Dr. Katja Matthes for numerous extremely fruitful discussions, for the provision of ready-for-use input data for the simulations and WACCM model output from the transient simulation with filtered forcings.

Dr. Kiyotaka Shibata at MRI in Tsukuba, Japan, for providing MRI-CCM model output from the transient simulation with filtered forcings.

Dr. Christoph Brühl at Max-Planck-Institute for Chemistry Mainz for inspiration to the sensitivity study about the solar influence on ozone at the solar rotational timescale.

Dr. Andreas Baumgärtner and Dr. Patrick Jöckel at Max-Planck-Institute for Chemistry Mainz and Deutsches Zentrum für Luft- und Raumfahrt Oberpfaffenhofen, respectively, for sharing their knowledge about the chemistry climate model and for providing tailor-made input data.

Dipl.-Phys. Christian Blume for preparing the input data for the EMAC-FUB simulation with filtered forcings.

Dr. Katja Grunow, Dr. Andreas Kerschbaumer and Dipl.-Met. Sophie Oberländer for careful and professional proofreading of this report. Dr. Katja Grunow and Dipl.-Phys. Anke Hamann-Reinus are, moreover, acknowledged for immediate help with Latex problems.

Manuela Vogelsang, M.A., and Dr. Anne Wetzel for proofreading this report with regard to linguistic and stylistic pitfalls.

Nicola Hoffleit for preparing Figure 2.5.

Markus Kunze, my room mate, for all the answers especially to questions concerning postprocessing programmes, for invaluable immediate help with most problems and for the excellent working atmosphere in our room.

Dr. Wolfgang Baumann, Dr. Bernd Kallies and Dr. Matthias Läuter at Konrad-Zuse-Zentrum für Informationstechnik Berlin as well as Gabriel Gaus and Dr. Claus-Peter Rückemann at RRZN Hannover for extraordinary service even on weekends to get the simulations to run again.

Professor Dr. Christoph Jacobi at Leipzig University for awakening my initial interest in processes taking place above the tropopause.

Janna Abalichin, Sophie Oberländer, Anke Hamann-Reinus, Stefanie Meul and Christian Blume, fellow PhD students in the working group "Physics of the Middle Atmosphere" who each in her or his own way contribute to a very comfortable atmosphere in our working group. Their encouragments and cheer-ups especially during the last months are very much appreciated.

Peter Névir, Eberhard Reimer, Gregor Leckebusch and Philipp Lorenz for countless car rides to the canteen as well as to the "usual" lunch group: Thorsten Weber, Antje Claussnitzer, Markus Donat, Heike Hübener, Dominik Renggli, Christian Blume, Tobias Pardowitz, Jens Grieger, Thomas Bergmann for helping the thoughts go away from science during the lunch break.

My friends near and far who had to wait for a sign of life from me during the last months: Eva Emmrich, Mia Hatje, Uli Lerche, Jule Lorenz, Toni Müller, Anja Vatterodt and Anne Wetzel.

Special thanks to my parents, Karin and Hellmuth Kubin, for always being there for me, as well as for calming me down, taking away the panic, damping attacks of perfectionism and for enduring the last months with rare and short visits.

Very special thanks to Dirk for being himself, for being there for me, for having great patience with me working every minute in the last months. I am looking forward to the future.

For privacy reasons the CV has been omitted in the electronic version.